

University of Nottingham
UK | CHINA | MALAYSIA

# Brain Oscillations, Connectomes and Neurophysiology

Lucrezia Liuzzi, M.Sci.

Thesis submitted to the University of Nottingham
for the degree of Doctor of Philosophy

May 2019

# Contents

**Abstract** **iv**

**Acknowledgements** **v**

**Thesis Introduction** **1**

**1 Generation and detection of the MEG signal** **9**
1.1 Brain Electrophysiology . . . . . 9
1.1.1 The Neuron . . . . . 9
1.1.2 Pyramidal Neurons versus Stellate cells . . . . . 10
1.1.3 The synapse and neurotransmission . . . . . 11
1.1.4 Equilibrium Potential . . . . . 13
1.1.5 Action Potentials . . . . . 14
1.1.6 Postsynaptic Potentials . . . . . 15
1.1.7 Magnetic fields at a distance . . . . . 16
1.2 Neuronal responses observable with MEG . . . . . 16
1.2.1 Evoked responses . . . . . 16
1.2.2 Oscillatory responses . . . . . 17
1.2.3 Oscillations and functional connectivity . . . . . 20
1.3 Instrumentation . . . . . 22
1.3.1 Magnetic field detection . . . . . 22
1.4 Superconductivity . . . . . 25
1.5 Josephson's Junction . . . . . 28
1.5.1 SQUIDs . . . . . 31
1.5.2 Gradiometers . . . . . 33
1.5.3 Higher order gradiometers . . . . . 35
1.5.4 The CTF-MEG system . . . . . 37

**2 Functional connectivity assessment in MEG** **39**
2.1 Forward solution . . . . . 39
2.1.1 The Geselowitz formula . . . . . 42
2.1.2 The Sarvas Equation . . . . . 43
2.1.3 Multiple sphere extension . . . . . 45
2.2 Inverse Problem . . . . . 47
2.2.1 Beamforming . . . . . 49
2.2.2 Source angle selection . . . . . 52
2.2.3 Induced responses localisation . . . . . 53
2.2.4 Beamforming with anatomical atlases . . . . . 54
2.3 Functional Connectivity . . . . . 56

2.3.1 Leakage correction . . . 60
2.4 Statistical methods . . . 63
2.4.1 Phase scrambling . . . 64

**A Sarvas solution for a uniform sphere 66**

**3 Optimizing beamforming for static functional connectivity 69**
3.1 Introduction . . . 69
3.2 Co-registration . . . 71
3.2.1 Standard . . . 71
3.2.2 Headcast . . . 72
3.3 Simulations . . . 74
3.3.1 Co-registration errors . . . 77
3.3.2 Recording duration . . . 80
3.4 MEG data . . . 82
3.4.1 Source orientation consistency . . . 84
3.4.2 Functional connectivity consistency . . . 86
3.4.3 Within session consistency . . . 91
3.5 Discussion . . . 94
3.6 Conclusion of chapter . . . 98

**B Between session correlation of functional connectivity, on a per region basis: additional figures 100**

**4 The functional role of the Beta rebound 104**
4.1 Introduction . . . 104
4.2 Experimental set-up . . . 106
4.2.1 Task . . . 107
4.2.2 Data acquisition . . . 110
4.3 Source power analysis . . . 111
4.3.1 Methods . . . 111
4.3.2 Results . . . 114
4.3.3 Induced sensory Gamma . . . 118
4.4 Functional connectivity analysis . . . 119
4.4.1 Methods . . . 119
4.4.2 Effect of attention on connectivity . . . 121
4.5 Likelihood of correct responses . . . 126
4.5.1 Behavioural results . . . 127
4.6 Discussion . . . 129

**C Further Atlas Based Analysis 132**

**5 Neurotransmission and beta band oscillations 139**
5.1 Introduction . . . 139
5.2 MR Basics . . . 140
5.2.1 Interaction with a static magnetic field . . . 141
5.2.2 Interaction with Radio frequency pulses . . . 144
5.2.3 Relaxation . . . 145
5.3 MRS . . . 148

5.3.1 Chemical shift . . . 148
5.3.2 J-coupling . . . 150
5.4 Methods . . . 151
5.4.1 Data acquisition . . . 151
5.4.2 Edited sequences . . . 153
5.4.3 Data processing . . . 154
5.4.4 Link to MEG and statistical techniques . . . 157
5.5 Results . . . 158
5.5.1 Relationship to MEG . . . 158
5.5.2 Relationship between run 1 and 2 . . . 161
5.5.3 Comparison of GABA and behavioural performance . . . 161
5.6 Discussion . . . 163

**D STEAM data** **165**

**6 Final Remarks** **173**
6.1 Study limitations . . . 174
6.2 The end . . . 175

**References** **176**

# Abstract

Magnetoencephalography (MEG) is a neuroimaging technique allowing the investigation of brain function non-invasively, by detecting changes in magnetic fields outside the head induced by ensembles of neurons firing synchronously. Oscillatory electrophysiological activity measured using MEG has been shown to support long range functional communication in the brain, showing close resemblance to known fMRI functional networks. Interest in functional connectivity is growing as disruptions in the functional connectome have been implicated in both neurological and mental health conditions. However, the connection between brain oscillations, functional connectivity and neurochemistry still remains largely unexplored. In this thesis I aim to shed light on this connection.

The thesis begins with a description of the theory behind neural signals measurable with MEG (chapter 1) and the details of source localisation and functional connectivity (chapter 2). Following this, there are three experimental chapters: in chapter 3 I test how practical aspects of experimental design affect the intra-subject repeatability of the MEG functional connectome. The use of a foam headcast, which is known to improve co-registration accuracy, is shown to increase significantly the between session repeatability of both beamformer reconstruction and functional connectivity estimation. Moreover longer recordings offer a large improvements in repeatability of functional connectivity, with analysis suggesting this result is caused by a genuine effect of brain state. In chapter 4 I present MEG data recorded during a sensory attention task, in which participants were asked to identify braille patterns presented to their fingers, whilst simultaneously switching attention between hands. Whilst a weight of evidence suggests that 'low' frequency (beta band) oscillations are representative of cortical inhibition, more recent studies have closely linked these same phenomena to functional connectivity. Results show that attentional modulation changes beta dynamics in primary sensory cortex, with attended stimuli generating lower post-stimulus responses (i.e. lower beta 'rebound'); this effect is driven by the transient formation and dissolution of distributed networks, which form in response to unattended stimuli, and likely facilitate top down inhibitory influence on the primary sensorimotor cortex. The results are related to subject behaviour, with high pre-stimulus beta connectivity leading to poor task performance. Finally, in chapter 5, combining MEG and Magnetic Resonance Spectroscopy (MRS), I show that beta oscillations are directly related to GABAergic signalling. The results here presented offer a mechanistic interpretation of the role played by beta oscillations in mediating inhibition. This has implications for our understanding of neural oscillations and connectivity in both the healthy brain and a range of disorders.

# Acknowledgements

First of all my greatest thanks go to my main supervisor Dr (now Professor!) Matt Brookes for giving amazing support and direction over the whole of my PhD, as well as reading this entire thesis in record time. Thank you for giving me more advice and opportunities that I ever thought possible.

I have many people to thank for the experimental work: my supervisor Prof. Peter Morris, as well as Chen and Bernard for setting up the spectroscopy sequences, teaching me everything MRS related and generally being the nicest people. Ryan and Gill, thank you for helping me scan what felt like an unmanageable number of volunteers and thanks to Mehri and Jan as well for help with scanning at the 7T. A large part of this thesis would also not have been possible without Dr Markus Bauer, who designed the 'braille study' and finally made the braille stimulators work after months of me hitting a wall.

To Prejaas, thank you for being my first point of contact at the beginning, teaching me about connectivity and being a never ending source of ideas every time I thought we hit a dead end. Without you I would have been lost in those first months. Also thank you for providing a very welcome distraction from writing this thesis and giving me an excuse to visit Amsterdam by inviting me to your wedding. I hope you manage to get back to research soon!

Not least my special thanks go to George, for fixing everything and always being the super helpful technical knowledge guru. To all the members of the MEG team, you are the best travel companions and an amazing bunch: I blame you all for now being able to drink full pints like a British person and Lauren, thank you for making me feel useful by showing me the most entertaining matlab errors.

Of course thanks to Lesley, the best person in the office, and the SPMIC as a whole. I could not have hoped for a better place or a nicest group of people: you all made my life better these past few years.

Finally to my mom, Franca, without whom I would have never come to Nottingham in the first place. Senza di te non sarei mai arrivata così lontano, sia geograficamente che figurativamente. Grazie di essere la mia migliore amica ma anche una gran rompiscatole. Avermi insegnato a contare prima che imparassi a camminare deve essere servito a qualcosa. Questa tesi è anche un po' merito tuo, la sempre orgogliosa 'mamma di Lucrezia'.

# Introduction

Brain imaging has become a flourishing field of research which has changed the way we can study and understand the human brain. The modern field of neuroimaging, allowing the non-invasive imaging of the living brain, started in the late $19^{\text{th}}$ century with the first x-ray images of the skull, proving measures of structure, and was followed with the recording of electrical brain activity from scalp electrodes, i.e. electroencephalography (EEG) [Berger, 1929], which provided a measure of brain function. Since then, new technologies such as computed tomography (CT), positron emission tomography (PET) [Fox et al., 1984] and magnetic resonance imaging (MRI) [Lauterber, 1973; Mansfield and Grannell, 1973] have significantly advanced our ability to image the living human brain. Nowadays these techniques are commonly used around the world for clinical diagnoses. Further, new advancements in MRI allow for high contrast anatomical images of the brain with sub-millimetre resolution. However, despite the advancement of our knowledge of brain structure, our understanding of brain function is still limited. In today's world, this has become one of the most significant and challenging scientific questions. Its solution is extremely important, particularly given the known problems with disorders surrounding mental health, dementia and neurodevelopment. The development of new techniques to understand brain function in health and disease is therefore critical.

## Functional Brain Imaging Techniques

There are a number of available technologies with which to measure brain function:

- Positron emission tomography (PET) can be effectively used to measure the transfer of specific tracer compounds through the brain, reflecting brain metabolic pathways. PET is based on the injection of radioactivity isotopes such as $^{18}$F, which can be used to follow glucose metabolism, and $^{15}$O for detection of oxygen consumption. The short-lived radionuclei used in PET emit a positron during decay, which combining with a nearby electron releases two gamma rays travelling in exactly opposite directions. The detection of these high energy photons allows precise reconstruction of the isotope position inside the brain, and hence tracking of cellular metabolism.

- Magnetic Resonance Spectroscopy (MRS) uses the chemical specificity of magnetic resonance to allow quantification of metabolites and neurotransmitters in vivo and is free from ionising radiation. $^{1}$H based MRS provides information on a large range of chemical compounds and can be performed in standard MRI scanners (though higher field scanners are preferable). Depending on the metabolite of interest $^{1}$H MRS can suffer from poor signal to noise, limited by short scan times for in vivo applications and spectral overlap. However, with appropriate radio frequency coils, MRS can also be performed on different atomic species, such as $^{13}$C (requiring injection of $^{13}$C isotope) and $^{31}$P, proving disparate information on a number of metabolic pathways.

- Functional MRI (fMRI) [Ogawa et al., 1990] can probe brain function without exposure to ionising radiation. fMRI does not require any additional equipment beyond a "high field" MRI scanner (3T field or above) and has proved very successful in functional neuroimaging thanks to its excellent spatial resolution and the nowadays large availability of MRI scanners for both research and clinical use. fMRI detects changes in blood oxygenation,

which fluctuates, depending on brain activity, on a timescale of seconds. The BOLD signal is reflective of neuronal metabolism, which although closely linked with ionic pumps and electrical firing in cells, remains an indirect measure of the underlying faster chemical and electrical processes.

- Functional near-infrared spectroscopy (fNIRS) is an optical technique giving information on localised haemodynamic responses on the outer surface of the cortex [Ferrari et al., 1985]. fNIRS is based on the different light absorbance of oxy and deoxy-hemoglobin in the near-infrared spectrum and can thus give similar brain functional information to BOLD fMRI, although with limited spatial resolution and constrained to surface regions of the brain.

- A direct measure of neuronal activity can be obtained by detecting their electrical activity through electroencephalography (EEG). EEG gives real time recording of electrical potential recorded on the scalp surface, induced by the synchronous electrical firing of thousands of neurons. Although the time resolution of EEG is excellent, its spatial specificity is severely limited by the complex electrical conductivity of the head. Spatially specific EEG can be recorded invasively with intracranial electroencephalography (iEEG) or electrocorticography (ECoG), although their applications are obviously severely limited to a small number of patients (and recording locations) with cortical electrodes implanted often in preparation of surgical removal of epileptic foci.

- Magnetoencephalography (MEG) [Cohen, 1968] is a non-invasive technique based on the detection of magnetic fields induced by the brain electrophysiological activity. MEG combines the strength of EEG (real time and direct measure of neuronal function) with good spatial resolution (of the order of a few millimetres). Current MEG systems provide coverage of the whole head, allowing the reconstruction of electrical activity of neurons over all regions of the brain cortex.

## Brain connectivity

All of the above techniques were originally used to pinpoint where, and when, brain "activity" occurs in response to some task. However in recent years the neuroimaging community has started to move away from this functionally segregated view of the brain, where each area is considered in isolation to be responsible for a specific function (e.g. hearing, movement, language etc.), towards a view of an integrated connectome, where separate brain areas operate in concert. The idea of a brain connectome can be considered anatomically by measuring the individual white matter tracts connecting both near and distal regions, leading to imaging techniques such as the MR based Diffusion Tensor Imaging (DTI). Anatomical imaging has shown that white matter connections can change over years through healthy growth, ageing and learning [Johansen-Berg, 2010; Maguire et al., 2000; Scholz et al., 2009].

However the brain is able to use this (in the short term) 'static' network of physical connections to perform a variety of functions with millisecond speed. It follows that if we aim to understand how the brain works we should aim to not only understand the structural connectome but also the functional connectome. This is particularly key in understanding various mental health disorders, which often do not present anatomical abnormalities. As an example a leading theory for explaining the cause of schizophrenia, the disconnection hypothesis [Friston, 1998], is based on a finding of abnormal functional connections in regions associated with salience in schizophrenia patients [Palaniyappan and Liddle, 2012]. Moreover recent MEG work has shown that "oscillations" (rhythmic activity synchronised across cell assemblies) that dominate electrophysiological measures are diminished in schizophrenia [Robson et al., 2016], with this decrease relating to symptoms severity. A similar effect of beta (13-30Hz) oscillatory amplitude was also shown in healthy subjects by the negative correlation of beta amplitude and schizotipy (a spectrum of 'schizophrenia-like' personality characteristics) [Hunt

et al., 2018]. Localised beta oscillations have also been demonstrated to be affected in other conditions, such as Autism Spectrum Disorder [Gaetz et al., 2010], and are hypothesised to have a top-down inhibitory function on the sensorimotor cortex. At the same time recent work [Brookes et al., 2011b; Hipp et al., 2012] has demonstrated that correlations of neuronal oscillations, detected from MEG data over separate brain regions, closely match fMRI canonical networks of functional connections [Biswal et al., 1995], with beta oscillations in particular showing the best agreement [Hunt et al., 2016]. It follows that studying the functional connectome, from the point of view of neural "oscillations" might yield new insights into healthy pathological brain function.

## Aims of thesis

The work of this thesis aims to bridge the gap between the well know modulation of beta amplitude localised in the sensorimotor cortex and whole brain networks of functional connections supported by the same oscillatory rhythm measured with MEG. The assessment of functional connectivity in MEG is still an emerging field and only in the last few years has it started to fully exploit the temporal resolution of electrophysiological data [Baker et al., 2014; O'Neill et al., 2015]. To this aim the thesis begins by investigating the technical aspects of functional connectivity measurement in MEG data (such as selection of connectivity metrics) and the reasons behind previously reported [Colclough et al., 2016] low reproducibility of MEG connectivity. We then apply whole brain connectivity analysis in task data to, for the first time, detect transient ($\sim$ 500ms) networks of functional connectivity significantly modulated by attention and correlating with behavioural outcome (i.e. task performance). The last piece of the puzzle is the underlying neurochemistry. If beta oscillations are indeed reflective of neural inhibition, it follows that they might be linked to inhibition at the synaptic level. Gaetz et al. [2011] previously demonstrated correlations between the major inhibitory neurotransmitter GABA

and beta rebound (although in a small cohort). Work by Muthukumaraswamy et al. [2013] reported that elevated GABA levels by pharmacological manipulation also induced increased beta oscillatory power. Here, through $^{1}$H MRS at 7T, we quantify GABA concentrations in the sensorimotor cortex of 46 subjects and demonstrate a correlation between their beta power and individual concentrations of GABA. Overall the work here presented brings together localised electrophysiological measures, dynamic functional connections and neurochemistry to elucidate the important mechanistic role of beta oscillations in the human brain.

## Structure of thesis

The work in this thesis is outlined through five chapters (1-5), covering the theory behind MEG signal detection, signal reconstruction methods and three experimental chapters.

- **Chapter 1: Generation and detection of the MEG signal**.

  Chapter 1 covers the physics behind MEG signal detection. The chapter starts from a physical model of neuronal currents, identifying which electrical phenomenon is behind the detectable electrical and magnetic potentials seen in non-invasive electrophysiology (M-EEG). The next section describes the type of neuronal responses observable with MEG, focusing on oscillatory responses and introducing the concept of functional connectivity, which will be key for the later experimental chapters. The bases of magnetic field detection in current MEG scanners are also described, outlining the physical principles of the superconducting quantum interference devices (SQUID) and the necessary components for effective MEG signal detection, such as environmental noise and gradiometry.

- **Chapter 2: Functional connectivity assessment in MEG**.

  The second theory chapter is centred on the MEG signal analysis, source reconstruction and measurements of functional connectivity. The first section

starts with the mathematical description of the forward problem in MEG and Sarvas spherical solution. The chapter then moves on to the inverse problem, focusing on the beamforming method for source estimation. The last section is centred on the connectivity metrics used in experimental chapters 3 and 4, introducing whole brain functional connectivity with anatomical atlases and considerations for experimental biases, such as spatial leakage. The chapter concludes with a brief description of some statistical methods for functional connectivity analysis.

- **Chapter 3: Optimizing beamforming for static functional connectivity**

  The first experimental chapter describes the work published in NeuroImage in 2017 [Liuzzi et al., 2017] setting the basis for accurate assessment of functional connectivity with beamforming source reconstruction. The work explores the effects of co-registration error and recording duration on the inverse solution and source angle selection, as well as on connectivity assessment with a range of common amplitude and phase metrics in both simulation and experiment. Co-registration error is tested through the use of custom made foam head-casts [Troebinger et al., 2014] in repeated resting state MEG recordings in three volunteers. The results show a clear improvement on repeatability of source estimation with the use of head-casts. The length of MEG recording showed a marked effect on the within subject stability of connectivity networks. Discrepancy between simulated 'stationary' connectivity and experimental measures provides further proof that the brain functional connectome is in fact time-changing, i.e. 'dynamic'.

- **Chapter 4: The functional role of the Beta rebound**

  The second experimental chapters further explores the idea of a dynamic functional connectivity in order to better analyse the inhibitory role of beta oscillations in the sensorimotor system. The work in this chapter is based on

a sensory discrimination MEG data-set collected in 46 healthy volunteers, 29 of whom were scanned twice, for a total of 75 separate data-sets. The analysis found significant effects of attention on the amplitude of beta rebound following sensory stimulation of the index finger, with beta rebound increasing in non-attended probe stimuli. Through dynamic connectivity analysis with the Phase Difference Derivative (PDD) metric, the beta rebound was shown to be part of a short lived ($\sim$ 500ms) wider connectivity network involving the sensory, motor, parietal and temporal cortices. We hypothesise that this integrative network is reflective of an attention driven 'top-down' shut down of the involved regions. As further proof of the beta inhibition hypothesis we confirmed that higher beta amplitude (in agreement with Jones et al. [2010]) as well as increased beta functional connectivity preceding a target were predictive of poorer task performance.

- **Chapter 5: Neurotransmission and beta band oscillations**

  Following chapter 4 we continue exploring the connection between beta oscillation and neuronal inhibition by showing a link with neurochemistry. In this final chapter we use Magnetic Resonance Spectroscopy (MRS) at high field (7T) to measure individual concentrations of the inhibitory neurotransmitter GABA in the sensorimotor cortex in the same cohort of subjects recruited in chapter 4. The chapter starts with a description of the Nuclear Magnetic Resonance (NMR) phenomenon and $^{1}$H MRS signal acquisition and analysis. MRS data collected with a STEAM sequence in 46 subjects showed a significant correlation of individual GABA levels and beta rebound amplitude and resting beta power measured with MEG.

The thesis ends with some final remarks and discussion in Chapter 6.

# Chapter 1

# Generation and detection of the MEG signal

This chapter will cover the cellular origin of the neuro-magnetic signal and the conditions necessary for it to propagate, and be detectable, at a distance. We will discuss different types of electrical activity such as evoked potentials and neural oscillations and introduce the physical concepts behind the instrumentation that detects these electrophysiological phenomena.

## 1.1 Brain Electrophysiology

### 1.1.1 The Neuron

The human brain is an incredibly complex organ formed from approximately 86 billion neurons and a similar number of non-neuronal cells [Azevedo et al., 2009]. Neurons are electrically excitable cells that receive and transmit electrical information; they form the basis of the human nervous system and are responsible for everything from sensory perception to conscious thought. Like every eukaryotic cell, neurons contain a cell body, called the soma, which contains the cell nucleus, and specialised cell structures (see Figure 1.2) which include:

- Dendrites: ramified extensions of the cell body ending in synapses to receive incoming information.
- Axons: extended projections of the neuron serving to carry outgoing signals to other neurons.

- The Axon Hillock: located at the base of the axon, is an electrically excitable structure, containing the greatest density of sodium channels, and serving to initiate axon action-potentials.

The distribution of neuronal cell bodies differentiates grey and white matter, with grey matter hosting most of the cell bodies and dendrites (accounting for 82% of the total brain mass [Azevedo et al., 2009]) while white matter is mostly formed of long myelinated axons, which are responsible for connecting distant areas of the brain and give white matter its lighter colour.

Glial cells, or glia, are non-neuronal cells that serve as support to the neurons in the brain, helping with ion homeostasis, nutrient transportation and structural support. The axons of neurons are surrounded by a myelin sheath, a lipid rich substance formed by specialised glia, helping to electrically insulate the axon and increasing the speed of signal transmission.

### 1.1.2 Pyramidal Neurons versus Stellate cells

Neurons in the cerebral cortex fall into two main morphological categories: stellate neurons present dendrites propagating from the soma in all directions (see Figure 1.1). The high symmetry of dendritic trees in stellate neurons means electric (as well as magnetic) fields produced by these neurons will tend to cancel out at a short distance. Pyramidal neurons are present in most structures of the central nervous system, they have extended apical dendritic trees with parallel branches, basal dendrites and a pyramidal shaped soma. Pyramidal neurons are often organised in sheets with apical dendrites oriented in the same direction, and perpendicular to the cortical surface. This coherent orientation of dendrites allows magnetic fields induced by post-synaptic potentials in pyramidal neurons to add constructively, creating signals strong enough to be detected outside the head.

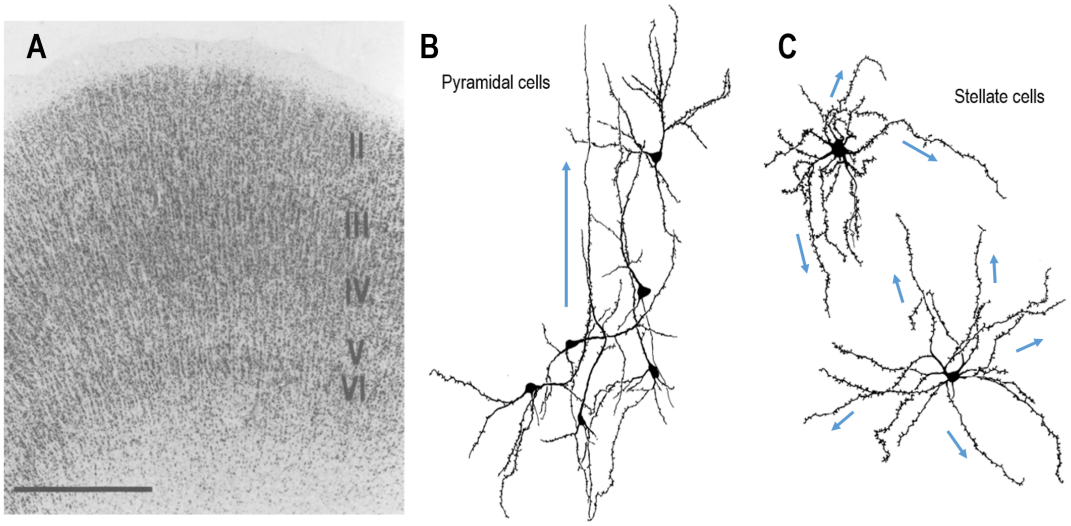



Figure 1.1: A) Cortical layers in the human auditory cortex and (B) examples of pyramidal and (C) stellate cells (pictures from Meyer et al. [1989]). The blue arrows indicate the current directions along the neurons.

### 1.1.3 The synapse and neurotransmission

Information is transmitted from neuron to neuron through a combination of electrical and chemical signalling. Electrical signalling is fundamental for long distance connections in the brain, while chemical signalling is typically used at points of contact between neurons. These points of contact are known as synapses (see Figure 1.2). Based on the direction of signal transmission we will denote the transmitting neuron as presynaptic and the receiving neuron as postsynaptic. Synapses can be excitatory (increasing intracellular potential), usually located on the dendrites, or inhibitory (decreasing intracellular potential), mostly located on the soma and/or on the axon [Spruston, 2008]. Neurotransmitter molecules are released from synaptic vesicles into the synaptic cleft and bind to receptors on the postsynaptic neuron. This chemical binding changes the morphology of proteins in the cell membrane, causing the opening of ion channels and flow of charged ions (such as $Na^+$, $K^+$ and $Cl^-$) along their concentration gradient. The sum of excitatory and inhibitory inputs determines the final intracellular potential and whether a neuron will fire. The main inhibitory neurotransmitter is GABA ($\gamma$-aminobutyric

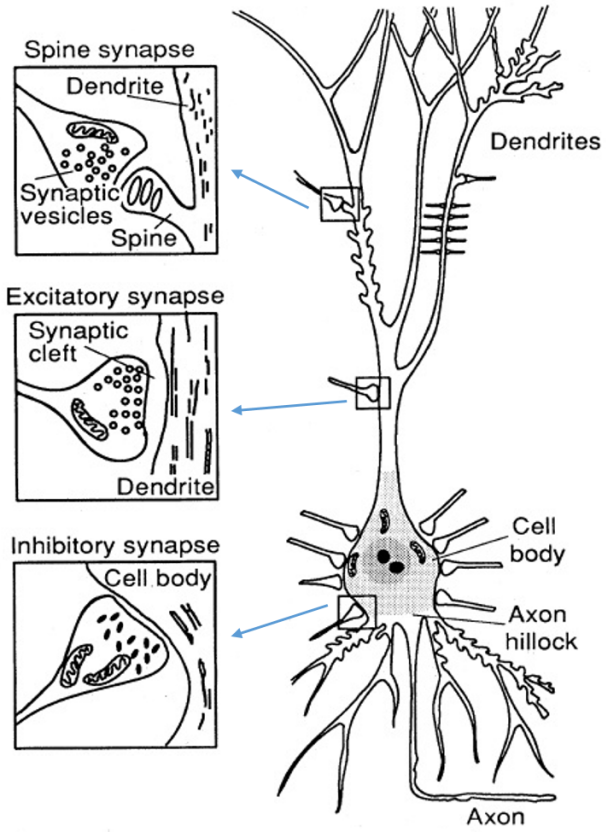



Figure 1.2: Diagram of a pyramidal neuron highlighting its specialised cell structures. Figure adapted from Hämäläinen et al. [1993].

acid) acting through synaptic $GABA_A$ and slower $GABA_B$ receptors[1]. GABA is also present in the cytoplasm, where it is involved in cellular metabolism, and in the extracellular space, where it acts to maintain a tonic cortical inhibition through extra-synaptic $GABA_A$ receptors [Belelli et al., 2009]. The most common excitatory neurotransmitters in the cortex are Glutamate (Glu), which also plays a key role in cellular metabolism, and Aspartate (Asp). GABA, Glu and Asp are all part of a common metabolic cycle and synthesized from the precursor Glutamine (Gln) [Albrecht et al., 2010]. Healthy brain function is mediated by a delicate balance of inhibition and excitation, enabled by these neurotransmitters.

[1] $GABA_B$ are metabotropic receptors that are indirectly linked to an ion channel by coupling with a G protein.

### 1.1.4 Equilibrium Potential

The intracellular and extracellular spaces are separated by a bilayer phospholipid membrane with a thickness of about 10nm. This barrier allows a cell to maintain different ion concentrations inside and outside the membrane. The most important ions for neuronal function are $Na^+$, $K^+$ and $Cl^-$. Their concentrations intra- and extra-cellularly during rest are maintained at 20 mmol/liter and 140 mmol/liter respectively for $Na^+$, 140 and 5 mmol/liter for $K^+$, and 20 to 120mmol for $Cl^-$. As the concentration of $K^+$ is much higher intracellularly and the diffusivity of $K^+$ ions is high, a Na-K pump works to maintain and re-establish equilibrium concentrations by actively pumping $K^+$ ions into the cell and $Na^+$ ions out of the cell.

As ions carry electric charge their different concentrations create a voltage across the cell membrane. At equilibrium the ion concentration $C$ is determined by thermodynamic laws which can be expressed by Boltzmann equation as:

$$C \sim \exp\left( -\frac{|e|V}{k_B T} \right), \tag{1.1}$$

Where $e$ is the electronic change, $V$ the electrical potential across the cell membrane and $k_B T$ the thermal energy given by Boltzmann constant and the absolute temperature. The voltage $V$ is then equal to the potential difference inside and outside the cell, giving the expression for Nerst equation:

$$V = V_{in} - V_{out} = \frac{k_B T}{|e|} \ln\left( \frac{C_{out}}{C_{in}} \right), \tag{1.2}$$

By adding the concentrations of all ionic pools and considering their permeability across the cell membrane, we can calculate $V$ to be about -70mV [Goldman, 1943].

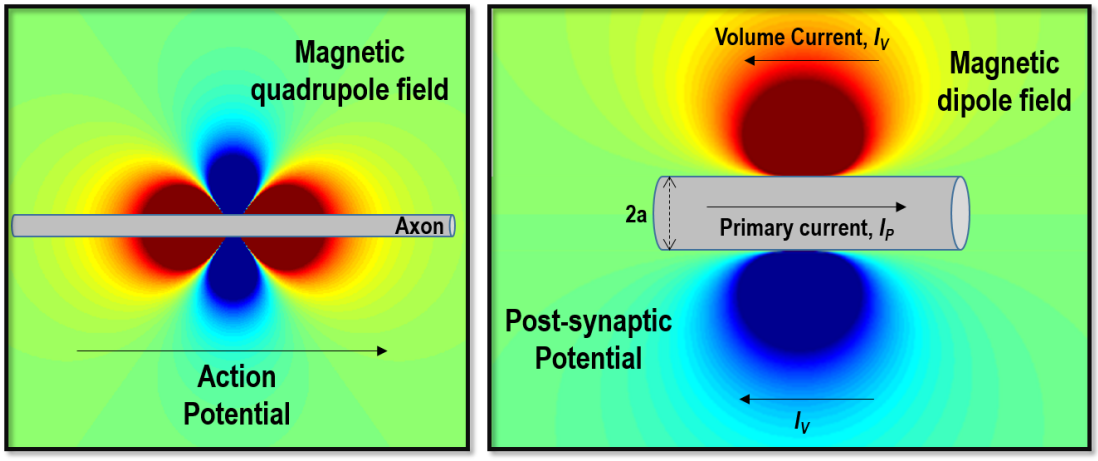



Figure 1.3: Schematic of the quadrupole potential induced by an action potential in an axon (left) and the dipole field of a post-synaptic potential in a dendrite (right).

### 1.1.5 Action Potentials

Propagation of electric currents in an axon, called action potentials, is initiated by the electrical potential at the axon hillock [Coombs et al., 1957]. When potential at the axon hillock reaches a threshold of about -55mV it triggers voltage dependent ion channels to open, changing the membrane permeability to $Na^+$ and $K^+$ ions. Following their concentration gradients the ions quickly cause the potential inside the cell to become positive (+40 mV) triggering the ion channels of neighbouring regions of the axon. Previously depolarised regions will slowly reestablish their equilibrium potential thanks to active ion pumps (causing a volume current in the opposite direction to the propagating potential). This cascade effect creates a wave of depolarisation which propagates in one direction along the axon without dimishing in amplitude. Action potentials allow the effective communication of both neighbouring and distal neurons with the final wave of depolarisation ending at a synapse of a target neuron to cause a post-synaptic potential. As the action potential is determined by the ionic concentrations its amplitude is unaffected by the strength of the triggering input, with more excitatory inputs causing instead higher firing frequency.

### 1.1.6 Postsynaptic Potentials

The opening of ion channels by a neurotransmitter at the synapse causes a post-synaptic potential (PSP) and a current inside the post-synaptic cell. Neurons will be excited or inhibited depending on the type of ion channels affected by the neurotransmitters: influx of $Na^+$ will cause the voltage to increase (depolarisation) causing an excitatory PSP, while influx of $Cl^-$ or outflux of $K^+$ will cause an hyperpolarisation of the postsynaptic cells which will be therefore less likely to fire (inhibition). Starting at the synapse the PSP decays exponentially along the direction of the dentrite [Rall, 1959]:

$$V_{PSP}(x) = \frac{\lambda r_{in}}{\pi a^2} I(x) = \frac{\lambda r_{in}}{\pi a^2} I_0 \exp(-x/\lambda), \tag{1.3}$$

with the exponential decay length parameter $\lambda = (a r_m / 2 r_{in})^{1/2}$, depending on the membrane resistance for a unit area $r_m$ ($\Omega m^2$), the resisitivity of the intracellular fluid $r_{in}$ ($\Omega m$) and the radius of the dendrite $a$.

As $\lambda$ is short ($\sim$ 0.1 - 0.2 mm) we can model the postsynaptic current as spatially invariant over the distance $\lambda$ to obtain a current dipole $Q = I\lambda$. If we know the voltage $V_{PSP}$ we can rearrange equation 1.3 to write that:

$$Q = I\lambda = \pi a^2 \sigma_{in} V_{PSP}, \tag{1.4}$$

where $\sigma_{in}$ is the intracellular conductivity.

Using the values of a = 0.5 $\mu$m, $\sigma_{in} = 1\Omega^{-1}m^{-1}$ and $V_{PSP}$ = 25 mV, we can estimate that the post synaptic potential would create a current dipole, $Q \approx$ 20 fAm [Hämäläinen et al., 1993]. However, more recent modelling, including dendritic compartments and conductivity of multiple ion species in pyramidal neurons, estimated $Q \approx 0.29 - 0.90$ pAm [Murakami and Okada, 2006], and this is in better agreement with empirical measurements [Kyuhou and Okada, 1993; Okada et al., 1997]. As the average signal measured with MEG requires a current dipole source of roughly 10 nAm [Hämäläinen et al., 1993], it follows that $10,000-$

$50,000$ neurons must be coherently "active" to produce a detectable magnetic field.

After cell depolarisation (or hyperpolarisation) ion pumps reestablish the equilibrium concentration, creating an extracellular current, called volume current, with opposite direction to the post synaptic current. Volume currents do not usually significantly contribute to the detected MEG signal as we will see in chapter 2.

### 1.1.7 Magnetic fields at a distance

Unlike dendritric currents, action potentials are better modelled by two opposite current dipoles (of about 100 fAm) forming together a current quadrupole. When detecting electric (and magnetic fields) at a distance $r$ from the current source, current dipoles create a field decreasing as $1/r^2$, while current quadrupoles drop off more quickly as $1/r^3$. Action potential are also much faster than dendritic currents, with lifetimes of about 1 ms and 10 ms respectively, meaning that the likelihood of action potentials synchronously firing is lower than for dendritic currents. Animal modelling confirmed these observations, concluding that post-synaptic currents in pyramidal neurons are most likely to be the main contributors to the origin of the MEG signal [Okada et al., 1997].

## 1.2 Neuronal responses observable with MEG

### 1.2.1 Evoked responses

Evoked responses are electrophysiological signal changes that are time and phase locked to a stimulus. Evoked responses mostly appear at stimulus on-set (or off-set) as a characteristic "spiking" or deflection in the recorded electrical signal. Their time and phase locked evolution means that the estimation of evoked response is improved by averaging successive repetitions of the same stimuli: the repeated evoked signal will be maintained while the noise (a non-phase locked signal) will decrease with the number of repeated trials (i.e. noise $\propto 1/\sqrt{n_{trials}}$,

assuming gaussian noise).

Evoked potentials have long been studied in MEG (see for example [Hari et al., 1980, 1990; Ahlfors et al., 1992]), and are routinely used in EEG for detecting abnormalities in the visual, auditory and sensorimotor systems as well as in speech processing [Walsh et al., 2005]. Evoked responses usually present a distinctive morphology of the electrical signal, named event related potential (ERP), with peaks appearing at fixed times following stimulation. In clinical settings delays in the timing of response peaks and changes in peak amplitude can be observed from EEG or MEG sensors placed over the brain's regions of interest.

### 1.2.2 Oscillatory responses

The first evidence of electrical currents in the animal brain was reported by Richard Caton [Caton, 1875] who performed measurements with a galvanometer in the brains of rabbits and monkeys and observed functional changes linked to movement and sensory stimulation. More than 50 years later, in 1929, Hans Berger first detected oscillatory electrical activity in the human brain with the first EEG system [Berger, 1929]. Berger observed the "alpha" rhythm, a spontaneous oscillation in the range of $8-13$ Hz which he showed to be modulated by visual stimuli. Indeed, more generally, oscillatory events in the brain are present spontaneously (i.e. at rest), can be modulated with stimulation, attention, and change during stages of sleep. Like evoked responses, induced oscillatory responses to tasks can be time locked to stimulus on-set and show specific dynamics depending on the type of stimulation. However, induced oscillations are not phase locked, meaning that averaging of induced responses over multiple trials would cause out-of-phase oscillations to sum destructively.

Oscillatory brain rhythms appear within various frequency ranges. They are typically classified in frequency bands which can originate from different brain regions and/or cortical layers and are associated with different functions:

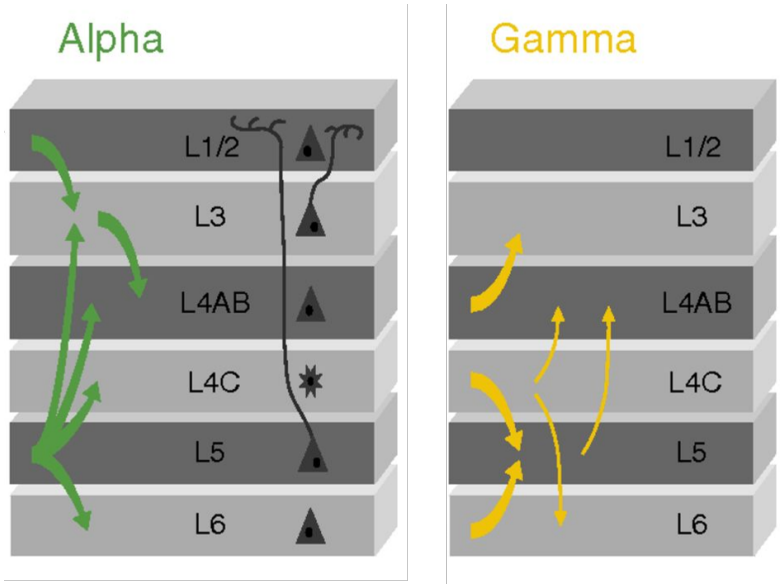



Figure 1.4: Information flow (assessed by Granger causality) between layers of the visual cortex in the alpha and gamma band, measured from invasive laminar electrodes in monkeys (Figure adapted from Van Kerkoerle et al. [2014]).

- Delta waves ($\delta$, $1-4$ Hz) are mostly associated with sleep and appear in both subcortical and cortical areas (with animal models pointing to the supragranular layers 2/3)[Hobson and Pace-Schott, 2002]. Increased delta power during wakefulness, as well as long range synchronisation in other low frequencies up to the alpha frequency range [Dunkley et al., 2015], has been shown to be a marker of impaired cognitive function in traumatic brain injury, probably reflecting axonal damage [Lewine et al., 2007; Huang et al., 2009].

- Theta waves ($\theta$, $4-8$ Hz) are thought to be involved in cognition in the frontal cortex, spatial navigation, memory consolidation in the pre-frontal cortex, and communication of the cortex and laminar layers with the hippocampus [Benchenane et al., 2010]. Observed alterations in the amplitude and timing of theta oscillations in the frontal and temporal lobes of schizophrenia patients, both at rest and during cognitive tasks, have also linked theta band dysfunction to impaired executive control [Schmiedt et al., 2005; Haenschel et al., 2009].

- Alpha waves ($\alpha$, $8-13$ Hz) are the highest amplitude oscillations in the human brain and present most strongly in the visual cortex. The alpha rhythm is thought to have an inhibitory role in the brain, e.g. alpha power decreases with alertness and following presentation of visual stimuli. In the visual cortex alpha waves have been found to originate from layers 1, 2 and 5 of pyramidal neurons, which are associated with feed-back processing in agreement with the hypothesis of alpha mediating top-down inhibitory control [Van Kerkoerle et al., 2014]. Significant evidence points to alpha waves being implicated in the gating of information from the visual cortex and in suppressing distraction for selective attention during stimulus processing [Jensen and Mazaheri, 2010; Zumer et al., 2014].

- Beta oscillations ($\beta$, $13-30$ Hz) are prominent in the sensory and motor cortices and more generally across parietal, temporal and occipital lobes [Hunt et al., 2016]. Recent modelling work and comparison with animal recordings indicate that beta waves originate from layer 4 of the cortex and they mostly manifest as short bursts ($< 150$ms) of increased oscillatory amplitude rather than a continuous rhythm [Sherman et al., 2016]. Like alpha waves, beta seems to have an inhibitory function, with beta power decreasing with sensory stimulation, motor planning and motor action. Beta waves have also shown to be modulated (with increased amplitude and slower frequency) by GABA agonist drugs such as benzodiazepine [Jensen et al., 2005]. At movement/stimulus cessation, beta oscillations transiently increase above resting amplitude, a phenomenon known as the beta rebound which has been shown to be affected by age (not present in children and gradually increasing with age [Gaetz et al., 2010]) and pathology (e.g. diminished in schizophrenia [Robson et al., 2016] and delayed in multiple sclerosis [Barratt et al., 2017]). Beta is also thought to be involved in long range connectivity in the cortex and functional connectivity networks in this frequency range have been shown to closely match canonical fMRI resting networks [Brookes et al.,

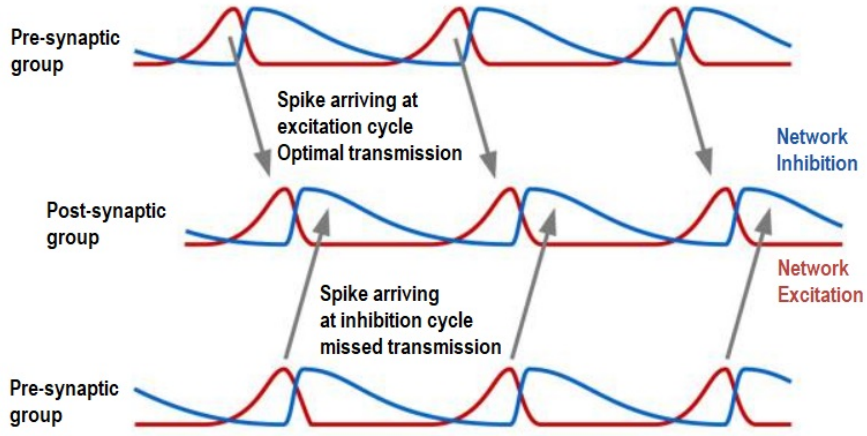



Figure 1.5: Diagram summarizing the concept of communication by coherence. Pre-synaptic neuronal groups can transmit information effectively when their output spikes find the post-synaptic group during an excitation cycle. Conversely spikes arriving at the post-synaptic group during the inhibitory cycle will not communicate with receiving neurons. Figure adapted from Fries [2015].

2011b; Hipp et al., 2012; Hunt et al., 2016].

- Gamma oscillations ($\gamma$, >30Hz) are high frequency oscillations mostly associated with bottom-up sensory perception. High frequency gamma oscillations are known to be present in various parts of the cortex from invasive recording (i.e. iEEG) but are usually hard to detect in non-invasive data (EEG or MEG) due to their low signal to noise ratio. Nevertheless gamma oscillations can be observed in the sensorimotor cortices and visual cortex where they originate in layer 4, with a feed-forward role in antithesis with the alpha rythm [Van Kerkoerle et al., 2014]. Gamma oscillations are also positively correlated with the blood oxygenation level (BOLD) signal measured in fMRI [Niessing et al., 2005].

### 1.2.3 Oscillations and functional connectivity

For the central nervous system to work effectively, separate brain regions must communicate and share information. These networks of connections are based on the anatomical architecture of the white matter axonal tracts, but it is their functional connections, the way information is shared and integrated between func-

tionally specialised areas, that ultimately determines behaviour. In non-invasive neuroimaging, functional connectivity has been linked to temporal correlations in the BOLD signal in fMRI [Biswal et al., 1995] and, more recently, to neural oscillations. The theory at the base of most functional connectivity methods in M/EEG was proposed by Pascal Fries [Fries, 2005] as "communication by coherence". This posits that effective interaction between neuronal assemblies is facilitated by synaptic inputs being received at high points of excitability (see Figure 1.5). Efficient information transfer thus requires potentials to be phase-locked with each other, while out of phase potentials will not be seen by the post-synaptic neurons. The concept of rhythmic synchronisation is mostly applied to neural oscillations though it was more recently extended to the gamma band non-linear and non-sinusoidal synaptic potentials [Fries, 2015].

Most connectivity metrics which are applied to MEG data are based on the communication by coherence principle and assess functional connections by signal coherence, phase-locking or time correlated signal amplitude. There is significant experimental evidence that oscillations are linked to long range connectivity. Temporal correlation between the amplitude envelopes of neural oscillations, particularly in the beta band [Brookes et al., 2011b; Hipp et al., 2012; Hunt et al., 2016] have shown to match the canonical resting state networks seen in fMRI and similar networks can be seen by measuring coherence or phase locking between regions [Liuzzi et al., 2017]. Although connectivity is often measured as an average over minutes of activity new techniques in MEG have shown that functional networks can form and dissolve within seconds [Brookes et al., 2014] or even milliseconds [Baker et al., 2014], a temporal scale that could be able to sustain perception and cognition (see Figure 1.6). The work presented in this thesis extends the current functional connectivity methodology, starting by assessing the robustness of connectivity estimation in terms of both data collection and analysis methods, and pushing forward its application in task data, where we present connectivity networks forming and dissolving on the millisecond time scale, relating to attention

and task performance.

## 1.3 Instrumentation

The magnetic signals produced by brain activity are several orders of magnitude smaller than environmental magnetic noise levels. Electronic devices, nearby traffic, the Earth's magnetic field and even other biomagnetic signals (such as the magnetic signal produced by the heart) all "drown out" the small signals from neuronal assemblies (see Figure 1.7). For this reason MEG requires both sophisticated sensors with sensitivity to magnetic fields in the fT range, and methods to reduce magnetic noise from various sources. In this section we will cover the instrumentation needed for MEG measurements, with a specific focus on the dc-SQUID detector and the characteristics of the 275 channel CTF MEG system used to acquire the data presented in this thesis.

### 1.3.1 Magnetic field detection

Magnetic field detectors, or magnetometers, need to satisfy multiple requirements to be viable for MEG measuremets:

1. They require a sensitivity to magnetic fields of the order of $10 - 1000$ fT;
2. Their operational range should be at least $1 - 100$ Hz in order to include the frequency range of spontaneous and induced responses (in fact invasive recordings suggest electrophysiological effects can extend up to 600 Hz [Curio, 2000]);
3. They need to be small enough so that multiple sensors can be placed as close as possible to the subject's head, to be able to accurately detect multiple sources.

The most popular magnetometers with the necessary requirements for MEG measurements are the cryogenically cooled Superconducting Quantum Interfer-

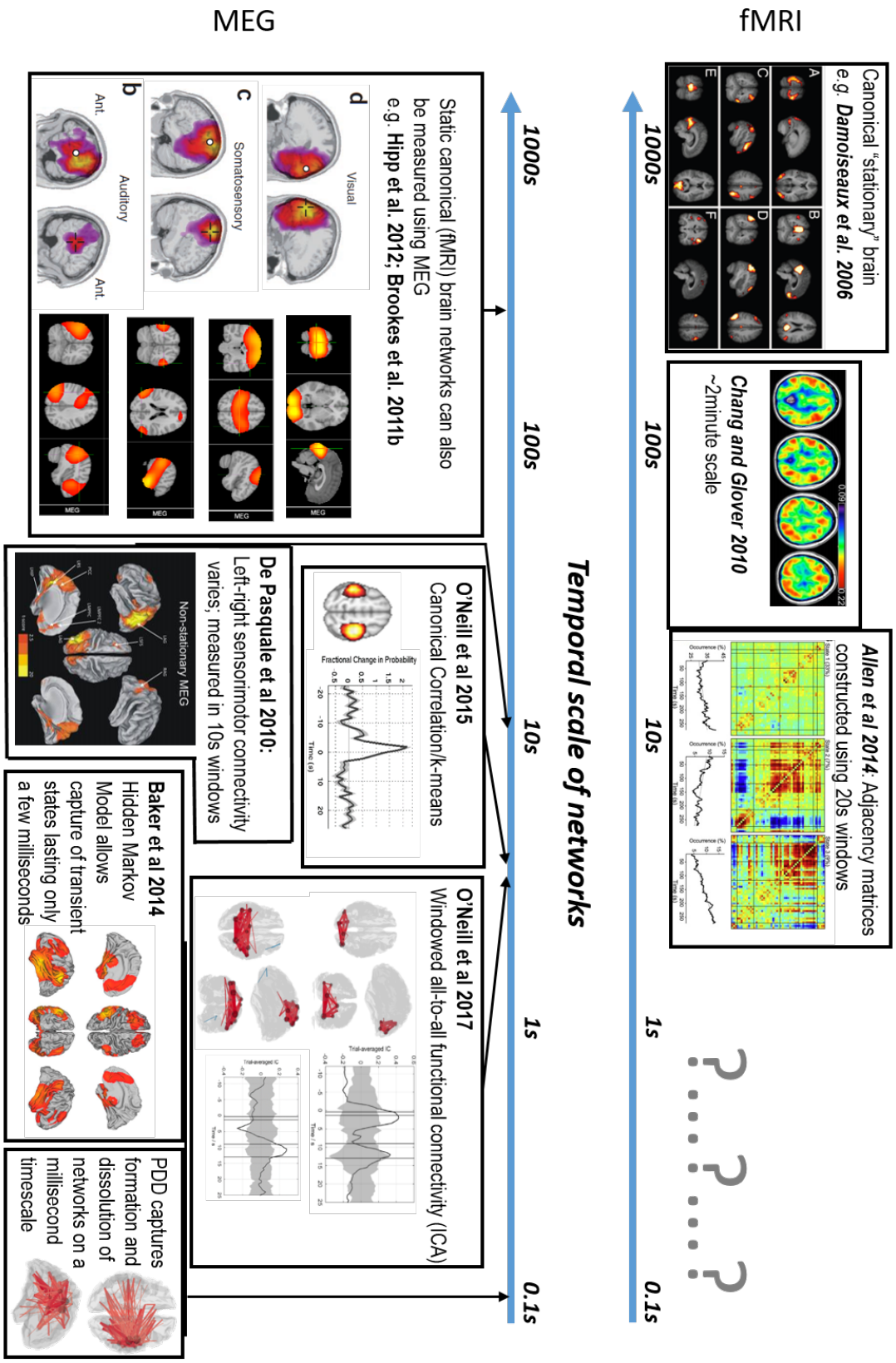



Figure 1.6: Temporal scale of functional connectivity networks measured with fMRI and MEG from minutes to the millisecond range [Damoiseaux et al., 2006; Chang and Glover, 2010; Allen et al., 2014; Hipp et al., 2012; Brookes et al., 2011b; O'Neill et al., 2015, 2017; De Pasquale et al., 2010; Baker et al., 2014]. Dynamic connectivity will be explored in chapter 4.

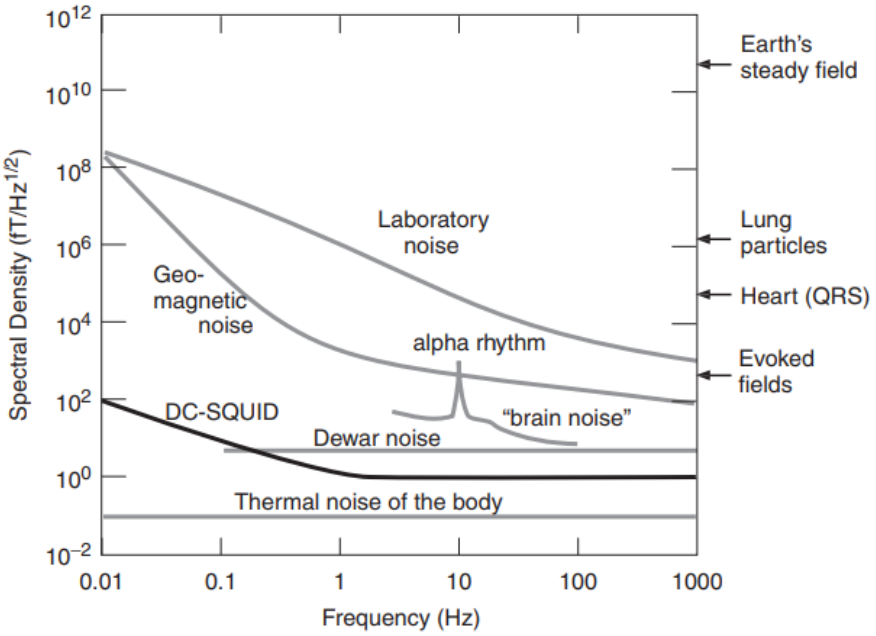



Figure 1.7: Sources of magnetic field noise by frequency in logarithmic scale. Figure from [Hansen et al., 2010].

ence Devices (SQUIDs). SQUIDs have been instrumental in making MEG a viable imaging technology, and commercially available MEG systems nowadays are equipped with arrays of up to 300 SQUID sensors.

Whilst the rest of this chapter is dedicated to SQUID sensors (as all data presented in this thesis were collected with a SQUID based MEG system), it is worth mentioning that recently a number of other detectors have been successfully used for MEG measurements such as High-$T_C$ SQUIDs, HyQUIDs and Optically Pumped Magnetometers (OPMs). High-$T_C$ SQUIDs are based on superconductive materials with a higher critical temperature than conventional SQUIDs, requiring liquid nitrogen (77K) instead of expensive liquid helium cooling (4.2K). The HyQUID$^{TM}$ (Hybrid Quantum Interference Device) is a class of sensor with sensitivity ostensibly better than the SQUID, operating at $T_C < 4$K maintained through pulse tube cooling [Shelly et al., 2016]. HyQUID based MEG systems are commercially available by York Instruments, but at the moment of writing no MEG work using this system has been published. The development of OPMs for MEG applications has seen perhaps the most significant progress in the last

few years, with laboratories now working on multi-channel systems [Borna et al., 2017; Boto et al., 2018; Iivanainen et al., 2018]. Although they operate on a narrower frequency range and have marginally lower sensitivity than SQUIDs, OPMs work at body temperature and can be positioned much closer to the head (in a configuration similar to an EEG cap), therefore detecting higher magnetic field amplitudes, giving higher signal to noise, and having the potential for improving source localisation [Boto et al., 2016; Iivanainen et al., 2016]. Some of the latest work has also shown that OPMs can record data during un-constrained head movement, while maintaining a signal quality surpassing that of conventional EEG and MEG systems [Boto et al., 2018].

## 1.4 Superconductivity

Superconductivity is a phenomenon by which a material cooled below a specific temperature, called the critical temperature $T_C$, conducts electricity with zero electrical resistance. Heike Kamerlingh Onnes, the physicist to first liquefy helium, discovered superconductivity in 1911 while studying the electrical resistance of mercury [Onnes, 1911]. Superconductors, unlike an ideal perfect conductor, expel the magnetic flux within the conductor after reaching their critical temperature, meaning that inside a superconductor the magnetic field $B = 0$. This property, called the Meissner effect [Meissner and Ochsenfeld, 1933], is only destroyed when the magnetic field around the superconductor reaches a critical amplitude. According to their response to magnetic fields, superconducting materials are classified in two categories. In type I superconductors, superconductivity is destroyed after reaching a critical magnetic field $H_C$. Type II superconductors, instead, exhibit a transition period where after reaching a lower critical field $H_{C1}$, magnetic flux starts to penetrate the superconductor lattice until superconductivity is lost when a higher critical field $H_{C2}$ is reached. Superconductors with high critical fields, suited for superconductive magnets and magnetometers, are usually type II

and made of alloy materials (e.g. $NbTi$, $Nb_3Sn$).

Superconductivity was described at the microscopic scale by Bardeen, Cooper and Schrieffer in 1957, in what is now referred to as BCS theory [Bardeen et al., 1957]. Microscopically, electrical resistance can be thought to arise from free electrons colliding with the crystal lattice (phonon) and impurities in the conductor material. According to BCS theory in a superconductor electrons travelling through the lattice can briefly distort the crystal structure, creating a "wake" of positive charge, that will then attract a second electron. This long range phonon interaction binds pairs of electrons together, called Cooper pairs. Cooper pairs behave like Bosons enabling multiple pairs to occupy the same quantum state. The distance between the first and second electron is called the coherence length and depends on the conductor material (usually several times the inter-atomic spacing). Quantum mechanically Cooper pairs are described by the same wave function, spatially limited by their coherence length: as multiple Cooper pairs exist simultaneously their wave functions overlap, forming a coherent condensate. In this condensate state, breaking one Cooper Pair will cause an unfavourable change in the energy of the whole system, so that small thermal interactions are not enough to affect it. The energy required to break a Cooper Pair is called the energy gap and it is equal to $3.5k_BT_C$, where $T_C$ is the superconductor critical temperature. The repulsive Coulomb interaction between the two negatively charged electrons is comparatively short-range thanks to the screening effect of the other electrons in the lattice, so that in a superconductive phase phonon interactions dominate over Coulomb forces. We can mathematically describe the whole ensemble of Cooper pairs with a macroscopic wavefunction or "order parameter":

$$\Psi = |\Psi(\mathbf{r})|\mathrm{e}^{i\mathbf{K}\cdot\mathbf{r}} \tag{1.5}$$

where $\mathbf{K}$ is the wave vector of the condensate and $|\Psi(\mathbf{r})|$ is the wave function for its ground state ($K = 0$) [Feynman et al., 1965; London, 1948]:

We can obtain the total number of Cooper Pairs $N$ in the superconductive

condensate by normalising equation 1.5:

$$\int_V \Psi\Psi^* \mathrm{d}\mathbf{r} = N \tag{1.6}$$

Now by expressing the scalar product $\mathbf{K}\cdot\mathbf{r} = \theta(\mathbf{r})$, i.e. the phase of the wavefunction dependent on position $\mathbf{r}$, we can write the wavefuntion as:

$$\Psi = \sqrt{\rho(\mathbf{r})}\mathrm{e}^{i\theta(\mathbf{r})} \tag{1.7}$$

where $\rho(\mathbf{r})$ is the spatial density of Cooper pairs. Since in weak fields the density is approximately spatially invariant we can assume $\rho(\mathbf{r}) = \rho$ .

The momentum density is equal to the number of Cooper pairs times their individual momentum $\mathbf{p}$. Classically the momentum of a charged particle in a magnetic field of vector potential $\mathbf{A}$ is given by:

$$\mathbf{p} = m\mathbf{v} + q\mathbf{A} \tag{1.8}$$

where $m$, $v$ and $q$ are the particle mass, velocity and charge respectively.

In the quantum mechanical formalism the momentum density $\rho\mathbf{p}$ is equal to the expectation value of the momentum operator $-i\hbar\boldsymbol{\nabla}$ , so that:

$$\rho\mathbf{p} = \langle\Psi| - i\hbar\boldsymbol{\nabla}|\Psi\rangle = -i\hbar\langle\Psi|\boldsymbol{\nabla}|\Psi\rangle = \rho\hbar\boldsymbol{\nabla}\theta(\mathbf{r}) \tag{1.9}$$

We now introduce the Cooper pair current density $\mathbf{J} = \rho q\mathbf{v}$, so by rearranging the equation for the velocity and substituting in equation 1.8:

$$\mathbf{p} = \hbar\boldsymbol{\nabla}\theta = q\Lambda\mathbf{J} + q\mathbf{A}, \qquad \Lambda = m/\rho q^2 \tag{1.10}$$

If we now consider a superconductive ring and integrate equation 1.10 around its contour we obtain:

$$\hbar\oint_C \boldsymbol{\nabla}\theta\cdot\mathrm{d}\mathbf{l} = q\oint_C (\Lambda\mathbf{J} + \mathbf{A})\cdot\mathrm{d}\mathbf{l} \tag{1.11}$$

Solving the integral on the left hand side gives $\hbar \lim_{\mathbf{r_b}\to\mathbf{r_a}}(\theta(\mathbf{r_b})-\theta(\mathbf{r_a})) = 2\pi\hbar n$, with $n \in \mathbb{Z}$, since our wavefunction $\Psi(\theta, \mathbf{r})$ must have the same value at the same point inside the ring. For the right hand side of the equation we can assume to be far from the surface of the superconductor so that $J = 0$ and than apply Stokes theorem:

$$q \oint_C (\mathbf{A}) \cdot \mathrm{d}\mathbf{l} = q \iint_S \boldsymbol{\nabla} \times \mathbf{A} \cdot \mathrm{d}\mathbf{S} = q \iint_S \mathbf{B} \cdot \mathrm{d}\mathbf{S} = q\Phi_C \tag{1.12}$$

Where $\Phi_C$ is the magnetic flux through the closed loop. Finally we can see that the flux through a superconductive ring is quantised as $\Phi_C = 2\pi\hbar n/q = n\Phi_0$. Since the charge of the Cooper pair $q = -2e$, the value of the flux quantum $\Phi_0 = h/2e = 2.07 \times 10^{-15}$ Wb.

## 1.5 Josephson's Junction

Let's now look at what happens with two superconductors separated by a thin layer of insulating material. If the distance between the two superconductors is small enough Cooper pairs may be able to tunnel through from one side of the junction to the other, like electrons tunneling through a potential barrier. This situation was first proposed by Josephson in 1962 [Josephson, 1962] and is now referred to as a Josephson junction.

As before let us describe the wavefunctions of the electrons of the superconductors:

$$\begin{aligned} \psi_1 &= \sqrt{\rho_1} e^{i\theta_1} \\ \psi_2 &= \sqrt{\rho_2} e^{i\theta_2} \end{aligned} \tag{1.13}$$

If the two superconductors sides have a potential difference $V$ and they are weakly coupled through the junction with a potential $K$, we can write their Schrödinger's equations as:

$$\begin{aligned} i\hbar\frac{\partial\psi_1}{\partial t} &= +\frac{qV}{2}\psi_1 + K\psi_2 \\ i\hbar\frac{\partial\psi_2}{\partial t} &= -\frac{qV}{2}\psi_2 + K\psi_1 \end{aligned} \tag{1.14}$$

By substituting equations 1.13 into equations 1.14 we arrive at two sets of equations for the time evolution of the electron densities $\dot{\rho}$ and of the phases $\dot{\theta}$.

We find that the change of charges of the two superconductors $\dot{\rho}_1 = -\dot{\rho}_2 = J$, where $J$ is the current through the junction:

$$J = \frac{2K}{\hbar}\sqrt{\rho_1\rho_2}\sin\delta \tag{1.15}$$

(where $\delta = \theta_2 - \theta_1$):

If the potential difference $V$ is maintained constant by an external battery the charge densities in the superconductors will be reestablished and remain constant over time. If we consider the two superconductors to be identical (so that they are made with the same material and have the same number of Cooper pairs) we then have $\rho_1 = \rho_2 = \rho_0$, and we can write:

$$J = J_0 \sin\delta \tag{1.16}$$

where $J_0 = 2K\rho_0/\hbar$.

The change in the phase difference is instead given by:

$$\dot{\delta} = \dot{\theta}_2 - \dot{\theta}_1 = qV/\hbar \tag{1.17}$$

and the time evolution of the phases is given by integrating the above equation:

$$\delta(t) = \delta_0 + q/\hbar \int V(t)\mathrm{d}t \tag{1.18}$$

The consequence of equations 1.16 and 1.18 is that when a DC voltage $V_0$ is applied across the junction, the phase $\delta$ will rapidly change over time (since

$qV_0 \mathrm{d}t/\hbar \gg 1$) causing no net current flowing across the junction, while in the absence of a voltage a current $-J_0 < J < J_0$ will be able to flow from one side of the junction to the other. The result of these equations is referred to as the DC Josephson effect.

Let us now consider connecting two Josephson junctions in parallel as seen Figure 1.8. The total current $J_{TOT}$ flowing through the system from point P to Q will be equal to the sum of the currents $J_A$ and $J_B$ flowing through the individual junctions. As both currents start from point P and end at point Q the change of their phases $\Delta\theta_{PQ}$ must be the same. We can calculate the total phase difference over the path of current $J_A$ by adding the phase difference over the junction $\delta_A$ to the phase difference given by equation 1.10 over the path (again considering the current in the bulk of the superconductor to be negligible). The total phase difference from one end to the other will then be:

$$\Delta\theta_{PQ} = \delta_A + \frac{q}{\hbar}\int_{pathA} \mathbf{A}\cdot \mathrm{d}\mathbf{l} \tag{1.19}$$

The same will be true for current $J_B$ so that:

$$\Delta\theta_{PQ} = \delta_B + \frac{q}{\hbar}\int_{pathB} \mathbf{A}\cdot \mathrm{d}\mathbf{l} \tag{1.20}$$

As $\Delta\theta_{PQ}$ must be the same we find:

$$\delta_B - \delta_A = \delta_0 - e\Phi/\hbar = \frac{q}{\hbar}\oint \mathbf{A}\cdot \mathrm{d}\mathbf{l} = \frac{2e\Phi}{\hbar} \tag{1.21}$$

Writing $\delta_A = \delta_0 - e\Phi/\hbar$ and $\delta_B = \delta_0 + e\Phi/\hbar$ we can define the total current $J_{TOT}$:

$$\begin{aligned} &J_{TOT} = J_A + J_B = J_0(\sin\delta_A + \sin\delta_B) = \\ &J_0\left[\sin\left(\delta_0 - \frac{e\Phi}{\hbar}\right) + \sin\left(\delta_0 + \frac{e\Phi}{\hbar}\right)\right] = 2J_0 \sin\delta_0 \cos\frac{e\Phi}{\hbar} \end{aligned} \tag{1.22}$$

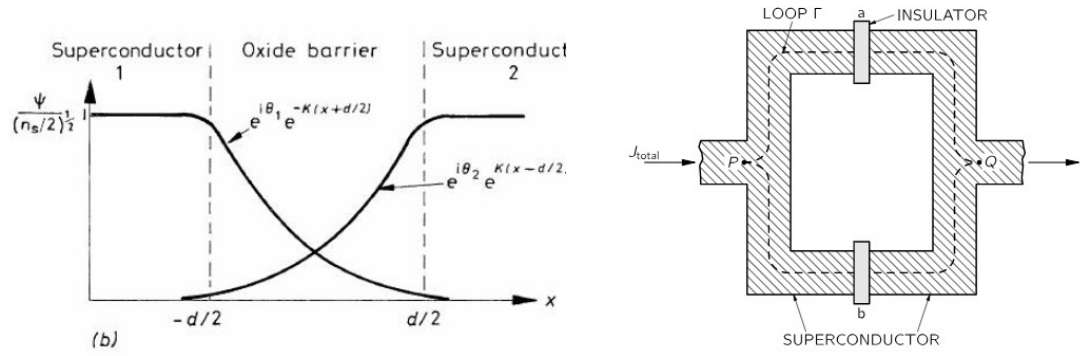



Figure 1.8: Schematic of a Josephson's junction: Potential at a Josephson junction showing the overlap of the wavefunctions over the insulating barrier (left) and diagram of two junctions in parallel allowing the detection of magnetic flux [Feynman et al., 1965].

Since $\sin(\delta_0)$ cannot be larger than 1, it follows :

$$J_{max} = 2J_0 \left| \cos \frac{e\Phi}{\hbar} \right| \tag{1.23}$$

So the maximum current through the two junctions system will vary periodically as a function of the magnetic flux through the closed loop. As $\Phi$ is a multiple of the small flux quantum, a two junction system outputs a current which is incredibly sensitive to small changes of magnetic field, with a loop of 1 $cm^2$ area reaching its maximum current output with a field of just $10^{-11}$ T. The response to magnetic flux of two Josephson junctions in parallel is the basis of dc-SQUID sensors.

### 1.5.1 SQUIDs

Brain magnetic fields are routinely detected in current MEG systems by means of SQUID sensors, i.e. Superconductive Quantum Interference devices. The SQUID was introduced by James Zimmerman [Zimmerman et al., 1970] in the late '60s: SQUIDs were first used for detection of magnetic signals from the human brain at the Massachusetts Institute of Technology [Cohen, 1972] following the first detection of biomagnetic signals from the human heart [Baule, 1963] and the measure-

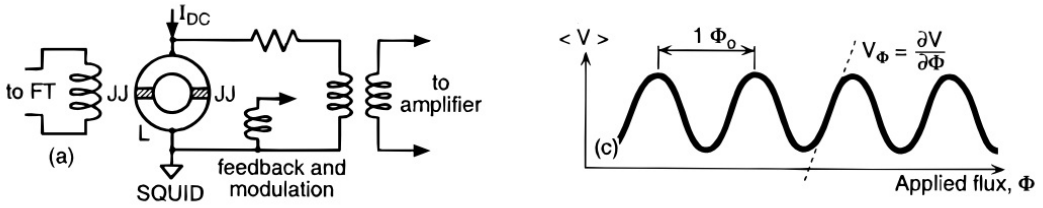



Figure 1.9: Diagram of a SQUID: a flux transformer (FT) induces a magnetic flux through the SQUID which is compensated by a feedback current [Vrba and Robinson, 2001].

ment of brain alpha rhythms with lower sensitivity coils. The use of SQUIDs was a large step forward in MEG detection, thanks to its higher sensitivity compared to traditional inductive coils. The first MEG experiments used radio frequency SQUIDs (rf-SQUIDs), a sensor composed of a single Josephson junction inductively coupled to a readout circuit which operated at radio-frequencies. Their popularity at the time came from the expensive manufacturing of Josephson junctions. Nowadays thin film superconductors can be mass-produced, making the use of the two junctions dc-SQUID the standard in MEG systems.

A diagram showing the operation of a typical dc-SQUID circuit is shown in Figure 1.9. A small DC current is applied to the SQUID by the control electronics so that the Josephson's junctions are kept close to their critical current $I_C$. When the critical current is exceeded the flux through the SQUID loop will jump by a quantum $\Phi_0$ causing a voltage drop across the junctions.

In an MEG system SQUIDs are placed far from the subject (e.g. higher in the liquid helium dewar) to avoid sources of interference. Detection of neural magnetic fields is achieved through flux transformers coupled to the SQUIDs sensors. The flux transformers consist of superconductive pick-up coils placed close to the head carrying the magnetically induced currents with no dissipation. The pick-up coils are then connected to a flux transformer that is inductively coupled to the SQUID sensors. It is worth noting that pick-up coils are only able to detect magnetic fields normal to the coil area, in accordance with Lenz's law. From this follows the very important consideration that SQUID based MEG systems are insensitive

to radially oriented dipole sources (we will explore the physical modelling of signal sources in more detail in chapter 2).

When the flux transformer induces a magnetic flux through the SQUID, the ring will respond with a shielding current $I_S$ that will work to maintain the flux through the SQUID constant by inducing an opposite flux $\Phi_S = LI_S$ dependent on the inductance $L$ of the SQUID. The shielding current exceeds the critical current causing a voltage drop across the ring which is detected by the electronics. The result is a periodic current output in the SQUID circuit as shown in Figure 1.9.

In order to obtain unambiguous information about magnetic field changes, SQUIDs need to operate within half a period of oscillation (i.e. half the flux quantum $\Phi_0$). This is achieved by operating the SQUIDs in a closed (or "fluxed locked") loop: the magnetic flux in the SQUID is locked at a constant value using a negative feedback current. The flux is locked at the sharpest point of the response curve where the transfer function $V_\Phi = \partial V/\partial\Phi$ is approximately linear. Any changes in flux through the loop will change the voltage $V_\Phi$, which will quickly be brought back to its locked point by the feedback circuit. It is the voltage of this feedback circuit across a load resistor that is read as output of the dc-SQUID magnetometer.

### 1.5.2 Gradiometers

In MEG we are interested in the magnetic fields produced by the neurons. As these fields decay quickly over distance SQUIDs pick-up coils are placed as close to the head as possible to maximise sensitivity. In order to reduce environmental noise MEG systems usually operate in magnetically shielded rooms (MSRs), bringing the background field to $\sim$ 25nT [Holmes et al., 2018]. Shielded rooms are necessary to remove most sources of electrical interference, such as laboratory electronics and the earth magnetic fields. Still, magnetic shielding is not always effective at dealing with low frequency noise ($<$ 10 Hz). Further, some sources of interference still remain in the shielded room such as magnetic noise from the body that is orders

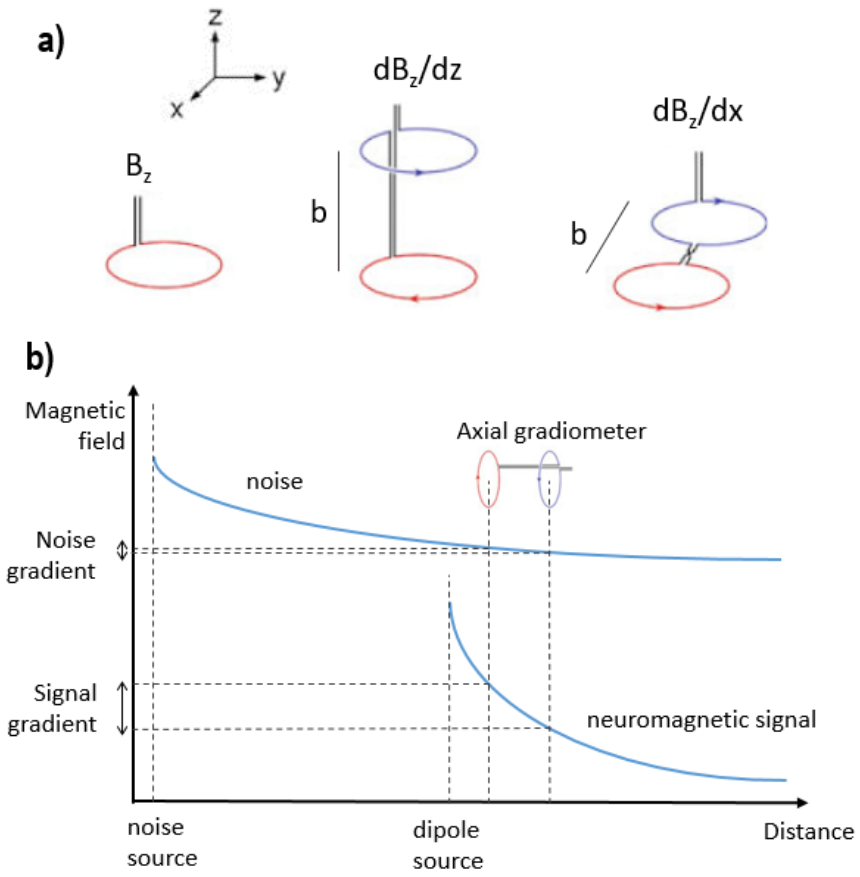



Figure 1.10: a) Example of pick-up coils in a magnetometer, axial gradiometer and planar gradiometer arrangement. b) Diagram showing the principle of an axial gradiometer: far away sources of noise have a small gradient over the gradiometer baseline, while a neuromagnetic signal, closer to the gradiometer, contributes more to the detected magnetic field gradient.

of magnitude larger than brain spontaneous oscillations (see Figure 1.7). For these reasons, in order to improve noise reduction, pick-up coils can be arranged in a gradiometer configuration.

Gradiometers measure the magnetic field gradient between two points and in doing so cancel out the contributions of far away sources of interference. The distance between the two pick-up coils, called the gradiometer baseline $b$, is usually in the range of 3-8 cm and must be optimised to achieve the best signal to noise for a typical depth of sources [Vrba and Robinson, 2001]. For pick-up coils of area

$A$ and vector normal to the surface $\mathbf{n}$ the flux of an ideal gradiometer is given by

$$g = A\mathbf{n}^T \begin{pmatrix} \partial B_x/\partial x & \partial B_x/\partial y & \partial B_x/\partial z \\ \partial B_y/\partial x & \partial B_y/\partial y & \partial B_y/\partial z \\ \partial B_z/\partial x & \partial B_z/\partial y & \partial B_z/\partial z \end{pmatrix} \mathbf{b} \tag{1.24}$$

where $\mathbf{b}$ is the gradiometer baseline vector.

The typical pick-up coils for magnetometers and the most common gradiometers are shown in Figure 1.10. Magnetometers have the best sensitivity to deep brain sources, while being most affected by sources of noise. Planar gradiometers maximise sensitivity to very close sources, such as the brain cortex, but have poor resolution to deeper sources: their main limitation is the planar separation (i.e. gradiometer baseline in the x-direction) as a longer baseline improves depth coverage, but will reduce the sensor density on the head. Axial gradiometers (in use in the CTF MEG scanners) have better sensitivity to deeper sources compared to planar gradiometers, while still offering the better signal cancellation of a gradiometer arrangement. The axial gradiometer is formed by two loops displaced along the direction normal to the pick-coil loop. The two gradiometer coils are wound in opposite directions and connected to the SQUID by the same lead so that magnetic fields invariant over the two gradiometer coils will cancel out. Closer sources, like post-synaptic dipole fields falling off as $1/r^2$, will instead be mostly preserved.

### 1.5.3 Higher order gradiometers

In principle it is possible to build gradiometers with more than two pick-up loops, to form second, third or even higher order gradiometers. Hardware solutions for higher order gradiometers are often impractical to build for MEG systems, but synthetic gradiometers, implemented through software or firmware, can offer equivalent improvements in noise cancellation. Synthetic gradiometers are often

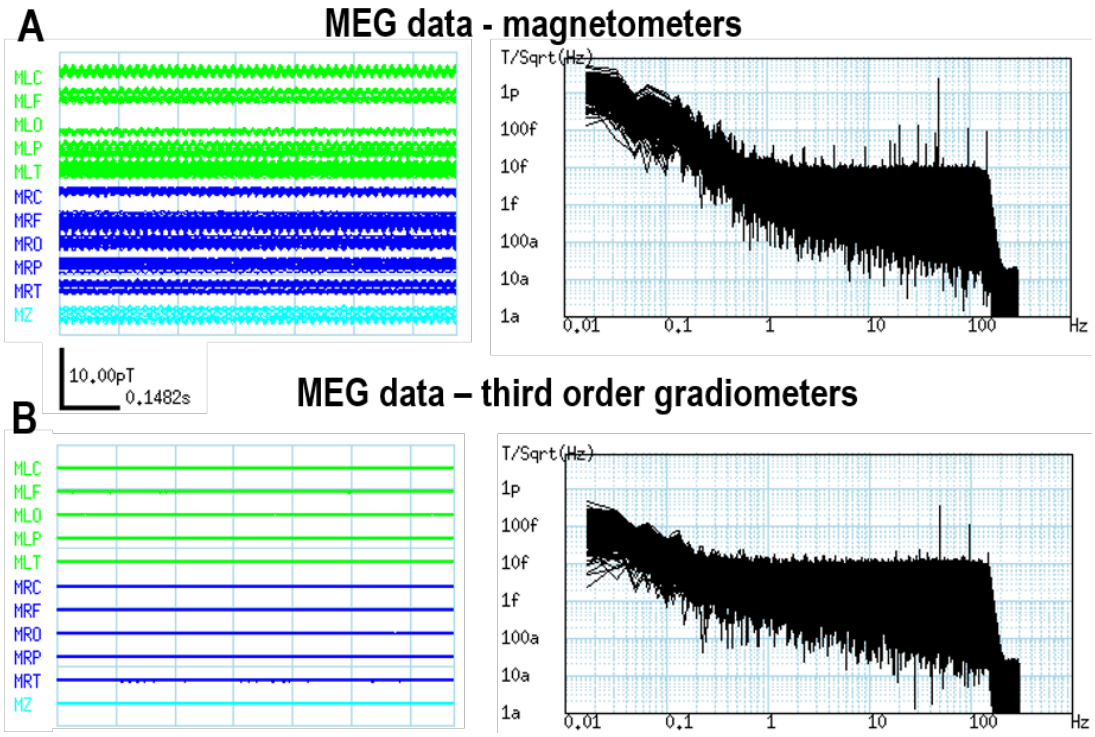



Figure 1.11: Example of 60s empty room noise recording with a 275 channel CTF MEG system. A) Data output of MEG sensors grouped by location (zoomed in to show 1s of data, left) and their overlaid frequency spectra in logarithmic scale (right). B) The same recording in A) corrected with third order synthetic gradiometers. The noise floor between $1 - 150$ Hz is reduced to $\sim$ 10fT. The remaining peaks at 50, 100 and 150 Hz are caused by the electric leads.

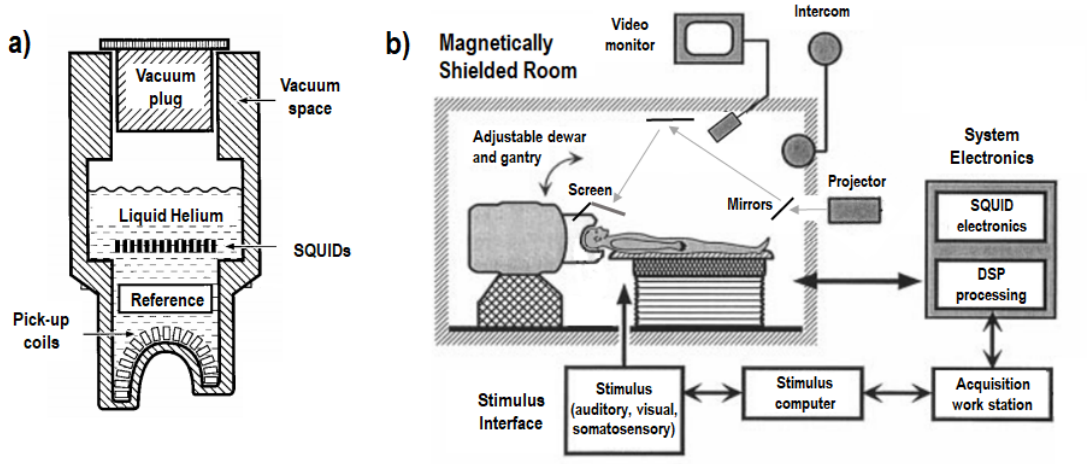



Figure 1.12: Diagram of CTF MEG dewar a) and experimental set-up b). Figures adapted from [Vrba and Robinson, 2001].

used in conjunction with reference sensors arrays (SQUID magnetometers and gradiometers) which are usually positioned about 20 cm from the main MEG sensors. The noise contribution at the main MEG sensors can be calculated by expanding into a Taylor series the magnetic field of the reference signals about the primary sensors' location. Using this technique allows for the construction of second and third order gradiometers [Vrba and Robinson, 2001]. Synthetic gradiometers can substantially improve the signal to noise of MEG sensors, including at low (vibrational) frequencies, and their effect is additive to the magnetic shielding of an MSR. Figure 1.11 shows an example of the effect of gradiometers on background noise in real MEG data.

### 1.5.4 The CTF-MEG system

The MEG data presented in this thesis were collected with a 275 channel CTF MEG scanner at the Sir Peter Mansfield Imaging Center of the University of Nottingham. A simplified diagram of the MEG laboratory is shown in Figure 1.12. The MEG scanner is mounted on a gantry and positioned in a $\mu$-metal magnetically shielded room. The gantry, together with an adjustable chair, allows the experimenter to record in upright or supine positions. CTF scanners use 275 axial gradiometers and 29 reference sensors for third order synthetic gradiometry

correction. The pick-up coils are arranged in a fixed helmet to cover as much of the head as possible. The pick-up coils and the SQUIDs are housed in a dewar where they are immersed in a bath of liquid helium to maintain superconductivity. Three head localisation coils are attached to the subject at the nasion and left/right preauricular points. The coils are energised at frequencies $> 1000$Hz during data collection in order to track the head motion of the subject in the scanner. As MEG is a passive technique it does not involve any type of radiation and it is inherently safe for subjects. The only risk is posed by the liquid helium in the dewar; as cryogenic liquids expand quickly they can substitute breathable air when evaporating. Evaporation rates of helium in the MEG dewar are routinely checked and an oxygen monitor is always placed inside the MSR when a subject is present. An intercom is used to communicate with the subject and a camera in the MSR is used for video monitoring. Within the shielded room the noise floor of sensors with third order gradiometer correction is $\sim$10fT for frequencies $>$ 1Hz (see Figure 1.11). Routinely MEG data are collected with a 600 Hz sampling rate, though higher sampling rates, such as 1200 Hz, are possible e.g. to detect entrainment in visual cortex. The acquisition and stimulus computers, as well as the electronics for data collection, are kept outside of the MSR. The stimulus computer is used to control experimental stimuli via peripheries such as a projector and somatosensory stimulation pads. The stimulus computer is connected to the acquisition computer through parallel port so that digital markers (triggers) can be used to synchronise the experimental paradigm and stimuli presentation to the MEG data. A long throw projector for the presentation of visual stimuli is also kept outside the MSR to avoid magnetic noise. Visual stimuli are back projected onto a screen through a hole in the MSR and adjustable mirrors are used to center the visual images on the screen in either upright or supine position.

# Chapter 2

# Functional connectivity assessment in MEG

This chapter covers the basics of MEG source reconstruction, from the electromagnetic principles behind the forward model (including mathematical derivations for a spherical conductor) to the beamforming inverse solution. In the second half of the chapter we will cover the analysis methods for estimation of functional connectivity on source localised MEG data and technical considerations to deal with spurious connectivity estimates.

## 2.1 Forward solution

MEG sensors detect magnetic fields (or field gradients) at $\sim 300$ discrete locations around the head. When assessing neural activity it is of interest to localise the source of the detected fields to separate functionally specific brain regions. The first step in source localisation is to model the magnetic field induced by electrical activity in neuronal populations. The physical laws of electromagnetic fields are described by Maxwell's equations:

$$\begin{aligned} \boldsymbol{\nabla} \cdot \mathbf{E} &= \rho/\varepsilon \\ \boldsymbol{\nabla} \times \mathbf{E} &= -\frac{\partial \mathbf{B}}{\partial t} \\ \boldsymbol{\nabla} \cdot \mathbf{B} &= 0 \\ \boldsymbol{\nabla} \times \mathbf{B} &= \mu\left(\mathbf{J} + \varepsilon\frac{\partial \mathbf{E}}{\partial t}\right) \end{aligned} \tag{2.1}$$

where $\mathbf{E}$ and $\mathbf{B}$ are the electric and magnetic fields respectively, $\rho$ is the charge density and $\varepsilon$ and $\mu$ are the permittivity and permeability of the propagating medium.

When modelling neuronal activity in the brain we can simplify Maxwell's equations by considering special conditions of the physical system:

1. First we can assume that the magnetic permeability of the brain, skull and other tissues in the head is constant and equal to that of free space meaning that $\mu = \mu_0$;

2. Second, the oscillatory frequencies of interest are relatively low ($< 1000$ Hz, see section 1.2) justifying the use of the quasistatic approximation.

For the quasistatic approximation to be valid the time derivative terms $\partial\mathbf{E}/\partial t$ and $\partial\mathbf{B}/\partial t$ must tend to zero. For the electric field this is true when $2\pi f\varepsilon/\sigma \ll 1$, where $\sigma$ is the conductivity of the propagating medium, $\varepsilon$ the electric permittivity and $f$ the oscillatory frequency. Substituting for typical values of the brain tissue, i.e. $\sigma = 0.3\Omega^{-1}m^{-1}$, $\varepsilon = 10^5\varepsilon_0$ and an oscillatory frequency $f = 100Hz$, we find that $2\pi f\varepsilon/\sigma \approx 10^{-3} \ll 1$. With the same parameters the spatial evolution of the electric field i.e. $\boldsymbol{\nabla} \times \mathbf{E}$ tends to zero for lengths $< 65$m [Hämäläinen et al., 1993]. Maxwell's equations (2.1) can then be simplified to:

$$\begin{aligned} \mathbf{E} &= -\boldsymbol{\nabla} V \\ \boldsymbol{\nabla} \times \mathbf{B} &= \mu_0 \mathbf{J} \qquad \boldsymbol{\nabla} \cdot \mathbf{B} = 0 \end{aligned} \tag{2.2}$$

Let us now consider the total current density in the brain, $\mathbf{J}$. By the Biot-Savart law we can obtain an expression for the magnetic field $\mathbf{B}$ outside the head by integrating over a "volume conductor" $G$ (i.e. the head volume) containing our total current density $\mathbf{J}$:

$$\mathbf{B}(\mathbf{r}) = \frac{\mu_0}{4\pi} \int_G \frac{\mathbf{J}(\mathbf{r}') \times \mathbf{R}}{|\mathbf{R}|^3} \mathrm{d}v', \tag{2.3}$$

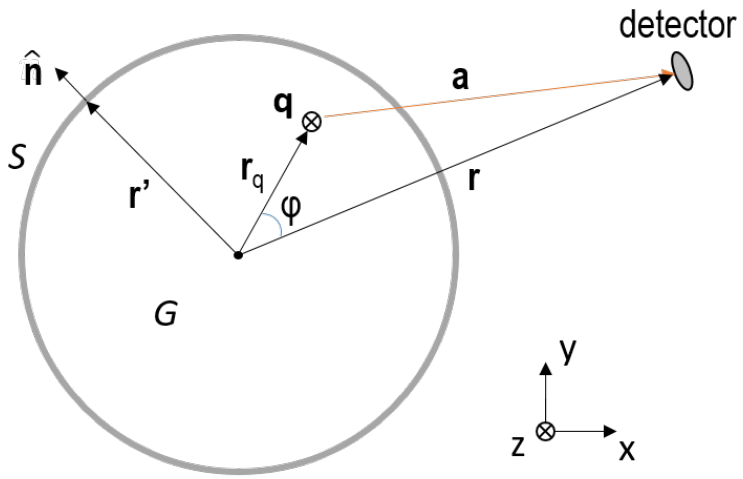



Figure 2.1: Single sphere model with dipole $\mathbf{q}$ at location $\mathbf{r}_q$ in a spherical volume conductor $G$. A detector is placed outside the volume at location $\mathbf{r}$.

where $\mathbf{r}'$ is a location inside the head, $\mathbf{r}$ is a location outside the head (where a detector might be placed) and the vector $\mathbf{R} = \mathbf{r} - \mathbf{r}'$.

As $\mathbf{J}$ corresponds to the current during post-synaptic events, we can divide it into two components reflecting the primary current inside the cell $\mathbf{J}^P$, and the volume current outside the cell $\mathbf{J}^V$. If we think of the volume current as moving in the opposite direction to the primary current and propagating through an homogeneous medium (i.e. the extracellular space) of conductivity $\sigma$ we can write:

$$\mathbf{J} = \mathbf{J}^P + \mathbf{J}^V = \mathbf{J}^P - \sigma \boldsymbol{\nabla} V, \tag{2.4}$$

We now need to find $V$. Recalling the vector identity $\boldsymbol{\nabla} \cdot \boldsymbol{\nabla} \times \mathbf{B} = 0$ and applying it to equation 2.2 we see that $\boldsymbol{\nabla} \cdot \mathbf{J} = 0$. It then follows from equation 2.4:

$$\begin{aligned} \boldsymbol{\nabla} \cdot \mathbf{J} &= \boldsymbol{\nabla} \cdot \mathbf{J}^P - \boldsymbol{\nabla} \cdot (\sigma \boldsymbol{\nabla} V) = 0 \\ \implies \boldsymbol{\nabla} \cdot (\sigma \boldsymbol{\nabla} V) &= \boldsymbol{\nabla} \cdot \mathbf{J}^P \end{aligned} \tag{2.5}$$

The solution of equation 2.5 can be hard to compute unless we consider a system with some specific symmetries [Sarvas, 1987].

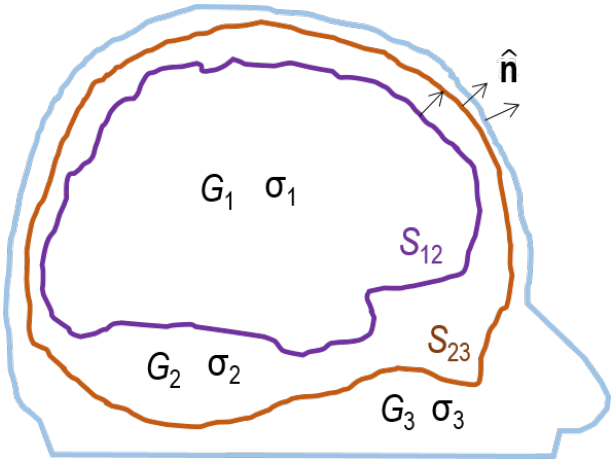



Figure 2.2: Illustration of a compartment model of the head for the forward solution. Each volume $G_i$ has a specific conductivity $\sigma_i$ and it is bounded by a surface $S_{ij}$ seprating it from neighbouring volume $G_j$. $\hat{\mathbf{n}}$ is a vector normal to the surface $S_{ij}$.

### 2.1.1 The Geselowitz formula

Let us assume that our conducting volume is composed of homogeneous compartments so that $\boldsymbol{\nabla}\sigma \neq 0$ only at the surface boundaries, as it is illustrated in Figure 2.2. The regions of uniform conductivity are named $G_i$, with $i = 1, ..., m$, their conductivities $\sigma_i$ and the surface boundaries between two regions $S_{ij}$. By substituting equation 2.4 into equation 2.3 we can separate the primary and volume current contributions to the magnetic field $\mathbf{B}$:

$$\begin{aligned}\mathbf{B}(\mathbf{r}) &= \frac{\mu_0}{4\pi}\int_G \left(\mathbf{J}^P(\mathbf{r}') - \sigma\boldsymbol{\nabla}'V(\mathbf{r}')\right) \times \frac{\mathbf{R}}{|\mathbf{R}|^3}\mathrm{d}v' \\ &= \mathbf{B}^P(\mathbf{r}) - \frac{\sigma\mu_0}{4\pi}\int_G \boldsymbol{\nabla}'V(\mathbf{r}') \times \frac{\mathbf{R}}{|\mathbf{R}|^3}\mathrm{d}v',\end{aligned} \tag{2.6}$$

where $\mathbf{B}^P(\mathbf{r})$ is the magnetic field induced by the primary current $\mathbf{J}^P$. The second term of equation 2.6 is the volume current term $\mathbf{B}^V(\mathbf{r})$, which is dependent on conductivity $\sigma$. Considering our compartments model, $\mathbf{B}^V(\mathbf{r})$ then becomes:

$$\mathbf{B}^V(\mathbf{r}) = -\frac{\mu_0}{4\pi}\sum_{i=1}^{m}\sigma_i\int_{G_i} \boldsymbol{\nabla}'V(\mathbf{r}') \times \frac{\mathbf{R}}{|\mathbf{R}|^3}\mathrm{d}v' \tag{2.7}$$

where we are summing over all volume compartments.

Noting that $\mathbf{R}/|\mathbf{R}|^3 = \boldsymbol{\nabla}'(1/|\mathbf{R}|)$ and recalling the identity $\boldsymbol{\nabla}\psi \times \boldsymbol{\nabla}\phi = \boldsymbol{\nabla} \times (\psi\boldsymbol{\nabla}\phi)$, we can write the integral in equation 2.7 as:

$$\int_{G_i} \boldsymbol{\nabla}' V(\mathbf{r}') \times \frac{\mathbf{R}}{|\mathbf{R}|^3} \mathrm{d}v' = \int_{G_i} \boldsymbol{\nabla}' \times V(\mathbf{r}') \frac{\mathbf{R}}{|\mathbf{R}|^3} \mathrm{d}v', \tag{2.8}$$

Now, using the divergence theorem:

$$\int_G \boldsymbol{\nabla} \times \mathbf{A} \mathrm{d}v = -\int_S \mathbf{A} \times \hat{\mathbf{n}} \mathrm{d}S, \tag{2.9}$$

to transform $\mathbf{B}^V$ into a surface integral, we can write equation 2.6 as:

$$\mathbf{B}(\mathbf{r}) = \mathbf{B}^P(\mathbf{r}) + \frac{\mu_0}{4\pi} \sum_{ij} (\sigma_i - \sigma_j) \int_{S_{ij}} V(\mathbf{r}') \frac{\mathbf{R}}{|\mathbf{R}|^3} \times \hat{\mathbf{n}} \mathrm{d}S', \tag{2.10}$$

where we are summing over all region boundaries. This is known as the Geselowitz equation for the magnetic field in a volume conductor [Geselowitz, 1970], where the volume currents are mathematically modelled as fictitious surface currents.

### 2.1.2 The Sarvas Equation

In the case of a conductor with spherical geometry we can show it is possible to obtain an expression for the magnetic field $\mathbf{B}(\mathbf{r})$ outside the head without referring to the volume currents (i.e. independent of both conductivity $\sigma$ and electric potential $V$).

Let us start by considering the radial component of the magnetic field, $B_r = \mathbf{B} \cdot \hat{\mathbf{e}}_r$. In equation 2.10 the unit vector $\hat{\mathbf{n}}$ points normal to the boundary surface, which for a spherical volume corresponds to the $\hat{\mathbf{e}}_{r'}$ direction (see Figure 2.1). We can then see that the radial component of the magnetic field given by the volume currents is equal to zero:

$$\mathbf{B}^V \cdot \hat{\mathbf{e}}_r \sim (\mathbf{R} \times \hat{\mathbf{n}}) \cdot \hat{\mathbf{e}}_r = (\mathbf{r} - \mathbf{r}') \times \hat{\mathbf{e}}_{r'} \cdot \hat{\mathbf{e}}_r = 0. \tag{2.11}$$

So $B_r$ depends only on the primary currents:

$$B_r = \frac{\mu_0}{4\pi} \int \mathbf{J}^P(\mathbf{r}') \times \frac{\mathbf{R}}{|\mathbf{R}|^3} \cdot \hat{\mathbf{e}}_r \mathrm{d}v' \tag{2.12}$$

In section 1.1 we saw that the main contributors to the MEG signal are post-synaptic potentials that can be approximated as current dipoles (as shown in Figure 1.3B). If we then consider our source to be a single current dipole $\mathbf{q}$ at point location $\mathbf{r}_q$ we can express the current density as:

$$\mathbf{J}^P(\mathbf{r}') = \mathbf{q}\delta(\mathbf{r}' - \mathbf{r}_q) \tag{2.13}$$

where $\delta$ is the Dirac Delta function.

The integral in equation 2.12 then reduces to:

$$\begin{aligned} B_r &= \frac{\mu_0}{4\pi} \int \mathbf{q}\delta(\mathbf{r}' - \mathbf{r}_q) \times \frac{\mathbf{R}}{|\mathbf{R}|^3} \cdot \hat{\mathbf{e}}_r \mathrm{d}v' \\ &= \frac{\mu_0}{4\pi} \mathbf{q} \times \frac{\mathbf{r} - \mathbf{r}_q}{|\mathbf{r} - \mathbf{r}_q|^3} \cdot \hat{\mathbf{e}}_r \end{aligned} \tag{2.14}$$

We now need to go back to the vector field $\mathbf{B}$ including non-radial components. From Maxwell's equations (see eq. 2.2) we know that $\boldsymbol{\nabla} \times \mathbf{B} = \mu_0 \mathbf{J}$. Since the current density is constrained inside the conductor it follows that outside the volume $\mathbf{J} = 0$ and $\boldsymbol{\nabla} \times \mathbf{B} = 0$. As we did for the electric field we can then express the magnetic field outside the head in terms of a scalar potential $U(\mathbf{r})$ as

$$\mathbf{B}(\mathbf{r}) = -\mu_0 \boldsymbol{\nabla} U(\mathbf{r}). \tag{2.15}$$

Since our problem has a spherical symmetry, in order to find an expression for $U(\mathbf{r})$ we only need to evaluate the line integral of $\boldsymbol{\nabla} U(\mathbf{r})$ in the radial direction outside the volume $G$. For a given $\mathbf{r}$ outside of $G$, we then integrate over $\mathbf{r} + t\hat{\mathbf{e}}_r$,

with $0 \leq t \leq \infty$ and $U(\mathbf{r})$ vanishing at infinity:

$$\begin{aligned} U(\mathbf{r}) &= -\int_0^\infty \boldsymbol{\nabla} U(\mathbf{r} + t\hat{\mathbf{e}}_r) \cdot \hat{\mathbf{e}}_r \\ &= \frac{1}{\mu_0}\int_0^\infty \mathbf{B}(\mathbf{r} + t\hat{\mathbf{e}}_r) \cdot \hat{\mathbf{e}}_r \mathrm{d}t = \frac{1}{\mu_0}\int_0^\infty B_r(\mathbf{r} + t\hat{\mathbf{e}}_r)\mathrm{d}t \\ &= \frac{1}{4\pi}\int_0^\infty \mathbf{q} \times \frac{\mathbf{r} + t\hat{\mathbf{e}}_r - \mathbf{r}_q}{|\mathbf{r} + t\hat{\mathbf{e}}_r - \mathbf{r}_q|^3} \cdot \hat{\mathbf{e}}_r \mathrm{d}t \\ &= -\frac{1}{4\pi}\mathbf{q} \times \mathbf{r}_q \cdot \hat{\mathbf{e}}_r \int_0^\infty \frac{\mathrm{d}t}{|\mathbf{r} + t\hat{\mathbf{e}}_r - \mathbf{r}_q|^3}, \end{aligned} \tag{2.16}$$

where we substituted the magnetic potential and field for equations 2.15 and 2.14 respectively, and simplified the radial component according to $\mathbf{q} \times \hat{\mathbf{e}}_r \cdot \hat{\mathbf{e}}_r = 0$.

Following the derivation proposed by Sarvas[1][Sarvas, 1987] we can write the solution of the integral in the form

$$U(\mathbf{r}) = -\frac{1}{4\pi}\frac{\mathbf{q} \times \mathbf{r}_q \cdot \mathbf{r}}{F}, \tag{2.17}$$

where $F = a(ra + r^2 - \mathbf{r}_q \cdot \mathbf{r})$, $\mathbf{a} = \mathbf{r} - \mathbf{r}_q$ and for ease of syntax $a = |\mathbf{a}|$ and $r = |\mathbf{r}|$.

Now we can substitute $U(\mathbf{r})$ in equation 2.15 to arrive at an expression for the magnetic field outside the volume $G$:

$$\mathbf{B}(\mathbf{r}) = \frac{\mu_0}{4\pi F^2}(F\mathbf{q} \times \mathbf{r}_q - \mathbf{q} \times \mathbf{r}_q \cdot \mathbf{r}\boldsymbol{\nabla} F) \tag{2.18}$$

with $\boldsymbol{\nabla} F = (a^2/r + \mathbf{a} \cdot \mathbf{r}/a + 2a + 2r)\mathbf{r} - (a + 2r + \mathbf{a} \cdot \mathbf{r}/a)\mathbf{r}_q$. From equations 2.17 and 2.18 it follows that a radially oriented dipole source in a spherical conductor does not contribute to the magnetic field, i.e. $\mathbf{q} \times \mathbf{r}_q = 0$.

### 2.1.3 Multiple sphere extension

Approximating the volume conductor as a single sphere allows us to have a quick analytical solution for the magnetic field generated by current dipole sources.

[1]Sarvas helpfully provides this solution without boring the reader with the details of the integration. Prompted by the integral being "easy to compute" the author decided to spend a weekend to re-familiarise herself with vector calculus and go through the derivation in appendix A.

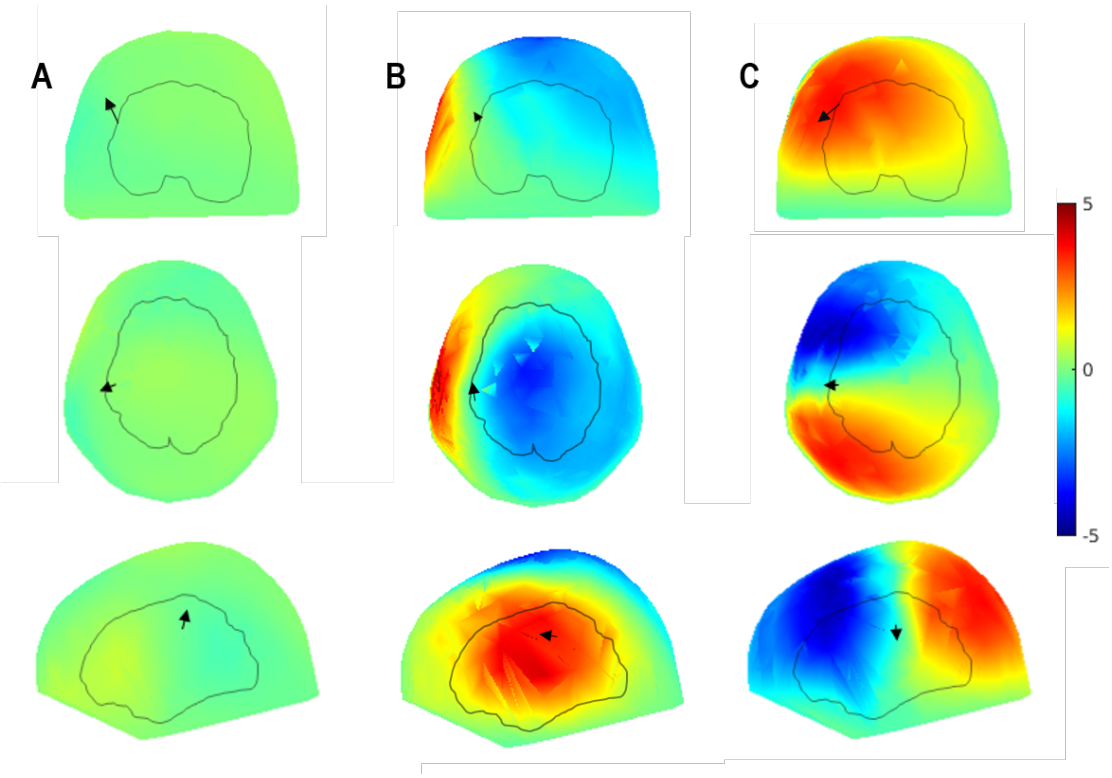



Figure 2.3: Examples of forward solutions constructed with Sarvas's equation (2.18) for a homogeneous spherical conductor and Huang et al. [2009] multiple sphere model. Magnetic field amplitudes are calculated at the sensor locations of a 275 channel CTF MEG system. Figures A, B and C show the solutions, displayed in coronal, axial and sagittal views, for three orthogonal dipoles (indicated by a black arrow) centred on the same location in the left sensorimotor cortex. A) Forward solution for a radially oriented unit dipole, note the magnetic fields tends to zero, i.e. radial dipoles are magnetically silent. B) and C) show forward solutions for two orthogonal dipoles both laying in the tangential plane.

Unfortunately the geometry of the head is not spherical, meaning that using a single sphere model does not perfectly reproduce the magnetic fields outside it. The most accurate approach for MEG forward modelling is to computationally model the cortex, skull and the scalp through a boundary element model (BEM) [Stenroos et al., 2014]. BEMs are highly beneficial in modelling the electric field in EEG, due to the varying permittivity of tissues, but their improvement in estimating the MEG forward model is still debatable (given the homogeneous magnetic permeability of the head, the necessary introduction of an estimated electrical conductivity for the volume currents calculation, as well as the computational cost of accurately modelling the cortical surface). An analytical solution with more realistic geometry, known as the "multiple local sphere" model was introduced by Huang et al. [1999]. The multiple spheres model is based on the idea that the spherical model is still approximately valid if we independently build a new sphere for each sensor so that, in the proximity of that sensor, the sphere optimally matches the brain surface. The result is a model of overlapping spheres, where the lead fields can still be estimated by equation 2.18. The multiple sphere model will be used as the standard forward model in all the work presented in this thesis.

## 2.2 Inverse Problem

Using the forward solution we can model how the magnetic field propagates from a dipole source in the brain to the MEG sensors. However in neuroimaging we are interested in mapping the electrical activity at the source location. In other words, given a series of magnetic fields measurements made outside the head, we want to reconstruct the source dipole current distribution in the brain. This is called the MEG inverse problem. It is mathematically ill posed as there is no unique combination of sources responsible for any one field pattern. In order to solve the problem we therefore have to set some assumptions or constraints.

We can start by considering the measured magnetic field $b_i(t)$ at each sensor $i$

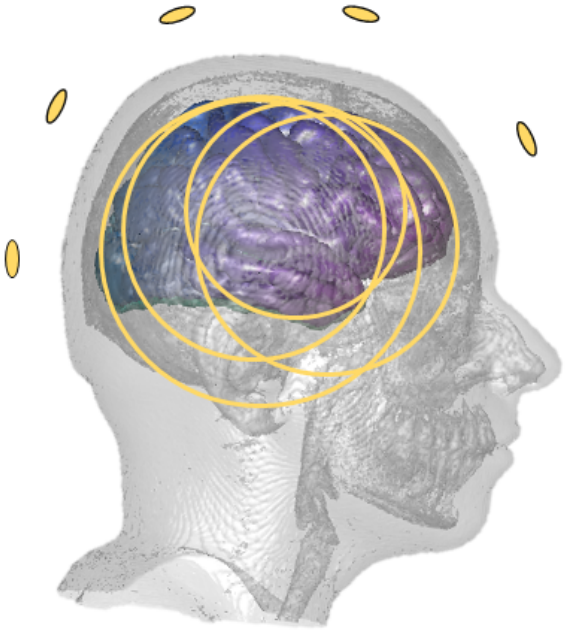


Figure 2.4: Schematic of multiple sphere model.

($i = 1, 2, ..., N$, where $N$ is the total number of MEG sensors). Given a dipole of strength $q(\mathbf{r}', t)$ there is a vector field $\mathbf{l}(\mathbf{r}')$, satisfying:

$$b_i(t) = \int_V \mathbf{l}_i(\mathbf{r}')q(\mathbf{r}', t)\mathrm{d}v' \tag{2.19}$$

$\mathbf{l}$ is called the forward field (derived from the forward solution) and models the magnetic field at sensor $i$ for a unit dipole at given location $\mathbf{r}'$. As the location and number of the sources is unknown we can simplify the problem by dividing the brain into $M$ discrete voxels, each containing a dipole source $q_j$ so that

$$b_i(t) = \sum_{j=1}^{M} \mathbf{l}_{i,j}q_j(t). \tag{2.20}$$

We can then express the magnetic field in matrix form:

$$\mathbf{B}(t) = \mathbf{L} \cdot \mathbf{q}(t), \tag{2.21}$$

$$\mathbf{L} = \begin{bmatrix} \mathbf{l}_{1,1} & \mathbf{l}_{1,2} & \cdots & \mathbf{l}_{1,M} \\ \mathbf{l}_{2,1} & \mathbf{l}_{2,2} & \cdots & \mathbf{l}_{2,M} \\ \vdots & \vdots & \ddots & \vdots \\ \mathbf{l}_{N,1} & \mathbf{l}_{N,2} & \cdots & \mathbf{l}_{N,M} \end{bmatrix}, \qquad \mathbf{q}(t) = \begin{bmatrix} q_1(t) \\ q_2(t) \\ \vdots \\ q_M(t) \end{bmatrix}. \tag{2.22}$$

where the lead field matrix $\mathbf{L}$ has dimensions $N \times M$ and contains complete information on how the dipoles in $\mathbf{q}(t)$ at the $M$ voxel locations map on to the $N$ MEG sensors. Equation 2.21 is known as the generative model for MEG data, describing how a current distribution creates the detected field. Mathematically in order to solve the inverse problem we have to invert the generative model to find $\mathbf{q}(t)$. Unfortunately $\mathbf{L}$ cannot simply be inverted as it is singular and not square. This is the mathematical manifestation of the ill posed nature of the MEG inverse problem. It follows that some sort of optimisation must therefore be used.

### 2.2.1 Beamforming

Beamforming is a popular inverse modelling technique that was originally developed for applications in radar and sonar, and has since found utility in M/EEG source reconstruction. Beamforming was selected as the inverse method solution for the work presented in this thesis, over other well-known approaches, such as minimum-norm estimates (MNE) [Hämäläinen and Ilmoniemi, 1994], as beamforming solutions provide good estimation of oscillatory activity and its underlying assumption of uncorrelated sources make it a prime choice for MEG functional connectivity estimation [Brookes et al., 2011a] (see section 2.3.1 on spatial leakage). Beamforming is a spatial filtering technique meaning that it estimates the strength of a dipole $q_\theta(t)$ with some predetermined location and orientation given by the vector $\boldsymbol{\theta}$. The basic premise is that $q_\theta(t)$ is reconstructed based upon a weighted sum of sensor measurements. Mathematically

$$\hat{q}_\theta(t) = \sum_{i=1}^{N} w_{i,\theta} b_i(t), \tag{2.23}$$

or in matrix from

$$\hat{q}_\theta(t) = \mathbf{w}_\theta^T \mathbf{B}(t), \tag{2.24}$$

where $\hat{q}_\theta$ represents the beamformer estimate of the true dipole source strength $q_\theta$ obtained from the MEG data $\mathbf{B}$. Almost all source reconstruction methods can be cast in this way and they differ based on the formulation of the weights. In beamforming the vector of weighting parameters $\mathbf{w}_\theta$ is determined to minimise the source power originating from locations $\boldsymbol{\theta} \neq \boldsymbol{\theta}_q$, while maintaining all of the signal coming from $\boldsymbol{\theta}_q$. Mathematically this can be expressed as:

$$min_{\mathbf{w}_\theta} E\big[\|\hat{q}_\theta\|^2\big], \text{ subject to } \mathbf{w}_\theta^T \mathbf{L}_\theta = 1 \tag{2.25}$$

The expectation value of the dipole magnitude squared can be estimated from equation 2.24:

$$\begin{aligned} E\big[\|\hat{q}_\theta\|^2\big] &= E\big[\big(\mathbf{w}_\theta^T \mathbf{B}(t)\big)\big(\mathbf{w}_\theta^T \mathbf{B}(t)\big)\big] \\ &= \big[\mathbf{w}_\theta^T \mathbf{C} \mathbf{w}_\theta\big], \end{aligned} \tag{2.26}$$

where $\mathbf{C} = E\big[\mathbf{B}(t)\mathbf{B}(t)^T\big]$ is approximated by the covariance matrix of the sensor data calculated over some time/frequency window of interest. A solution for the weights can be found using the method of Lagrange multipliers [Van Veen et al., 1997]. Following the solution detailed in Sekihara and Nagarajan [2008] we can define the Lagrangian $\mathcal{L}$ and the scalar Lagrange multiplier $\kappa$ with the form

$$\mathcal{L}(\mathbf{w}, \kappa) = \mathbf{w}^T \mathbf{C} \mathbf{w} + \kappa(\mathbf{w}^T \mathbf{L} - 1). \tag{2.27}$$

The weight vector $\mathbf{w}$ satisfying the conditions of the beamformer in equation 2.25 will minimise the Lagrangian $\mathcal{L}(\mathbf{w}, \kappa)$. We can then find the derivative of $\mathcal{L}(\mathbf{w}, \kappa)$ with respect to $\mathbf{w}$

$$\frac{\partial \mathcal{L}(\mathbf{w}, \kappa)}{\partial \mathbf{w}} = 2\mathbf{C}\mathbf{w} + \kappa \mathbf{L}, \tag{2.28}$$

and set it to zero to find its minimum

$$\mathbf{w} = -\kappa \mathbf{C}^{-1}\mathbf{L}/2. \tag{2.29}$$

As $\mathbf{w}^T\mathbf{L} = 1$ it then follows from our minimum solution that $\kappa = -2/[\mathbf{L}^T\mathbf{C}^{-1}\mathbf{L}]$, and substituting this back into equation 2.29 we arrive at the expression for the beamformer weights [Van Veen et al., 1997]:

$$\mathbf{w}_\theta = \frac{\mathbf{C}^{-1}\mathbf{L}_\theta}{\mathbf{L}_\theta^T\mathbf{C}^{-1}\mathbf{L}_\theta}. \tag{2.30}$$

The expression of the weights depends on the inverse of the covariance matrix, which is estimated by the sensor data. In practice $\mathbf{C}$ can be close to singular (matrix determinant $\ll 1$) meaning that while $\mathbf{C}^{-1}$ can be calculated the solution will be unstable. It is possible to stabilise the beamformer source power estimation by regularising the covariance matrix through Tikhonov regularisation [Tikhonov, 1943], so that

$$\mathbf{C}_r = \mathbf{C} + \mu\mathbf{\Sigma} \tag{2.31}$$

where $\mathbf{\Sigma}$ is the noise covariance matrix. The minimisation function therefore becomes

$$min_{\mathbf{w}_\theta}\left[\mathbf{w}_\theta^T(\mathbf{C} + \mu\mathbf{\Sigma})\mathbf{w}_\theta\right], \text{ subject to } \mathbf{w}_\theta^T\mathbf{L}_\theta = 1, \tag{2.32}$$

and the weights can be expressed as

$$\mathbf{w}_\theta = \frac{(\mathbf{C} + \mu\mathbf{\Sigma})^{-1}\mathbf{L}_\theta}{\mathbf{L}_\theta^T(\mathbf{C} + \mu\mathbf{\Sigma})^{-1}\mathbf{L}_\theta}. \tag{2.33}$$

From equation 2.32 we see that beamformer regularisation acts to minimise both the variance of the source signal $\mathbf{w}_\theta^T\mathbf{C}\mathbf{w}_\theta$, as well as random uncorrelated noise $\mathbf{w}_\theta^T\mathbf{\Sigma}\mathbf{w}_\theta$. The regularisation parameter $\mu$ adjusts the balance between improving the accuracy (i.e. the SNR) of the beamformer solution at the cost of spatially broadening the filter (i.e. neighbouring sensors containing the same neu-

romagnetic signals will be clustered together and hence source reconstructed time courses in adjacent voxels will be highly correlated) [Brookes et al., 2008].

### 2.2.2 Source angle selection

So far in our derivation of the inverse solution we assumed that the location and orientation $\boldsymbol{\theta}$ of the source dipole is known. The orientation of the dipoles can be assumed to be normal to an individual cortical mesh model [Dale and Sereno, 1993], but in practice this is not always feasible to compute accurately (e.g. in the case of imperfect co-registration). The more common approach is to select the orientation in a data driven way, so as to obtain the best SNR in a given location. In spherical models this problem can be simplified further by fixing the orientation to be tangential to the radial direction (as radial sources are silent), so the orientation can be expressed by the azimuthal angle $\phi$. As the total power over time is given by $\mathbf{w}_\theta^T \mathbf{C} \mathbf{w}_\theta$, we can calculate weight vectors for dipoles at location $\mathbf{r}$ with orientations ranging from $0 \leq \phi \leq \pi$ and create a pseudo-Z statistic for each estimated orientation as

$$\mathbb{Z}_{\mathbf{r},\phi} = \frac{\mathbf{w}_{\mathbf{r},\phi}^T \mathbf{C} \mathbf{w}_{\mathbf{r},\phi}}{\mathbf{w}_{\mathbf{r},\phi}^T \boldsymbol{\Sigma} \mathbf{w}_{\mathbf{r},\phi}}, \tag{2.34}$$

where $\Sigma$ is the noise covariance matrix [Vrba, 2002]. Equation 2.34 effectively represents the beamformer projected signal to noise ratio. It is challenging to perfectly estimate the sensor noise during the MEG data recording, and so we usually assume that all sensors have equal noise, that is temporally independent across sensors, so that $\Sigma = \nu^2 \mathbf{I}$, with $\nu^2$ being the variance of the noise and $\mathbf{I}$ the identity matrix. The noise variance can then be estimated by the minimum singular value of the data covariance matrix and a linear search for the maximum $\mathbb{Z}_{\mathbf{r},\phi}$ determines the dipole orientation in the tangential plane. An alternative method accounting for non-spherical models, and dipoles possibly oriented in the radial direction, was proposed by Sekihara et al. [2004] where lead fields at location $\mathbf{r}$ are calculated for unit dipoles at three orthogonal orientations $[i, j, k]$, i.e. $\mathbf{L}_r = [l_{\mathbf{r},i}, l_{\mathbf{r},j}, l_{\mathbf{r},k}]$. The optimum source orientation is then equal to the eigenvector

corresponding to the minimum eigenvalue of the matrix ($\mathbf{L_r}^T\mathbf{C}^{-1}\mathbf{L_r}$). In a spherical model this effectively collapses to the same result in the tangential plane.

### 2.2.3 Induced responses localisation

Following equation 2.24 we can estimate the source time course at each selected voxel location. When selecting voxels over the whole brain volume it is important to note that the noise distribution will be different when moving away from the sensors and this will affect the power of the estimated sources, i.e. far from the sensors, noise power dominates over genuine source power. In beamformers the weights in equation 2.30 have higher norm towards the center of the brain due to the lead fields norm decreasing in the same direction. This causes a bias towards the center of the brain with deeper sources having a higher variance. The effect can be compensated by dividing the weights by their norm

$$\begin{aligned} \|\mathbf{w}_\theta\| &= \sqrt{\mathbf{w}_\theta^T\mathbf{w}_\theta} \\ &= \sqrt{\frac{\mathbf{L}_\theta^T\mathbf{C}^{-1}\mathbf{C}^{-1}\mathbf{L}_\theta}{(\mathbf{L}_\theta^T\mathbf{C}^{-1}\mathbf{L}_\theta)^2}} = \frac{\sqrt{\mathbf{L}_\theta^T\mathbf{C}^{-2}\mathbf{L}_\theta}}{\mathbf{L}_\theta^T\mathbf{C}^{-1}\mathbf{L}_\theta} \end{aligned} \tag{2.35}$$

giving the depth corrected weights equation

$$\mathbf{w}_\theta^{norm} = \frac{\mathbf{C}^{-1}\mathbf{L}_\theta}{\sqrt{\mathbf{L}_\theta^T\mathbf{C}^{-2}\mathbf{L}_\theta}} \tag{2.36}$$

In order to determine the location of sources of interest over the whole brain volume we can apply relevant statistics. Where we may be interested in absolute source power we can calculate a pseudo-Z statistic

$$Z_\theta^2 = \hat{Q}_\theta^2/\hat{\nu}_\theta^2, \tag{2.37}$$

where $\hat{Q}_\theta^2 = \mathbf{w}_\theta^T\mathbf{C}\mathbf{w}_\theta$ is the total power and $\hat{\nu}_\theta^2 = \mathbf{w}_\theta^T\mathbf{\Sigma}\mathbf{w}_\theta$ is the estimated noise power. Rather than the absolute power of a source, when looking at task data we are most often interested in sources showing significant changes in power relative

to a control time window. In this case we can calculate the data covariance $\mathbf{C}^{(a)}$ during an active window of interest $(a)$ and estimate the total source power $\hat{Q}_\theta^{(a)2} = \mathbf{w}_\theta^T \mathbf{C}^{(a)} \mathbf{w}_\theta$ and noise power $\hat{\nu}_\theta^{(a)2}$ during the same time window. We can then select a control window of the same duration $(c)$, with covariance $\mathbf{C}^{(c)}$, source power $\hat{Q}_\theta^{(c)2} = \mathbf{w}_\theta^T \mathbf{C}^{(c)} \mathbf{w}_\theta$ and noise power $\hat{\nu}_\theta^{(c)2}$. In order to localise sources showing power modulations in the active window compared to control we can build a pseudo-T statistic:

$$\mathrm{T}_\theta = \frac{\hat{Q}_\theta^{(a)2} - \hat{Q}_\theta^{(c)2}}{\hat{\nu}_\theta^{(a)2} + \hat{\nu}_\theta^{(c)2}}. \tag{2.38}$$

### 2.2.4 Beamforming with anatomical atlases

In order to meaningfully interpret brain electrophysiological signals we are often interested in looking at both their location and time evolution. MEG source reconstruction allows us to reconstruct electrical activity at any arbitrary location in the brain, usually on a regular grid, and identify areas with maximum variance at some time of interest associated with task and/or stimulus presentation. We can then obtain 5 dimensional data with location in 3-dimensional space, time and frequency characteristics. The analysis of such multidimensional data-sets are difficult because of the complexity of appropriate statistical techniques and the requirements on computer memory. Therefore the analysis of MEG data is often simplified by fixing some of the dimensional variables: filtering the signal at a pre-determined frequency band and selecting time windows allows us to obtain spatial information, or conversely, by selecting a voxel of interest we can generate a time and frequency spectrum.

Another method to simplify the spatial information in MEG signal is to represent, with a single representative time course, the activity of multiple voxels in a cortical region. As the human brain is functionally organised in anatomically separate regions we can segment the cortex according to defined anatomical markers. This technique is called parcellation and anatomical atlases are referenced to

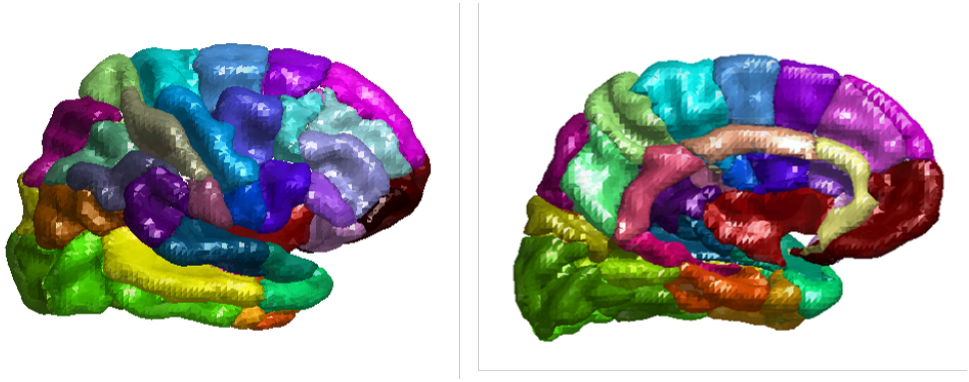


Figure 2.5: Outer (left) and inner (right) views of an individual brain cortex parcellated according to the MarsAtlas by matching key cortical sulci to a template brain.

standard brains, obtained by averaging the brain anatomy of tens or sometime hundreds of subjects [Mazziotta et al., 1995, 2001]. Several anatomical atlases are available, with one of the most commonly used being the Automated Anatomical Labeling (AAL) atlas [Tzourio-Mazoyer et al., 2002], which we adopted for functional connectivity analysis in chapter 3. As part of the work presented in chapter 4 of this thesis, we instead selected the MarsAtlas [Auzias et al., 2016], a cortical atlas with 82 regions of interest with more detail in parietal and frontal cortex compared to the AAL atlas (see Figure 2.5), thus potentially offering better spatial discrimination in studies involving the sensorimotor system.

#### Time course estimate: centroid, Gaussian Kernel, PCA

After parcellating the brain, the next step is to determine a single representative time course for each regions of interest. The simplest method is to select the centroid of the ROI volume and calculate the source reconstructed time course at that location. When using beamforming a high regularisation parameter (e.g. 5% of the maximum singular value of the covariance matrix) is used in order to spatially smooth the result and simultaneously improve the signal to noise of the solution. Another approach is to calculate all virtual electrodes within the ROI and scale their amplitude based on a spatially decaying Gaussian Kernel with maximum on the centroid location. The scaled time courses are then summed

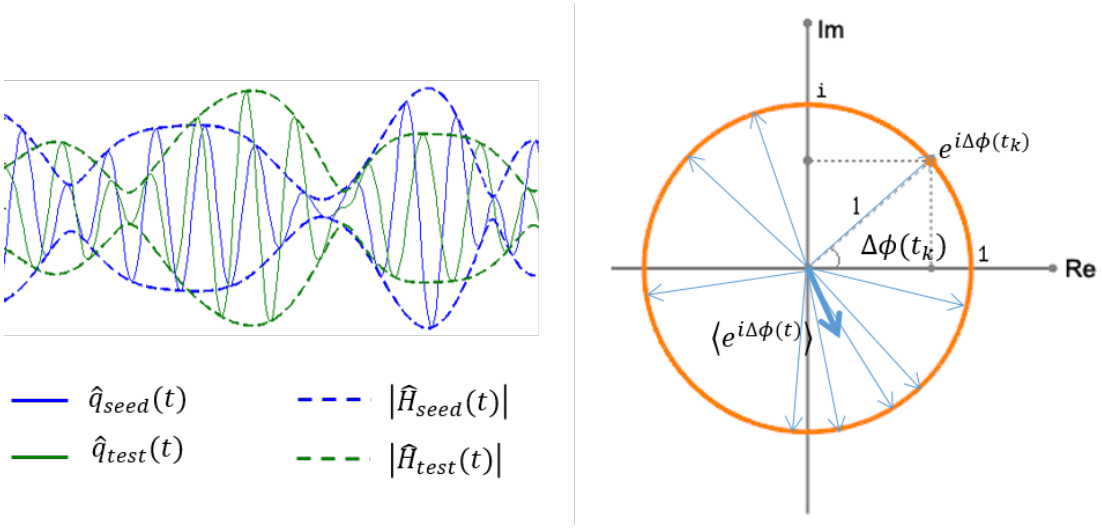



Figure 2.6: Diagrams of the principle of Amplitude Envelope Correlation (left) and Phase Locking Value (right).

together to obtain an average representation of the whole region. In some cortical atlases closely following the cortical surface, such as the MARS atlas, the centroid often falls outside the ROI volume. In this case Principal Component Analysis (PCA) can be used to select the principal component of all voxels within the ROI.

## 2.3 Functional Connectivity

The temporal complexity of MEG signals means that a number of models to characterise functional connectivity have been proposed. Most of these can be divided into two categories which exploit either phase or amplitude information. Phase methods (e.g. coherence, imaginary coherence, phase locking value or phase lag index) seek to measure a stable phase relationship between band limited signals measured at spatially separate locations. Amplitude methods (e.g. amplitude envelope correlation) seek to characterise temporal correlation between the envelopes of those same band limited signals. Both classes of metric are implemented in the work presented in this thesis and are described here in detail.

- **Amplitude Envelope Correlation** (**AEC**) [Brookes et al., 2012; Hipp et al., 2012]: Reconstructed data, $\hat{q}_{seed}(t)$ and $\hat{q}_{test}(t)$ (derived from equation 2.24 at locations $\boldsymbol{\theta}_{seed}$ and $\boldsymbol{\theta}_{test}$) are frequency filtered into a band of interest

and Hilbert transformed to derive their analytic signal, $\mathcal{H}_{seed}$ and $\mathcal{H}_{test}$. The absolute value of the analytic signal is then computed to generate the Hilbert envelope of band limited oscillations (see Figure 2.6). Pearson correlation, measured between amplitude envelopes then yields an estimate of amplitude envelope based functional connectivity.

$$AEC = corr(|\mathcal{H}_{seed}|, |\mathcal{H}_{test}|) = \frac{|\mathcal{H}_{seed}||\mathcal{H}_{test}|^T}{\sqrt{|\mathcal{H}_{seed}||\mathcal{H}_{seed}|^T}\sqrt{|\mathcal{H}_{test}||\mathcal{H}_{test}|^T}} \quad (2.39)$$

where each envelope $|\mathcal{H}|$ has been mean corrected.

- **Coherence** (**Coh**) and **Imaginary Coherence** (**ICoh**): Denoting $x = \hat{q}_{seed}(t)$ and $y = \hat{q}_{test}(t)$ coherency is calculated as

$$C_{xy}(f) = \frac{S_{xy}(f)}{\sqrt{S_{xx}(f)S_{yy}(f)}}, \quad (2.40)$$

where $S_{xy}$ denotes the cross spectral density (if $x \neq y$ ) or auto spectral density (if $x = y$). The result, $C_{xy}(f)$, is a complex number, the magnitude of which is between 0 and 1, with high values indicating the presence of a strong fixed phase relationship between $\hat{q}_{seed}(t)$ and $\hat{q}_{test}(t)$ at frequency $f$. Coherence is then defined as the absolute value of coherency Coh $= |C_{xy}(f)|$ and, for frequency band analysis, it is averaged over the frequency range of interest. Imaginary coherence [Nolte et al., 2004] is simply the imaginary part of coherency ICoh $= \text{Im}[C_{xy}(f)]$, and is often employed to remove zero-phase-lag effects, which are artefactually inflated as a result of the ill-posed inverse problem smearing a single source over many neighbouring voxels (i.e. signal leakage, see section 2.3.1).

- **Phase Locking Value** (**PLV**) [Lachaux et al., 1999] assesses the extent to which the phase difference between two signals changes over time; high PLV indicates a phase difference that remains constant (i.e. a fixed phase relationship), reflecting instantaneous (zero-phase difference) or lagged (non-zero

phase difference) communication between neuron assemblies. $\hat{q}_{seed}(t)$ and $\hat{q}_{test}(t)$ are frequency filtered and Hilbert transformed to generate the analytic signals $\mathcal{H}_{seed}(t)$ and $\mathcal{H}_{test}(t)$. Instantaneous phases of the two signals, $\hat{\phi}_{seed}(t)$ and $\hat{\phi}_{test}(t)$, are then extracted, as $\hat{\phi}_x = \text{atan}(\text{Im}[\mathcal{H}_x(t)]/\,\text{Re}[\mathcal{H}_x(t)])$, and the phase difference generated so that $\Delta\hat{\phi}(t) = \hat{\phi}_{seed}(t) - \hat{\phi}_{test}(t)$. Phase locking value is defined as

$$PLV = \left|\left\langle \exp\left(i\Delta\hat{\phi}(t)\right)\right\rangle\right| \tag{2.41}$$

Phase locking value is usually estimated in overlapping time windows as phase relationships are only expected to last for a few tens of milliseconds (depending on the frequency band of interest).

- **Phase Lag Index** (**PLI**) [Stam et al., 2007] is related to PLV but eliminates the zero phase lag components to avoid overestimating connectivity due to signal leakage effects. PLI is defined as

$$\begin{aligned} PLI &= |\langle sign(\text{Im}\,[\Psi])\rangle| \\ \text{with } \Psi &= \exp\left(i\Delta\hat{\phi}(t)\right) \end{aligned} \tag{2.42}$$

  where the imaginary part eliminates any linear relationships and taking its sign assigns a binary value at each time point $t$ corresponding to $\hat{q}_{seed}(t)$ leading or lagging over $\hat{q}_{test}(t)$. A modified version of PLI, called weighted PLI (wPLI) was proposed by Vinck et al. [2011]:

$$wPLI = \frac{|\langle \text{Im}[\Psi])\rangle|}{\langle|\text{Im}[\Psi]|\rangle} \tag{2.43}$$

- **Phase Difference Derivative** (**PDD**) [Breakspear et al., 2004] is a dynamic connectivity measure based on phase locking. Starting with the phase difference time course $\Delta\hat{\phi}(t)$ we estimate its rate of change over time i.e. its time derivative $\text{d}\Delta\hat{\phi}(t)/\text{d}t$, if the phase difference is constant over time

(phase-locking) it follows that the phase derivative will tend to zero, conversely a high value of phase derivative implies that the phase relationship of the two time courses is independent. The "phase difference derivative" metric has been originally defined as a binary time course

$$PDD(t) = \begin{cases} 1 \text{ if } \left|\frac{\mathrm{d}\Delta\hat{\phi}(t)}{\mathrm{d}t}\right| \leq k \\ 0 \text{ if } \left|\frac{\mathrm{d}\Delta\hat{\phi}(t)}{\mathrm{d}t}\right| > k \end{cases}, \tag{2.44}$$

where $k$ is a cut-off parameter depends on the sample frequency and frequency band of the data. However, in order to avoid the arbitrariness of the cut off parameter, a better implementation defines

$$PDD(t) = \exp\left\{-\left|\frac{\mathrm{d}\Delta\hat{\phi}(t)}{\mathrm{d}t}\right|\right\}. \tag{2.45}$$

As PDD is time dependent it can be be correlated with other dynamical characteristics of the signal, such as signal amplitude in a frequency band [Tewarie et al., 2018], and compared to task paradigms.

Note that whilst the above list contains some popular approaches it is not an exhaustive list and other functional connectivity methods have been used in the literature: for example Mutual Information [Palus, 1997] and Synchronisation Likelihood [Stam and Van Dijk, 2002] assess similarities in phase or amplitude without assuming a linear relationship; Wavelet coherence [Grinsted et al., 2004], similar to standard coherence, determines frequency characteristics through wavelet transform. Some metrics also give information about the direction of information transfer between two nodes, the most notable examples being Granger's Causality [Granger, 1969], Phase Slope Index [Nolte et al., 2008], Transfer Entropy [Schreiber, 2000] and Partially Directed Coherence [Baccalá and Sameshima, 2001]. However these metrics will not feature in the experimental work here presented.

| Metric | Type | Directed | Linear | Leakage |
|---|---|---|---|---|
| Amplitude Envelope Correlation | Amplitude Coupling | No | Yes | Yes |
| Coherence | Spectral Coherence | No | Yes | Yes |
| Imaginary Coherence | Spectral Coherence | No | Yes | No |
| Phase Locking Value | Phase Coupling | No | No | Yes |
| Phase Lag Index | Phase Coupling | No | No | No |
| Phase Slope Index | Phase Coupling | Yes | Yes | No |
| Phase Difference Derivative | Phase Coupling | No | Yes | Yes |
| Mutual Information | Amplitude or Phase | No | No | Yes |
| Transfer Entropy | Amplitude or Phase | Yes | No | No |
| Granger Causality | Autoregressive model | Yes | Yes | unsure |
| Partially Directed Coherence | Autoregressive model | Yes | Yes | unsure |
| Synchronisation Likelihood | Generalised synchronisation | No | No | Yes |

Table 2.1: List of some of the most common connectivity metrics used in M/EEG data (table adapted from O'Neill et al. [2018]). Functional connectivity metrics are classified based on their type (e.g. amplitude or phase coupling), measurement of directionality of information, assumption of a linear relationship between time courses, and whether they are affected by spatial leakage.

### 2.3.1 Leakage correction

Due to the ill posed nature of the inverse problem source localisation is affected by spatial blurring or "signal leakage". This can result in two uncorrelated sources having their reconstructed time courses erroneously correlated. If ignored, this can artificially inflate the level of connectivity between two sources. The way leakage propagates across the source space is non-trivial, and solutions need to be implemented to reduce this effect on functional connectivity. Some have proposed to use parcellation methods optimised to minimise spatial leakage, but this approach comes with the caveat of spatial leakage being dependent on individual head geometry and positioning with respect to the sensors, becoming difficult to implement on multiple subject studies. Multiple solutions exist, though all are currently based on the same principle: leakage propagates instantaneously due to inverse reconstruction being time independent, so any zero-lagged relationship between two sources must be discounted or removed from the data entirely. Obviously, this does come at the expense of removing genuine zero-lag connectivity. Some of the connectivity metrics described above, such as PLI and Imaginary Coherence, only consider non-zeros phase lagged relationships to avoid confounds of

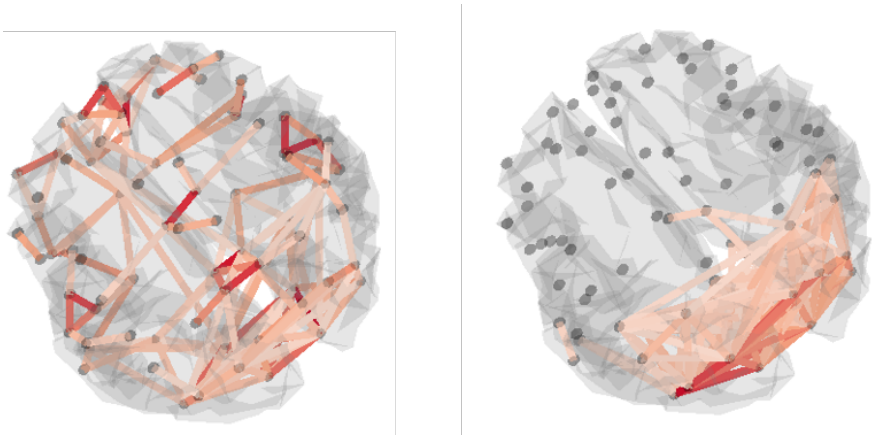


Figure 2.7: Glass brain representation of whole brain functional connectivity viewed from above. Each dot corresponds to an ROI derived by an anatomical atlas, and lines indicate functional connections (connectivity) between two ROIs, with colour intensity signifying strength of connectivity. The graphs show the strongest 5% connections of the same beamformed time courses where amplitude envelope correlation (AEC) was calculated without leakage correction (left) and following leakage correction (right). Note that when no leakage correction is applied functional connectivity is dominated by short range spurious connections from spatially blurred sources. After linear correlations are minimised most spurious connections disappear and real functional connections can emerge (in this case an occipital network).

leakage. Other metrics, such as amplitude based AEC and phase metrics including zero-lag relationships (e.g. Coh, PLV and PDD), require some correction to eliminate linear dependencies in the source reconstructed signals.

### Pairwise

A method to reduce leakage in connectivity estimation was proposed independently by Brookes et al. [2011b] and Hipp et al. [2012] for amplitude envelope calcualtions. Consider two beamformed time courses at separate locations $\hat{\mathbf{q}}_1$ and $\hat{\mathbf{q}}_2$. Leakage effects mean that $\hat{\mathbf{q}}_1$ and $\hat{\mathbf{q}}_2$ will be artifactually mixed with zero-lag such that

$$\hat{\mathbf{q}}_1 = \mathbf{q}_{1M} + \beta \mathbf{q}_2 \tag{2.46}$$

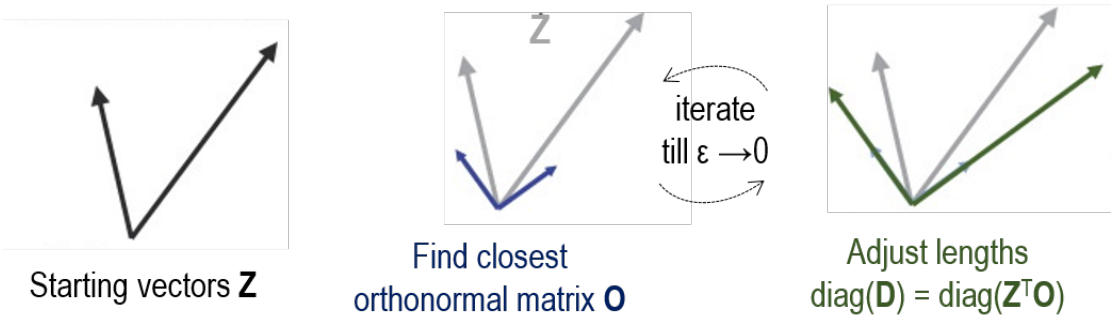



Figure 2.8: Schematic of multivariate leakage correction method. Figure adapted from [Colclough et al., 2015].

where $\hat{\mathbf{q}}_1$ is the beamformer estimate of $\mathbf{q}_1$ and $\beta$ is the effect size relating to the leakage magnitude which can be estimated as

$$\beta = \hat{\mathbf{q}}_1 \hat{\mathbf{q}}_2^{+} \tag{2.47}$$

with $\hat{\mathbf{q}}_2^{+}$ indicating the Moore-Penrose psuedo-inverse. Note that if we want to estimate $\hat{\mathbf{q}}_2$ without the effect of $\hat{\mathbf{q}}_1$ we will formulate the problem as $\hat{\mathbf{q}}_2 = \hat{\mathbf{q}}_{2M} + \beta' \hat{\mathbf{q}}_1$ which will have $\beta' \neq \beta$ and for a zero-lag functional connectivity estimation $FC[\hat{\mathbf{q}}_{1M}, \hat{\mathbf{q}}_2] \neq FC[\hat{\mathbf{q}}_1, \hat{\mathbf{q}}_{2M}]$. Where we aim to estimate an all-to-all connectivity matrix $M$ (with size $N \times N$, where $N$ is the number of ROIs) we thus estimate

$$M_{ij} = (FC[\hat{\mathbf{q}}_{iM}, \hat{\mathbf{q}}_j] + FC[\hat{\mathbf{q}}_i, \hat{\mathbf{q}}_{jM}])/2 \tag{2.48}$$

where we must apply the pairwise correction and calculate connectivity independently for all pairs of $i, j = 1, \ldots, N$.

### Multivariate

Another solution for leakage correction when dealing with all-to-all connectivity assessment is to symmetrically orthogonalise the entire set of regions of interest simultaneously [Colclough et al., 2015]. The method is based of Löwdin orthogonalisation [Löwdin, 1950] and it produces a set of mutually orthognonal timecourses in one single computation. The source localised data $\mathbf{Z}$ will have dimensions $N \times R$

with $N \geq R$, where $N$ is the number of time points and $R$ the number of ROIs. We are looking for a matrix $\mathbf{P}$ of orthogonalised time courses which has minimal difference from the uncorrected data $\mathbf{Z}$, i.e. the Frobenius norm

$$\epsilon = \|\mathbf{Z} - \mathbf{P}\|^2 = trace[(\mathbf{Z} - \mathbf{P})^T(\mathbf{Z} - \mathbf{P})] \sim 0 \tag{2.49}$$

should be minimised. As $\mathbf{P}$ should contain orthogonal vectors it can be expressed as $\mathbf{P} = \mathbf{OD}$, where $\mathbf{O}$ is a matrix of orthonormal vectors and $\mathbf{D}$ is a diagonal matrix, so that $\mathbf{P}^T\mathbf{P} = \mathbf{D}^2$. According to Löwdin's orthogonalisation $\epsilon$ is minimised when $\mathbf{O} = \mathbf{UV}^T$, where $\mathbf{U}$ and $\mathbf{V}$ are derived by the singular value decomposition of $\mathbf{ZD} = \mathbf{U\Sigma V}^T$. Starting with $\mathbf{D} = \mathbf{I}_N$, the identity matrix, we can then estimate $\mathbf{P}$ by iterativly orthogonalising and adjusting the vector amplitudes. The maximum number of time courses which can be orthgonalised this way is limited to the rank of the data, which for source localised data will depend on the number of MEG sensors, as well as on the duration and bandwidth of the data.

## 2.4 Statistical methods

One of the greatest difficulties of assessing dynamic functional connectivity is to determine whether observed fluctuations over time are a result of a non-stationary process or just an artifact of variability due to noise and changes of SNR [Betzel et al., 2016; Hindriks et al., 2016; Lindquist et al., 2014]. In order to test for significant differences in functional connectivity it is therefore necessary to apply appropriate statistical tests.

Assessing significant differences in connectivity is relatively straightforward in task data where it is possible to compare multiple active and control time windows, or when studying clinical populations by comparing patient and control groups. In these cases it is possible to build a null-distribution from the control group data for each time point or window of interest. Differences between the tested condition

and control group can then be assessed with non-parametric statistical tests, e.g. Wilcox rank-sum test between the sample and control distributions, or a T-test, where the null distribution of the connectivity difference can be constructed by randomly permuting labels of the sample and control groups for $N$ times (where $N \gg$ number of samples).

Following the example of fMRI [Hutchison et al., 2013] in recent years multiple studies have been interested in assessing fast changes in functional connectivity in the resting state in the healthy population. In these situations trial averaging cannot be implemented nor it is possible to build a subject control group. Observed fluctuation in functional connectivity will then have to be compared against surrogate data presenting non-dynamic or "static" connectivity to test for spurious fluctuations due to the choice of window.

### 2.4.1 Phase scrambling

One of the most popular methods for generating surrogate data is based on multivariate phase randomisation [Prichard and Theiler, 1994] which creates a surrogate data matrix with the same dimensions of the original data, preserving its covariance calculated over all time points $N$, but smoothing out covariance changes over shorter time scales. Let us consider a univariate time series $s(t)$ (with size $N$) and its Fourier transform $\mathrm{F}[s(t)] = A(f)\exp\{i\phi(f)\}$, where $A(f)$ and $\phi(f)$ are the amplitude and phase of each Fourier component respectively. Phase randomisation of $s(t)$ is achieved by randomly rotating the phase of each Fourier component by an angle $\eta(f)$ such that

$$\tilde{s}(t) = \mathrm{F}^{-1}\Big[A(f)\exp\big\{i\big(\phi(f)+\eta(f)\big)\big\}\Big]. \tag{2.50}$$

$\tilde{s}(t)$ will have the same power spectrum of the original data and maintain its autocorrelation. In the case of multivariate data (dimensions $N \times R$) in order to maintain the correlation between different signals we simply need to add the same

random angle $\eta(f)$ to all $j = 1, \ldots, R$

$$\tilde{s}_j(t) = \mathrm{F}^{-1}\Big[A_j(f)\exp\big\{i\big(\phi_j(f) + \eta(f)\big)\big\}\Big]. \tag{2.51}$$

For each iteration of phase randomisation a new set of random angles $\eta(f)$ will be selected allowing the construction of a null distribution with the same static spectral characteristics of the original data. Multivariate phase randomisation has been shown to be effective in selecting significance threshold in MEG data, particularly to account for signal leakage [Brookes et al., 2014].

When calculating significant time variability in functional connectivity phase randomisation can be a useful technique to create a time course preserving time averaged "stationary" connectivity for phase based connectivity metrics, particularly coherence (equation 2.40) as the cross-spectral density is maintained.

When assessing changes in amplitude correlation (equation 2.39) an appropriate null distribution from surrogate data will have to preserve linear correlation of the signal envelopes i.e. stationary connectivity. The phase randomisation method described assumes the data to be Gaussian: while this is approximately true for the MEG source reconstructed signals, their envelopes are strongly non-gaussian, i.e. applying equation 2.51 to mean correct envelopes will significantly distort their covariance structure. A possible work-around, which has also been proposed for correlations of the BOLD signal in fMRI, is to apply an amplitude adjusted Fourier transform technique: an algorithm was proposed by Schreiber and Schmitz [1996] which iteratively applies the original distribution of $s(t)$ values to phase randomised data $\tilde{s}(t)$ (from equation 2.51) so as to best match the original power spectrum (i.e. maintain the covariance of the data).

# Appendix A

# Sarvas solution for a uniform sphere

We start with equation 2.16 for the magnetic potential outside of a uniform conductive sphere, induced by an electric dipole $\mathbf{q}$ (see Figure A.1):

$$U(\mathbf{r}) = -\frac{1}{4\pi}\mathbf{q} \times \mathbf{r}_q \cdot \hat{\mathbf{e}}_r \int_0^\infty \frac{\mathrm{d}t}{|\mathbf{r} + t\hat{\mathbf{e}}_r - \mathbf{r}_q|^3}. \tag{A.1}$$

Before we can solve the integral we need to expand the absolute value in the denominator. Consider the cartesian coordinate system $[\hat{\mathbf{e}}_r, \hat{\mathbf{e}}_v, \hat{\mathbf{e}}_z]$ where $\mathbf{r} = r\hat{\mathbf{e}}_r$ and $\mathbf{r}_q = (\mathbf{r}_q \cdot \hat{\mathbf{e}}_r)\hat{\mathbf{e}}_r + (\mathbf{r}_q \cdot \hat{\mathbf{e}}_v)\hat{\mathbf{e}}_v$. We can then write

$$\begin{aligned} |\mathbf{r} + t\hat{\mathbf{e}}_r - \mathbf{r}_q| &= |(r + t - \mathbf{r}_q \cdot \hat{\mathbf{e}}_r)\hat{\mathbf{e}}_r - (\mathbf{r}_q \cdot \hat{\mathbf{e}}_v)\hat{\mathbf{e}}_v| \\ &= \sqrt{(r + t - \mathbf{r}_q \cdot \hat{\mathbf{e}}_r)^2 + (\mathbf{r}_q \cdot \hat{\mathbf{e}}_v)^2}. \end{aligned} \tag{A.2}$$

Using Sarvas suggestion we can define the vector

$$\mathbf{a} = \mathbf{r} - \mathbf{r}_q = a_r\hat{\mathbf{e}}_r - a_v\hat{\mathbf{e}}_v, \tag{A.3}$$

with $a_r = \mathbf{a} \cdot \hat{\mathbf{e}}_r = (r - \mathbf{r}_q \cdot \hat{\mathbf{e}}_r)$ and $a_v = -\mathbf{a} \cdot \hat{\mathbf{e}}_v = (\mathbf{r}_q \cdot \hat{\mathbf{e}}_v)$.

Using equation A.2 the integral in A.1 therefore becomes:

$$\int_0^\infty [(a_r + t)^2 + a_v^2]^{-3/2}\mathrm{d}t \tag{A.4}$$

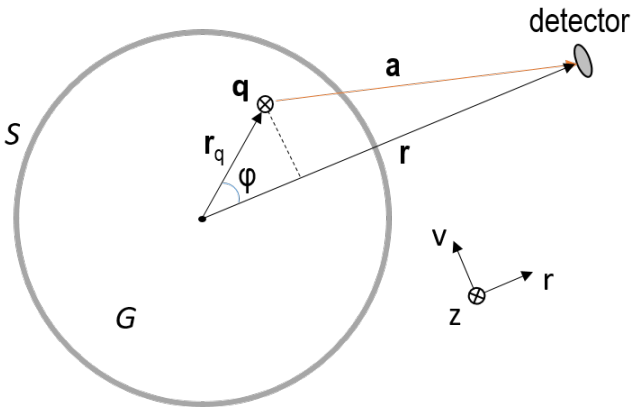



Figure A.1: Uniform conductive sphere with dipole source **q** and its location vector $\mathbf{r}_q$ lying on the **rv**-plane.

which can be solved with a trigonometric substitution:

$$\begin{aligned} \tan(u) &= \frac{a_r + t}{a_v} \\ t &= a_v \tan(u) - a_r, \end{aligned} \tag{A.5}$$

giving the differential

$$\frac{\mathrm{d}t}{\mathrm{d}u} = \frac{a_v}{\cos^2(u)} = a_v \sec^2(u). \tag{A.6}$$

The integral in A.4 can then be solved as:

$$\begin{aligned} &\int_{t=0}^{\infty} [a_v^2 \tan^2(u) + a_v^2]^{-3/2} a_v \sec^2(u) \mathrm{d}u = \\ &\frac{1}{a_v^2} \int_{t=0}^{\infty} [\sec^2(u)]^{-3/2} \sec^2(u) \mathrm{d}u = \\ &\frac{1}{a_v^2} \int_{t=0}^{\infty} \sec^{-1}(u) \mathrm{d}u = \\ &\frac{1}{a_v^2} \int_{t=0}^{\infty} \cos(u) \mathrm{d}u = \\ &\frac{1}{a_v^2} \sin(u) \Big|_{t=0}^{\infty} \end{aligned} \tag{A.7}$$

where we used the trigonometric identity $\tan^2(u) + 1 = \sec^2(u)$.

We now can use the transformation in A.5 to substitute back for $t$:

$$\sin(u) = \sin\left(\operatorname{atan}\left(\frac{a_r + t}{a_v}\right)\right) = \frac{a_r + t}{[(a_r + t)^2 + a_v^2]^{1/2}} \tag{A.8}$$

and evaluate the integral limits in A.7:

$$\frac{1}{a_v^2}\left.\frac{a_r+t}{[(a_r+t)^2+a_v^2]^{1/2}}\right|_{t=0}^{\infty}=\frac{1}{a_v^2}\left[1-\frac{a_r}{(a_r^2+a_v^2)^{1/2}}\right] \tag{A.9}$$

Now recalling that $a^2=a_r^2+a_v^2$ (from A.3) we can write the integral solution as

$$\frac{a-a_r}{a\cdot a_v^2}=\frac{a-a_r}{a(a^2-a_r^2)}=\frac{a-a_r}{a(a-a_r)(a+a_r)}=\frac{1}{a(a+a_r)} \tag{A.10}$$

and the magnetic potential $U(\mathbf{r})$ in equation A.1 is now

$$\begin{aligned}U(\mathbf{r})&=-\frac{1}{4\pi}\mathbf{q}\times\mathbf{r}_q\cdot\hat{\mathbf{e}}_r\frac{1}{a(a+a_r)}\\&=-\frac{1}{4\pi}\mathbf{q}\times\mathbf{r}_q\cdot\hat{\mathbf{e}}_r r\frac{1}{ra(a+r-\mathbf{r}_q\cdot\hat{\mathbf{e}}_r)}\\&=-\frac{1}{4\pi}\mathbf{q}\times\mathbf{r}_q\cdot\mathbf{r}\frac{1}{a(ra+r^2-\mathbf{r}_q\cdot\mathbf{r})}\end{aligned} \tag{A.11}$$

which is the solution by Sarvas [1987] in equation 2.17.

# Chapter 3

# Optimizing beamforming for static functional connectivity

In this first experimental chapter we test how practical aspects of experimental design affect the intra-subject repeatability of the MEG functional connectome; specifically we assess the effect of coregistration method and data recording duration. We show that the use of a foam head-cast, which is known to improve co-registration accuracy, increased significantly the between session repeatability of both beamformer reconstruction and functional connectivity estimation. We also show that recording duration is a critical parameter, with large improvements in repeatability apparent when using ten minute, compared to five minute recordings. Further analyses suggest that the origin of this latter effect is not underpinned by technical aspects of source reconstruction, but rather by a genuine effect of brain state; short recordings are simply inefficient at capturing the canonical MEG connectome in a single subject. The work described in this chapter provides important insights on MEG experimental design for functional connectivity studies. This work was published in NeuroImage in 2017 [Liuzzi et al., 2017].

## 3.1 Introduction

The study of functional connectivity using magnetoencephalography (MEG) is an expanding area of neuroimaging, and adds an extra dimension to the more common assessments made using fMRI. This increase in popularity is driven by growing importance of characterising electrophysiological connectivity, with numerous demonstrations that connections are perturbed in pathologies [Friston, 1998; Guggisberg et al., 2008; Kessler et al., 2014; Schnitzler and Gross, 2005; Stufflebeam et al., 2011; van Dellen et al., 2012]. However, demonstrations have typically been made on large subject groups, with little attention paid to the ac-

curacy of measurements within individual subjects. Such accuracy is critical if MEG connectivity is to provide diagnostic and clinically relevant information.

To date, most studies that have examined the robustness of MEG connectivity estimation suggest relatively poor reproducibility. For example, Wens et al. [2014] showed that whilst group level connectivity within several well-known networks is stable, there is significant variability at the individual subject level. Colclough et al. [2016] tested the between session repeatability of a large number of functional connectivity measurements, showing that although group level inference is reliable, network metrics vary across individuals. The authors also showed that even separate measures in a single subject lack reproducibility. Tewarie et al. [2016] used MEG to predict the canonical RSNs observed in fMRI; whilst predictions were robust at the group level, they fared less well within individuals and no significant inter-individual differences in connectivity were predicted. Similarly, O'Neill et al. [2017] showed that dynamic measures of functional connectivity are also variable across subjects. Although the reason for this poor reliability is not well understood, it likely results from a combination of genuine differences [Finn et al., 2015] (i.e. even within a single subject, differences in brain state between two experimental recordings could generate marked differences in network connectivity) and instrumental imprecision. The reasons of the latter are MEG's low signal to noise ratio (SNR) due to environmental noise (discussed in chapter 1) and the ill-posed inverse problem in source localisation which reduces spatial resolution (seen in chapter 2).

In this first experimental chapter, using simulations and experiments, we probe how test-retest repeatability of functional connectivity in MEG can be optimised by changing practical aspects of experimental design. We concentrate on two parameters; recording duration and co-registration method. It is clear that longer recordings will maximise SNR, and previous work [Brookes et al., 2008, 2010] shows that source reconstruction accuracy and spatial resolution are improved

as recording duration (or bandwidth) is increased. Here, using simulated and experimental MEG data, we investigate the effect that changing recording duration has on network connectivity. Investigating the effect of co-registration error in real MEG data is challenging since such errors are inherent to all experimental measures and no ground truth is known. Here, we address this issue by adopting a recently developed approach, employing foam head-casts (constructed using 3D printing) [Troebinger et al., 2014]. In what follows, we will show that recording duration and co-registration have a marked effect on the repeatability of source localisation, and functional connectivity. Our results will provide advice for the design of future scanning protocols, particularly in studies of individual subjects.

## 3.2 Co-registration

The accuracy of source localisation is dependent not only on data quality, but also on precise forward models (models of magnetic fields that would be observed at the sensors given a known current distribution, see section 2.1). Forward models, in turn, require accurate knowledge of the location and orientation of MEG sensors relative to brain anatomy. Importantly (and perhaps counterintuitively) as SNR is increased, the requirement for high spatial precision also increases. Unfortunately at present, co-registration (matching the MEG coordinates, i.e. head position inside the MEG helmet, to an individual anatomical MRI) usually relies on digitisation and surface matching procedures which can cause errors of several millimetres that propagate into source reconstructions. If the potential of MEG to characterise network connectivity in individual subjects is to be realised, then these sources of error must first be minimised.

### 3.2.1 Standard

The position of the head relative to the MEG sensors can be continuously recorded through fiducial coils (see section 1.5.4). Matching to an MRI coordinate space

can then be achieved by accurately positioning the fiducial coils to identifiable anatomical markers (naison, pre-auricolar points) or more commonly by digitising the participant's head surface along with the fiducial positions. At the Nottingham MEG laboratory the digitisation is achieved using a Polhemus FASTRAK 3D digitiser system: a stylus is used to "draw" on the subject's head creating a set of triangulated points thanks to a transmitter, positioned behind the subject, and a receiver, usually placed on top of the subject's head. Inaccuracies in the digitisation can occur due to interference with the trasmitter/receiver (e.g. electronics or moving metallic objects such as phones or watches) or often by movement of the reference sensor, which is usually kept in place underneath a tight cap or taped to the subject's head. The localisation of the fiducial markers is compared at the beginning and end of the head digitisation procedure in order to check that coordinate mismatch is below 5 mm. When a set of $400 - 500$ coordinate points is collected they are then matched to the MRI head surface, extracted from an isotropic MPRAGE sequence, through an iterative closest point algorithm.

### 3.2.2 Headcast

A recently developed approach for improved co-registration (relative to the standard approach above) employs foam head-casts (constructed using 3D printing) [Troebinger et al., 2014] with fixed slots for the fiducial coils (see Figure 3.1C). The internal surface of these head-casts fits the subject's scalp, whilst the external surface fits the inside of the MEG scanner helmet. In this way we are able to lock the head in place, minimising motion and co-registration error.

Here, for the head-cast co-registration, an anatomical MR image of the subjects' head was acquired using a 3DTFE (Turbo Field gradient Echo) sequence running on a Philips Ingenia 3T system at a resolution of $1\text{mm}^3$. Sequence parameters (TR = 4.5ms; TE = 1.97ms; FOV (ap,fh,rl) = $256 \times 256 \times 183$; Orientation: sagittal; BW = 775 Hz) were optimised such that the scalp and face

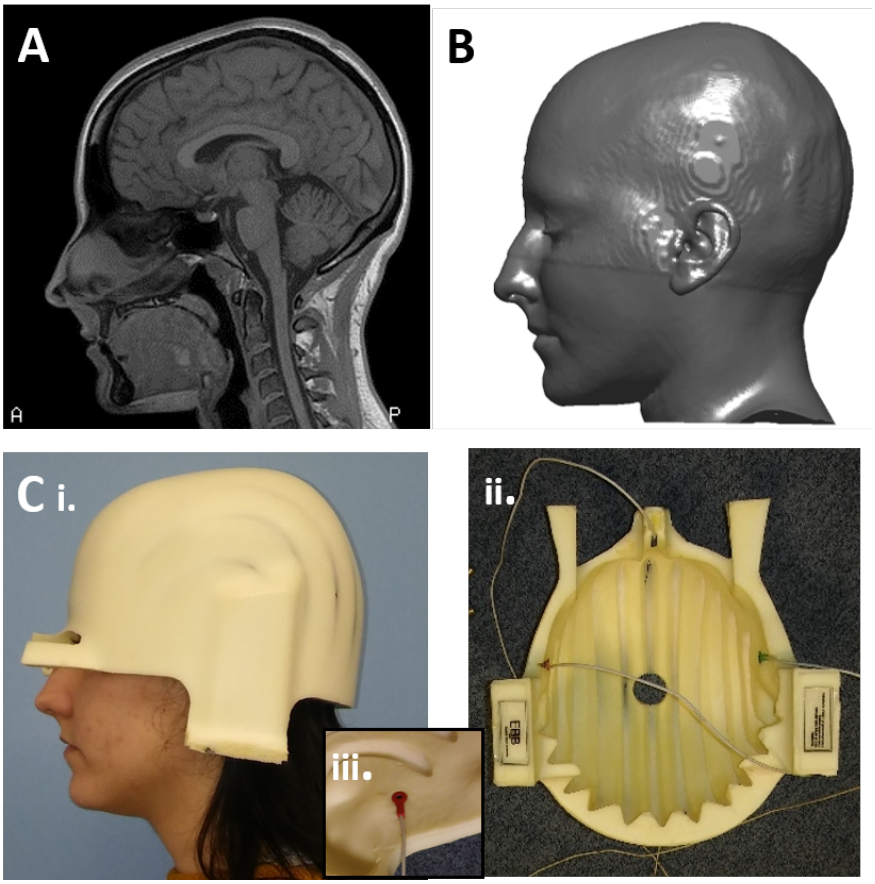



Figure 3.1: Subject specific foam head-cast. A) Sagittal slice showing the anatomical MRI scan. B) Scalp surface extracted from the MRI scan. C) i) Subject wearing the foam head-cast. ii) Foam head-cast. iii) Head localisation coil in situ.

surfaces were reconstructed accurately (i.e. a high bandwidth/voxel was used in order to minimise spatial distortion due to susceptibility effects around the air tissue interfaces). A single subject example is shown in Figure 3.1A. Following acquisition, we used this image to generate a foam head-cast, the internal surface of which was fitted to the subjects' scalp, whilst the external surface was fitted to the MEG scanner helmet. The procedure is described fully in Meyer et al. [2017]. Briefly, a 3D mesh representing the outer surface of the head and face was extracted from the anatomical MRI (see Figure 3.1B). This virtual 3D model of the subjects' head was placed inside a virtual realisation of the MEG helmet. The head-model was augmented with spacing elements, to optimise the distance between the scalp and sensors. In addition, a 3D representation of three head localisation coils, used for localising head position in the scanner was added, with coils placed at the nasion and left and right preauricular points. This 3D representation of the head surface, spacers, and localisation coils was 3D printed and placed inside a manufacturer-provided replica of the MEG-helmet. Finally, liquid resin was poured into the negative space between the surfaces. This expands and sets, resulting flexible foam subject-specific head-casts which can also house the localising coils (see Figure 3.1C).

## 3.3 Simulations

In order to examine the effect of co-registration error and recording duration on connectivity estimation, we first undertook a set of simulations. All simulations were based upon the geometry of a CTF 275 channel axial gradiometer system (5 cm baseline) operating in third order gradiometer configuration. Brain anatomy, head shape, and system geometry were based upon a real experimental recording session. In everything that follows, the simulated sampling frequency was 600 Hz; all simulated sources were assumed to be dipolar; the forward field was computed using a multiple local sphere head model and the formula derived by Sarvas [1987]

as described in section 2.1. The locations of all simulated sources were set according to the centre of mass of 78 anatomically defined cortical regions, extracted from the automated anatomical labelling (AAL) atlas.

Two dipoles, henceforth known as the seed and test dipole, were simulated in homologous regions of somatosensory cortex, with locations and orientations represented by $\boldsymbol{\theta}_{seed}$ and $\boldsymbol{\theta}_{test}$ respectively. The vector $\boldsymbol{\theta}$ represents both location (set according to the AAL regions) and orientation, which was confined to the tangential plane and set at a random angle with respect to the azimuthal direction (see section 2.2.1). The dipole timecourses, denoted $q_{seed}(t)$ and $q_{test}(t)$, were simulated in order to mimic genuine functional connectivity between regions. Mathematically,

$$\begin{aligned} q_{seed}(t) &= b(t) + e_1(t), \\ q_{test}(t) &= b(t+\tau) + e_2(t). \end{aligned} \tag{3.1}$$

Here, $b(t)$ was generated by frequency filtering Gaussian noise into the beta band ($13-30$ Hz). This was added to $q_{seed}(t)$ and a time/phase shifted version was added to $q_{test}(t)$ in order to simulate functional connectivity between locations. In addition, $e_1(t)$ and $e_2(t)$, which represent two orthogonal beta band filtered Gaussian noise timecourses, with amplitude equal to 30% of $b(t)$, were added. In this way, the simulated timecourses represent regional brain signals which exhibit partial connectivity. Note that $\tau = 10$ ms. To make the simulation more realistic, in addition to the seed and test dipoles, we simulated a further 76 dipoles located at the centres of mass of the remaining AAL regions. These "dipoles of no interest" had amplitude equal to 5% of the seed and test signals. The final dataset was simulated as

$$\mathbf{B}(t) = a_{seed}\mathbf{l}(\boldsymbol{\theta}_{seed})q_{seed}(t) + a_{test}\mathbf{l}(\boldsymbol{\theta}_{test})q_{test}(t) + \left[\sum_{i=1}^{76} a_i\mathbf{l}(\boldsymbol{\theta}_i)q_i(t)\right] + \mathbf{E}(t). \tag{3.2}$$

Here, $a_{seed}$ and $a_{test}$ represent the amplitudes of the seed and test dipoles respec-

tively. $\mathbf{l}(\boldsymbol{\theta})$ represents the forward field for location/orientation $\boldsymbol{\theta}$. The summation represents the contribution of the dipoles of no interest and $\mathbf{E}(t)$ represents sensor level interference. Notice that $\mathbf{B}(t)$, $\mathbf{E}(t)$ and $\mathbf{l}(\boldsymbol{\theta})$ are vectors of dimension $N_{chans} \times 1$, where $N_{chans}$ represents the number of MEG sensors. $\mathbf{E}(t)$ was generated using real MEG data from an empty room noise recording, acquired using a 275 channel CTF system in third order gradiometer configuration, and filtered into the beta band. The simulated SNR (defined as the ratio of the norms of the field from all dipoles and the interference field) was set to 1.

Following simulation of MEG data, reconstruction in source space was achieved via beamforming to generate estimates, $\hat{q}_{seed}(t)$ and $\hat{q}_{test}(t)$. Source orientation was estimated by calculating the weights of 180 possible orientations constrained to the tangential plane as describe in section 2.2.2 (equation 2.34).

Here, we chose 5 separate connectivity metrics: Amplitude Envelope Correlation (AEC), Coherence (Coh), Imaginary Coherence (ICoh), Phase Locking Value (PLV) and Phase Lag Index (PLI) (see section 2.3 for a detailed description of the connectivity metrics): AEC assesses temporal correlation between the amplitude envelopes of band limited signals; Coherence and Imaginary Coherence are a measure of cross spectral density of two oscillatory signals; PLV and PLI estimate a fixed phase relationships between neuronal signals, which are assumed to reflect functional coupling, based on the concept of communication by coherence [Fries, 2005] (introduced in section 1.2). PLV and PLI were estimated as the average over 50% overlapping 10 s long windows covering the whole simulated dataset in line with previous work [Colclough et al., 2016; Fraschini et al., 2016]. As AEC, Coh and PLV include zero-phase lag relationships prior to their calculation we corrected for signal leakage. For our simulations, we used a simple pairwise orthogonalisation between $\hat{q}_{seed}$ and $\hat{q}_{test}$. For the experimental work described later, we were interested in all-to-all connectivity between 78 cortical regions and therefore we used a multivariate orthogonalisation scheme [Colclough et al., 2015].

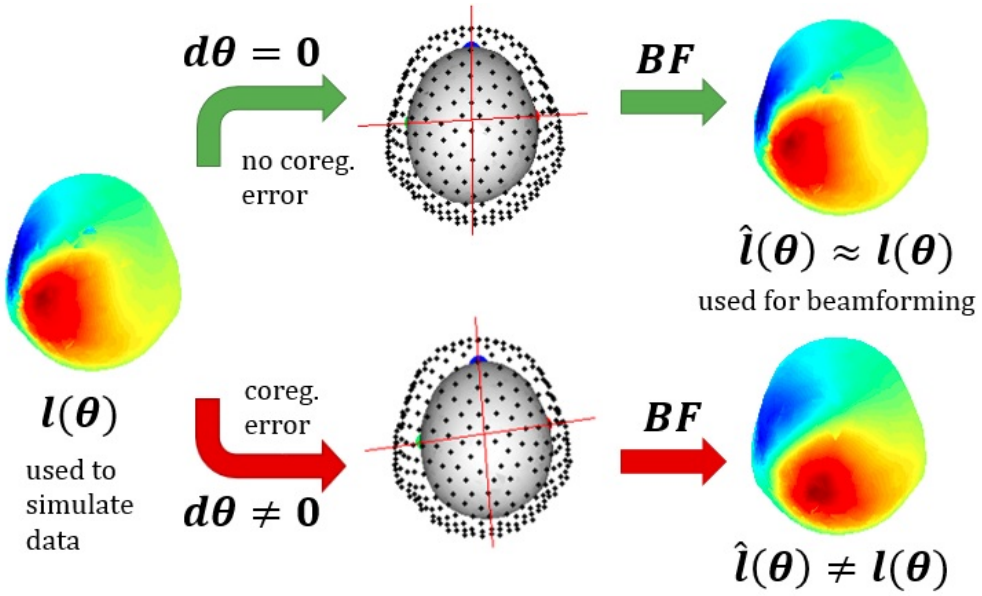



Figure 3.2: Schematic showing the basic principle of the co-registration error simulation. Note that co-registration error manifests as a difference between the true lead field $\mathbf{l}(\boldsymbol{\theta})$ and that used for reconstruction $\hat{\mathbf{l}}(\boldsymbol{\theta})$.

### 3.3.1 Co-registration errors

Co-registration errors and subject movement during an MEG recording represent a stochastic error on the assumed locations of the MEG sensors with respect to the head. This error manifests in source reconstruction as a difference between the "real" lead field, $\mathbf{l}(\boldsymbol{\theta})$, and the lead field used for beamformer reconstruction, $\hat{\mathbf{l}}(\boldsymbol{\theta})$. Here, we simulated co-registration error by adding a random translational and rotational error to the MEG sensor locations and orientations; this was achieved by a simple coordinate transform. The absolute value of translational and rotational error was fixed, while the proportions along or about each axis were randomised with values taken from a Gaussian distribution. In other words, for translational error, an absolute value was fixed at, say 1mm, but the direction of the error was random. Similarly, for rotational error, a value was fixed, say 1° and the axes about which this rotation occurred (the contribution of pitch, yaw and roll) was random (see Figure 3.2). Our simulation added translational and rotational error simultaneously and proportionally (i.e. 1 mm/1°; 2 mm/2° and so on up to 15 mm/15°). For each absolute error value, the simulation was repeated 100

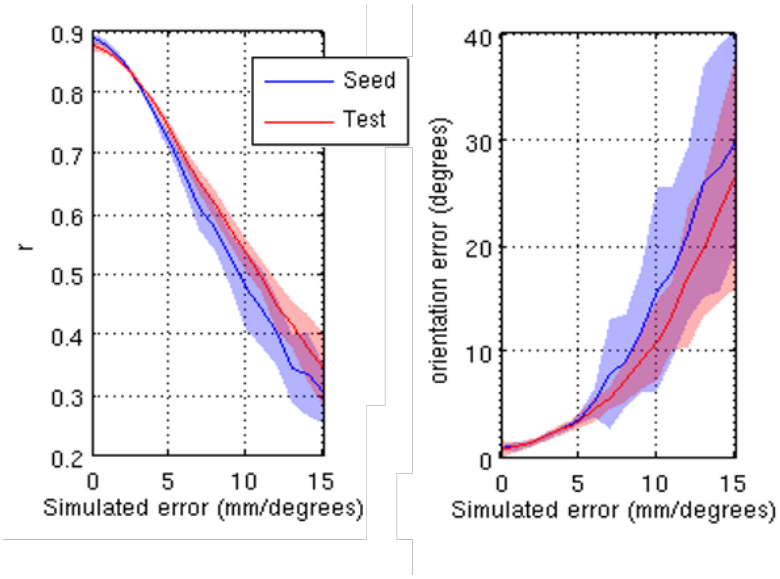



Figure 3.3: Beamformer reconstruction accuracy (measured as correlation between $q(t)$ and $\hat{q}(t)$, left hand panel) and error in dipole orientation (right hand panel) plotted against co-registration error. Shaded regions show standard deviation across different simulated MEG datasets.

times (different error directions/rotations each time) and results averaged. This whole process was repeated 10 times with different realisations of simulated dipole timecourses. Results were averaged over iterations.

Figure 3.3 shows beamformer reconstruction accuracy plotted as a function of co-registration error. The left hand panel shows correlation between the simulated and reconstructed seed and test timecourses (i.e. temporal correlation between $q_{seed}(t)$ and $\hat{q}_{seed}(t)$ is given in blue and equivalently correlation between $q_{test}(t)$ and $\hat{q}_{test}(t)$ is given in red). The right hand plot shows the angular error (in degrees) between the simulated and reconstructed dipole orientation for the seed (blue) and test (red) sources. Recall that simulated co-registration error (x-axes) represents both a translation and rotation (i.e. a value of 10 means 10 mm translation error accompanied by a 10° rotational error): translation and rotational errors were combined as they showed comparable effects on the reconstruction accuracy. The error bars show standard deviation across 10 independent runs of the simulation (different realisations of simulated MEG data). As would be expected, a drop in reconstruction accuracy is observed with increasing co-registration error, and this

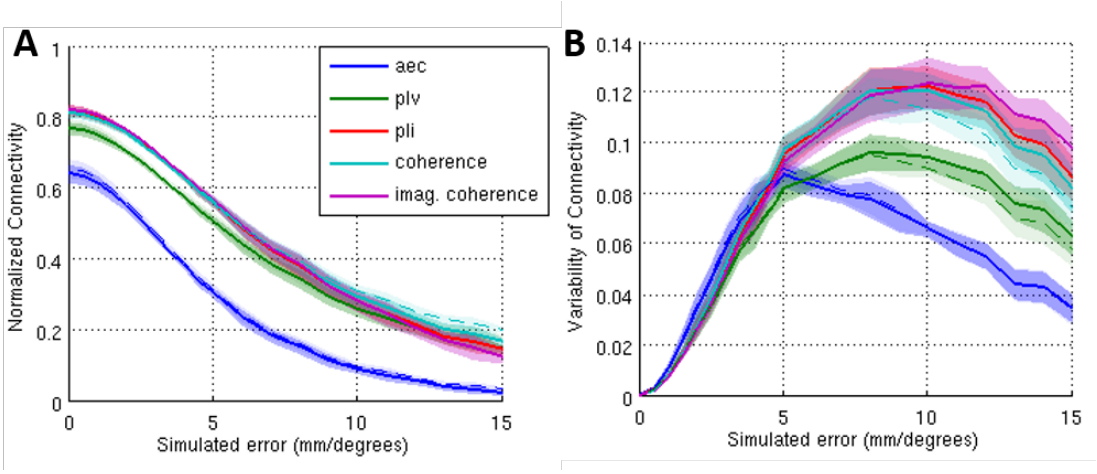



Figure 3.4: The effect on co-registration error on functional connectivity. A) Functional connectivity between the simulated seed and test sources versus co-registration error. B) The variability of functional connectivity across different realisations of the co-registration error. Shaded regions show standard deviation across different simulated MEG datasets. Dashed lines refer to connectivity calculated without correcting for signal leakage.

is accompanied by an increase in the error on the reconstructed dipolar orientation. Interestingly large beamformer reconstruction errors are observed even for modest co-registration errors (e.g. an error of 10 mm/degrees reduces correlation between simulated and reconstructed timecourses to $\sim 0.5$).

Figure 3.4 shows the effect of co-registration error on functional connectivity estimation for all 5 connectivity methods. In both plots, AEC, PLV, PLI, Coh and ICoh are shown in blue, green, red, cyan and magenta respectively. The shaded regions show the standard deviation across 10 realisations of simulated MEG data. In Figure 3.4A, connectivity is shown, normalised to its true value (i.e. a value of 1 would indicate perfect reconstruction of the connection strength). Figure 3.4B shows variability in functional connectivity; this is computed as the standard deviation of the functional connectivity estimate between the seed and test sources, made using a single MEG dataset, with 100 different co-registration errors. In other words, this variability simulates a case where the same data could be acquired but with different co-registration errors. As for reconstruction accuracy, translation and rotational errors were combined as they showed comparable

effects on the functional connectivity estimate. Note again the significant effect of co-registration error; even for low (5 mm/degree) errors, the magnitude of the connectivity estimate can fall sharply (e.g. to $\sim$ 50% of the value with no co-registration error) and variability can be as large as 20% of the connectivity value for the phase based metrics and up to 40% of AEC. Note that variability falls with very large co-registration error since there is no genuine connectivity left.

### 3.3.2 Recording duration

Differences in recording duration were achieved by simulating different amounts of MEG data. Data duration was varied between 20 s and 60 s in steps of 10 s, and between 60 s and 560 s in steps of 30 s. For each duration, a MEG dataset was simulated 10 times and results averaged over iterations.

Figure 3.5 shows the effect of recording duration on beamformer reconstruction accuracy and functional connectivity estimation. Figure 3.5A shows beamformer reconstruction accuracy (upper panel) and reconstructed orientation error (bottom panel) both as a function of recording duration. The shaded area shows standard deviation across simulation iterations, the blue curves show the seed source and the red curves show the test source. Note that, in good agreement with previous work [Brookes et al., 2008], the beamformer reconstruction accuracy falls sharply when recording duration is less than approximately 60 s (see Figure 3.5A). This is the result of a poorly estimated covariance matrix used for beamformer estimation.

Figure 3.5B (upper panel) shows connectivity estimation versus recording duration. In agreement with Figure 3.5A, connectivity estimation improves with recording duration as would be expected. However estimates tend to plateau after approximately 2 minutes of data are recorded. Note that this effect is purely a result of errors in connectivity estimation, however in real data, genuine differences in brain state (connectivity dynamics [Hutchison et al., 2013]) can also cause variability in the connectivity estimate. This will be addressed further in

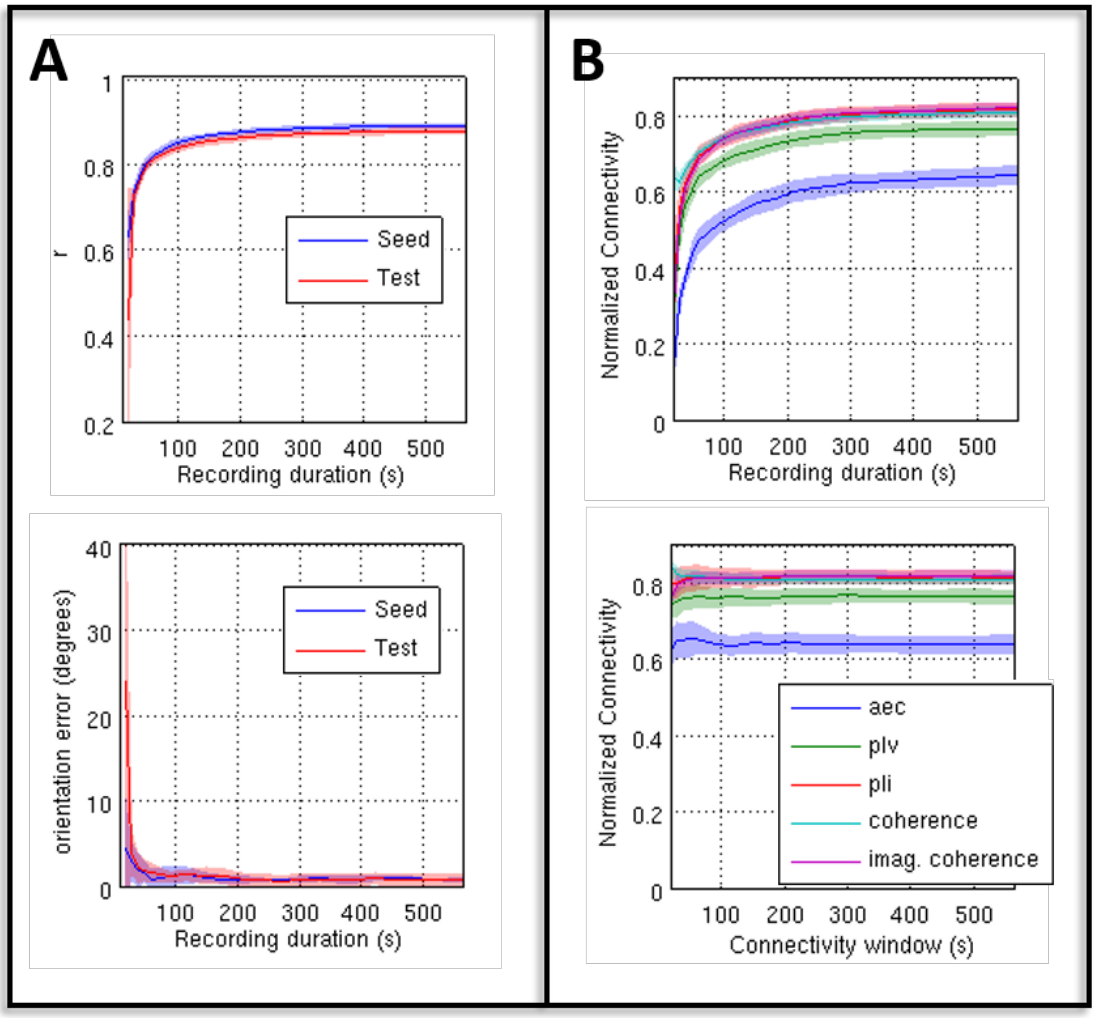



Figure 3.5: The effect of recording duration. A) Beamformer reconstruction accuracy (upper panel) and error in reconstructed dipole orientation (lower panel) as a function of recording duration. B) Measured connectivity between the simulated seed and test timecourses (normalised to the true value). The upper plot shows the case where beamforming and connectivity are calculated in a limited window (i.e. x-axis represents total recording duration). The lower plot shows a case where the beamformer parameters are calculated using 560 s of data but the connectivity is calculated in a limited window (i.e. x-axis represents only the connectivity window size).

the real MEG data analysis. It is noteworthy that reducing recording duration will effect connectivity estimation in two ways. First, beamformer reconstruction accuracy will decline (as shown in Figure 3.5A). Second, following reconstruction of timecourses $\hat{q}_{seed}(t)$ and $\hat{q}_{test}(t)$, estimation of connectivity between them will be made using fewer data points, reducing its reliability. Here, to separate these effects, we undertook measurements in which beamforming was applied using 560 s of data, and connectivity estimated in a smaller window. The results are shown in Figure 3.5B lower panel. It is clear that the effects observed in Figure 3.5A are dominated by the beamformer. I.e. If beamformer weights are calculated over large windows, the effect of limited data duration on connectivity (down to 20 s) are practically negligible.

## 3.4 MEG data

Three subjects (all aged 26, 2 male) took part in the study, which was approved by the University of Nottingham Medical School Research Ethics Committee. All subjects underwent a structural MRI scan, followed by 10 resting state MEG recordings.

All MEG data were acquired using a 275-channel whole head CTF system in third order synthetic gradiometer configuration. The subjects were scanned in five separate sessions, on consecutive days. Sessions were conducted at the same time each day for the same subject. Each session comprised two recordings, one in which the subject wore the head-cast and one "standard" recording (with no head-cast). For both scans subjects were asked to sit in the MEG system, keep as still as possible and "think of nothing" while focusing on a centrally presented fixation cross (projected onto a back projection screen $\sim$ 40 cm in front of the subject). All acquisitions were 10 minutes in duration. The position of the subjects head was measured continuously and a maximum movement of $\sim$ 5 mm was accepted. Co-registration between the MEG sensor geometry was achieved in two ways:

- For the head-cast acquisition, the coils were held rigidly in the head-cast and their location relative to the brain anatomy was known from the virtual 3D model of the subjects head used in the head-cast design. Co-registration was therefore enabled by translating these known coordinates to the anatomical MRI.

- For the standard acquisition, the coils were taped firmly to the subject's skin at the three fiducial locations. Prior to MEG acquisition, the coil locations were measured relative to the scalp surface using a 3D digitiser (Polhemus; Colchester, VT). Co-registration of MEG data to anatomical MRI was achieved by matching the digitised head surface to the equivalent surface extracted from the MRI.

It is noteworthy that the standard acquisition represents a procedure for co-registration used routinely in most MEG laboratories, but is nevertheless prone to inaccuracy. The head-cast has been shown as a useful methodology to minimise co-registration error [Troebinger et al., 2014; Meyer et al., 2017].

All MEG data were inspected visually. Any segments containing artifacts such as SQUID resets or excessive muscle activity were removed (eye-blinks were not removed). Head movement was acceptable for all subjects and all sessions; without the head-cast, subjects moved 2.5±1.7 mm (mean ± standard deviation over sessions and subjects). With the head-cast, subjects moved 0.4±0.2 mm. A maximum of 40 s of data per recording had to be removed for poor quality, making the maximum available recording duration 560 s. Data were then frequency filtered into the $\beta$ range ($13 - 30$ Hz) using a least-square linear phase finite impulse response filter, implemented in Matlab. For the functional connectivity analysis, data covariance was estimated in the $1 - 150$ Hz range and frequency filtering in the beta band was run after the virtual electrode reconstruction. All results presented here are based upon the beta band. The reason for this choice was a weight of literature that points towards connections in many long range networks

being mediated by neural oscillations in this range [Hall et al., 2014a; Hipp et al., 2012; Hunt et al., 2016].

### 3.4.1 Source orientation consistency

An inherent limitation when using real MEG data is that, since no underlying ground truth is known about the location or strength of an electrical source, it is challenging to track the inaccuracies inherent to reconstruction. However, the MEG signal is thought to be generated by synchronised electrical activity in pyramidal neurons, which are oriented approximately perpendicular to the cortical surface (as seen in chapter 1). This means that across two independent MEG sessions, whilst the strength of the activity of such neurons may change, their orientation, being defined only by anatomy, will not. For this reason, at any one brain location, reconstructed source orientation for two independent MEG sessions should be equivalent (a similar argument has been employed in work tracking the efficacy of source reconstruction algorithms [Stevenson et al., 2014]). Using this idea, we aimed to test the effect of co-registration method (head-cast and standard) and recording duration, on beamformer reconstruction reliability across sessions.

A scalar beamformer (equivalent to that used above in our simulations section) was used to reconstruct sources at the vertices of a regular 8mm grid spanning the whole of source space (i.e. the whole brain). For beamformer reconstruction, covariance matrices were generated independently for each acquisition. No regularisation was employed in order to maximise spatial specificity. Modelled source dipoles were limited to the tangential plane and source orientation was measured as the direction with highest signal to noise ratio (equation 2.34). For every voxel, and each recording, this optimum orientation was stored and beamformer repeatability was inferred as the difference in orientation (measured as an angle) between pairs of sessions within each subject (i.e. for a single voxel we compared orientation on - day 1 to day 2; - day 1 to day 3 and so on. 5 separate sessions gave 10

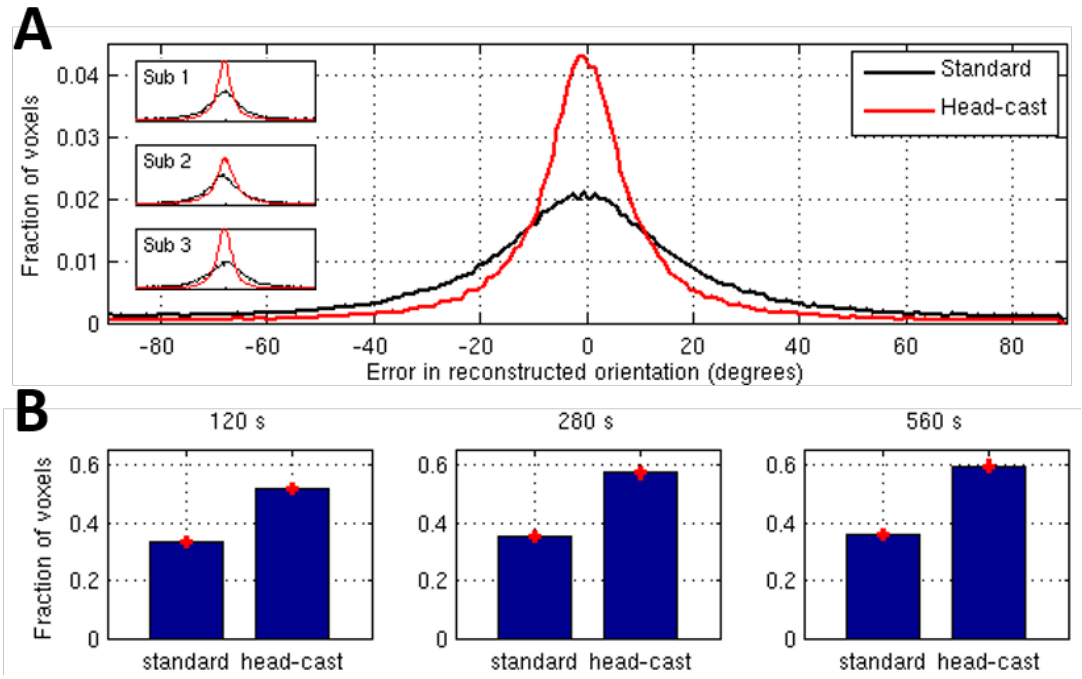



Figure 3.6: Between session consistencies of beamformer reconstructed source orientation. A) Histogram showing orientation difference (measured as an angle in degrees) in beamformer source reconstruction between sessions. The red curve shows the case with head-cast co-registration and the black curve shows the case with standard co-registration. The main plot shows all subjects combined; inset plots shows the three subjects separately on the same scale. B) Bar charts showing the fraction of voxels (collapsed across subjects) with an angle error of less than 10 degrees. The three plots show the case for three different recording durations, 120 s, 280 s and 560 s.

comparisons). This analysis was undertaken separately for each individual, and results were averaged across people. The analysis was undertaken independently for three recording durations (560 s, 280 s, 120 s), and for the head-cast and standard co-registration procedures.

Figure 3.6 shows the effect of recording duration and co-registration method on the repeatability of the beamformer reconstructed orientation. The upper plot shows a histogram of orientation differences between MEG sessions. I.e. the x-axis represents the angular difference in orientation of a source at a single voxel in a single subject scanned in two separate sessions. The y-axis shows the number of voxels. The centre plot collapses data over all pairs of recording sessions and subjects. The smaller plots (inset) show the case for each subject individually.

The red line shows the case for head-cast co-registration; the black line shows the case for standard co-registration. As expected, in both cases, beamformer projected source orientations are consistent between sessions (histogram centred about zero). However note that the spread of angles is less when co-registration is achieved using a head-cast. This observation is further depicted by the bar charts in Figure 3.6B, which show the fraction of voxels with an angular discrepancy between sessions of less than 10 degrees. The three plots show the case for 120 s recordings, 280 s recordings and 560 s recordings. In order to test if there is a significant increase in voxels count when using the head-cast we ran a permutation test. An empirical null distribution of the voxel count difference was constructed by pooling together the voxel count (of angular error below 10 degrees) from all subjects and all between session comparisons (n = 60, 2 co-registration methods $\times$ 3 subjects $\times$ 10 between session comparisons) and iteratively (10,000 iterations) randomising the co-registration method label. We then tested the probability that the observed difference fell outside the 95% confidence interval of the null distribution. The head-cast shows a significant improvement (p-value $< 10^{-10}$) of the between session angular error compared to standard co-registration for all three tested recording durations. These data confirm previous reports [Troebinger et al., 2014; Meyer et al., 2017] in demonstrating the utility of head-cast technology to improve the within subject consistence of MEG reconstructions. Also noteworthy is the effect of recording duration, with a lower angle error with longer recordings; this is particularly noticeable for the data recorded with a head-cast.

### 3.4.2 Functional connectivity consistency

Functional connectivity was assessed between 78 cortical regions defined according to the AAL parcellation. Beamformer reconstructed signals were computed at the centre of mass of each of these regions. Reconstruction was based upon either the first 560 s, 280 s or 120 s of MEG data from each recording. The beamformer was applied as described above. The 78 regional timecourses were orthogonalised

using the multivariate method and functional connectivity between all possible region pairs was then estimated. For each subject and each recording, this gave a single $78 \times 78$ connectivity matrix for each metric, showing beta band coupling between all regions.

We aimed to test the between session reproducibility of intra-subject measures of functional connectivity. To this end, all of the derived connectivity matrices were first reshaped into one dimensional vectors, which we term connectivity vectors (note that we removed the redundancy inherent in all connectivity matrices due to their symmetry, as well as the leading diagonal which represents only connectivity of a region with itself). Following this, we measured Pearson correlation between connectivity vectors derived using MEG data acquired in different sessions in the same subject. This was repeated for all session pairs. Data acquired with and without the head-cast were treated separately and their comparison was used to assess the effect of co-registration method. Correlation values were also derived independently using either 560 s, 280 s or 120 s of MEG data to assess the effect of recording duration.

In order to assess whether the effects of head-cast or data recording duration were significant, a permutation test was employed. First, the values of correlation between connectivity vectors for two conditions (e.g. head-cast or standard), for all possible session pairs within a subject, and for all subjects, were averaged and the difference calculated. This difference was then compared to an empirical null distribution. To generate the null, we reasoned that if no effect was measurable then the condition labels apportioned to different recordings would have no meaning. These were therefore switched randomly and the difference between 'sham' conditions calculated. Comparison of the true value with the empirical null then gave rise to a p-value. Significance was assigned for p-values less than 0.05.

Figure 3.7A shows a visual comparison of the connectivity matrices for all three

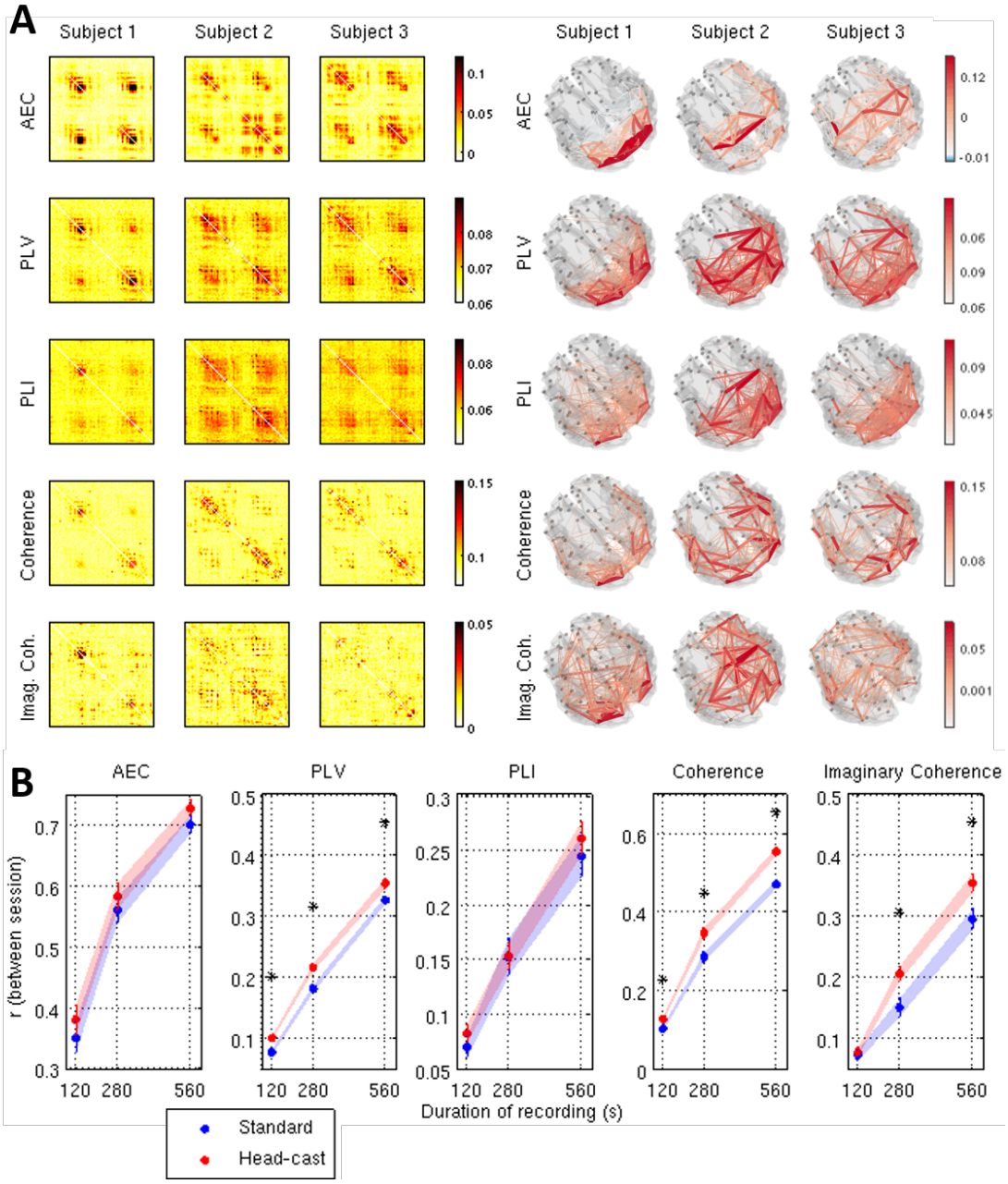



Figure 3.7: Between session consistency of functional connectivity measurement. A) Connectivity matrices for all three subjects and each of the five connectivity metrics. 3D brain images show the top 10 percent of connections. B) Between session correlation of measured connectivity vectors as a function of duration of a recording. The 5 plots show the 5 separate metrics (AEC, Coh, ICoh, PLI and PLV). The red lines show the case with the head-cast co-registration and the blue lines show the case with standard co-registration. A star (*) indicates a significant effect of co-registration method.

subjects and each of the five connectivity metrics. Note that these matrices have been averaged across all sessions (head-cast and standard) within each subject using all 560 s of data. The 3D brains show a graphical representation of the top 10% of connections. Figure 3.7B shows the between session correlation of measured connectivity vectors for different recording durations. The 5 plots show the 5 separate connectivity metrics (AEC, Coh, ICoh, PLI and PLV). The red lines show the case with head-cast co-registration and the blue lines show the case with standard co-registration. A star (*) indicates a significant effect of co-registration, p-values less than 0.05, assessed with a permutation test of the two condition labels, e.g. head-cast or standard.

Note that between session correlation is higher with the head-cast for all metrics, but this is only significant when using the phase based measures Coh, ICoh and PLV. There is also a notable difference between metrics with AEC being the most reliable measure across sessions, and PLI the least reliable. This is in agreement with other published work [Colclough et al., 2016]. By far the biggest effect comes from data recording duration, with reproducibility across sessions increasing markedly when moving from 120 s to 560 s recordings.

Finally, Figure 3.8 show between session correlations of connectivity, independently for each AAL region. Here, rather than measure correlation between sessions over an entire connectivity matrix, correlation is measured column by column (i.e. for each AAL region independently). Red shows brain regions with high between session reproducibility and blue shows regions with low between session reproducibility. The left hand column shows the case for standard co-registration and the right hand column shows the case for head-cast co-registration. The three rows show three different recording durations. Panel A shows the case for AEC and B shows the case for Coherence (selected since it proved to be the most reliable (across sessions) of the phase based metrics). In agreement with results shown in Figure 3.7, the significant effect of head-cast can be seen for the coherence mea-

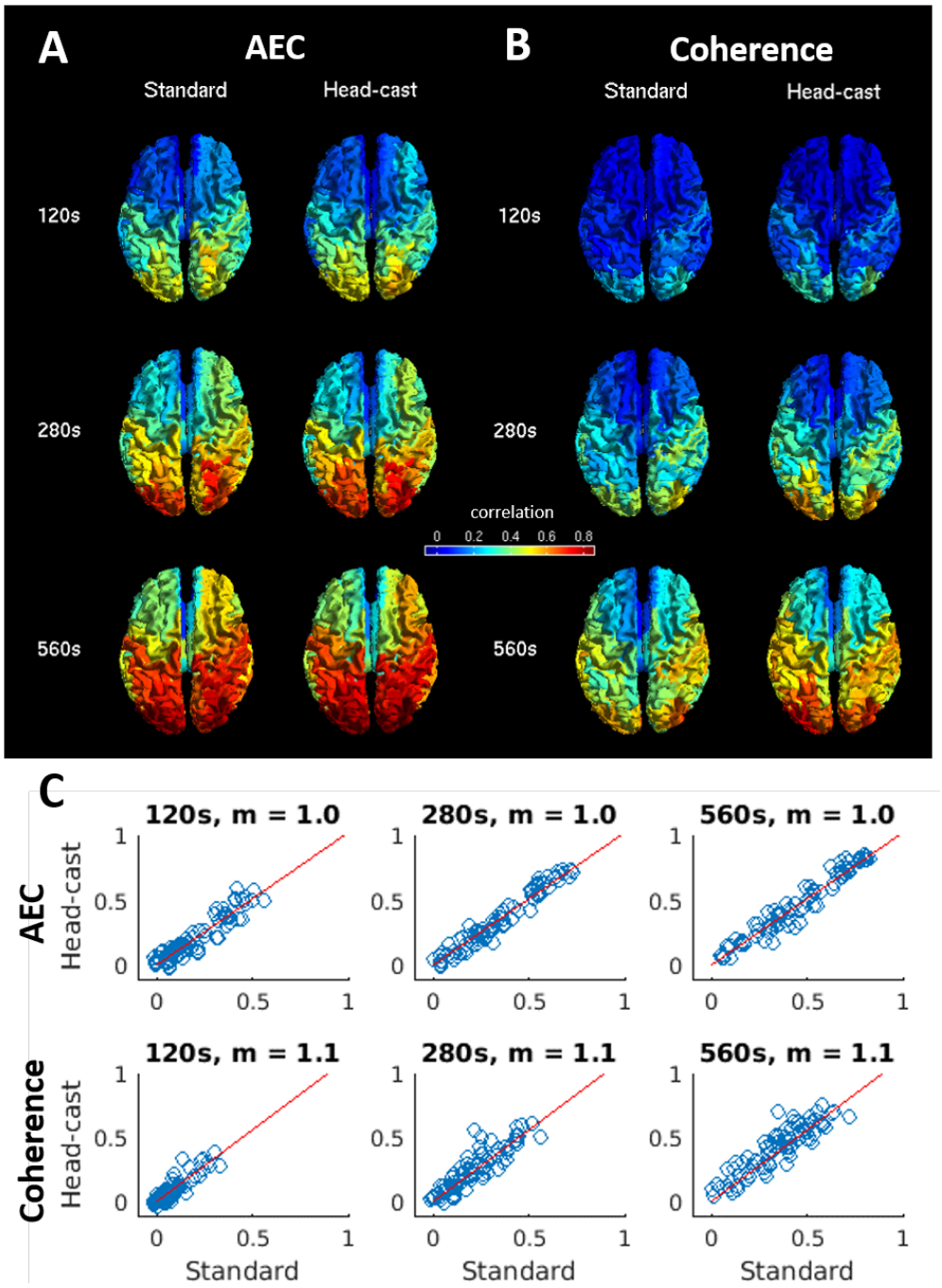



Figure 3.8: Between session correlation of functional connectivity, on a 'per region' basis. A) Between session correlations of connectivity profiles measured using AEC in the beta band. The left hand column shows the case for standard co-registration. The right hand column shows the case for head-cast co-registration. The three rows show three different recording durations. B) Equivalent to A, but for Coherence. Figures for PLV, PLI and Imaginary Coherence are included in appendix B. C) Comparison of standard co-registration and head-cast for AEC and Coherence. Each dot corresponds to the between session correlation of functional connectivity from one AAL region to the rest of the brain. Gradient of the linear fit is m = 1.0 for AEC (no improvement by using a head-cast) and m = 1.1 for Coherence (small improvement on a 'per region' comparison).

surements. In addition, the comparatively large effect of recording duration can be seen clearly. It is noteworthy that the highest between session reliability is observed in the parietal and occipital lobes and this is consistent with functional connectivity in beta band being dominated by these brain areas, as shown in Figure 3.7 (see also Hunt et al. [2016]). However it is important to point out that this is likely because results are derived from resting state data. It is well known that cognitive tasks induce strong transient activity and connectivity in frontal areas [Fox et al., 2005; Brookes et al., 2014]. However, the signal to noise ratio of these frontal networks is typically lower. We would therefore not only speculate that the advantages of data recording duration and head-cast shown here, dominated by the posterior brain areas, would be observed in frontal regions for task positive data. But we also suggest that these advantages are potentially more important in task positive studies in order to compensate for their lower SNR.

### 3.4.3 Within session consistency

Any observable effect of recording duration could result from two possible sources; 1) beamformer reconstruction error (i.e. similar to the underlying cause of the effect shown in Figure 3.5) or 2) genuine differences in brain state. In order to assess this, connectivity matrices were computed using two 280 s windows, or two 120 s windows, derived from the same session (e.g. within a single 560 s recording in one session, we compare a connectivity matrix acquired in the first 280 s, to a connectivity matrix acquired in the final 280 s). To eliminate the effect of the beamformer reconstruction, the same beamformer weighting parameters were used, i.e. beamformer weights were derived using data acquired across the whole recording (encapsulating both time windows). It was reasoned that if an effect of data duration was observed in the between session comparisons, but not the within session comparisons, then such an effect would likely be due to the beamformer reconstruction. However if an effect was measurable in both the between session and within session comparisons, this likely represents differences in brain state.

Figure 3.9 shows the within session consistency of both beamformer orientation reconstruction and connectivity calculation. Figure 3.9A shows a histogram of orientation differences between different time windows within the same MEG session. Here, beamformer reconstructed dipole orientation has been reconstructed within the first 280s, and the final 280s of each MEG recording and compared (i.e. Figure 3.9A shows orientation consistency within a MEG session, as distinct from between MEG sessions as was shown in Figure 3.6A). The red line shows the case with head-cast co-registration whereas the black line shows the standard co-registration. Interestingly, the effect of the head-cast that was apparent in the between session recording has been eliminated. This shows that, whilst between session consistency is improved by using the head-cast, within session consistency is approximately equal - this would be expected since the head-cast is predominantly improving co-registration error which does not change within a session.

Figure 3.9B (green and pink crosses) shows the correlation between connectivity vectors measured using different time windows within the same recording session. Note here that beamformer parameters are the same for all windows and hence the effect of the beamformer is removed. The pink lines show within session connectivity correlation with a head-cast and the green lines show within session connectivity correlation without a head-cast. For comparison, the red and blue lines show the equivalent between session values for comparison (i.e. these are the same as in Figure 3.7). Note that the effect of head-cast co-registration on the within session correlation is mostly eliminated. An improvement in reproducibility for within session, compared to between session is observed, but this is most apparent when comparing between session correlation using standard co-registration, with within session correlation. Most importantly, the effect of recording duration remains. This implies that the significant effect of recording duration on the reliability of functional connectivity (shown in Figure 3.7) is not down to beamformer reconstruction accuracy, but rather represents changes in brain state, either between session, or between time windows in the same session.

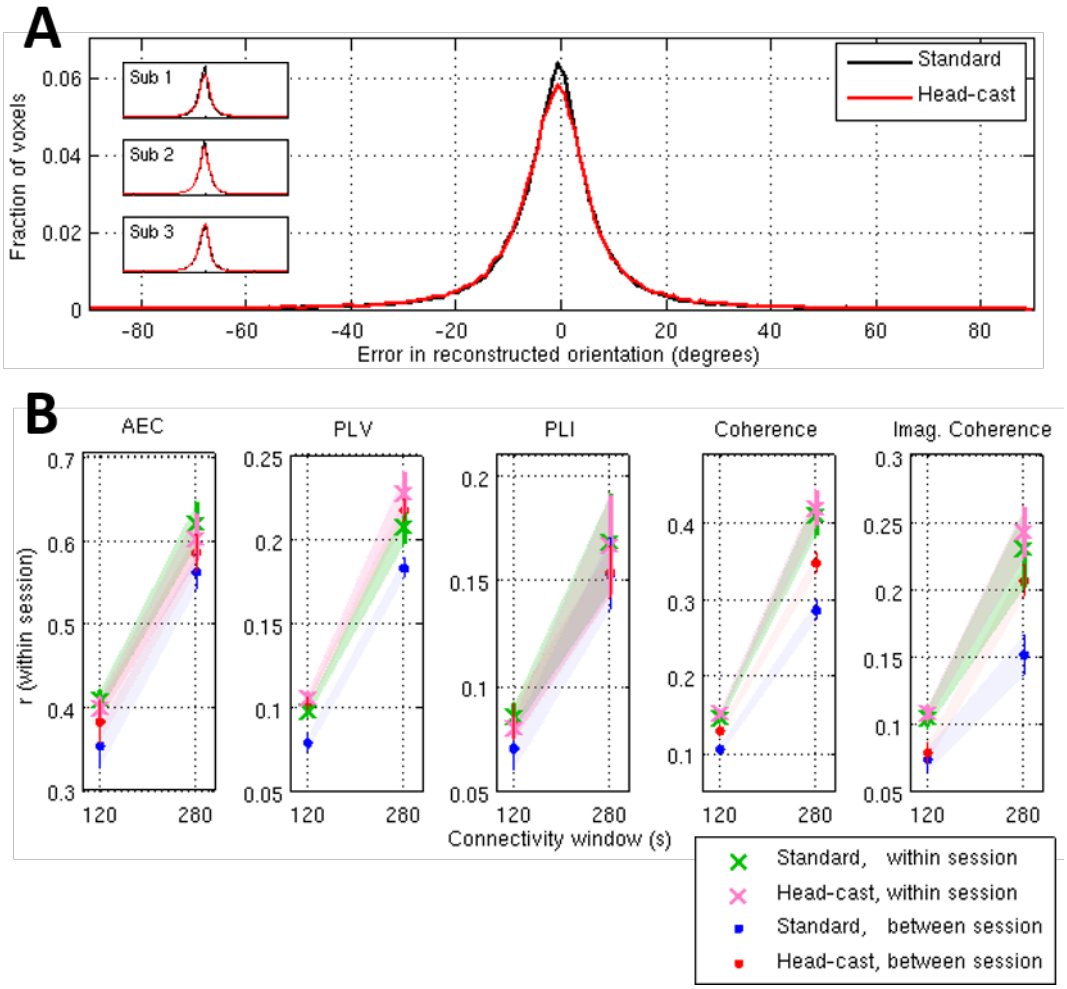



Figure 3.9: Within session consistency of orientation reconstruction and functional connectivity. A) Histogram showing orientation difference (measured as an angle in degrees) in beamformer source reconstruction for multiple windows within a single session. The main plot shows all subjects combined; inset plots shows the three subjects separately on the same scale. B) Correlation of connectivity vectors measured in multiple time windows in the same session. The 5 plots show the 5 separate connectivity metrics AEC, Coh, ICoh, PLI and PLV). The pink crosses show the case with the head-cast co-registration and the green crosses show the case with standard co-registration. For comparison, the red and blue dots show the between session results (copied from Figure 3.6B).

## 3.5 Discussion

We aimed to test how practical aspects of experimental design affect the intra-subject repeatability of MEG functional connectivity measurement. Specifically we assessed the effects of co-registration method and data recording duration on the between session reliability of network estimation. Our results showed that the use of a foam head-cast, which is known to improve co-registration accuracy [Meyer et al., 2017; Troebinger et al., 2014], increased significantly the between session repeatability of both MEG reconstruction accuracy and connectivity estimation. This was the case for all MEG connectivity metrics, but was strongest for phase based methods. Further, we showed that recording duration is a critical parameter, with large improvements in repeatability apparent when using ten minute, compared to five minute recordings. Further analyses suggest that the origin of this effect is not underpinned by technical aspects of source reconstruction, but rather by a genuine effect of brain state.

Co-registration error has been identified as one of the most significant problems with MEG source reconstruction. Perhaps counter-intuitively, as the signal to noise ratio of MEG measurements has increased (i.e. as system architecture has improved), the sensitivity of source reconstruction, particularly using adaptive methods such as beamforming, to co-registration accuracy has also increased [Boto et al., 2016]. This means that in modern multi-channel systems, even modest errors in knowledge of sensor location and orientation relative to brain anatomy generate a significant degradation in reconstruction accuracy. The extent of this problem is shown clearly by our simulations. We show that even relatively small errors have a significant impact on both beamformer reconstruction and connectivity estimation; for example, for simulated sources in left and right motor cortex, a translational error in co-registration of 5mm, coupled with a rotational error of 5° reduces reconstruction accuracy from 88% to 70%. Such errors propagate to connectivity estimation, and have the effect of reducing the measured magni-

tude of functional connectivity and increasing the variability of connectivity over simulated recordings.

In real data, assessing the effect of co-registration error is challenging since the ground truth of precisely where the head is with respect to the MEG helmet is never known. Nevertheless, by exploiting the fact that source orientation, which is defined purely by brain anatomy, should be constant across multiple MEG acquisitions, we were able to show that source reconstruction accuracy is improved significantly by the use of head-cast technology. In agreement with our simulations, this improvement is translated to connectivity estimation with between session reproducibility of connectivity significantly higher when using the head-cast for 3 of our 5 connectivity metrics. The biggest improvement was for coherence which showed approximately a 20% improvement in between session reliability when using the head-cast compared to standard co-registration. Interestingly, whilst a significant effect of co-registration method was observed for 3 out of 4 phase based metrics, the improvement in between session reliability for AEC failed to reach statistical significance. There are two potential reasons for this: first, the between session reliability of AEC is already high ($\sim$ 70%, which is in line with previous estimates [Colclough et al., 2016]). The effect of the head-cast may therefore be minimised. Second, it could be that phase based metrics are more susceptible to co-registration error than amplitude based metrics. It is noteworthy that of the 4 phase metrics, PLI also failed to show a significant effect of head-cast. However, of all the measures tested here, PLI showed the lowest between session reliability ($\sim$ 25% - again in line with previous results [Colclough et al., 2016]).

Our co-registration results show clearly that both beamformer reconstruction and connectivity estimation are improved by the head-cast method of co-registration. However, whether head-cast technology should become commonplace for all MEG acquisitions is debatable. It is important to note that the three individuals who took part in our study were all experienced subjects (indeed this

was evidenced by the relatively low levels of movement when they were scanned without a head-cast). All three tolerated the use of the head-cast well, however whether scanner naïve individuals would cope so well is unclear. The head-casts are made from foam and are therefore relatively soft and comfortable to wear. However, they do restrict head movement when the subject is in the scanner, and subjects can become warm. This means, potentially, that some people (particularly infants, or some patient groups) may find wearing a head-cast worrisome, or claustrophobic. This could limit their utility for broader use. A second limitation is cost: the head-cast construction process is relatively involved and costly, and this may be prohibitive for studies with large subject numbers; the modification of the design to a cheaper method, perhaps using only subject specific foam pads rather than a whole head-cast, might be advantageous. Finally, even when using a head-cast, co-registration error can arise due to, for example, movement of the head localisation coils inside the cast, localisation of the magnetic signature of the coils, or even differences in brain position within the skull between a seated MEG measurement and a supine MRI measurement, meaning that co-registration will always involve some inherent error. Overall, our results certainly provide sufficient motivation to suggest that novel methods for co-registration should be sought for future MEG investigations, particularly if individual subject results are required. However, whether those methods should be limited to head-casts, or other (e.g. optical) co-registration techniques remains a topic for future work.

The effect of recording duration manifests in two ways.

1. There is a technical limitation generated when reconstructing data and measuring functional connectivity using a reduced number of data points. This manifests firstly as an error in the data covariance matrix used for beamformer weights generation [Brookes et al., 2008]; fewer data points mean a larger covariance matrix error, and ultimately a lower beamformer projected power. Second, when estimating functional connectivity itself, most

correlative or coherence based measures are highly sensitive to the number of degrees of freedom in the timecourses used to generate them.

2. In addition to the technical limitation, the well characterised dynamic nature of functional connectivity, which changes over seconds, and even milliseconds [Baker et al., 2014; Brookes et al., 2014; Hutchison et al., 2013; O'Neill et al., 2015; Vidaurre et al., 2016] must be considered, since there is a question regarding how well a short time window can capture the canonical MEG networks, if those networks are constantly changing across multiple timescales.

Here, we first probed this question in simulation; our simulations do not take into account brain state and for this reason only the technical limitations are addressed. Our results show that beamformer reconstruction and connectivity are indeed impacted by recording duration; but mainly for recording durations below 100 s (see Figure 3.5). Above 100 s, these effects tend to plateau, and so for the typical windows that might be used for resting state MEG acquisition (several minutes), one might infer that recording duration would have little effect. Our simulations also showed that these effects are dominated by inaccuracies in beamforming, rather than the reduced degrees of freedom available for functional connectivity measurement.[1]

In apparent contradiction to the evidence from the simulations, in real data we showed that changing recording duration (above 100 s) had by far the largest effect on between session repeatability of connectivity. This therefore implies that the underlying source of this effect is related not to technical limitations, but rather to genuine problems with characterising brain state. In support of this, we also measured within session correlation between connectivity matrices, where data within

[1] As an aside, it should be noted that these simulations are based on the beta band only; the technical limitations on data recording duration are related not only to the time window, but also to the bandwidth of the data, since the number of temporal degrees of freedom in a timecourse is given by twice the product of the bandwidth and the window duration. This means that for frequency bands with smaller bandwidth, the curves in Figure 3.5 would tend to their plateau value slower.

two time windows used for connectivity estimation were reconstructed using the same beamformer weighting parameters; this, in effect, removes the technical limitations associated with beamformer reconstruction using limited data. Our results show that within session (beamformer limitations removed) and between session (beamformer limitations present) correlation between connectivity matrices was approximately equivalent. This, coupled with the evidence from simulation that using a 17 Hz (beta) bandwidth, 100 s should be sufficient to characterise adequately connectivity from a technical point of view, suggests that the significant variation of connectivity reliability with recording duration is a genuine effect; put simply, short recordings are not sufficient for capturing the canonical MEG network in a single subject. It follows directly that, to maximise intra- (and indeed inter-) subject reliability in future resting state MEG studies, data recording durations should be a minimum of 10 minutes, and even longer (e.g. 15 min) recordings may provide further advantages.

## 3.6 Conclusion of chapter

The study of functional connectivity using MEG is an expanding area, the importance of which is evidenced by recent demonstrations of utility in clinical studies. However, previous reports suggest that whilst comparisons of MEG derived connectivity between large group studies are robust, single session recordings, even in the same individual, lack repeatability. Our results showed that the use of a foam head-cast increased the between session repeatability of both MEG reconstruction accuracy and connectivity estimation. Further, we showed that recording duration is a critical parameter, with large improvements in repeatability apparent when using ten minute, compared to five minute recordings, providing important insights on experimental design.

Our results also highlight the importance of the selection of connectivity metric, with the amplitude metric AEC appearing the most robust to assess time

averaged functional connectomes. Time dynamics of functional connectivity also play an important role, even when estimating "stationary" connections. Phase metrics, such as PLV and PLI, are centered on the idea of transient phase locking between regions and are reliant on window selection. The low reproducibility of phase metrics may be linked to a mismatch between the selected window (here 2s long), in which average phase locking is estimated, and the timing of coherent oscillations of neuron assemblies. In the resting state it is perhaps impossible to manually select appropriate time windows for connectivity assessment, as no "ground truth" is known, nor can be inferred by time-locked events (such as in task data). A self guided and data driven selection of both connectivity lifetimes and topography could sidestep this issue and, in recent years, Hidden Markov Models (HMM) have seen good success in this regard: HMMs and HMM-MARs (mutivariate autoregressive models [Vidaurre et al., 2016]) determine a discrete set of states derived from the data [Baker et al., 2014], without the need of specifying a state time window a priori. The results from HMM and HMM-MAR analysis point to functional connections having a lifetime of tens of milliseconds [Baker et al., 2014; Vidaurre et al., 2016]. In the next experimental chapter we will further explore the idea of dynamic functional connectivity, this time assessed through a continuous phase locking metric (i.e. Phase Difference Derivative), by looking at connectome changes at the millisecond scale following stimulus presentation.

# Appendix B

# Between session correlation of functional connectivity, on a per region basis: additional figures

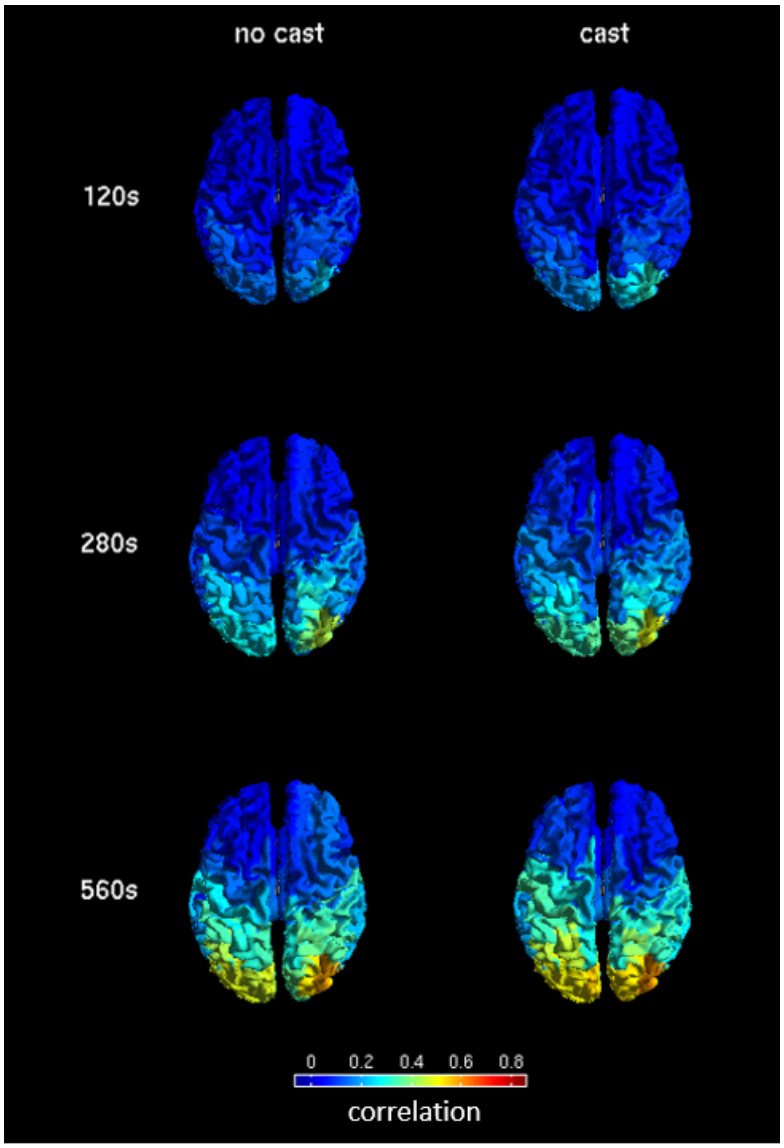



Figure B.1: Between session correlations of connectivity profiles on a 'per region' basis measured using PLV in the beta band. The left hand column shows the case for standard co-registration. The right hand column shows the case for head-cast co-registration. The three rows show three different recording durations.

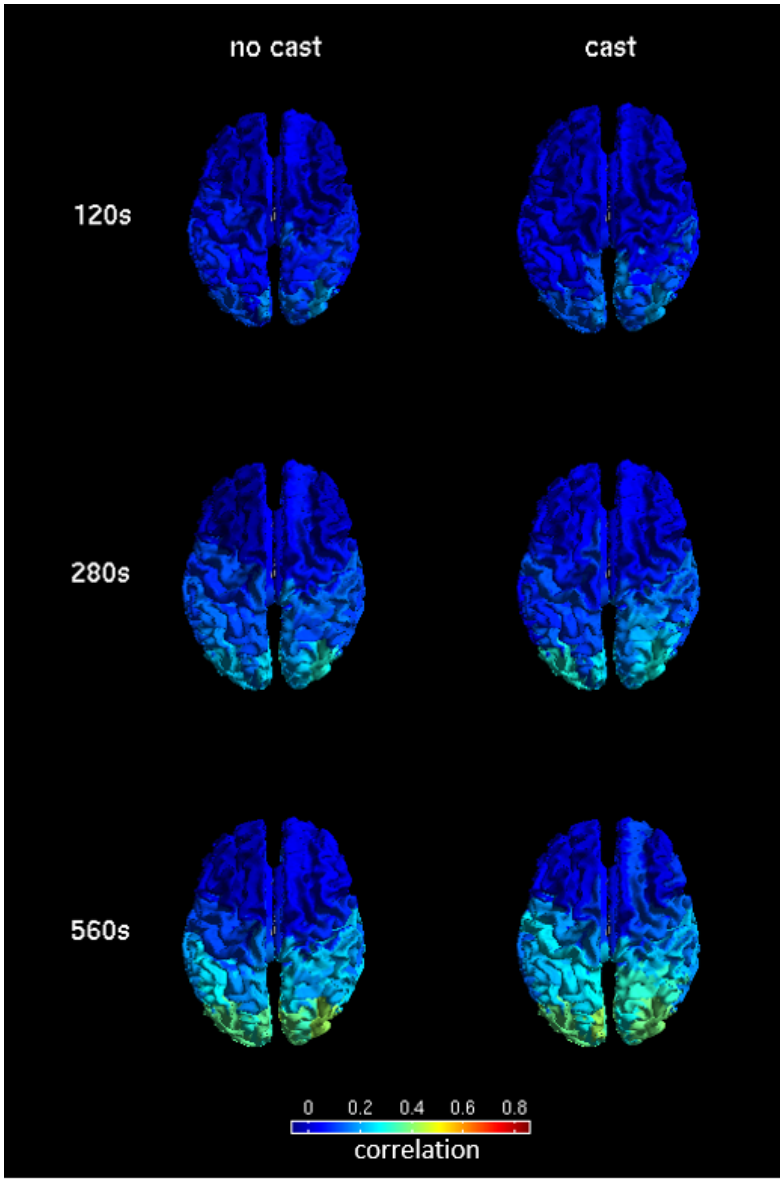



Figure B.2: Between session correlations of connectivity profiles on a 'per region' basis measured using PLI in the beta band. The left hand column shows the case for standard co-registration. The right hand column shows the case for head-cast co-registration. The three rows show three different recording durations.

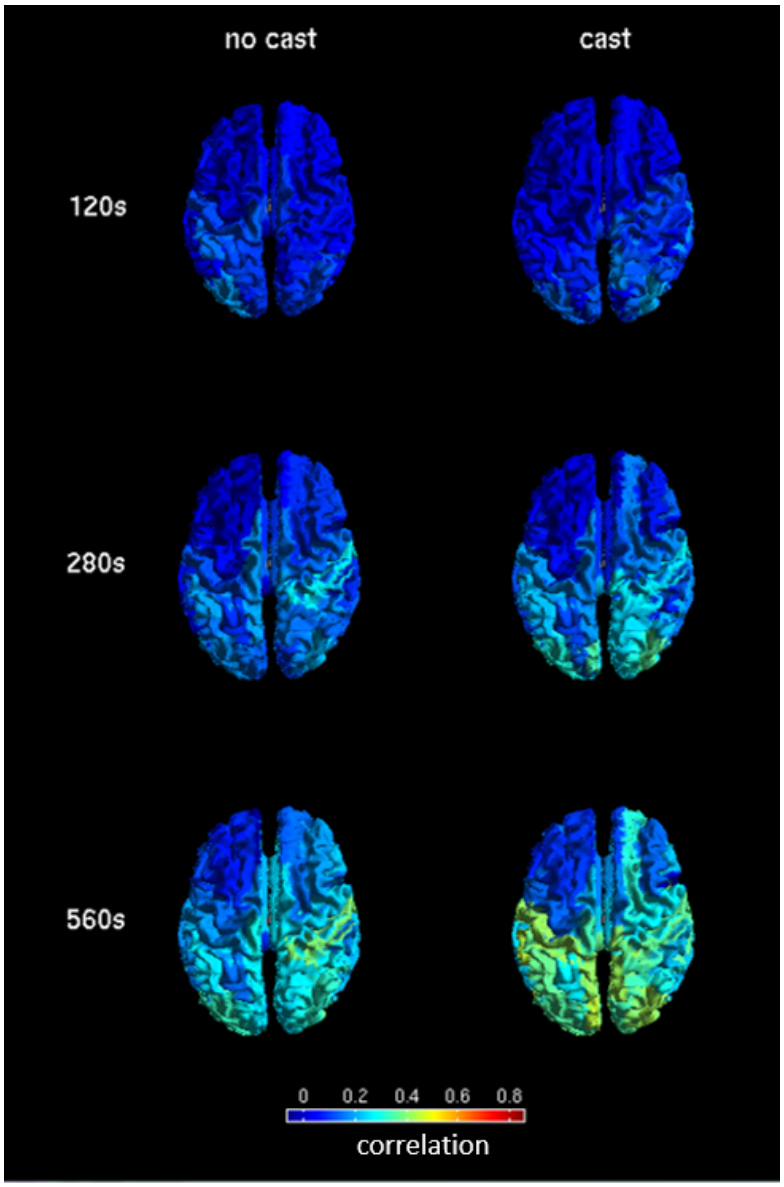



Figure B.3: Between session correlations of connectivity profiles on a 'per region' basis measured using Imaginary Coherence in the beta band. The left hand column shows the case for standard co-registration. The right hand column shows the case for head-cast co-registration. The three rows show three different recording durations.

# Chapter 4

# The functional role of the Beta rebound

In the previous chapter we showed that the electrophysiological functional connectome can be derived based upon assessment of neural oscillations. This supports previous literature linking established functional brain connectivity derived from fMRI measurements and beta band connectivity from MEG recordings. However, more generally, changes in neural oscillations are thought to represent inhibition or excitation of neuronal populations, with a weight of evidence suggesting that "low" frequency (beta band) oscillations are representative of cortical inhibition. Here we attempt to bring these two separate theories together. We recorded MEG data during a sensory attention task, in which participants were asked to identify braille patterns presented to their fingers, whilst simultaneously switching attention between hands. Our results show that attentional modulation changes beta dynamics in primary sensory cortex, with attended stimuli generating lower post-stimulus responses (i.e. lower beta "rebound"). Using the Phase Difference Derivative we further show that this effect is driven by the transient formation and dissolution of distributed networks, which form in response to unattended stimuli, and likely facilitate top down inhibitory influence on the primary sensorimotor cortex. We relate our results to subject behaviour, showing that high pre-stimulus beta connectivity leads to poor task performance. This work forms the basis of a grant funded by the Medical Research Council and is currently being submitted for scientific publication.

## 4.1 Introduction

The relationship between oscillations and connectivity is based upon a hypothesis of 'communication via coherence' [Fries, 2005] (see section 1.2). This hypothesis is supported by extant evidence; e.g. canonical resting state networks (RSNs) are observable when assessing temporal correlation between the amplitude envelopes of beta oscillations [Brookes et al., 2011a] and similar connectomes result from

measurement of inter-regional phase locking [Liuzzi et al., 2017] as was shown in chapter 3. Such observations promote the idea that oscillations support intrinsic coupling modes [Engel et al., 2013], however most studies have been limited to time averaged metrics. As we saw in the last chapter, even 5 minutes of data are not enough to offer stable connectome measurements and so it is imperative that we begin to understand the connectome not as a static time averaged matrix but as a dynamically evolving entity. Recently, new techniques exploiting the high temporal resolution of electrophysiological imaging, have enabled measurements that show evolution and dissolution of networks at rapid timescales [O'Neill et al., 2018], and significant relationships are observed between periods of phase locking, and high oscillatory amplitude [Vidaurre et al., 2017; Tewarie et al., 2018]. However the neurochemical basis of connectivity, and its relationship with inhibition and behaviour have not been probed.

Oscillatory amplitude is transiently modulated by external stimulation in a spectrally specific way; the onset of stimulation typically generates a decrease in the amplitude of 'low' frequency (alpha $8-13$ Hz, and beta $13-30$ Hz) oscillations, and a concomitant increase in higher frequency amplitude [Pfurtscheller and Da Silva, 1999], both localised to functionally specific regions [Barratt et al., 2018]. This has led to a hypothesis that low-frequencies denote inhibition, and high-frequencies excitation (as was previously introduced in section 1.2).

Modulation of rolandic beta oscillations can be induced by movement, somatosensory stimulation, imagined movement, or motor planning. Generally, we observe a decrease in resting beta amplitude throughout stimulation, followed by an increase (above baseline) on stimulus cessation (the 'beta rebound'). These effects have been shown to be abnormal in a number of disorders [Schnitzler and Gross, 2005; Robson et al., 2016; Barratt et al., 2017], underlining the importance of determining a mechanistic role. Rolandic beta is also modulated by changing attention; e.g. attending to a stimulus on the left hand generates a decreased beta

amplitude in right sensorimotor cortex, and an increase in the left [Bauer et al., 2012]. Taken together, these studies, suggest a link between high amplitude beta and inhibition. This is supported by links to Gamma-aminobutyric acid (GABA), which will be explored later in chapter 5.

In this chapter we aim to measure both beta amplitude modulations and transient connectivity throughout a spatially-selective attention task, which uses tactile stimulation to modulate sensory attention. Specifically we aimed to test the following hypotheses:

1. Attention will alter post-stimulus beta amplitude with unattended stimuli resulting in larger responses (i.e. more inhibition);

2. pre-stimulus beta amplitude will predict behaviour, with a larger pre-stimulus beta amplitude (i.e. more inhibition) leading to more errors;

3. for both 1. and 2., higher beta modulation will be driven by more long range connectivity (i.e. an inhibitory network providing top-down control).

## 4.2 Experimental set-up

A total of 48 healthy participants, age 23.4 $\pm$ 3.7 years (mean $\pm$ standard deviation), 19 male, were recruited from the University of Nottingham campus area[1]; for 2 participants it was not possible to collect a structural MRI and they were therefore excluded from the rest of the analysis. Of the 46 remaining participants, 29 took part twice, with the two runs separated, on average, by 9 months (the remaining 17 were unable to return). On average participants spent about 3 hours for each run of the study including a MEG and a MR session. The MEG session included a somatosensory attention task (described in detail in this chapter), a somatosensory stimulation scan (duration $\sim$ 7 minutes, not presented in this thesis) and a 10 minutes resting state scan. This was followed by a MR session with

[1]All data were acquired by the author.

the 7T scanner including structural scans and MR proton spectroscopy (the latter will be described in chapter 5).

### 4.2.1 Task

The task comprised somatosensory stimulation of the index fingers using a 'braille' stimulator as part of a delayed-match-to-sample-task [Bauer et al., 2006]. Figure 4.1 shows the MEG system with the braille simulators and button response pads placed on the arms of the chair. Each braille stimulator had 8 pins, all independently controllable, however, for consistency with previous literature [Bauer et al., 2006], only 5 braille patterns were used throughout the task, and these are shown in Figure 4.1D. The stimulators themselves were MEG compatible Braille P-16 cells acquired from Metec (Metc AG, Stuttgart, https://www.metec-ag.de). Each stimulator contained 8 pins in a $4 \times 2$ layout. Pins were separated by 2 mm, and controlled using piezoelectric crystals, enabling placement up or down. To control the stimulators we used a driving circuit built in house, with serial shift register and DC converter [Bauer et al., 2006]. The stimulators and the response button boxes were housed in wooden bases that could be placed on MEG chair armrests inside the MSR. The stimulators interfaced through parallel port and were synchronised to the study protocol using psychtoolbox (Matlab, MathWorks, Natick, MA). Digital triggers corresponding to the experimental trials and stimuli were sent to the MEG system and a clock strobe signal sequence was sent to the stimulators to produce the desired patterns.

The timing of the task paradigm, for a single trial, is shown in Figure 4.2. A single trial lasted 16 s. At the beginning of each trial (time window 1 s $<$ t $<$ 3 s) a sample pattern (chosen at random from the five possible patterns) was presented to the index fingers of both hands, simultaneously. The participant must remember this sample, and correctly identify it later in the trial. Following this, a visual attention cue, in the form of an arrow pointing either left or right, was shown (via

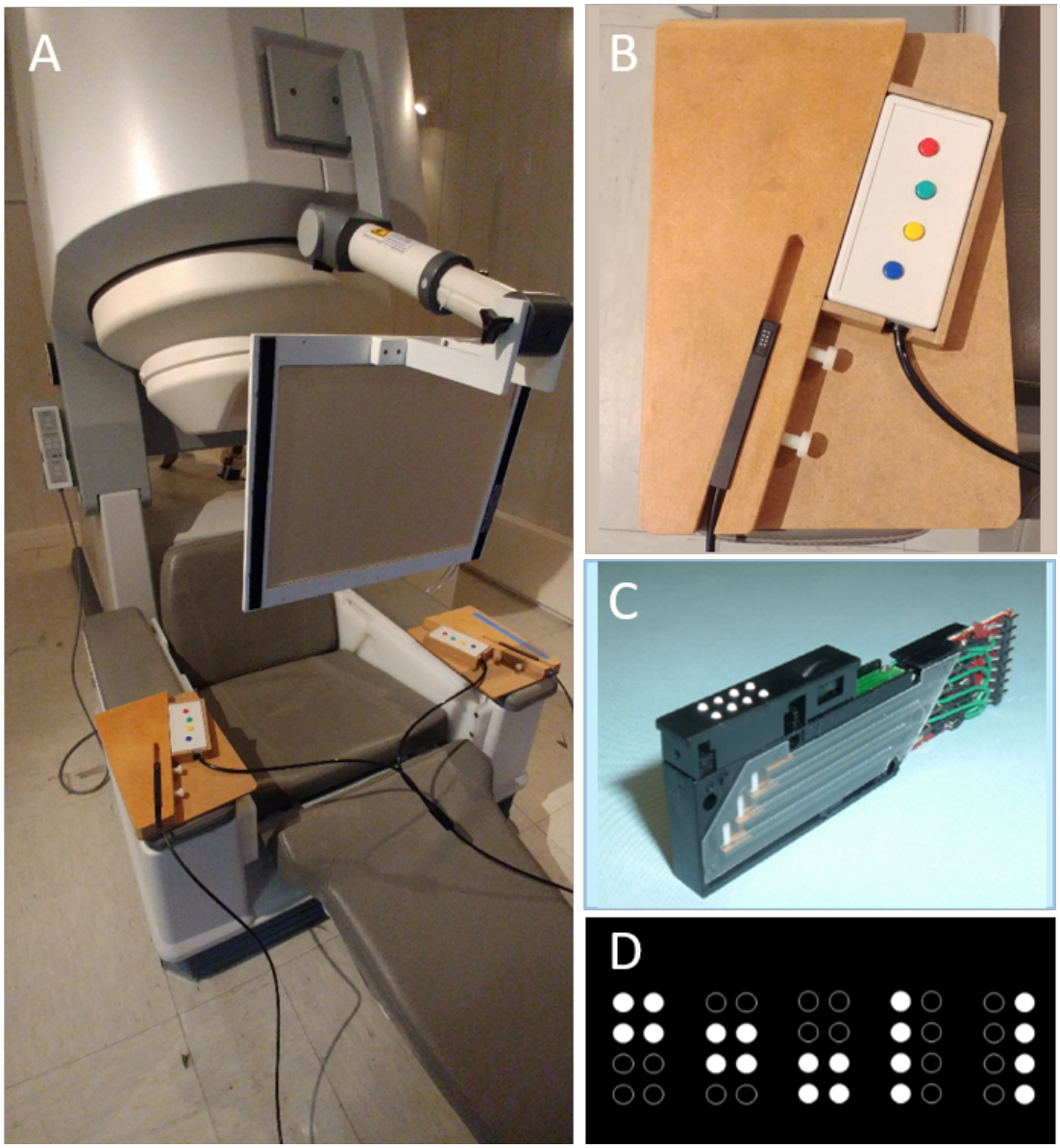



Figure 4.1: Experimental set-up A) 275 channel CTF-MEG system with braille stimulators and response buttons in the experimental configuration. B) Braille stimulators and response buttons in custom made wooden frame. C) Metec Braille P-16 cells without outer case, picture property of Metec (http://web.metec-ag.de/, website accessed in 2017). D) The five different braille patterns used during the experiment: all patterns have 4 pins up (white dots) and 4 pins down (black dots).

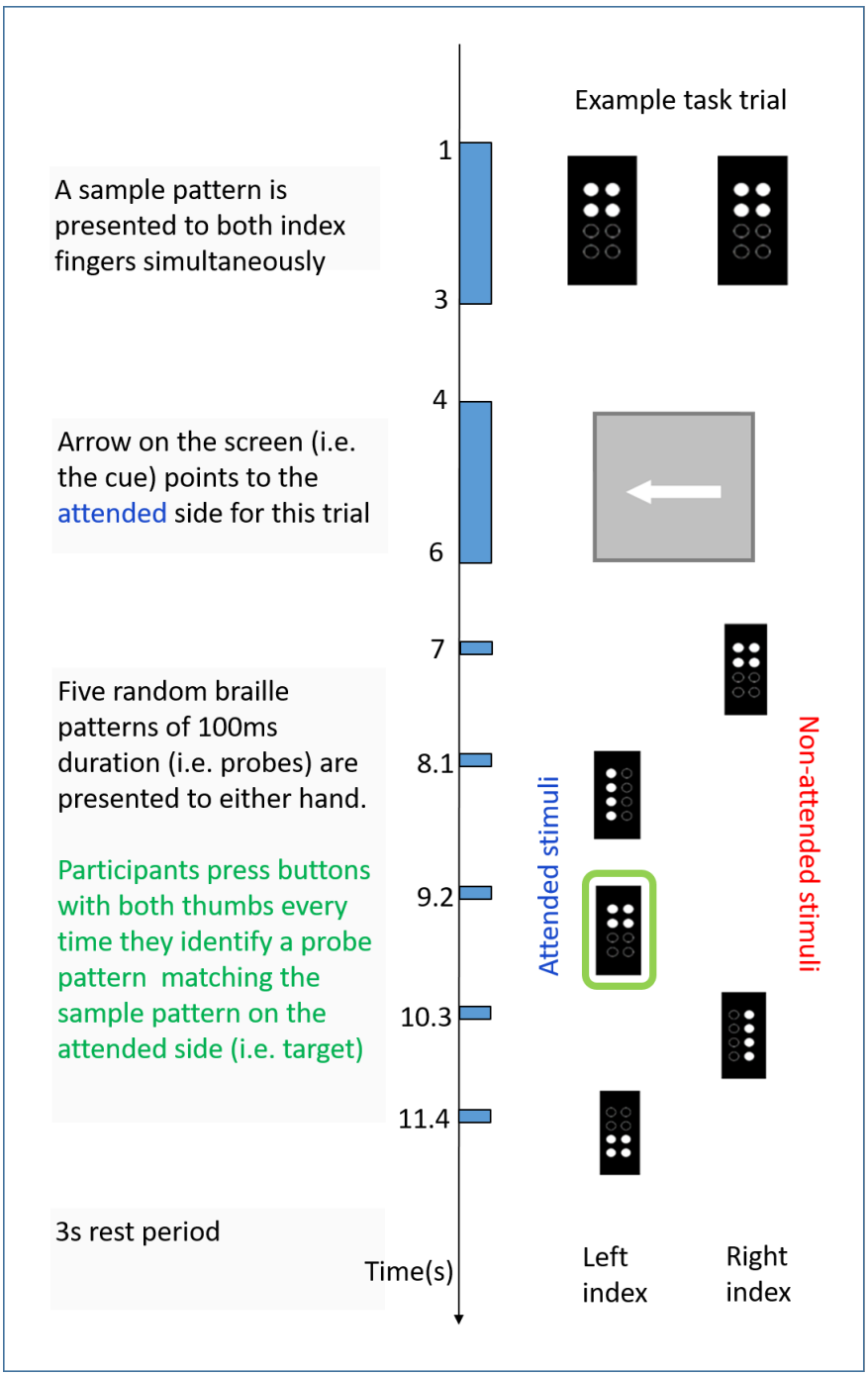



Figure 4.2: Schematic diagram of the braille attention task. A single trial lasted 16 s. At the beginning of each trial (time window 1 s $<$ t $<$ 3 s) a sample pattern (chosen at random from the five possible patterns) was presented to the index fingers of both hands, simultaneously. The attentional cue appears in the 4 s $<$ t $<$ 6 s window, and indicates (for this trial) whether the participant should attend only to their left or right hand. This is then followed by a sequence of five probe patterns, at t = 7, 8.1, 9.2, 10.3 and 11.4 s each lasting 100 ms.

projection onto a back projection screen placed ∼40 cm in front of the subject). This attentional cue appears in the 4 s $<$ t $<$ 6 s window, and indicates (for this trial) whether the participant should attend only to their left or right hand. This is then followed by a sequence of five probe patterns, (starting at t = 7 s) each lasting 100 ms and with an interval of 1.1 s. Each pattern was chosen at random and appeared on either the left or right hand. The participant was instructed to press a button, with both of their thumbs, if the sample pattern appears on the attended hand; any stimulus appearing on their non-attended hand should be ignored. The probability of a "target" (i.e. matched probe and sample on attended side) was 10%. The sequence of attentional cues was pseudorandomised, but with 50% of trials directing the subject left, and 50 % right. A total of 80 trials were presented, but once every 10 trials a rest block (duration 16 s) was incorporated in order to give subjects a brief rest, and also to quantify resting amplitude of neural oscillations. Feedback showing the number of correct and incorrect button responses was also displayed during the rest trials to keep participants engaged. Prior to MEG measurement, all participants were trained on the task, until they were able to perform it correctly.

### 4.2.2 Data acquisition

MEG data were acquired using the CTF 275-channel MEG system (described in section 1.5.4), operating in third order synthetic gradiometer configuration with a sample rate of 600 Hz. Subject head position in the scanner helmet was recorded continuously throughout data acquisition, via the three fiducial coils. Co-registration between MEG data and brain anatomy was achieved via surface matching using a Polhemus 3D digitiser for all but four subjects for whom foam head-casts were available (as described in section 3.2). The resulting head surface was fitted to an equivalent surface extracted from an anatomical MRI scan acquired at 7T (MPRAGE: 1 mm$^3$ isotropic resolution, matrix size =$256 \times 256 \times 180$, TE/TR/TI =3.5/7.3/987ms, FA =8°, shot interval =2s, SENSE factor =2). Fol-

lowing acquisition, all MEG data were inspected visually and any trials containing artefacts were removed. All trials exceeding a motion threshold of 5.5 mm were also eliminated. Although care was taken to reduce head motion by using padding and insuring comfort of the participant before starting data collection, a noticeable number of participants struggled to remain still for the full duration of the sensory attention experiment (lasting 23 min 28 s). When participants exceeded the motion threshold before completing the majority ($\sim 75\%$) of the experiment, data collection was interrupted and subjects were re-positioned in the scanner before recommencing data collection. 13 out of 46 participants in the first run, and 5 out of 29 participants in the second run had to be re-positioned. In these cases pre-processing and source localisation were run independently for the two separate data sets and trials were then concatenated in source space.

## 4.3 Source power analysis

In the first part of the analysis we aimed to localise the maximum task induced modulation of beta power in the sensorimotor cortex and compare attentional variations in the time frequency spectra.

### 4.3.1 Methods

Following pre-processing (including dc baseline correction in each trial and frequency filtering at $1-150$Hz through CTF software), our data were processed using a beamformer spatial filter. We constructed pseudo-T-Statistical maps, contrasting beta power in the 0.1 - 0.5 s window relative to probe presentation (excluding targets and button presses) to a control window of equivalent duration during the rest period (i.e. in the time window 13.5 s $<$ t $<$ 16 s relative to trial start). These maps, which were overlaid onto anatomical MRIs for each subject, show the spatial signature of maximum beta change induced by the probe stimuli.

For the beamformer weights calculation, covariance was calculated in a fre-

quency window spanning the beta band ($13 - 30$ Hz) and in a time window encompassing the entire experiment. The resulting covariance matrix was regularised using the Tikhonov method with the regularisation parameter set to 4 times the minimum singular value of the unregularised covariance matrix. In order to identify activation peaks in individual MRI space, pseudo-T-Stat maps with 1 mm resolution were first calculated with a LCMV beamformer implemented through CTF software (SAMMenu). The identified activation peaks, showing maximum decrease in beta power in the primary sensory cortex, were selected for all further time frequency spectra analysis.

Time frequency spectra, showing the evolution of neural oscillatory amplitude across the task trial, were also calculated using beamforming. Here, the covariance window was increased, in frequency, to $1 - 150$ Hz to capture the entire spectral content of the signal. We derived broadband electrophysiological signals from peaks (defined by the pseudo-T-statistical images) in left and right primary sensory cortex. These signals were then filtered into a range of (50% overlapping) frequency bands. For each band, the instantaneous oscillatory amplitude was derived using a Hilbert Transform and normalised to the average resting beta amplitude (derived in the rest blocks). Concatenating these envelope signals in the frequency direction resulted in unaveraged time frequency spectra, for all trials, from 2 brain locations. We then averaged responses both contralateral and ipsilateral to the attended hand. Specifically, we averaged all responses in left sensory cortex in trials when the subject was asked to attend right along with all responses in right sensory cortex in trials when the subject was asked to attend left. This gave a single averaged spectrogram from contralateral sensory cortex. Similarly, we also derived an ipsilateral spectrum.

In addition, we derived time frequency spectra, time locked to the presentation of the (non-target) probe stimuli excluding any button presses. Again we collapsed across signals in left and right sensory cortex to give 4 conditions:

1. Attended stimuli in contralateral cortex (i.e. collapsing across responses in left sensory cortex with right stimulation and right attention cue, and right sensory cortex with left stimulation and left attention cue).

2. Non attended stimuli in contralateral cortex (i.e. responses in left sensory cortex with right stimulation but left attention cue, and right sensory cortex with left stimulation but right attention cue).

3. Attended stimuli in ipsilateral cortex.

4. Non-attended stimuli in ipsilateral cortex.

Finally, in order to further visualise the beta rebound, we derived just the beta signal only, in the contralateral sensory cortex, using a beamformer with covariance measured in just the beta band. Oscillatory envelopes were again derived using the Hilbert Transform and averaged across attended and non-attended stimuli.

In all TFS analyses, oscillatory amplitude is reported as the fractional change from the average rest amplitude in the same frequency band, where rest amplitude is assessed in each subject over the entire rest periods (i.e. 8 trials of 16 s).

In order to test, statistically, for a difference in the size of the rebound between attended and non-attended stimuli, we used a permutation test. We reasoned that if the difference could be explained by random fluctuations in the signal then switching the label (attended or non-attended) would make no difference to the result. For each time point in the averaged beta signal, we had a measure of beta amplitude in 46 individuals, 29 of whom had been scanned twice – therefore a total of 75 values of amplitude in the attended case, and 75 values in the non-attended case. We computed a t-statistic both with the correct labels, and with the labels randomly permuted across individuals. 100,000 iterations of this randomisation were undertaken and an empirical null distribution constructed. We then derived a p-value, per time point, via comparison of the t-statistic in the correctly labelled case, to the t-statistics in the null distribution. In order to correct for multiple

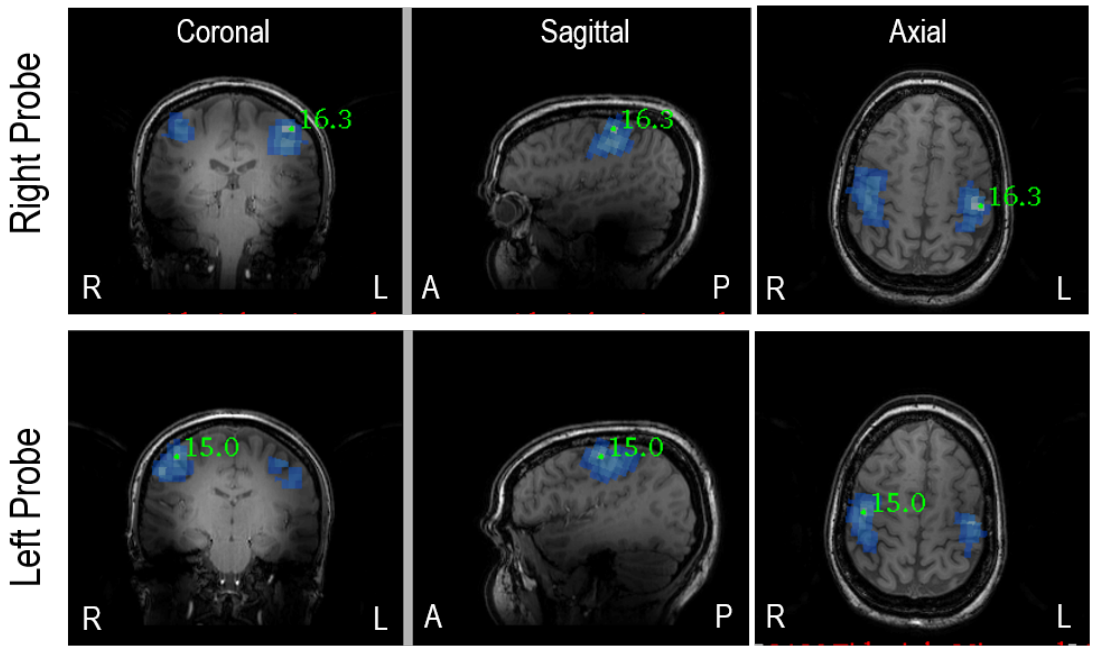



Figure 4.3: Individual psuedo T-Statistic map (derived with SAMMenu software (CTF)) contrasting the 0.1 - 0.5 s window relative to right (top row) or left (bottom row) probe presentation to the control window 13.5 - 16 s relative to trial start. The peak beta ERD are localised around the central sulcus (primary sensory/motor cortex) contralateral to probe presentation. ERD is also seen around the central sulcus ipsilateral to probe presentation.

comparisons across time points we used Bonferroni correction, where temporal degrees of freedom of the amplitude of a bandpass limited signal were computed as "time window" × "bandwith" = $1.1 \times (30 - 13) = 18.7$.[2]

### 4.3.2 Results

#### Beta amplitude modulation

Assessment of the spatial signature of beta modulation (Figure 4.3) showed that responses were localised to contralateral and to a lesser extent ipsilateral primary sensory cortex. Time frequency spectrograms (TFSs), showing modulation of oscillatory amplitude across frequency, were generated in left and right sensory cortex; these are shown in Figures 4.4 and 4.5, where red indicates an increase in oscillatory amplitude relative to baseline (i.e. beta amplitude during rest), and blue indicates a decrease. Figure 4.4 shows the TFS across the whole trial: in

[2]Derived from the Nyquist-Shannon theorem, see e.g. [Anderson and Johnnesson, 2006].

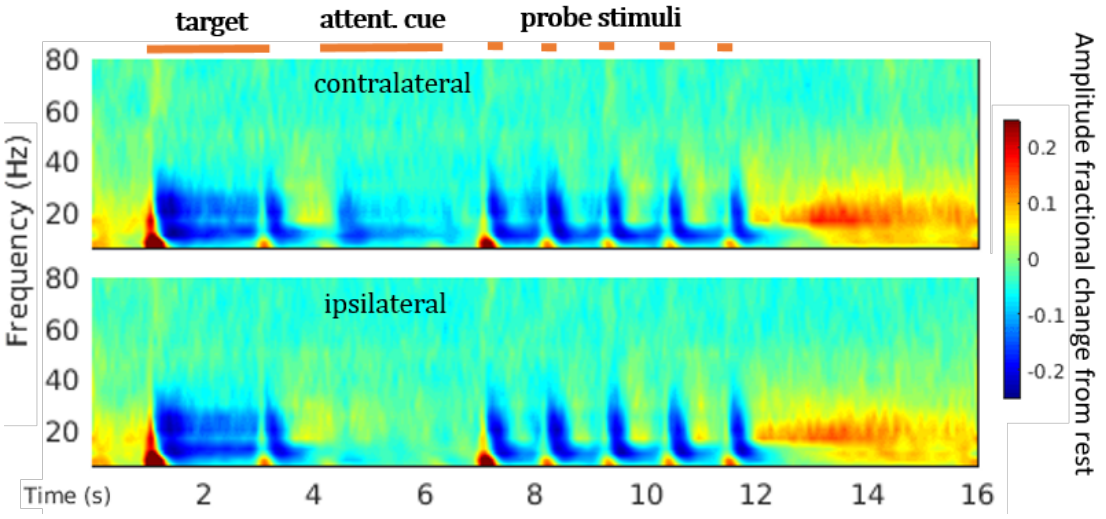



Figure 4.4: Average (n=75) TFSs extracted from primary somatosensory cortex; the upper panel shows responses contralateral to the attended hand; the lower panel show responses ipsilateral to the attended hand. Colourbar indicates fractional change from rest beta amplitude.

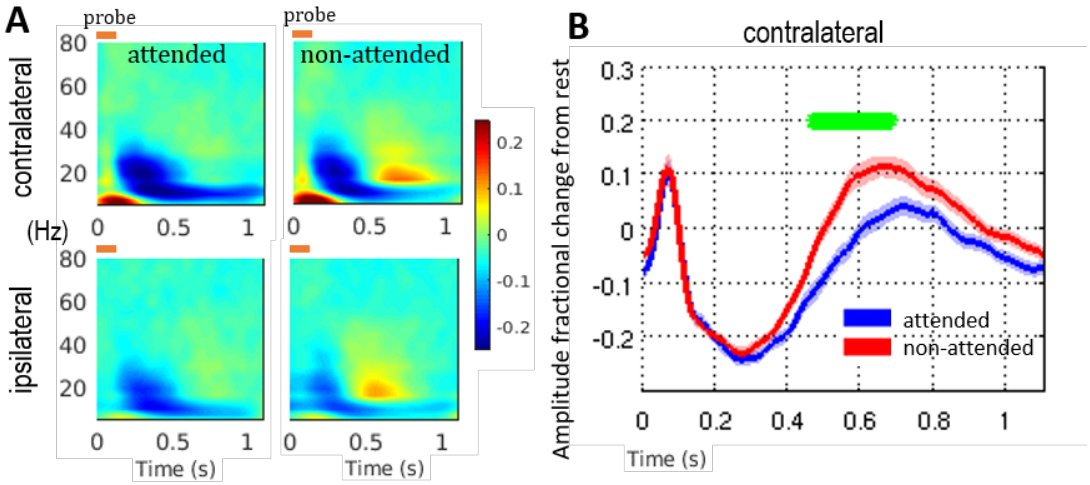



Figure 4.5: A) The 4 spectrograms show the average (n=75) contralateral (top panels) and ipsilateral (bottom panels) sensory cortex response to probe patterns. The left-hand plots show an average across probe stimuli presented to the attended hand; the right-hand plots shows unattended stimuli. Colourbar indicates fractional change from rest beta amplitude. B) Line graphs summarising the result in (A), for the contralateral cortex in the beta band only. Note the significant modulation of the beta rebound by attention (shaded areas correspond to standard error across subjects, green line indicates significant difference).

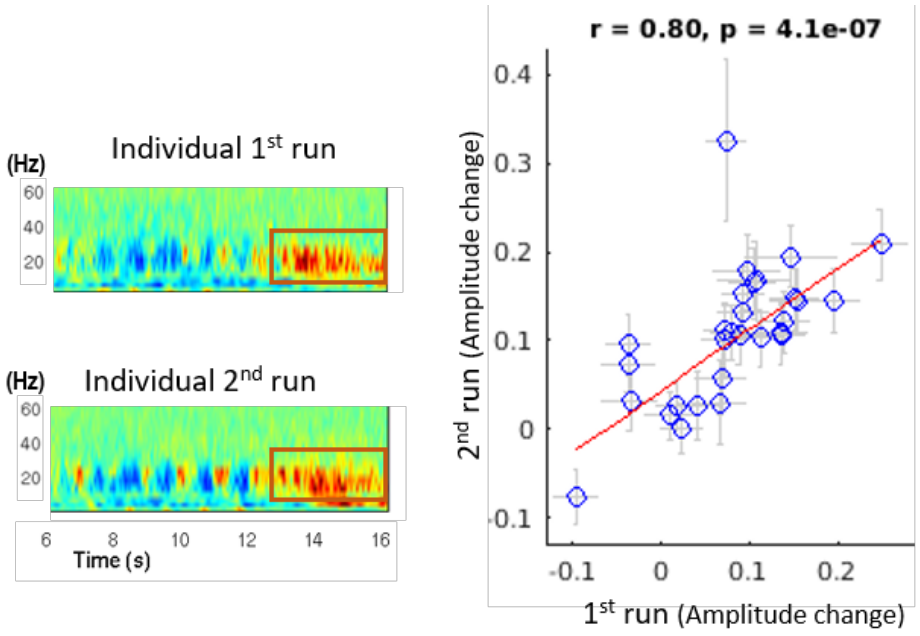



Figure 4.6: Beta rebound, measured in individual subjects across two runs – note the significant correlation showing that rebound amplitude is robust within subjects. Beta rebound is reported as fractional change from rest beta amplitude.

the upper panel, recall we have averaged responses contralateral to the attended hand (i.e. collapsing left sensory cortex when attending to the right hand, and the right sensory cortex when attending to the left hand). The lower panel shows the response ipsilateral to the attended hand. Notice that, in contralateral sensory cortex, the attentional cue generates a decrease in beta amplitude. Figure 4.5A shows responses to the probe patterns (i.e. non-target probes and excluding any button presses). The 4 individual TFSs were extracted from primary sensory cortex either contralateral (top panels) or ipsilateral (bottom panels) to the stimulated hand. The left-hand plots show an average over trials where stimuli were attended; the right hand plots shows unattended stimuli. Note the attentional modulation of the beta rebound which is diminished in the attended case. Figure 4.5B shows a line graph, summarising this result for contralateral cortex, and highlighting the significant ($p < 0.05$, corrected for multiple comparisons over time points) reduction of the beta rebound (in the 0.47 s to 0.67 s time window) following an attended stimulus.

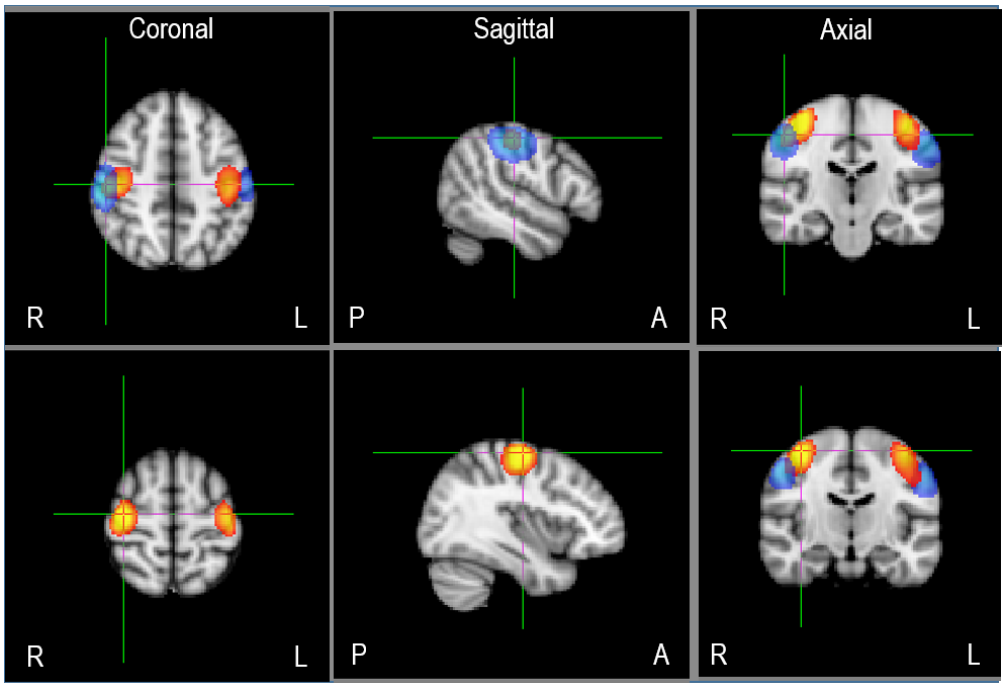



Figure 4.7: Average pseudo-T-Statistics maps of beta ERD (0.1 - 0.5 s window relative to right and left probe presentations) and beta rebound (13.5 - 16 s relative to trial start) contrasted to rest trials. Individual images have been transformed to MNI space using FLIRT and thresholded to show peak locations. The top row shows the view centred on the peak ERD, the bottom row shows the same map centered on the peak ERS (both in the right hemisphere). ERS appears localised superior and anterior compared ERD with the grand-average ERS-ERD peak distance being 19.39 mm and 21.26 mm in the right and left hemispheres respectively.

### Consistency of first and second run

In order to test the repeatability of the beta band findings, for the 29 people who were scanned twice, we plotted beta amplitude recording during run 1, against that recorded during run 2. Here, beta amplitude was measured in the 12.5 s to 16 s window relative to trial start. We computed Pearson correlation and the associated statistical significance. Figure 4.6 shows the beta rebound amplitude (measured in the 12.5 s - 16 s time window relative to trial start), for run 1 and 2 plotted against each other (i.e. each point represents a different subject). Note the highly significant ($p < 0.001$) correlation across subjects, showing that beta amplitude is a robust feature across scans in the same participant, even if data are acquired many months apart.

**Average T-stat maps**

To obtain average localisation maps pseudo-T-Statistics were calculated on a regular 2 mm grid spanning the entire brain space with a SAM beamformer implemented in Matlab. For visualisation individual images were transformed to MNI space using FLIRT [Jenkinson and Smith, 2001; Jenkinson et al., 2002; Greve and Fischl, 2009] and averaged across subjects. Average pseudo-T-Stat maps were constructed for different active and control windows in order to localise beta ERD following probe presentation (0.1 - 0.5 s window relative to probe presentation contrasted to equivalent rest window) and the beta rebound, seen most robustly at the end of each task trial (13.5 s $<$ t $<$ 16 s relative to trial start contrasted to equivalent rest window for beta rebound localisation). Figure 4.7 shows the results of the average pseudo-T-Stat maps: beta rebound localises forward, along the central sulcus, and higher compared to beta ERD in line with previous literature [Jurkiewicz et al., 2006].

### 4.3.3 Induced sensory Gamma

Sensory stimulation is known to induce high frequency gamma oscillations in addition to the lower frequency effects seen above [Bauer et al., 2006]. As activity in the gamma frequency range ($>$ 40Hz) is not noticeable in Figure 4.5 we ran a separate TFS analysis focused on the gamma band: covariance for the beamformer weights was calculated in the $40-150$ Hz frequency band and the source localised signal was successively filtered into a range of (50% overlapping) frequency bands. The resulting TFS presented in Figure 4.8A, show an increase in gamma power around stimulus presentation in contralateral sensory cortex. In order to better estimate gamma amplitude we calculated the beamformer weights in the $55-95$ Hz band (with an equivalent method to that used for Figure 4.5B). Figure 4.8B shows that gamma power in contralateral sensory cortex initially peaks at $\sim$ 70ms, followed by stronger peak at $\sim$ 150 ms relative to probe presentation. Attended stimuli also show an increase in gamma power lasting till $\sim$ 500ms relative to the

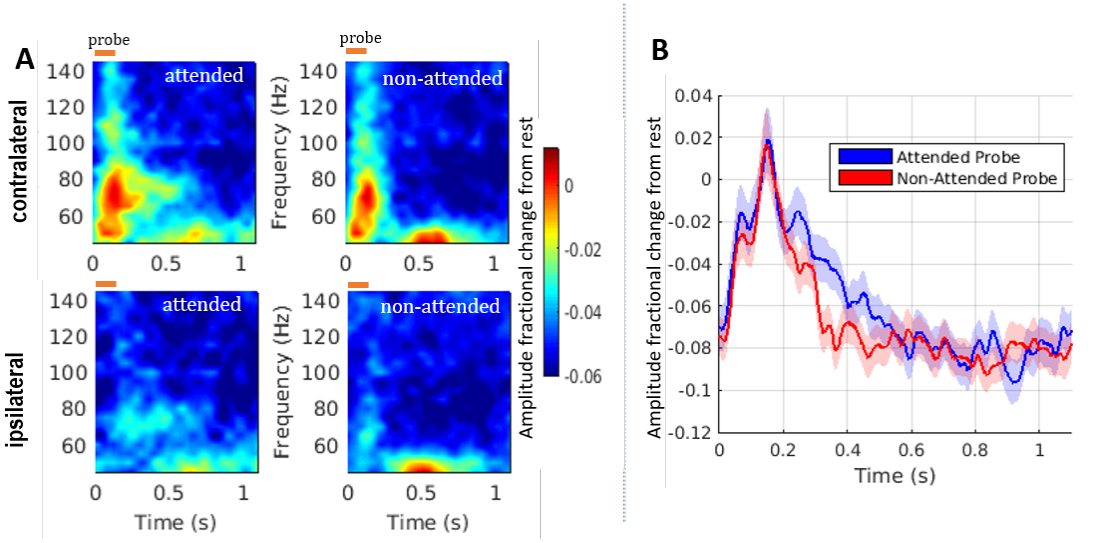



Figure 4.8: A) Average (n=75) contralateral (top panels) and ipsilateral (bottom panels) sensory cortex response to probe patterns in the gamma band ($40-150$ Hz). The left-hand plots show an average across probe stimuli presented to the attended hand; the right-hand plots shows unattended stimuli. B) Line graphs summarising the result in (A), for the contralateral cortex in the $55-95$ Hz band only. Shaded areas correspond to standard error over subjects.

0.6 - 1 s post-stimulus period, in line with the results by Bauer et al. [2006], although this attentional effect did not reach statistical significance when corrected for multiple comparisons. The increased low frequency gamma power at $\sim 0.5$ s in the non-attended condition is the high frequency end of the beta rebound (see Figure 4.5A). The average Gamma amplitude shows a modulation of only $\sim 10\%$ from rest gamma power. The gamma baseline during the task appears to be $\sim 8\%$ lower than the rest gamma power: this is probably because of increased movement and muscle artefacts during the rest period in between task trials.

## 4.4 Functional connectivity analysis

### 4.4.1 Methods

In order to estimate functional connectivity we reconstructed brain activity from 82 regions of interest determined by the Mars anatomical cortical atlas [Auzias et al., 2016]. Individual brain anatomy was downsampled to 2 mm resolution. The standard brain (MNI 152) was then warped to individual space, with the same

transform applied to the Mars atlas, in order to identify Mars cortical regions in native space. We aimed to generate a single electrophysiological signal from each region. To this end, sensor data were filtered to $1-150$ Hz and then a beamformer was applied. For each region, we identified a set of voxels (on a 2 mm grid) which belonged to that region (with $> 80\%$ probability). We then derived a beamformer reconstruction of the electrophysiological signal at each voxel (covariance computed in the $1 - 150$ Hz frequency range in a time window spanning the entire experiment; the resulting covariance matrix was regularised using the Tikhonov method with a regularisation parameter equal to 1% of the maximum eigenvalue of the unregularised matrix). These voxel timecourses were then collapsed into a single regional timecourse by taking the first principal component. This process was applied sequentially to all regions, yielding 82 separate regional signals.

[For comparison with the signal amplitude analysis, i.e. Figure 4.5, we calculated amplitude modulation following attended and non-attended probes in the 82 ROIs derived with the Mars atlas. These results are presented in appendix C.]

We sought to estimate functional connectivity between all possible region pairs using the Phase Difference Derivative methodology [Breakspear et al., 2004]. Phase Difference Derivative (PDD) assesses the extent to which the phase difference between two signals changes over time and yields a continuous connectivity time course (PDD is described in more details in section 2.3). PDD was selected after initial analysis showed it had the best sensitivity to detect attentional differences in this data set among a range of other phase and amplitude metrics (see Figure C.1 in appendix C).

Prior to connectivity estimation we first frequency filtered the source localised data in the beta band ($13 - 30$ Hz) and then corrected for spatial leakage. It is important to note that the source leakage problem is made more difficult because leakage can change in time [O'Neill et al., 2018], due to changes in signal amplitude. For this reason, orthogonalisation (where possible) should be applied

independently within the time windows in which connectivity is to be measured. With this in mind, for the leakage correction step, we concatenated beamformer projected data, extracted from the time window of interest, for the same condition over all trials, and applied pairwise orthogonalisation (as described in section 2.3.1) independently to these two conditions prior to PDD measurement. Following this, we extracted the phase of beta oscillation from the Hilbert transform of the leakage corrected time courses and estimated PDD for the attended and non-attended conditions (non-target probes, excluding any button presses).

Finally, we aimed to statistically test for differences in functional connectivity between attended and non-attended conditions, in the post stimulus (i.e. beta rebound) period. We selected the 0.4 s $<$ t $<$ 1.0 s window relative to the presentation of the probe stimulus, such that it followed the maximum beta ERD and encompassed the whole rebound period (as seen from the TFS analysis in Figure 4.5). We estimated PDD for the attended and non-attended conditions and ran a permutation test, as described above, to test statistical significance. In order to correct for multiple comparisons across the 3321 region pairs, we applied a false discovery rate correction [Benjamini and Hochberg, 1995].

### 4.4.2 Effect of attention on connectivity

In Figure 4.9, the left panel shows time courses of connectivity strength, measured between the right somatosensory cortex and the rest of the brain, following left hand stimulation (PDD time courses were smoothed with the moving average method with a span of 50 points, equivalent to 83 ms). The blue line shows attended stimuli, whilst the red line shows unattended stimuli. The right panel shows the equivalent graph, for right hand stimulation and left sensorimotor cortex connectivity. In both cases, the result shows a transient difference in functional connectivity, driven by attention, with inattention supported by a connectivity increase. In order to elucidate the spatial signature of the network driving these

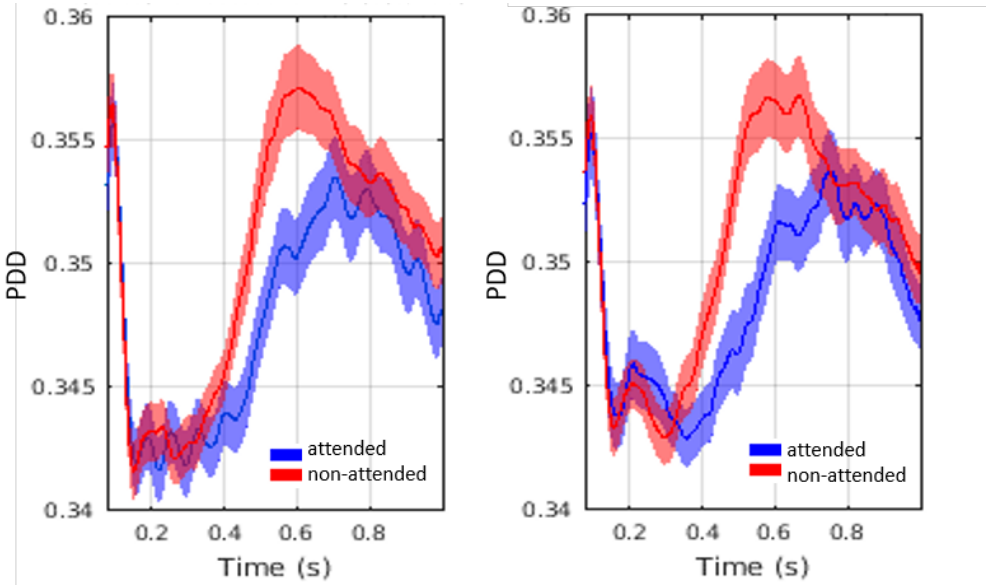



Figure 4.9: Time courses showing modulation of functional connectivity between contralateral primary sensory cortex and the rest of the brain, during presentation of a probe stimulus; the right plot shows right hand stimulation (seed in left S1) and the left plot shows left hand stimulation (seed in right S1). In both cases the blue line shows the average across attended stimuli whereas the red line shows the average of unattended stimuli. Shaded regions correspond to standard error over subjects.

differences, we calculated which of all of the possible connections in the brain are significantly affected by attention.

The matrix in Figure 4.10A shows mean PDD between all possible pairs of brain regions, in the 400 ms to 1000 ms time window following presentation of each probe pattern (note that the window was chosen to include the whole beta rebound and we have collapsed across all stimuli, regardless of stimulated hand or attention). In the 'brain plot', the line thickness and colour represent connectivity strength between regions, and the highest 15% of connections are shown. Note that, in agreement with previous work [Hunt et al., 2016], beta connectivity is dominated by posterior parietal and occipital networks. In Figures 4.10B and 4.10C, the matrices show attentionally modulated differences in connectivity, measured for all region pairs. In the brain plots, the lines show the individual connections that demonstrate a significant ($p < 0.01$ corrected for multiple comparisons using FDR correction across all possible region pairs) difference in

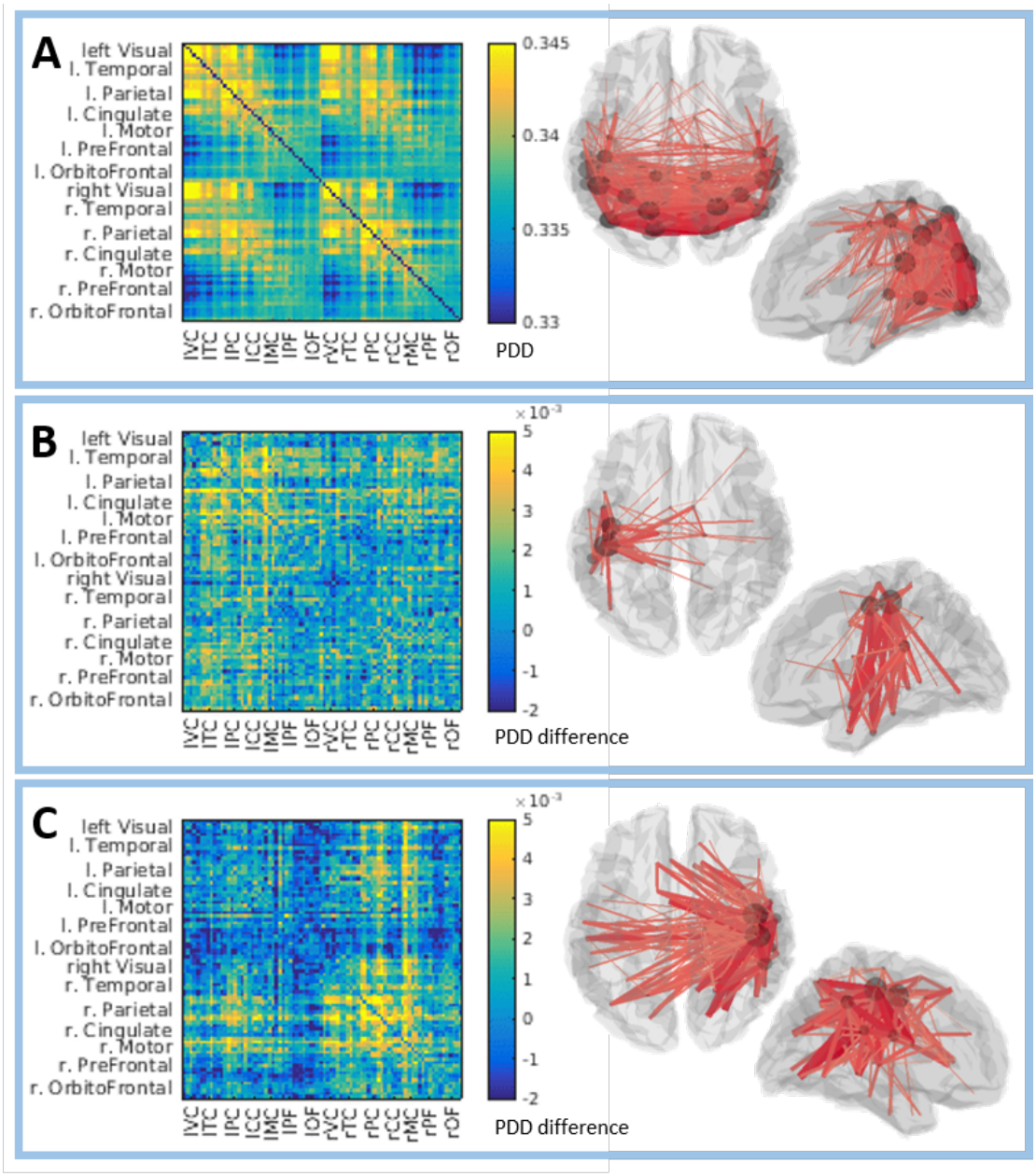



Figure 4.10: Functional connectivity is modulated by attention: A) averaged connectivity matrix showing the dominant beta band mediated connections in the 400 ms to 1000 ms time window following presentation of the probe patterns (results collapsed across left- and right-hand stimulation and left and right attentional cues). B) Whole brain connectivity difference between unattended and attended (i.e. unattended - attended) stimuli for right hand stimulus presentation (400-1000 ms after probe). The matrix shows connectivity difference for all region pairs, and the brain plot shows the connections that modulate significantly with attention. C) equivalent to (B) but for left hand stimulus presentation. Note that, similar to oscillatory amplitude, connectivity is significantly modulated by attentional mechanisms with a sensorimotor network forming and dissolving in the case of an unattended stimulus.

connectivity strength; the grey circles show the brain regions whose connectivity strength is most affected. Figure 4.10B shows the case for right hand stimulation whilst Figure 4.10C shows the case for left hand stimulation. Note that the modulated networks are centred on primary sensorimotor cortex, with projections to frontal regions (e.g. supplementary motor area), ipsilateral sensorimotor regions, posterior parietal and temporal regions, including the secondary somatosensory area. These widespread networks are significantly more engaged (i.e. connected) during periods of in-attention suggesting that they play an inhibitory role.

Connectivity strength closely follows the modulation of signal amplitude in the sensorimotor cortex (Figure 4.5). While oscillatory amplitude and connectivity have been shown to be dependently linked (see the simulation work by Tewarie et al. [2018]), it is possible to detect an increase in connectivity merely by an increase in SNR of the underlying signal [Bastos and Schoffelen, 2016]. In order to check for this confound we calculated the correlations between average beta amplitude (representative of SNR in each in ROI) over the beta rebound period (400-1000ms) and PDD strength over the same time window. Pearson correlations between all 82 ROIs showed no significant correlations between the average beta amplitude in each ROI and the estimated connectivity strength from that same ROI to the rest of the brain (Figure 4.11A). As beta amplitude can vary between subjects we also calculated correlations between the beta rebound amplitude in left sensorimotor cortex of each subject and their corresponding connectivity strength from left sensorimotor cortex to the rest of the brain. No correlation between individual beta amplitude and PDD strength was observed (Figure 4.11B) indicating that connectivity differences cannot be entirely explained by variation in the SNR of the underlying signal.

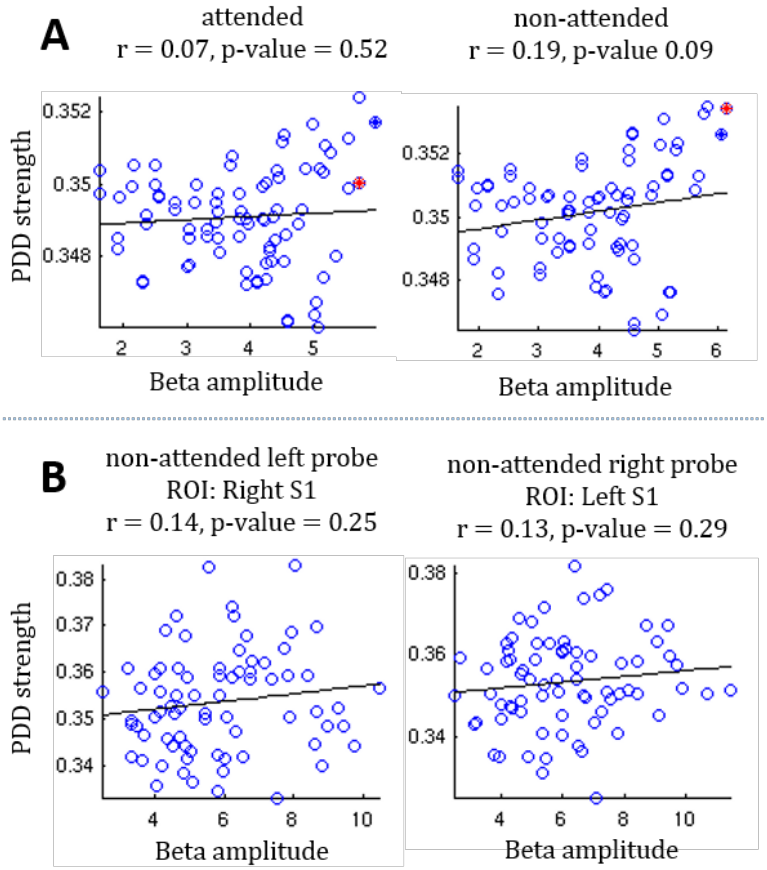



Figure 4.11: A) Correlations of Beta amplitude in each ROI and connectivity (PDD) strength from that ROI to the rest of the brain, averaged over all subjects (n=75) and over the beta rebound window, $0.4 - 1$s from stimulus presentation. Correlations were estimated through Pearson correlation. The plot on the left hand side shows the correlation for attended probe stimuli; on the right it the same for non-attended stimuli. Each dot in the graph corresponds to a separate ROI, with the filled dots indicating primary sensory cortex, contralateral (red) and ipsilateral (blue) to the probe stimuli (right and left probes have been averaged together). The average beta amplitude in each ROI does not significantly correlate with connectivity strength. B) Correlations of Beta amplitude in primary sensory cortex (S1) and connectivity (PDD) strength from that ROI to the rest of the brain, averaged over the beta rebound window, $0.4-1$ s following the presentation of a non-attended probe. Here each dot corresponds to a separate subject. The graph on the left shows right S1 for a non-attended probe to the left index finger. The graph on the right shows the equivalent case for left S1 and a non-attended right probe. We found no correlation between individual beta amplitude in S1 and PDD strength over the beta rebound period.

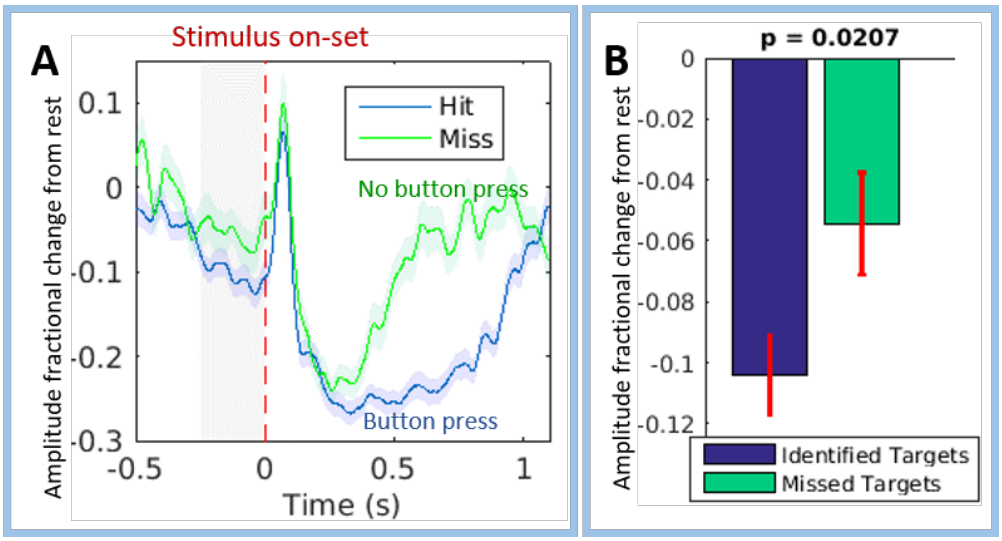



Figure 4.12: Behavioural correlates of beta amplitude. A) Average beta amplitude during presentation of a target stimulus in contralateral primary sensory cortex. Target presentation was at time zero. Correctly identified (Hit) targets are shown in blue, missed targets in green. Blue and green shaded regions indicate standard error over subjects. Grey shaded region indicates the 250 ms preceding target presentation. Note that the prolonged beta desynchronisation for Hit targets is caused by the motor response (button presses), which is absent for Missed targets. B) Beta amplitude averaged over the 250 ms preceding a correctly identified or missed target. Error bars correspond to standard error over subjects.

## 4.5 Likelihood of correct responses

We aimed to test for significant differences in both beta amplitude, and connectivity, between target stimuli that were correctly identified (hits) and incorrectly missed (misses). In order to do this we first identified hit and miss trials and averaged beta amplitude, in contralateral sensory cortex, for these two trial types. We then averaged beta amplitude over time, in the 250 ms preceding target presentation, and tested for differences using our permutation test method. In addition, we measured PDD strength in the primary contralateral sensory cortex as a function of time (i.e. strength here represents connectivity between primary contralateral sensory cortices and all other regions), again independently for hits and misses. We averaged these strength metrics in the 250 ms preceding target presentation, and tested for differences between hit and miss trials.

### 4.5.1 Behavioural results

Target braille patterns were identified correctly with $67 \pm 17\%$ accuracy (mean $\pm$ standard deviation over subjects). The average reaction time was $562 \pm 84$ ms (mean $\pm$ standard deviation) which is in line with previous literature [Bauer et al., 2006]. We found no significant difference in accuracy or reaction times for right- or left-hand targets. Given the putative inhibitory nature of beta oscillations, we reasoned that a high pre-stimulus beta amplitude would result in a lower behavioural accuracy, and to test this we separated correctly identified and missed targets, and computed beta amplitude averaged over these trials. Figure 4.12A shows a time course of beta amplitude in contralateral sensory cortex throughout the presentation of target braille patterns. Correctly identified patterns are shown in blue, missed targets in green. The bar plot in Figure 4.12B shows the mean beta amplitude in the 250 ms preceding stimulus presentation in contralateral sensory cortex. In agreement with our hypothesis, a significantly ($p = 0.02$) lower beta amplitude (lower inhibition) results in a better chance of successful target identification. We extended this finding, testing the hypothesis that long-range connectivity would also be lower in successfully identified (compared to missed) target trials. Figure 4.13A shows the spatial topography of the connectivity strength in the 250 ms window preceding target presentation. The bar plot in Figure 4.13B shows the mean functional connectivity between contralateral sensory cortex and the rest of the brain, in the 250 ms preceding a target stimulus presentation, for correctly identified and missed targets. Mirroring the amplitude result, missed targets tended to be associated with significantly ($p = 0.014$) higher levels of connectivity. The spatial topography of the difference in connectivity strength between a Missed and a Hit target is shown in Figures 4.13C and D for a right and left target respectively.

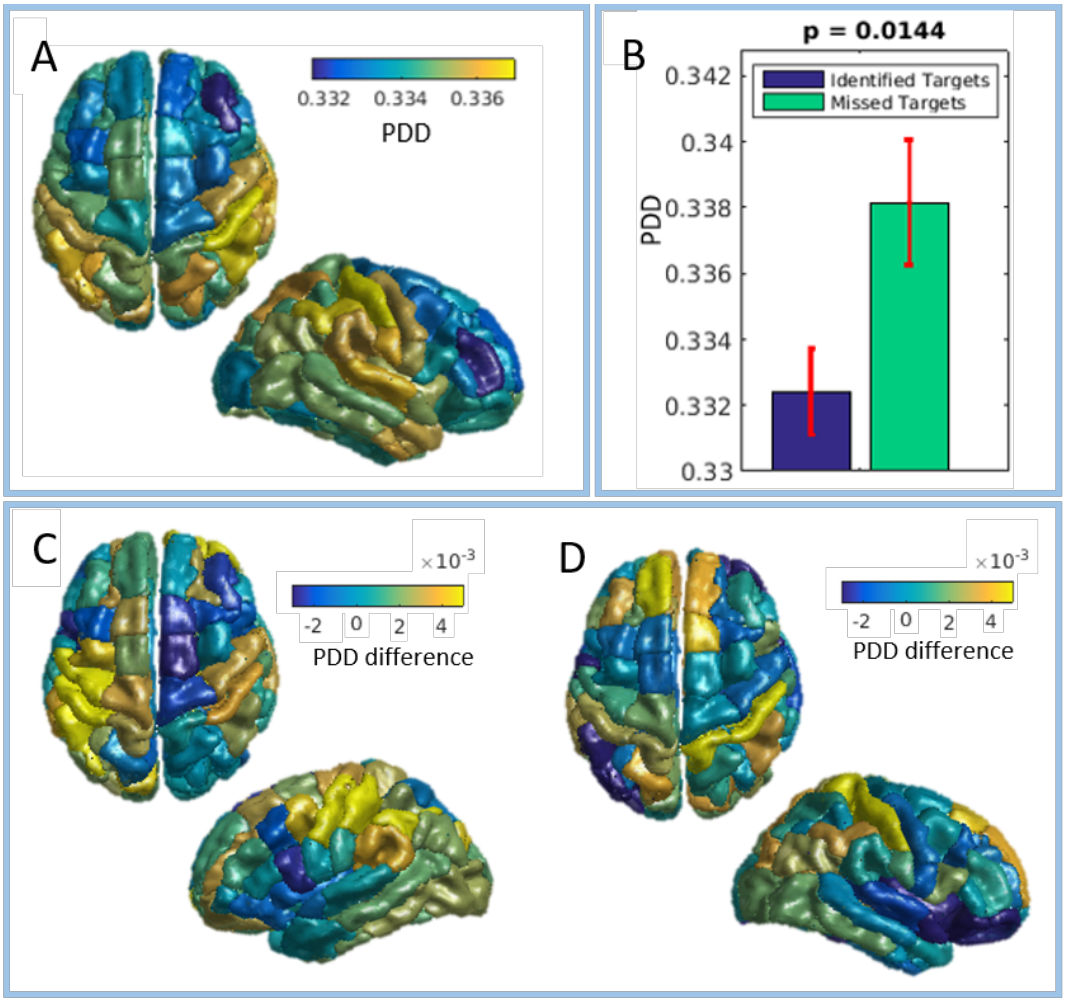



Figure 4.13: Behavioural correlates of beta connectivity. A) Spatial topography of the average connectivity strength in the 250 ms window preceding target presentation; notice a focus on parietal and primary sensory cortices. B) Functional connectivity between contralateral sensory cortex and the rest of the brain, again averaged in the 250 ms window preceding the target presentation. Error bars correspond to standard error over subjects. C) Spatial topography of the difference (Miss target - Hit target) in connectivity strength in the 250 ms window preceding a right target presentation; notice that beta connectivity in left parietal and primary sensory cortices (contralateral to the target) is stronger preceding a missed target. D) Same as C) but for a left target presentation; this time the maximum difference is on the right primary sensory cortex, again contralateral to the incoming target.

## 4.6 Discussion

Our data on beta amplitude modulation with the sensory attention task (Figure 4.5) show that inattention to a stimulus results in an earlier and stronger beta rebound, compared to attended stimuli, and this is in strong agreement with previous work [Bauer et al., 2006, 2012]. While desynchronisation of beta power following sensory stimulation of the index finger was localised to the hand area of the primary sensory cortex, beta rebound localised to the hand area of the primary motor cortex (see Figure 4.7) in agreement with previous observations by Jurkiewicz et al. [2006]. Our analysis found that stimulus presentation was also associated with increased gamma power in contralateral primary sensory cortex, showing longer duration in attended stimuli, up to $\sim$ 500ms from stimulus on-set (Figure 4.8). This result, in agreement with Bauer et al. [2006] support the notion that gamma oscillations have a feed-forward role in the brain cortex opposite to lower frequency oscillations.

The observed attentional modulation of the beta rebound supports the idea that the rebound itself is actively forcing a "shut-down" of processing in the primary somatosensory area, in order to re-establish a 'status quo' (or resting state) and prevent feed forward of information to other areas of the sensory processing hierarchy. In order to understand how high oscillatory amplitude might promote inhibition, we first point out that the information processing capacity of a neural assembly is reduced when cells are forced to fire in synchrony, and enhanced when cells are allowed to fire independently. Indeed this idea is the basis of a number of methods which use neural network entropy (or complexity) to measure information encoding rates [Brookes et al., 2015]. Another way of thinking about this is, if one wanted to ensure shutdown of active processing within a neural network, one way to do it would be to drive all the cells into synchrony such that they lose their capacity to encode information. This notion is supported by our experimental observation; when attention is directed away from a stimulus, the primary

sensory cortex is placed in a state in which there is a significantly greater likelihood of cells firing in concert, and consequently a lower likelihood of processing information [Jensen and Mazaheri, 2010].

Our functional connectivity analysis, for the first time, sheds some light on the mechanism of how this 'shut-down' comes about. Our connectivity results (Figures 4.10 and 4.9) show that high levels of phase synchrony, between the primary sensory cortex and a broader network, underlies the beta rebound. The broader network captures a number of brain regions including bilateral sensorimotor cortices, supplementary motor area, and temporal regions including the secondary somatosensory area. These areas are consistent with the sensorimotor resting state network [Biswal et al., 1995], which is known to be supported by beta band oscillations [Brookes et al., 2011b; Hipp et al., 2012]. A limitation of the present findings is that directionality of information flow within the transient networks shown in Figure 4.10 is unknown, and therefore it is impossible to say from these data whether primary sensory cortex drives, or is driven by, the broader network. However, the communication by coherence hypothesis posits that phase locked oscillations provide optimum windows for the passage of action potentials. It is therefore tempting to speculate that if multiple regions transiently fire phase locked volleys of action potentials, this will drive a phase locked rhythm at the targeted area, in this case the primary sensory cortex. This imposed synchrony would generate the well-known beta rebound in sensory cortex, removing its ability to encode information and initiating a shut-down of local processing. This simple mechanistic interpretation of the rebound, which is perhaps best thought of as 'inhibition by coherence', suggests that the beta signal could carry a top-down influence on primary cortical areas, also in line with the known layer-specific profile [Buffalo et al., 2011]. Here, using highly temporally resolved functional connectivity metrics, we have been able to image this influence directly.

Though speculative and simplified, our interpretation offers a model of beta

oscillations which helps to explain previous work. A number of papers have shown that resting state networks, including the sensorimotor network, can be imaged via measurement of beta band oscillations [Brookes et al., 2011b]. A popular approach to revealing these networks is measurement of amplitude envelope correlation [Brookes et al., 2011b,a; Hipp et al., 2012] whereby one seeks statistically significant correlation between spatially separate regions, across a long time window (usually many minutes) as was also the case for the work presented in chapter 3. Our finding in this paper suggests that the beta envelope signals themselves fluctuate because of transient periods of inhibition, which come and go over time, and involve long range phase synchrony. So it is not surprising that time averages see significant correlation between signals derived from the nodes of canonical networks. The importance of understanding beta oscillations is further underlined by the results showing a link between oscillatory amplitude and behaviour. Previous studies [Jones et al., 2010] have demonstrated that a higher pre-stimulus beta power is associated with poorer task performance. Our results agree by showing that in trials where the subject correctly recognised a target braille pattern, they had significantly lower pre-stimulus beta amplitude compared to trials in which they incorrectly failed to recognise a target. We take this observation further by showing, for the first time, significant modulation of connectivity, with higher connectivity relating to lower success rate. This is broadly consistent with the theory posited above that high beta power denotes cells being driven into a state in which their capacity to encode information is limited.

# Appendix C

# Further Atlas Based Analysis

Figure C.1 shows beta band functional connectivity computed in the $0.4 - 1$ s window following a left hand probe (equivalent to the matrix plots in Figure 4.10) for 5 different connectivity metrics. Though the connectivity metrics show similar spatial topography, PDD was the least noisy and was the only metric to show significant connectivity changes with attention.

In the main analysis we obtained separate broadband ($1-150$ Hz) time courses for each of the 82 ROIs of the Mars cortical atlas. Each time course can be further filtered in a frequency band of choice and its band limited oscillatory amplitude calculated as was done for the voxel based analysis presented in Figure 4.5B. Figure C.2A shows whole brain amplitude changes in the beta band following attended (left column) and non-attended (right column) probes. The y-axis corresponds to the ROI locations with the contralateral and ipsilateral hemispheres presented in separate panels (top and bottom respectively); the x-axis indicates time following probe presentation ($0 - 1.1$s). Primary sensory and primary motor cortices show the strongest beta rhythm changes in agreement with the single voxel analysis. Figure C.2B shows PDD strength time courses, equivalent to Figure 4.9, but for all ROIs and averaging over right and left hand probes. Figures C.3 to C.6 show other frequency bands. Results are averaged over all subjects.

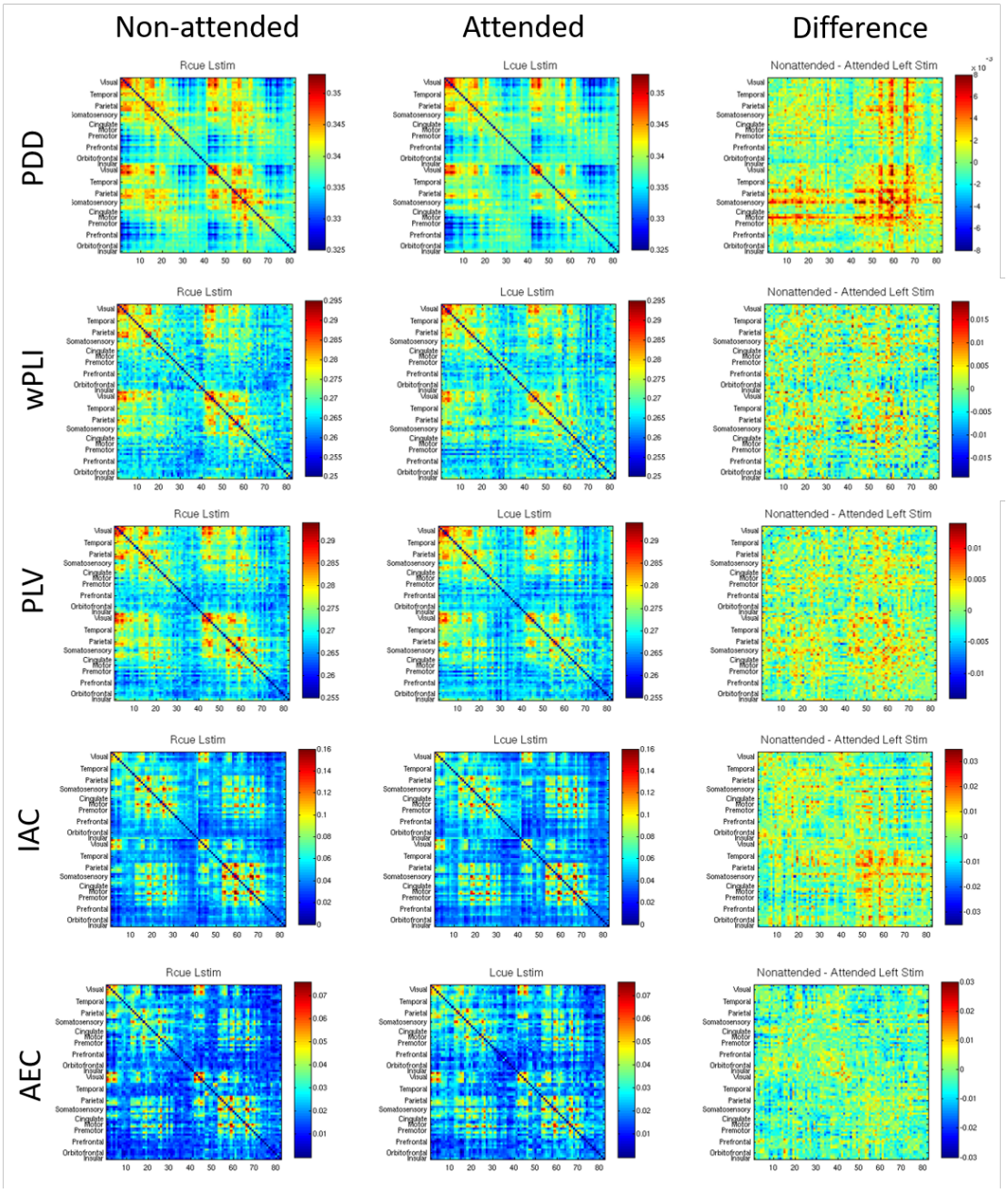



Figure C.1: Beta band functional connectivity calculated in the 0.4-1s window following a left hand probe. The three columns (from left to right) show connecitvity matrices for a non-attended stimulus, an attended stimulus and the differnce between the two (non-attended minus attended). Analysis shows average FC over all subjects, first and second run (n=75). All metrics (with the exception of wPLI) were calculated following pairwise leakage correction as described in chapter 4. Note the similar topography of all phase metrics (PDD, wPLI, PLV) and the two amplitude metrics (AEC and IAC, i.e. instantaneous amplitude correlation [Tewarie et al., 2019]). Only PDD showed significantly different edges surviving multiple comparisons correction.

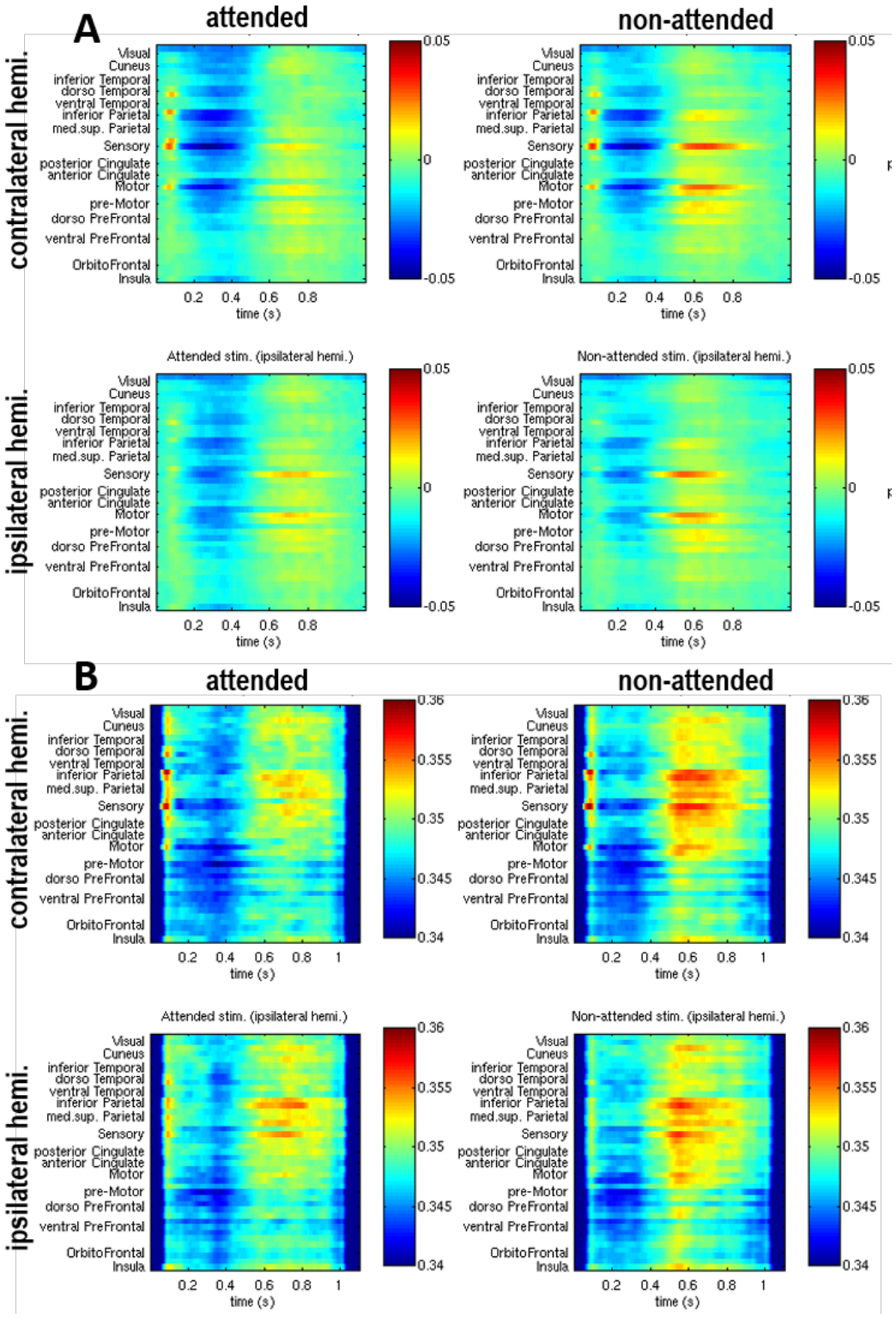



Figure C.2: **Beta band (13−30Hz)** whole brain analysis based on the Mars atlas. Each panel refers to probe presentation (t=0s), averaging over left and right hand probes, and separating attended (left column) and non-attened (right column). A) Beta amplitude (as fractional change from rest) in all ROIs; B) PDD strength time courses (average connectivity from seed ROI to all other 81 ROIs). PDD is smoothed with a moving average method with a span of 50 points, i.e. 83 ms.

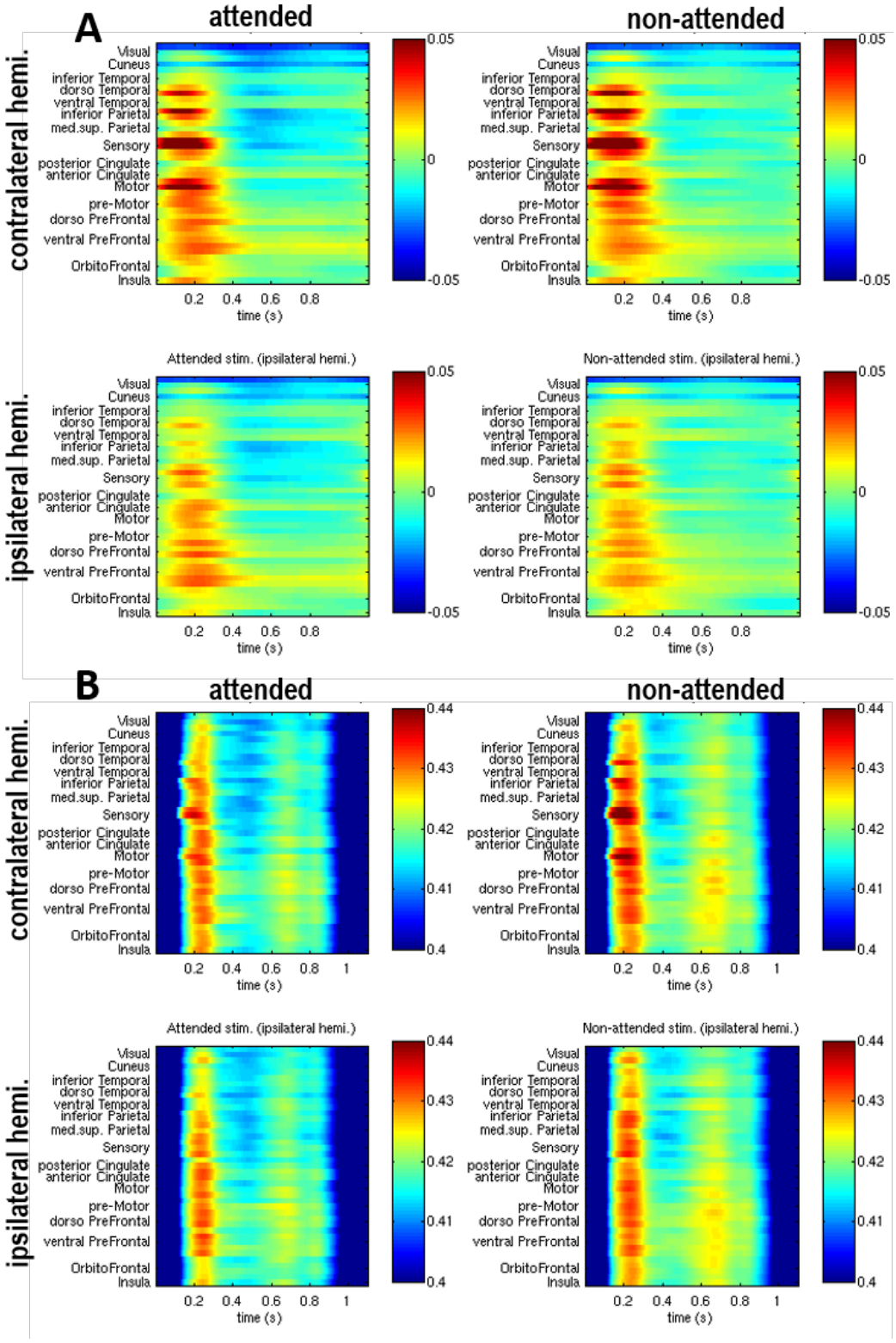



Figure C.3: **Theta band (4−8Hz)** whole brain analysis based on the Mars atlas. Each panel refers to probe presentation (t=0s), averaging over left and right hand probes, and separating attended (left column) and non-attened (right column). A) Theta amplitude (as fractional change from rest) in all ROIs; B) PDD strength time courses (average connectivity from seed ROI to all other 81 ROIs). PDD is smoothed with a moving average method with a span of 100 points, i.e. 167 ms.

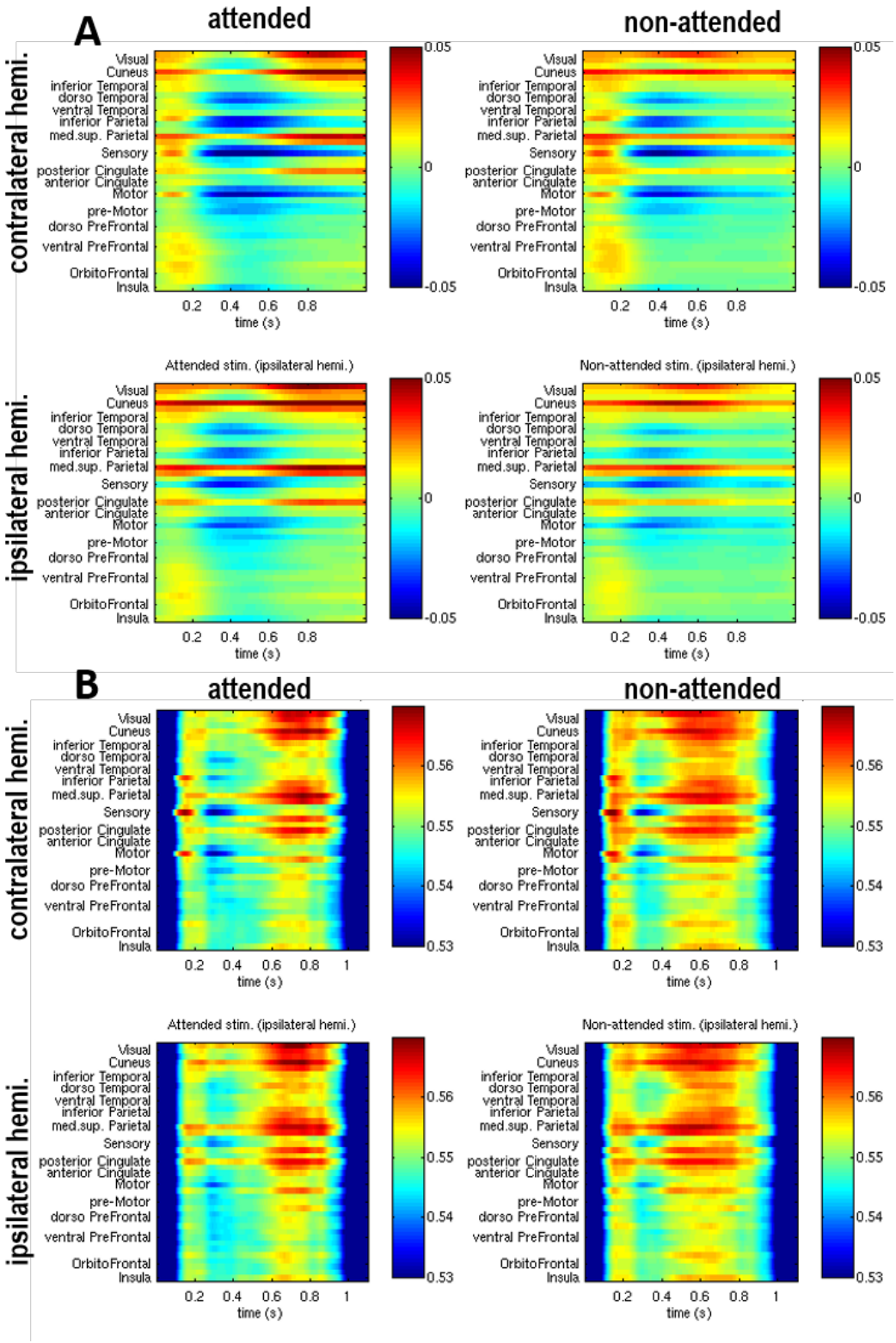



Figure C.4: **Alpha band (8−13Hz)** whole brain analysis based on the Mars atlas. Each panel refers to probe presentation (t=0s), averaging over left and right hand probes, and separating attended (left column) and non-attened (right column). A) Alpha amplitude (as fractional change from rest) in all ROIs; B) PDD strength time courses (average connectivity from seed ROI to all other 81 ROIs). PDD is smoothed with a moving average method with a span of 57 points, i.e. 95 ms.

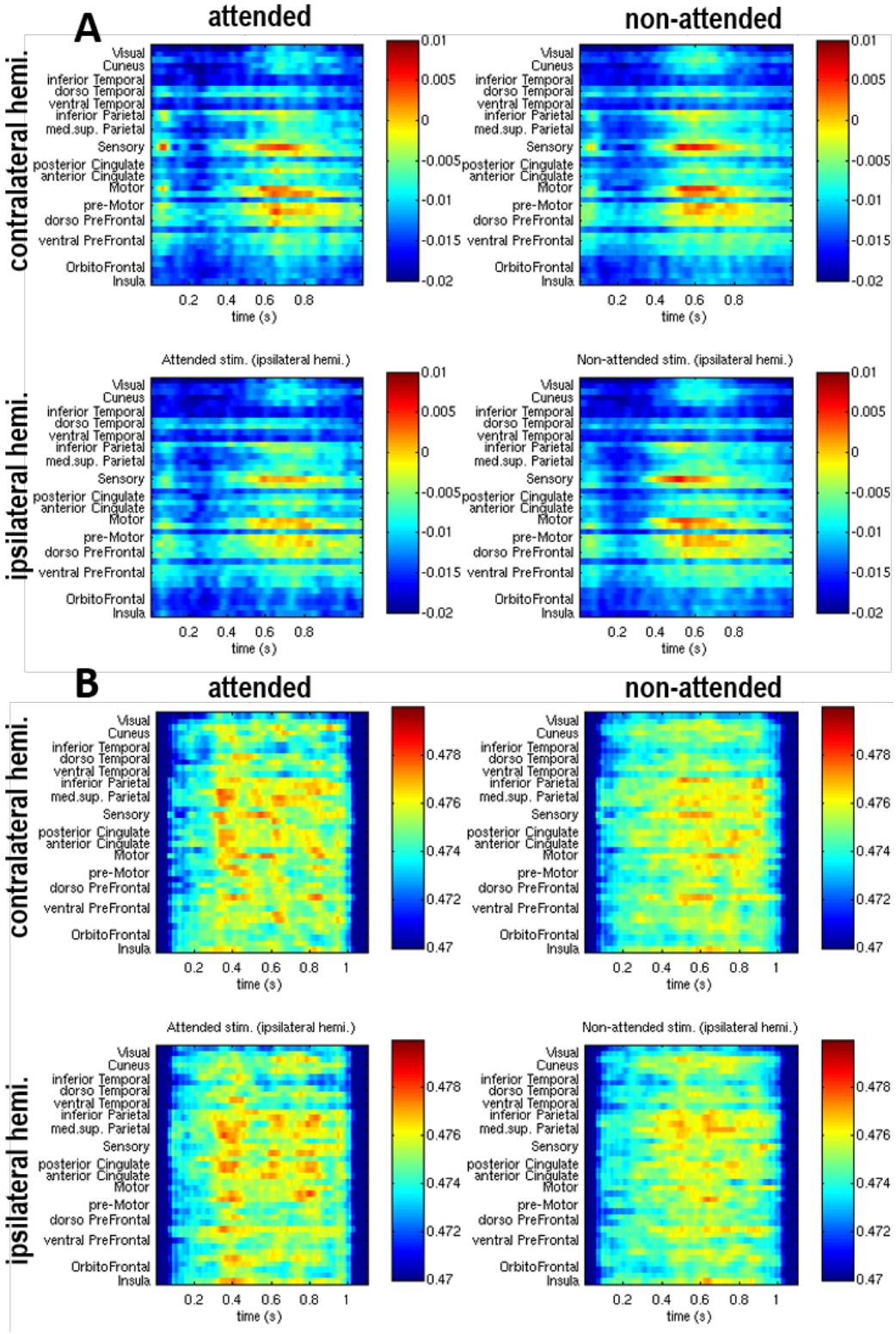



Figure C.5: **Low gamma (30−48Hz)** whole brain analysis based on the Mars atlas. Each panel refers to probe presentation (t=0s), averaging over left and right hand probes, and separating attended (left column) and non-attened (right column). A) Gamma amplitude (as fractional change from rest) in all ROIs; B) PDD strength time courses (average connectivity from seed ROI to all other 81 ROIs). PDD is smoothed with a moving average method with a span of 50 points, i.e. 83 ms.

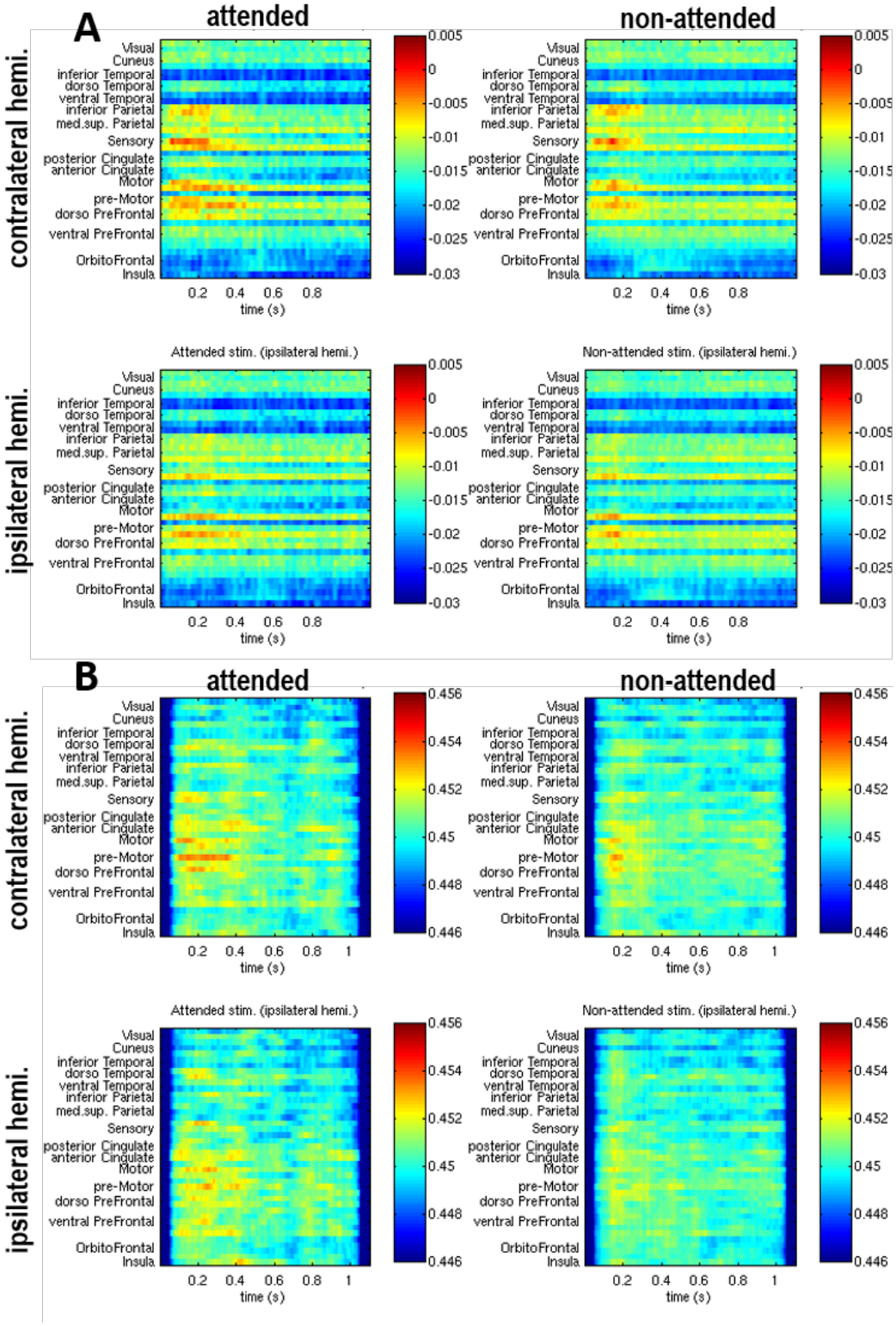



Figure C.6: **High gamma (55−90Hz)** whole brain analysis based on the Mars atlas. Each panel refers to probe presentation (t=0s), averaging over left and right hand probes, and separating attended (left column) and non-attened (right column). A) Gamma amplitude (as fractional change from rest) in all ROIs; B) PDD strength time courses (average connectivity from seed ROI to all other 81 ROIs). PDD is smoothed with a moving average method with a span of 50 points, i.e. 83 ms.

# Chapter 5

# Neurotransmission and beta band oscillations

In this final experimental chapter we collected proton MR spectra in the same cohort of participants who took part in the MEG study presented in chapter 4. GABA and other metabolite concentrations in the sensorimotor cortex were quantified using a STEAM sequence acquired at rest using a 7T MR system. In the first half of this chapter we will cover the basis of Magnetic Resonance Spectroscopy (MRS). The second part of the chapter is dedicated to the experimental acquisition of the MRS data, spectral analysis and the results, which show a significant correlation of individual GABA concentration to beta rebound and resting state beta amplitude in 43 subjects.

## 5.1 Introduction

The 'inhibition hypothesis' of beta oscillations (explored in the previous chapter through the attentional modulation of the beta rebound and functional connectivity analysis) is more directly supported by links to the principal cortical inhibitory neurotransmitter, Gamma-aminobutyric acid (GABA). For example, Jensen et al. [2005] showed that beta amplitude is increased by administration of the GABAergic agonist benzodiazepine. Hall et al. [2011] showed that increased GABAergic drive, facilitated by diazepam, also altered beta modulation. Muthukumaraswamy et al. [2013] used tiagabine to block presynaptic GABA re-uptake (and consequently increase tonic GABA), and this caused an enhancement of baseline beta amplitude. These studies show that beta oscillations can be systematically modulated via pharmacological manipulation of GABA. In a recent study [Gaetz et al.,

2011], the authors attempted to provide a more direct link between GABA and beta oscillations, by measuring a relationship between resting GABA level, measured using magnetic resonance spectroscopy (MRS) and beta rebound amplitude. Their work suggested that individuals with higher resting GABA tended to have a higher beta rebound. However, this study had the potential shortcoming of a small sample size (n=9); this is important since a previous study linking MRS and oscillatory measurements [Muthukumaraswamy et al., 2009] using a similar sample size (n=12) was not supported when employing a larger cohort (n=50) [Cousijn et al., 2014]. Direct experimental evidence for a correlation between inter-individual differences in GABA level and beta oscillations therefore remains controversial. In this final experimental chapter we attempt to bridge the gap between the functional role of beta oscillations and their possible link to synaptic transmission and neurochemistry. In the same group of participants who took part in the MEG sensory attention experiment described in chapter 4, we measured GABA concentration in the left sensorimotor cortex through Magnetic Resonance Spectroscopy (MRS).

## 5.2 MR Basics

The nuclear magnetic resonance (NMR) phenomenon, discovered independently by physicists Edward Purcell and Felix Bloch in 1946, is based on the intrinsic spin property of nuclei in a strong external magnetic field and their interaction with resonant electromagnetic pulses [Bloch, 1946; Purcell et al., 1946]. Only atomic nuclei with spin $I \neq 0$ can be studied with NMR. The spin quantum number, $I$ depends on the number of protons and neutrons in a nucleus and can take integer or half-integer values. Protons and neutrons are both fermions (with half-integer spin) that form pairs of opposing spins according to the Pauli exclusion principle. Therefore the total spin of an atomic nucleus is given by the unpaired protons and neutrons in the nuclear energy levels:

- atoms with an odd number of protons and odd number of neutrons have non-zero integer spin (1 unpaired proton and 1 unpaired neutron), e.g. $^{14}$N;
- nuclei with either an odd number of protons or an odd number of neutrons have half-integer spin, e.g. $^{1}$H and $^{13}$C with $I = 1/2$;
- nuclei with an even number of both protons and neutrons have zero spin, $I = 0$ (all protons and neutrons are paired), e.g. $^{12}$C.

In medical imaging we are usually interested in biologically abundant non-zero spin nuclei such as $^{1}$H, $^{13}$C, $^{31}$P, $^{23}$Na and $^{39}$K.

The spin quantum number is related to the spin angular momentum $\mathbf{J}$:

$$|\mathbf{J}| = \hbar\sqrt{I(I+1)}, \tag{5.1}$$

with $\mathbf{J}$ pointing along the rotation axis of the nucleus, and a magnetic dipole moment $\boldsymbol{\mu}$

$$\boldsymbol{\mu} = \gamma\mathbf{J} \tag{5.2}$$

dependent on the gyromagnetic ratio $\gamma = q/(2m_p)g$, where $q$ is the charge of nucleus, $m_p$ is the mass of the proton, and $g$ is the g-factor. From quantum mechanics the spin angular momentum can only have $(2I+1)$ possible orientations with quantum number $m = -I, -I+1, \ldots, I-1, I$ (e.g. spin $I = 1/2$ nuclei therefore have two possible orientations with $m = \pm 1/2$). In this chapter we will consider hydrogen $^{1}$H (or proton) NMR: $^{1}$H magnetic resonance forms the basis of most Magnetic Resonance Imaging (MRI) and Magnetic Resonance Spectroscopy (MRS) thanks to its high natural abundance, its high concentration in the human body and high gyromagnetic ratio ($\gamma = 42.576$ MHzT$^{-1}$).

### 5.2.1 Interaction with a static magnetic field

In the classical physics description, when a magnetic field $\mathbf{B}_0$ is applied to a nucleus, its intrinsic dipole moment will experience a torque $\boldsymbol{\tau} = \boldsymbol{\mu} \times \mathbf{B}_0$ trying

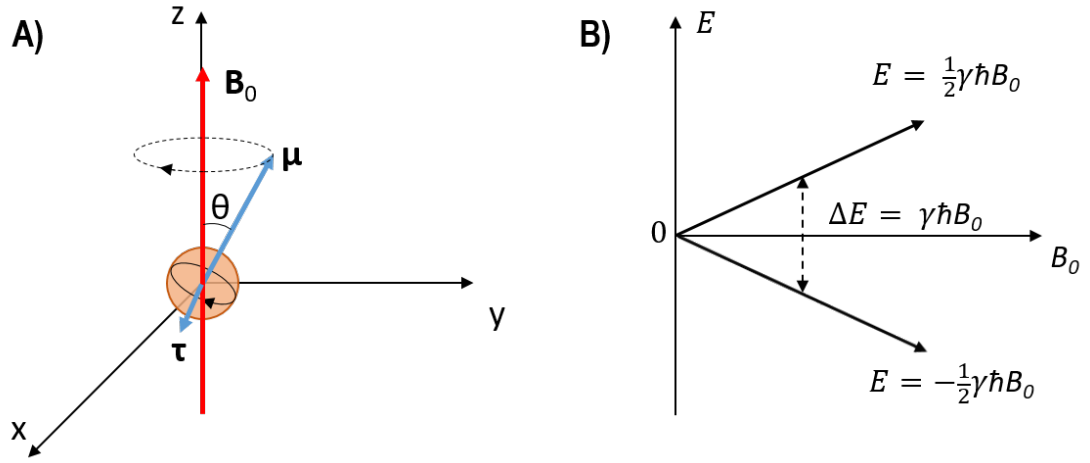



Figure 5.1: A) Precession of the magnetic moment $\boldsymbol{\mu}$ of an atomic nucleus about a magnetic field $\mathbf{B}_0$ oriented along the z-axis. B) Energy level diagram for a spin $I = 1/2$ nucleus in a magnetic a magnetic field.

to align the spin in the direction of the magnetic field. As the nucleus also has an angular momentum $\mathbf{J}$ the spin will precess about $\mathbf{B}_0$ instead of aligning with it (this is illustrated in Figure 5.1A). As torque is defined as the rate of change of angular momentum, i.e. $\boldsymbol{\tau} = \mathrm{d}\mathbf{J} \,/\, \mathrm{d}t$, we find

$$\frac{\mathrm{d}\mathbf{J}}{\mathrm{d}t} = \boldsymbol{\mu} \times \mathbf{B}_0 \tag{5.3}$$

and using equation 5.2

$$\frac{\mathrm{d}\boldsymbol{\mu}}{\mathrm{d}t} = \gamma \boldsymbol{\mu} \times \mathbf{B}_0 \tag{5.4}$$

The angular frequency of the spin precession is called the Larmor frequency and depends on the gyromagnetic ratio of the nuclei and the magnitude of the external magnetic field:

$$\omega_L = \gamma B_0. \tag{5.5}$$

In the absence of an external magnetic field all orientations of the magnetic dipole moment have equal energy. When a magnetic field $\mathbf{B}_0$ is applied in the z-direction, the energy levels split, an effect known as Zeeman splitting (see Figure

5.1B). For each state $m$ the z-component of the magnetic moment is given by

$$\mu_z = \gamma J_z = m\gamma\hbar \tag{5.6}$$

with the direction of the precession depending on the sign of the gyromagnetic ratio $\gamma$. The corresponding energy $E$ for state $m$ is given by

$$E = -\boldsymbol{\mu} \cdot \mathbf{B}_0 = -\mu_z B_0 = -m\gamma\hbar B_0, \tag{5.7}$$

with the gap between two adjacent energy levels being

$$\Delta E = \gamma\hbar B_0. \tag{5.8}$$

For a hydrogen nucleus (proton with spin $I = 1/2$ and $m = \pm 1/2$) the spins will align either parallel or anti-parallel with the magnetic field, giving two energy levels. At thermal equilibrium with an applied magnetic field the spins are distributed over energy levels according to Boltzmann distribution

$$\frac{n_{-1/2}}{n_{+1/2}} = \exp\left(-\frac{\Delta E}{k_B T}\right) = \exp\left(-\frac{\hbar\gamma B_0}{k_B T}\right) \tag{5.9}$$

where $n_{-1/2}$ is the number of spins in the high energy state $m = -1/2$, and $n_{+1/2}$ is the number of spins in the low energy state $m = 1/2$, $k_B$ is the Boltzmann constant and $T$ the absolute temperature. If we consider physical conditions with a magnetic field $B_0 = 7\text{T}$ and body temperature $T = 310\text{K}$, the ratio of spin populations of hydrogen nuclei is equal to

$$\begin{aligned} \frac{n_{-1/2}}{n_{+1/2}} &= \exp\left(-\frac{1.0546 \times 10^{-34}\text{Js} \times 42.576 \times 10^{6}\text{HzT}^{-1} \times 7\text{T}}{1.3807 \times 10^{-23}\text{JK}^{-1} \times 310\text{K}}\right) \\ &= 0.99999266 \end{aligned} \tag{5.10}$$

meaning that the population of the two spin energy states is almost equal, with only a very small excess of lower energy spins. It is this small difference in spin

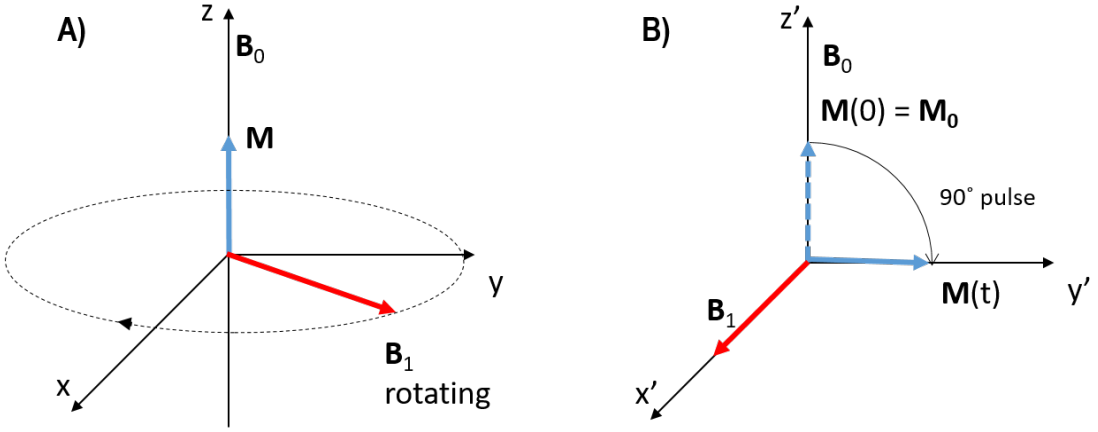



Figure 5.2: A) The $\mathbf{B}_1$ radio frequency field in the xy plane oscillating with frequency $\omega$. B) When the RF frequency matches the Larmor frequency $\omega = \omega_L$ the $\mathbf{B}_1$ field appears static in the reference frame of the spin magnetisation (rotating frame). In the case of a 90° pulse $\mathbf{B}_1$ acts to flip $\mathbf{M}$ into the xy plane.

populations that gives rise to a macroscopic, or bulk, magnetisation $\mathbf{M} = \Sigma_i \boldsymbol{\mu}_i$, (where $\boldsymbol{\mu}_i$ is the magnetisation of an individual spin $i$), aligned with the $\mathbf{B}_0$ external magnetic field, that is the basis of NMR applications.

### 5.2.2 Interaction with Radio frequency pulses

A nucleus can undergo a transition from a lower energy level to a higher energy level (e.g. from $m = 1/2$ to $m = -1/2$) by absorbing a photon with energy equal to $\Delta E$. The energy of a photon is dependent on its frequency, i.e. $E = \hbar\omega$, from which it follows that the frequency $\omega$ of the photon required to excite a spin to its higher energy level, will be equal to the Larmor frequency:

$$\begin{aligned} \Delta E &= E \\ \gamma\hbar B_0 &= \hbar\omega \\ \Rightarrow\ \omega &= \gamma B_0 = \omega_L. \end{aligned} \tag{5.11}$$

This oscillating electromagnetic field is referred to as $\mathbf{B}_1$ or the radio frequency (RF) field, as in NMR the required resonance frequencies fall into the RF range (kHz - MHz range). $\mathbf{B}_1$ is generated by a transmitter coil and it is usually applied in the transverse plane, perpendicular to the $\mathbf{B}_0$ field. In the reference frame of the

individual atoms magnetisation $\boldsymbol{\mu}_i$, which are rotating with frequency $\omega_L$ around the z direction, $B_1$ appears stationary and it adds a magnetic field component in the xy plane (see Figure 5.2). The overall effect of the RF field is to rotate the bulk magnetisation $\mathbf{M}$ towards the xy plane by an angle $\alpha$, known as the flip angle, which is dependent on the duration of the applied RF pulse, $t_{RF}$, the amplitude of the RF field $B_1$, and the gyromagnetic ratio:

$$\alpha = \int_0^{t_{RF}} \gamma B_1(t) \mathrm{d}t. \tag{5.12}$$

In the case of a hard RF pulse with constant $B_1$, i.e. a rectangular pulse envelope, the calculation of the flip angle reduces to $\alpha = \gamma B_1 t_{RF}$. In practice, in most imaging and localised spectroscopy experiments, SINC and Gaussian RF pulses are usually prefered as they offer better spectral and spatial selectivity.

### 5.2.3 Relaxation

After a flip angle has been applied to the bulk magnetisation and the RF pulse has been switched off, the nuclear magnetic moments are again only under the influence of the $\mathbf{B}_0$ magnetic field. The bulk magnetisation will then relax back to its thermal equilibrium by re-emitting the energy absorbed by the RF pulse. Spin relaxation can happen by energy exchange to the surrounding environment known as spin-lattice relaxation, causing the longitudinal (z-component) magnetisation to recover to its equilibrium value $M_0$, and by spin-spin interactions, or transverse relaxation, causing the transverse xy-component to decay back to zero. Relaxation effects on the bulk magnetisation $\mathbf{M}$, can be described by Bloch equations as

$$\frac{\mathrm{d}\mathbf{M}}{\mathrm{d}t} = \gamma(\mathbf{M} \times \mathbf{B}) - \frac{(M_z - M_0)\mathbf{k}}{T_1} - \frac{M_x\mathbf{i} + M_y\mathbf{j}}{T_2}, \tag{5.13}$$

where $T_1$ is the longitudinal relaxation constant and $T_2$ is the transverse relaxation constant.

Let us first consider the longitudinal relaxation by focusing on the z-component

of the Bloch equation 5.13. Since our external field is $\mathbf{B}_0 = [0, 0, B_0]$, the Bloch equation can be simplified to

$$\frac{\mathrm{d}M_z}{\mathrm{d}t} = -\frac{(M_z - M_0)\mathbf{k}}{T_1}, \tag{5.14}$$

which is solved to give the time evolution of the longitudinal magnetisation

$$M_z(t) = M_0 + (M_z(0) - M_0)e^{-t/T_1}, \tag{5.15}$$

where $M_z(0)$ is the value of the longitudinal magnetisation at time $t = 0$, i.e. when the RF pulse is switched off. The relaxation time constant $T_1$ depends on various factors affecting spin-lattice interactions, such as the mobility of the lattice and temperature (the gyromagnetic ratio $\gamma$ and $B_0$ can also affect $T_1$). $T_1$ is often used as contrast in MR imaging as the longitudinal relaxation of water is dependent on the type of tissue. The different $T_1$ of water in brain tissues should also be taken into account in MR spectroscopy when calculating the concentration of metabolites in the brain (see section 5.4.3): in this work we used the $T_1$ values at 7T of the Grey matter = 1940 ms, White matter = 1130 ms and Cerebrospinal fluid = 4300 ms [Wright et al., 2008; Rooney et al., 2007].

Under the same $\mathbf{B}_0 = [0, 0, B_0]$ condition, the transverse relaxation is giving by the **i** and **j** components of the Bloch equation (5.13), i.e.

$$\begin{aligned} \frac{\mathrm{d}M_x(t)}{\mathrm{d}t} &= \gamma B_0 M_y(t) - \frac{M_x(t)}{T_2} \\ \frac{\mathrm{d}M_y(t)}{\mathrm{d}t} &= -\gamma B_0 M_x(t) - \frac{M_y(t)}{T_2} \end{aligned} \tag{5.16}$$

giving the solutions

$$\begin{aligned} M_x(t) &= M_{xy}(0)\sin(\omega_L t)e^{-t/T_2} \\ M_y(t) &= M_{xy}(0)\cos(\omega_L t)e^{-t/T_2} \end{aligned} \tag{5.17}$$

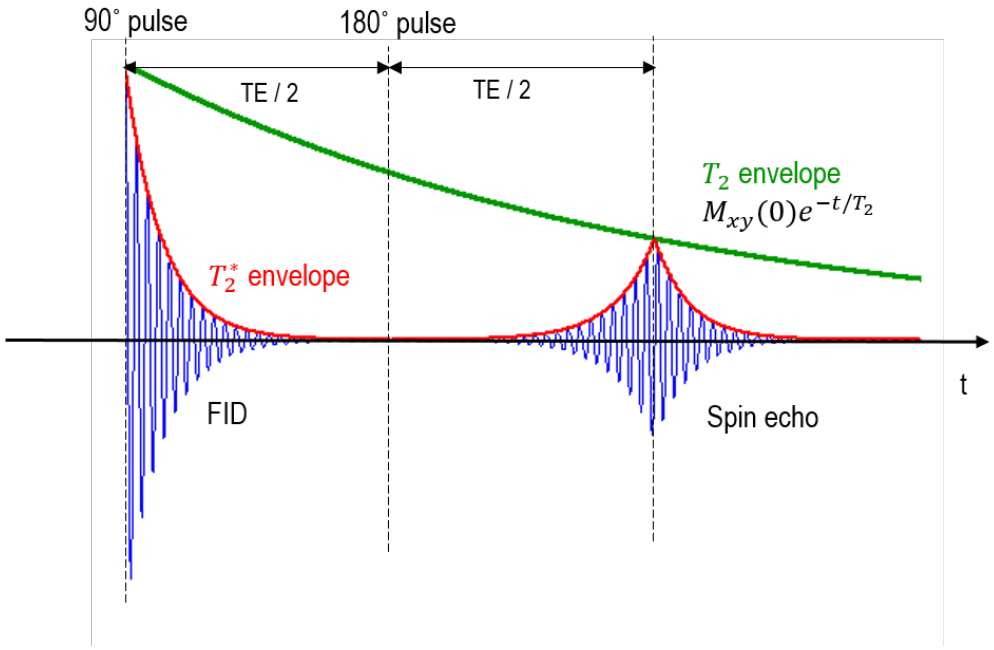



Figure 5.3: Diagram of a spin echo pulse sequence. Following a 90° RF pulse at $t = 0$ the transverse magnetisation follows a free induction deacy (FID) with $T_2^*$ time constant (red line). At time $t = TE/2$ a 180° pulse is applied causing the signal to refocus at the echo time $t = TE$ with amplitude dependent on the $T_2$ relaxation (curve in green).

where $M_{xy}(0)$ is the initial value of the transverse magnetisation at $t = 0$ following the RF pulse and $T_2$ is the transverse relaxation time constant. The bulk transverse magnetisation decays due to spin-spin interactions affecting the local magnetic field and causing a loss of phase coherence in individual spins. The inhomogeneity of the static $B_0$ field also causes an extra dephasing effect, characterised by the time constant $T_2'$, adding to the spin-spin interactions. In NMR experiments the detectable transverse relaxation is therefore given by the time constant $T_2^*$, dependent on both $T_2$ and $T_2'$ relaxations:

$$\frac{1}{T_2^*} = \frac{1}{T_2} + \frac{1}{T_2'}. \tag{5.18}$$

In a spin 1/2 system, a 90° pulse can be applied to flip the magnetisation into the xy plane, making $M_z(t = 0) = 0$. In this case the system is said to be excited or saturated. Following a 90° RF pulse the transverse magnetisation starts to dephase as spins start precessing with slightly different phases due to differences

in their local magnetic field. This process is referred to as free induction decay (FID) and follows an exponential decay with $T_2^*$ time constant. By applying a refocusing pulse, e.g. a 180° pulse in the y-direction, it is possible to refocus the transverse magnetisation: the time at which maximum $M_{xy}$ refocusing occurs is called the echo time (TE) and the effect is known as a spin echo [Hahn, 1950]. The recovered signal at TE will be smaller than the initial transverse magnetisation $M_{xy}(0)$ due to the non-coherent spin-spin interaction, causing loss of the bulk magnetisation which cannot be rephased. Spin echo sequences can therefore be used to measure pure $T_2$ relaxation effects (see Figure 5.3).

## 5.3 MRS

While magnetic resonance imaging (MRI) gives structural information based on the magnetic properties (e.g. relaxation) of tissues, magnetic resonance spectroscopy (MRS) provides information on the chemical composition of a selected volume. MRS can be used in vivo to detect concentrations of metabolically relevant molecules and neurotransmitters as well as neurochemical changes in the brain due to physiological processes or disease. MRS is based on the detection of free induction decay (FID) signals and chemical shift.

### 5.3.1 Chemical shift

Nuclei of the same atomic species will resonate at slightly different frequencies depending on their molecular environment, an effect known as chemical shift. The effective field experienced by a spin is given by:

$$B_{local} = (1 - \sigma)B_0, \tag{5.19}$$

with $\sigma$ being the shielding constant determined by the electron clouds around the nucleus opposing the magnetic field $B_0$. The resonant frequency of a nucleus in a

chemical environment is therefore also affected and it can be defined as

$$\omega_0 = \gamma(1 - \sigma)B_0. \tag{5.20}$$

This resonant frequency shift gives rise to a unique frequency peak in the MR spectra for the detected nuclei in a specific chemical structure. The same atomic species (e.g. $^1$H) in a different molecule (and with different chemical bonds within a molecule) can therefore be distinguished. The chemical shift, $\delta$, is defined as the relative difference between the resonant frequency of a nucleus $\omega_0$ and the frequency of the nucleus in a reference chemical environment, $\omega_{ref}$. Chemical shift is usually measured in parts-per-million (ppm) and mathematically is equal to

$$\delta = \frac{(\omega_0 - \omega_{ref}) \times 10^6}{\omega_{ref}}. \tag{5.21}$$

For in vivo application, the commonly used reference for $^1$H MRS in the brain is the methyl resonance of N-acetyl aspartate, which is set at 2.01 ppm, while the 'zero' is traditionally given by the methyl resonance of Tetramethylsilane (TMS).

The concentration of metabolites can be determined by measuring the area under the curve of their individual resonance peaks in the MR spectrum. As $^1$H only has one electron for chemical bonding its chemical shift range is quite narrow ($\sim$ 10 ppm). Together with the abundance of proton resonances in vivo this leads to a significant overlap of resonance peaks in MR spectra making the unambiguous detection and quantification of individual resonances more challenging, particularly for molecules with low concentrations. As the chemical shift effect linearly increases with magnetic field $B_0$ (equation 5.20) the use of higher magnetic fields increases spectral dispersion and can improve spectra fitting and quantification.

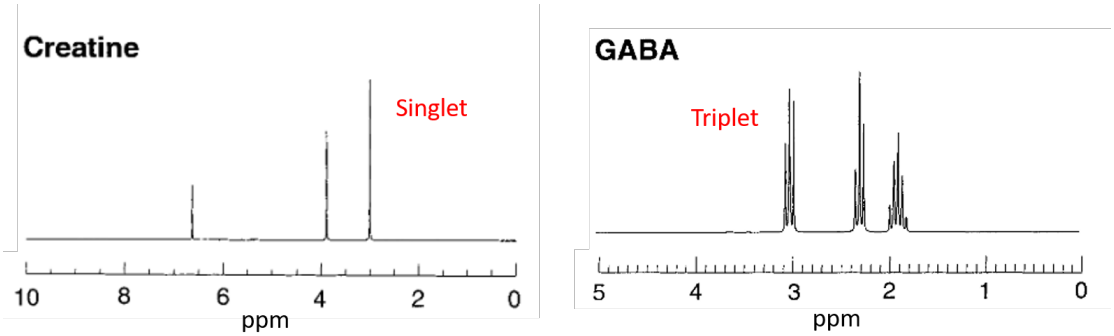



Figure 5.4: Simulated spectral patterns for GABA and Creatine at a field strength of 4.0 T (Figure adapted from Govindaraju et al. [2000]). Creatine has three singlet peaks while GABA has two triplets and one quintet peak due to J-coupling interactions.

### 5.3.2 J-coupling

In addition to multiple peaks due to chemical shifts, MR spectra are often characterised by multiplets or peak splitting caused by the intra molecular J-coupling [Govindaraju et al., 2000] (see Figure 5.4). J-coupling, (also called spin-spin coupling, or scalar coupling) arises from the interaction between nuclei with different chemical shift via electrons in covalent bonds: the Pauli exclusion principle causes the electrons in the covalent bond to have opposing spin states (spin up and spin down) and this affects the nuclei through hyperfine couplings (Fermi contact interaction), which make it energetically favourable for the nuclear spin to be anti-parallel to the electronic spin. The frequency difference between multiplets is called the coupling constant, J (reported in Hz), and it is independent of magnetic field strength. J-coupling can be homonuclear (e.g. $^{1}H-^{1}H$) or heteronuclear (e.g. $^{1}H-^{13}C$). The effect of J-coupling is observable when the distance between two chemically non-equivalent nuclei is no greater than three bond lengths.

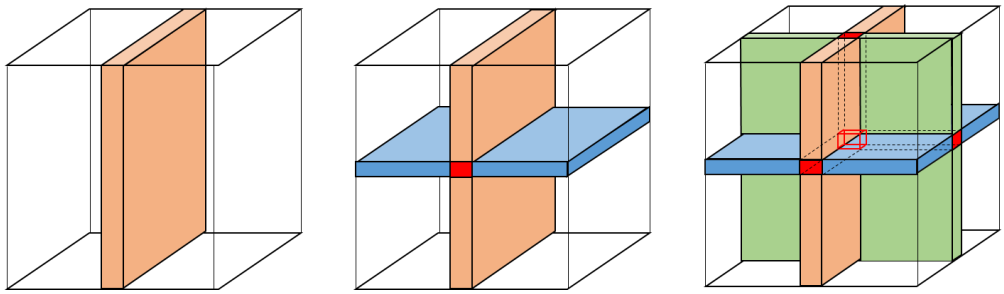


Figure 5.5: Single voxel localisation diagram. The VOI (in red) is localised from the intersection of three slice selection RF pulses.

## 5.4 Methods

### 5.4.1 Data acquisition

In MR spectroscopy, we wish to detect a spectrum at a specific location in the brain, called the volume of interest (VOI). Spatial localisation also allows for improvements in spectra resolution and signal to noise ratio (narrow line widths) and exclusion of unwanted peaks from outside the VOI, such as lipids from the skin. One of the main approaches for spatial localisation in MRS is single voxel spectroscopy (SVS) where we detect the MRS signal from a single defined volume [Klose, 2008]. Spatial encoding in SVS is achieved by applying magnetic field gradients in three orthogonal directions: small magnetic field gradients are superimposed on the static magnetic field $B_0$ so that spins at different positions will experience a unique and spatially specific magnetic field. The variations in local magnetic field will affect the Larmor frequency (see equation 5.5). By applying a linear gradient along one axis, it is possible to only excite spins in a slice of the sample through a RF pulse. The thickness of the slice ($\Delta z$) is determined by how narrow we make the bandwidth ($\Delta\omega$) of the RF pulse and by the gradient amplitude ($G_z$):

$$\Delta z = \frac{\Delta\omega}{\gamma G_z}. \tag{5.22}$$

In SVS, orthogonal magnetic gradients are applied in three directions together with slice-selective RF pulses to collect the echo signal from the VOI, where the three slices intersect (see Figure 5.5). Multi-voxel techniques known as Chemical

Shift Imaging (CSI) or MR Spectroscopy Imaging (MRSI) can also be used in MRS to acquire multiple spectra from voxels in planes or 3-dimensional volumes, though they usually offer lower spectral quality compared to SVS sequences.

Here we implemented two different SVS techniques: Stimulated Echo Aquisition Mode (STEAM) [Frahm et al., 1989] and semiadiabatic Localisation by Adiabatic Refocusing (sLASER) [Scheenen et al., 2008]. Point RESolved Spectroscopy (PRESS) [Ordidge et al., 1986; Bottomley, 1984] is also a widely used localisation technique in MRS, although difficulty in achieving good 180° flip angles and necessarily long echo times make it non-ideal for use at 7T field.

### MR system

In order to prevent artefacts due to subject magnetisation [Gross et al., 2013], all MRS data were acquired after the MEG session; out of 46 participants 41 underwent MEG and MR scanning on the same day, 5 participants were scanned within 2 days. All MR measurements were performed on a 7T Philips Achieva scanner (Philips Medical Systems, Best, Netherlands) equipped with a 32-channel receive head coil and a surrounding volume transmit coil. Quadrature detection was used to produce real and imaginary components of the detected signal from the receive coil (by mixing the detected signal with two out of phase reference signals) and allowing to distinguish between the negative and positive frequencies relative to the reference frequency, $\omega_0$.

### Proton MRS STEAM sequence

STEAM sequences allow for very short echo times, allowing the detection of short $T_2$ metabolites. The use of 90° pulses improves the sharper definition of the VOI edges, and their high bandwidth which reduces chemical shift displacement artefacts compared to PRESS sequences, is particularly important at 7T field, as well as reducing tissue energy deposition (SAR). The downside of STEAM is its diminished signal to noise due to use of stimulated echos instead of spin echos.

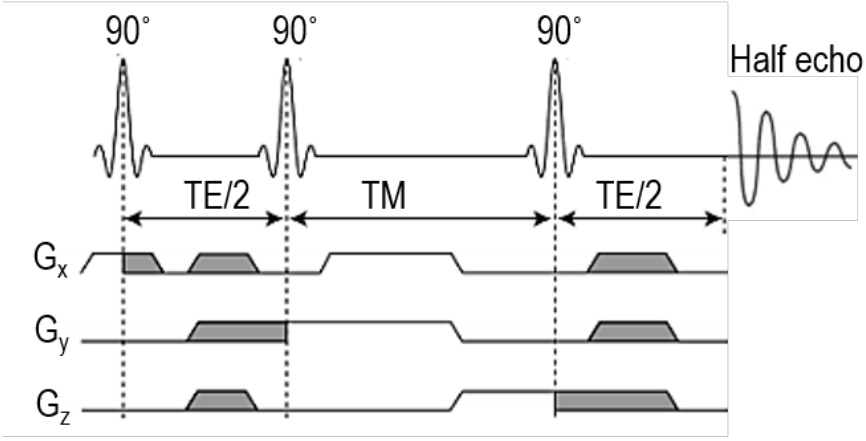



Figure 5.6: Diagram of STEAM pulse sequence. (Figure adapted from Thompson and Allen [2001]).

A schematic diagram of the STEAM pulse sequence is shown in Figure 5.6. The STEAM sequence uses three 90° RF pulses to obtain a stimulated echo (STE) signal at time TM+TE, where TM is the mixing time. The parameters used were a TE/TM/TR of 14/15/2000 ms for the first 13 participants, and 17/15/2000 ms for the remaining participants. The data acquisition sample size was 4096, with a 4000 Hz bandwidth. MOIST (Multiply Optimised Insensitive Suppression Train) [Murdoch and Lampman, 1993] available on the Philips Achieva system was used for water suppression. The VOI size was $15 \times 20 \times 30$ mm$^3$ and this was manually placed over the left primary sensorimotor cortex. Voxels were tilted in the coronal plane and positioned so as to avoid visible arteries, cerebrospinal fluid (CFS) and non-brain tissues. Two REST saturation bands were used to improve suppression of potential water and lipid extra-voxel signal contamination from the scalp. Four non-suppressed water reference spectra were acquired from the same voxel for phase and eddy current correction and for use as an internal concentration reference.

### 5.4.2 Edited sequences

Due to the significant overlap of metabolites in $^1$H spectroscopy, spectral edited sequences are often preferred for the measurement of low concentration metabolites.

J-difference spectral editing is based on the different time evolution of J-coupled and uncoupeld spins in spin echo sequences following a frequency-selective pulse (referred to as the editing pulse). Previous work at lower field (3T) has used the Mescher-Garwood (MEGA) editing scheme in combination with a PRESS sequence (MEGA-PRESS), while at 7T MEGA-sLASER sequences, less affected by chemical shift anisotropy, have shown to accurately estimate GABA in multiple studies [Andreychenko et al., 2012; Chen et al., 2017]. As part of this experiment we collected a macromolecule eliminated MEGA-sLASER sequence (TR/TE =5000/72 ms, voxel size =15 × 20 × 30 $mm^3$, spectral bandwidth = 4000 Hz, samples = 4096, phase cycle step = 2) with VAPOR (variable pulse power and optimised relaxation delay) water suppression [Tkáč et al., 1999], previously optimised by Chen et al. [2017]. sLASER spatial localisation is based on adiabatic pulses, gradually sweeping the frequency of the $B_1$ field to impart a flip angle to the spin system. Adiabatic RF pulses must exceed a threshold amplitude in order to remain in the adiabatic regime. During the period of data acquisition the power output of the RF power amplifiers of the 7T scanner declined, unpredictably affecting the sLASER sequence. The acquired MEGA-sLASER spectra were therefore excluded from this further analysis. The STEAM sequence, using 90° RF pulses, while also affected by RF amplifier issues was more robust to $B_1$ issues.

### 5.4.3 Data processing

Prior to metabolite quantification, spectra were pre-processed with custom scripts developed in MATLAB. The main pre-processing steps involved the initial reconstruction from the 32 channel raw signals [Hall et al., 2014b], zero-order phase correction, frequency alignment performed relative to the choline peak (at 3.2 ppm) and elimination of any poor quality dynamics before spectral averaging.

Absolute quantification of metabolite levels was obtained through the LCModel

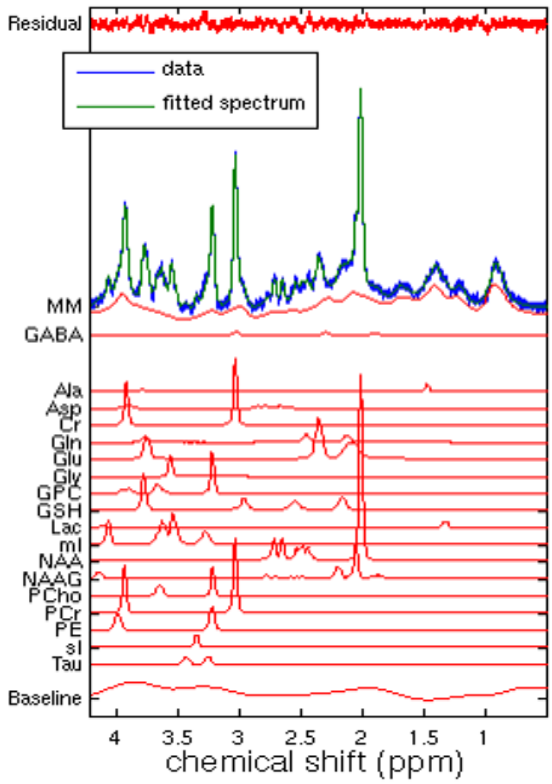



Figure 5.7: Example STEAM spectrum acquired from the sensorimotor cortex with individual metabolite concentrations estimated through LCModel software.

software package. LCModel works by fitting the obtained spectra with a derived basis set of expected metabolites. For this analysis we fitted for 20 metabolites: alanine (Ala), aspartate (Asp), choline (Cho), creatine (Cr), $\gamma$-aminobutyric acid (GABA), glucose (Glc), glutamate (Glu), glutamine (Gln), glycine (Gly), glycerophosphocholine (GPC), glutathione (GSH), lactate (Lac), myo-Inositol (mI), N-acetylaspartate (NAA), N-acetylaspartylglutamate (NAAG), phosphocholine(PCh), phosphocreatine (PCr), phosphorylethanolamine (PE), scyllo-Inositol (sI) and taurine (Tau). In order to account for the contribution of macromoles we also included a macromolecule spectrum experimentally acquired in vivo. An example STEAM spectrum fitted with LCModel is shown in Figure 5.7. LCModel analysis was performed in the chemical shift range between 0.2 and 4.2 ppm and allowing for a flexible baseline, in order to compensate for non-ideal water and lipid suppression. LCModel is able to correct for eddy currents and residual water by providing

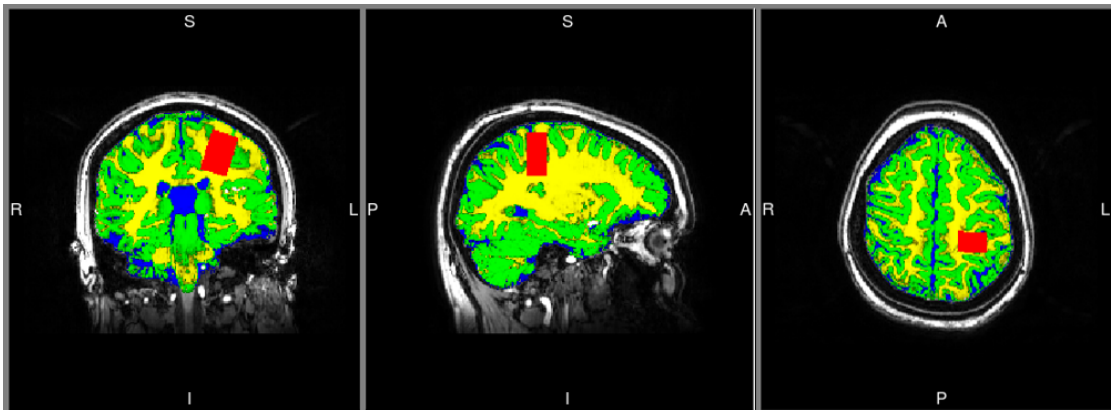



Figure 5.8: Tissue segmentation created with SPM8 is highlighted in green (cortex), yellow (white matter) and blue (CSF). MRS voxel (in red) was placed manually over the left central sulcus. Tissue fractions were used for relaxation correction of metabolite concentrations.

the software with a reference water spectrum. As the GABA peaks overlap with peaks from higher concentration metabolites (such as Cr at $\sim$ 3 ppm), we allowed all peaks of individual metabolites to shift from the basis set expected frequency by only 0.001 ppm ($\sim$ 0.3 Hz) in order to avoid LCModel overfitting the spectra and overestimating GABA concentration. Estimated metabolites are reported in absolute concentrations (mM units) and with an estimated standard deviation (or goodness of fit parameter) expressed in percentage, i.e. the Cramér-Rao lower bound. GABA and Glutamate concentrations were reported as absolute concentrations and as relative concentrations to total creatine (tCr), estimated as the sum of Cr and PCr. Total Creatine is often used as the reference metabolite for in vivo proton spectroscopy as its concentration in the brain is relatively constant.

The tissue composition inside the MRS voxel was measured from an MPRAGE image collected during the same MR session. Estimates of the grey matter (GM), white matter (WM) and cerebrospinal fluid (CSF) were determined through the Statistical Parametric Mapping (SPM8) software package [Ashburner and Friston, 2005]. An example of SPM8 derived tissue segmentation is shown in Figure 5.8.

Metabolite concentrations obtained in LCModel were corrected for differences in relaxation times and all metabolites were referred to the brain tissue (white and grey matter) fraction in the spectroscopy volume. The concentration of the

metabolites of interest [G] (for GABA, Glu and tCr) estimated by LCModel were further corrected for differences in relaxation times according to

$$[G_{corr}] = [G] \times \frac{\sum_i^{GM,WM,CSF} c_{w,i} \exp\left(-\frac{TE}{T_{2w,i}}\right)(1 - \exp\left(-\frac{TR}{T_{1w,i}}\right))f_i}{\exp\left(-\frac{TE}{T_{2G}}\right)(1 - \exp\left(-\frac{TR}{T_{1G}}\right))} \tag{5.23}$$

where $c_{w,i}$ is the visible water concentration of each tissue $i$, $f_i$ is the tissue fraction in the VOI, $T_{2w,i}$ and $T_{1w,i}$ the time constants for water in the tissue, and $T_{2G}$ and $T_{1G}$ the time constants for the metabolite (see e.g. [Harris et al., 2015]). Relaxation times for individual metabolites were obtained from Andreychenko et al. [2012].

### 5.4.4 Link to MEG and statistical techniques

To compare GABA concentration and beta amplitude, we quantified beta amplitude in two ways. First, we used our resting state recording to measure the resting beta level, as the average oscillatory amplitude across the ten minute measurement – giving a quantification of resting beta amplitude. Secondly, we used the task data to measure beta modulation; specifically, in trials in which the attentional cue pointed to the right hand, we measured fractional change in beta amplitude (with respect to rest) in left sensory cortex in the 12.5 s to 16 s window (relative to the start of the trial) – this gave a measure of beta modulation. We then plotted GABA level against our two beta measures independently and tested for a significant relationship. Note that two subjects were excluded from these analyses on the basis of MRS data quality (high residual water, pronounced lipid artefacts and GABA Cramér-Rao lower bounds $> 30\%$). One further subject was excluded for having beta amplitude greater than 3 standard deviations from the mean. All processed spectra are presented in appendix D.

We further tested whether GABA concentrations referenced to tCr or to the excitatory neurotransmitter Glutamate correlated with individual behavioural per-

formance. Specifically we tested for GABA correlations to accuracy and reaction time. Individual accuracy at performing the task was estimated as (true positives + true negatives)/(true positives + false positives + true negatives + false negatives), where 'true positives' are the number of correctly identified targets, 'false positives' are the number of misidentified non-target probes, 'true negatives' are the number of correctly ignored non-targets probes and 'false negatives' are the number of missed targets. Reaction time was calculated as the average time taken to correctly press the buttons following the presentation of a target pattern.

## 5.5 Results

### 5.5.1 Relationship to MEG

For the 43 subjects analysed in the MRS experiment, the average spectral linewidth was $8.8 \pm 1.0$ Hz. The Cramér-Rao lower bounds for GABA ranged from 9% to 22%. Both beta modulation and resting beta power were plotted against GABA concentration, with results shown in Figures 5.9A and 5.9B respectively. In both cases, and in agreement with our hypothesis, we found a significant ($p = 0.01$ for resting beta and 0.02 for beta modulation) relationship, with those subjects with higher GABA concentration demonstrating higher resting power and task induced change. For comparison, Figures 5.9C and 5.9D show beta rebound plotted against Glutamate and total Creatine, respectively. Note that, unlike GABA, no measurable relationships were found.

The same analysis was run for GABA and Glutamate concentrations which were both normalised relative to total Creatine. In agreement with absolute concentrations, beta rebound and resting beta power correlate significantly with GABA/tCr concentration with p-value of 0.02 and 0.007 respectively. Glu/tCr shows no significant relationship. Results are shown in Figure 5.10.

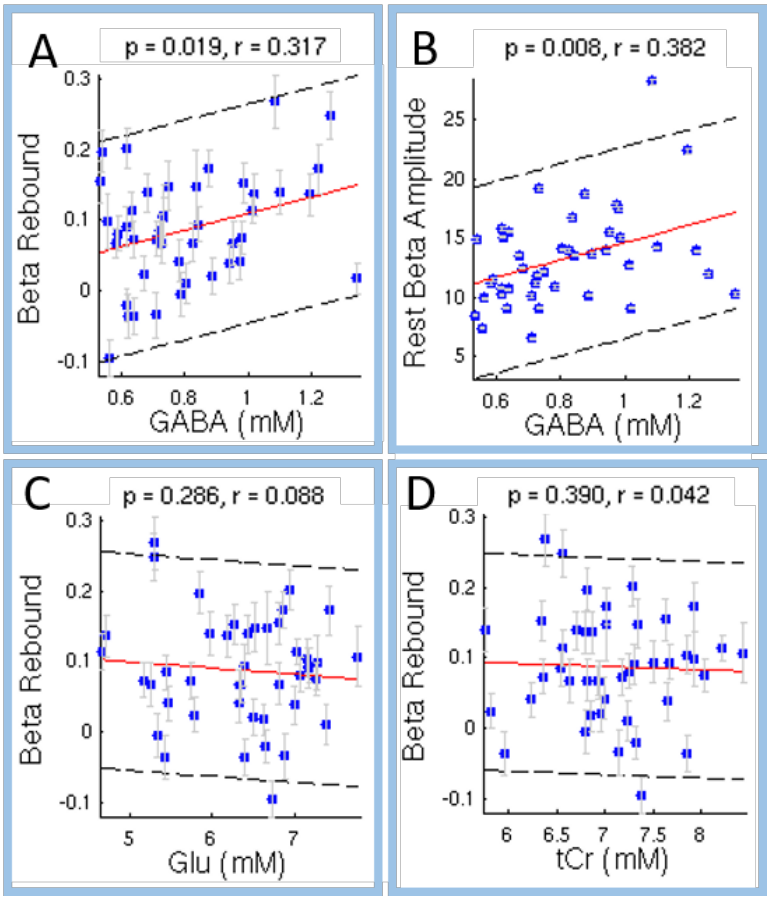



Figure 5.9: A) GABA concentration plotted versus beta modulation, both measured in left sensorimotor cortex – each data point represents a different subject and error bars denote standard error of beta amplitude over time. Note the significant (p = 0.02) correlation. B) GABA concentration versus resting beta amplitude, also in left sensorimotor cortex. Again note significant (p = 0.01) correlation, with subjects with higher GABA concentration having larger resting beta amplitude. C) Beta rebound versus Glutamate. D) Beta rebound versus total Creatine.

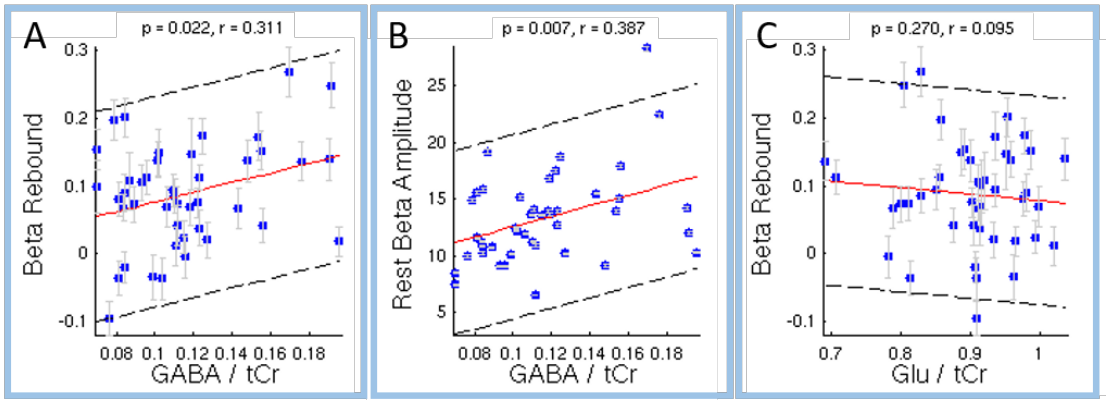



Figure 5.10: Metabolite ratios versus beta oscillations. A) Beta rebound plotted against the ratio of GABA to total Creatine. B) Resting beta power plotted against the ratio of GABA to total Creatine. C) Beta rebound plotted against the ratio of Glutamate to total Creatine.

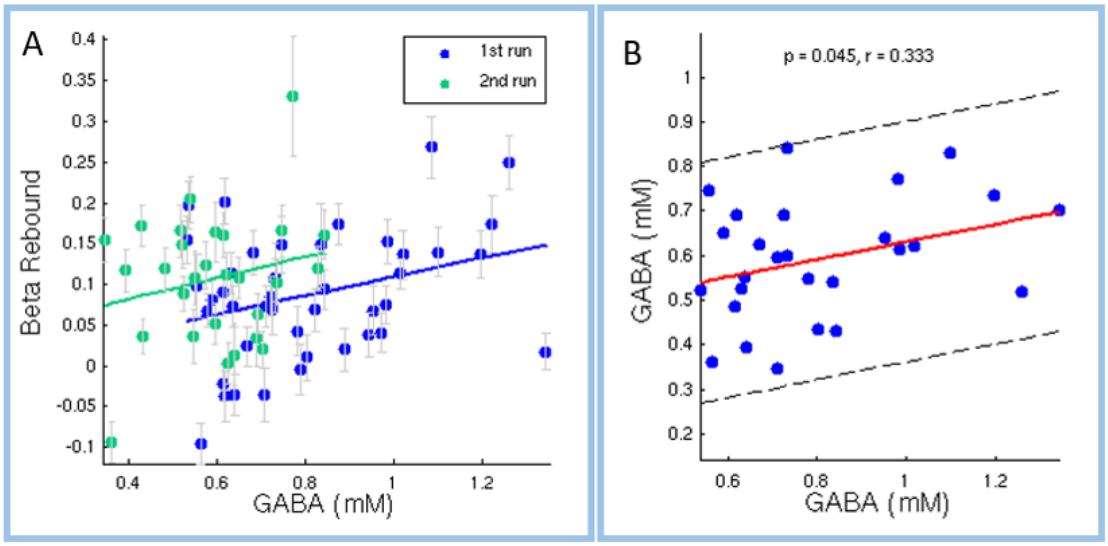



Figure 5.11: Correlation of Beta rebound to GABA concentration in 43 subjects and repeated measures in subset of 28 subjects. A) GABA concentration plotted versus beta modulation, both measured in left sensorimotor cortex – each data point represents a different subject. Blue data points refer to the initial 43 subjects, green data points to subset of 28 subjects acquired after 9 months. Error bars show standard error of beta amplitude estimation over time. B) GABA concentration measured in left sensorimotor cortex in the second run (vertical axis) plotted against GABA measured in the first run (horizontal axis) in a subset of 27 subjects (each represented as a data point; subjects with evident poor data quality in either run were excluded). Although we see a significant correlation ($p = 0.045$) of GABA measures between runs, the second run showed overall lower estimates of GABA concentration.

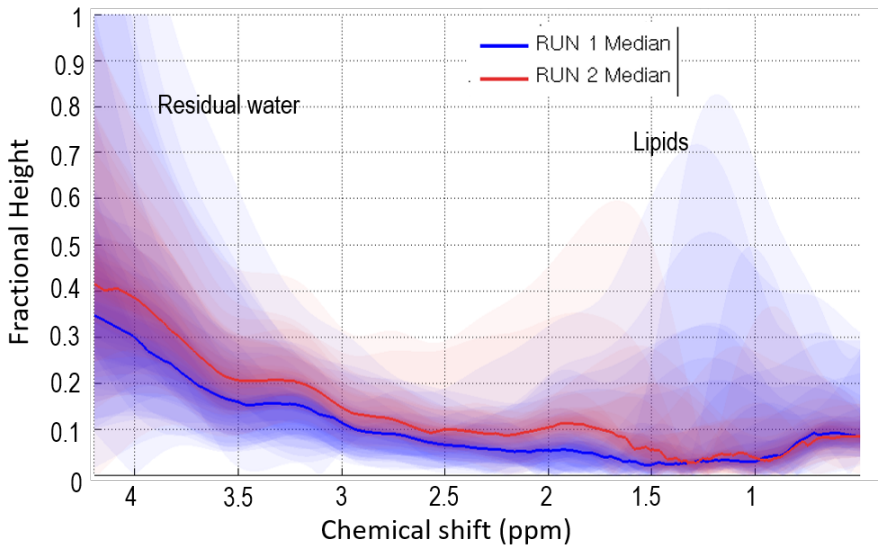



Figure 5.12: Absolute value of LCModel estimated baseline for STEAM spectra in run 1 (blue) and run 2 (red). Baseline amplitude is reported as fractional height of the NAA peak (at 2ppm). Shaded region is the overlay of individual spectral baselines.

### 5.5.2 Relationship between run 1 and 2

MRS measures were acquired twice in 29 subjects, and correlations between beta rebound and GABA estimates, for these two runs, are compared in Figure 5.11 (one subject with Cramér-Rao lower bounds = 35% was excluded from the analysis). In run 2, a similar trend was noted to that identified in run 1, where higher beta rebound tended to be predicted by higher GABA. However, in the second run this relationship failed to reach statistical significance. In addition, despite a significant ($p = 0.045$) correlation between GABA estimates across runs, GABA tended to be lower in run 2. Results from LCModel further suggested that the overall GABA Cramér-Rao lower bounds (range 13% to 31%) were higher in the second run, indicating poorer data quality. We speculate that this lower spectral quality was a result of a decline in performance of the RF power amplifier between runs. The spectral baselines for both runs estimated through LCModel are shown in Figure 5.12. Run 1 showed, on average, a flatter baseline than run 2. Both runs included a few scans with notably poor water suppression or lipid contamination.

### 5.5.3 Comparison of GABA and behavioural performance

Figure 5.13 shows GABA/tCr and GABA/Glu plotted against task accuracy. We see a significant negative correlation ($p=0.04$, not corrected for multiple comparisons) of accuracy and GABA/Glu ratio in the second run (29 participants), but no similar trend can be observed in the first run (44 participants) or by pooling together the data of both runs (73 participants). Figure 5.14 shows the comparison of GABA/tCr and GABA/Glu to reaction times. No correlation could be seen when comparing GABA and reaction time in either run.

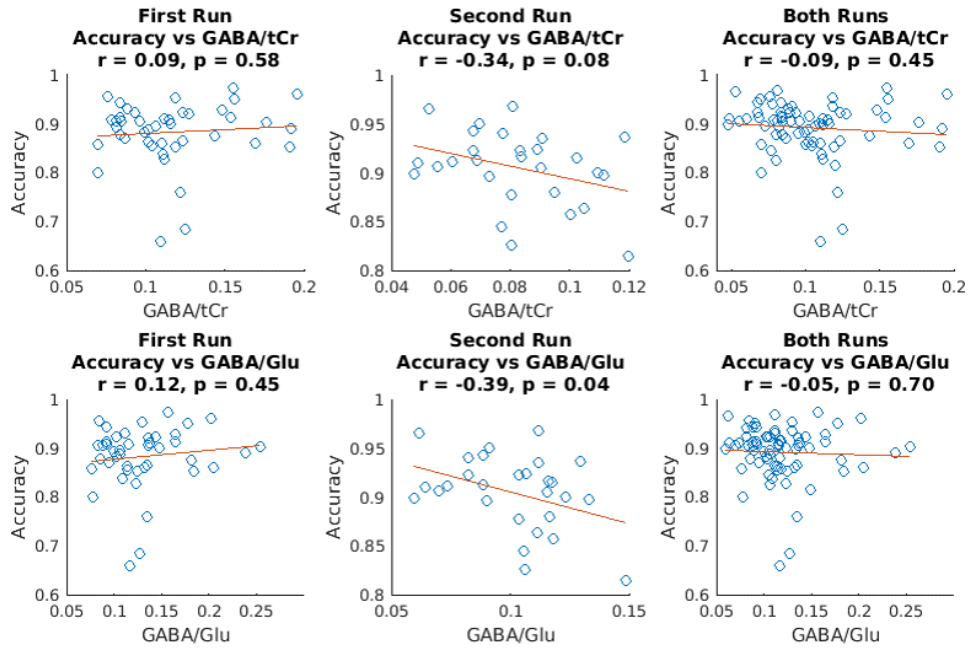



Figure 5.13: GABA concentration compared to individual task accuracy. Top row shows GABA ratio to total Creatine (tCr), bottom row shows GABA ratio to Glutamate (Glu). Pearson correlations are calculated separately for the first and second run and for the two runs combined (plots presented in order from left to right).

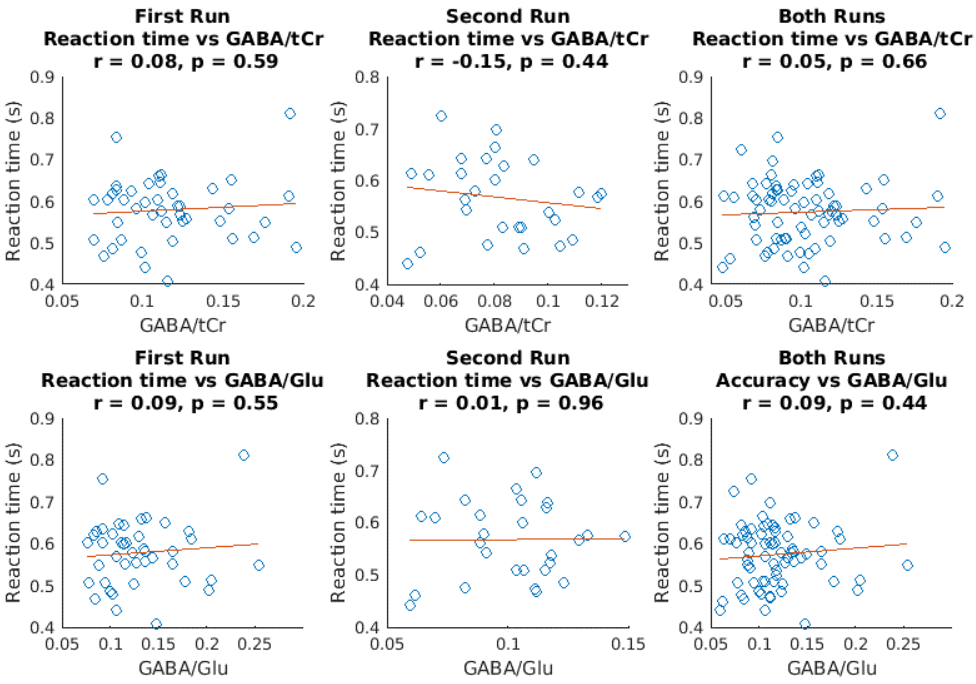



Figure 5.14: GABA concentration compared to individual reaction times (i.e. time of button press responses to target stimuli). Top row shows GABA ratio to total Creatine (tCr), bottom row shows GABA ratio to Glutamate (Glu). Pearson correlations are calculated separately for the first and second run and for the two runs combined (plots presented in order from left to right).

## 5.6 Discussion

Our results in Figure 5.9 link the generation of beta oscillations to localised concentrations of GABA, with individuals demonstrating measurably high GABA concentration tending to have higher resting state beta power, and a larger beta rebound. MRS has limited specificity, since it cannot target GABA molecules that are actively used for neurotransmission (i.e. those which presumably drive beta oscillations themselves). Rather, recent evidence [Stagg et al., 2011] suggests that MRS is most sensitive to tonic GABA (i.e. endogenous GABA present in the extracellular space). Nevertheless, our finding suggests that this tonic GABA is, in some way, associated with the neurochemical control of beta oscillations, and it is tempting to speculate that tonic GABA offers a means to maintain cortical inhibition in the resting state, and that this inhibition is mediated (electrophysiologically) by beta band oscillations. This would mean that measurements of resting GABA level, and resting beta power, are both effectively complementary measures of neural inhibition.

However, interpretation of this finding must be undertaken with caution. Previous studies attempting to correlate MRS measures of neurotransmitter levels and MEG derived electrophysiology have been problematic, with small sample size studies [Muthukumaraswamy et al., 2009] not being reproduced by subsequent investigation in a larger cohort [Cousijn et al., 2014]. Here we attempted to mitigate this problem by having a relatively large sample size (comparable to that of Cousijn et al. [2014]) and by scanning a number of these individuals twice. Our result showed a moderate, but nevertheless significant relationship in the first run of 46 subjects, and a similar trend in the second acquisition with 29 subjects, suggesting that this is a robust finding. Further, our finding agrees with earlier work [Gaetz et al., 2011] (though this study also had small sample size). Our work thus adds to a weight of evidence from MRS [Gaetz et al., 2011] and from neuro-pharmacological manipulation [Jensen et al., 2005; Hall et al., 2011; Muthukumaraswamy et al., 2013], which suggests a direct relationship between

beta oscillations and GABA. However it is interesting to note that, although beta rebound and rest beta power show a correlation to GABA concentration, GABA was not significantly related to subject accuracy or reaction times, mitigating the interpretation of a direct link between resting GABA levels measured with MRS and sensorimotor cortex function.

# Appendix D

# STEAM data

In this appendix we present all STEAM spectra acquired from 46 subjects in the first run, and a subset of 29 subjects who took part in the second run. Spectra have been pre-processed and subsequently analysed through the LCModel software package. Spectra are presented baseline corrected (baseline estimated through LCModel). Each panel shows the data (in blue), the overall model fit by LCModel (in red), the GABA metabolite fit (in black), the residual of the model fit (in green above the spectra) and the estimated baseline (in green below the spectra).

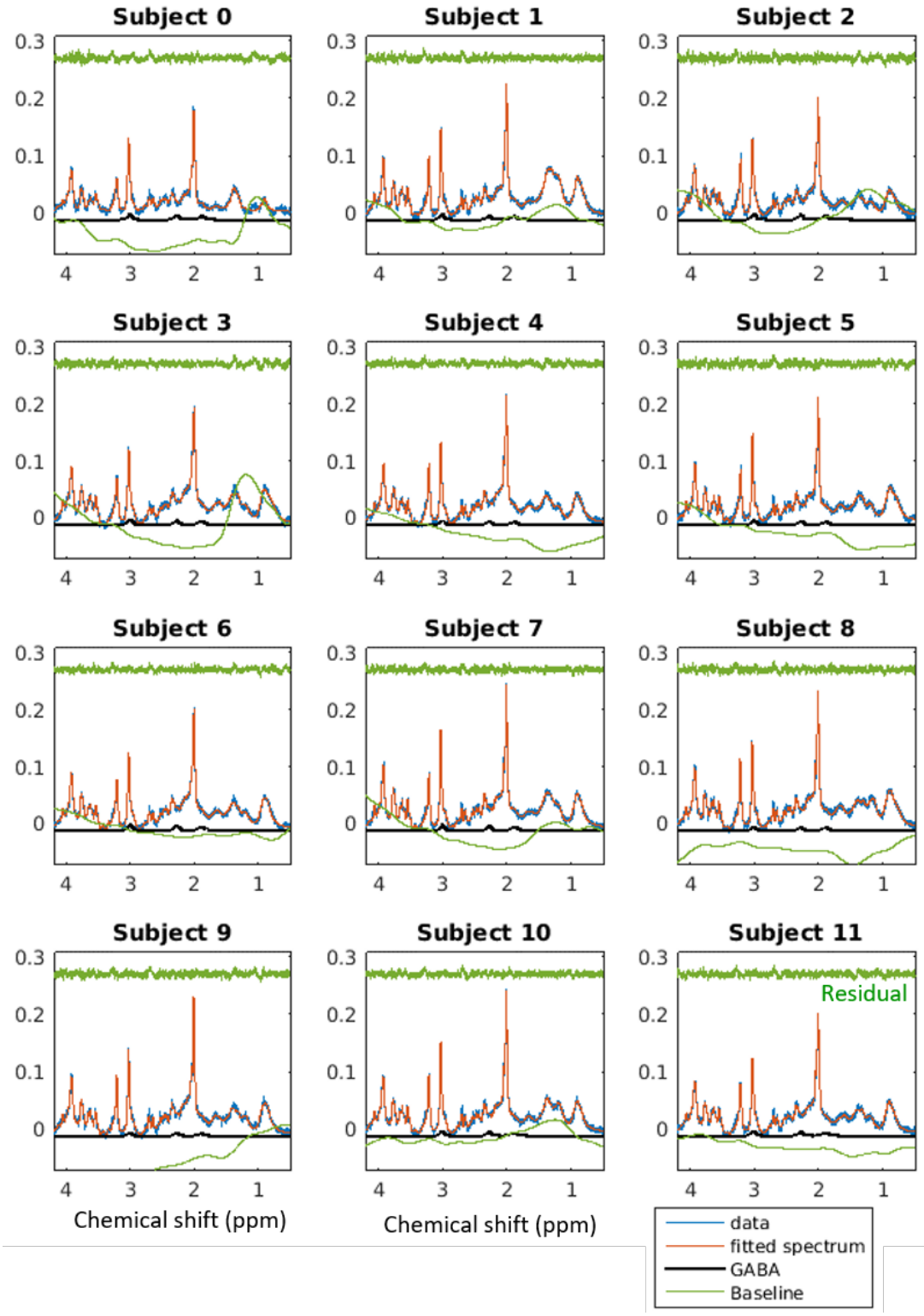



Figure D.1: First Run: STEAM data fitted by LCModel.

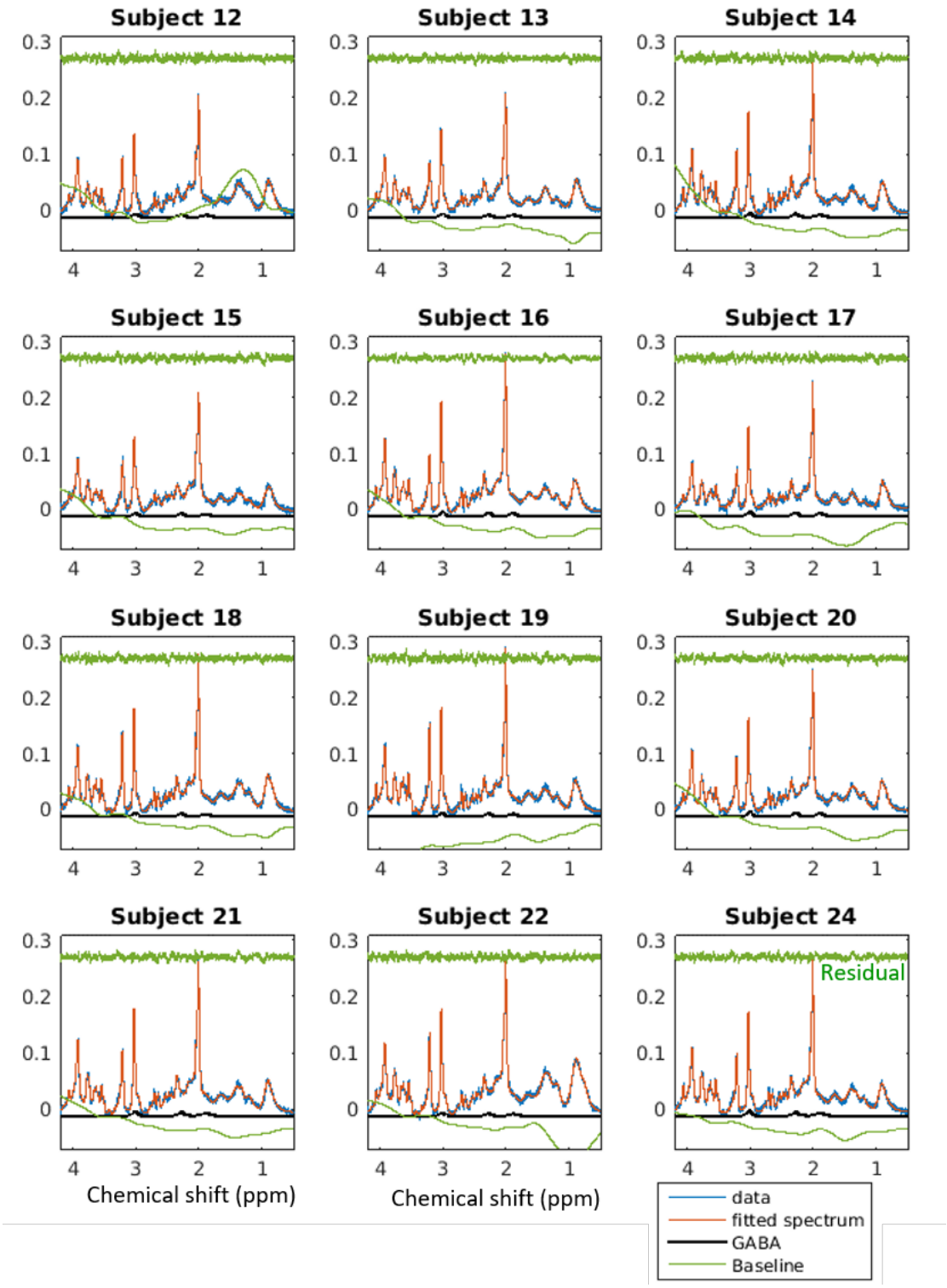



Figure D.2: First Run: STEAM data fitted by LCModel. Subject 23 did not take part in the MRI session.

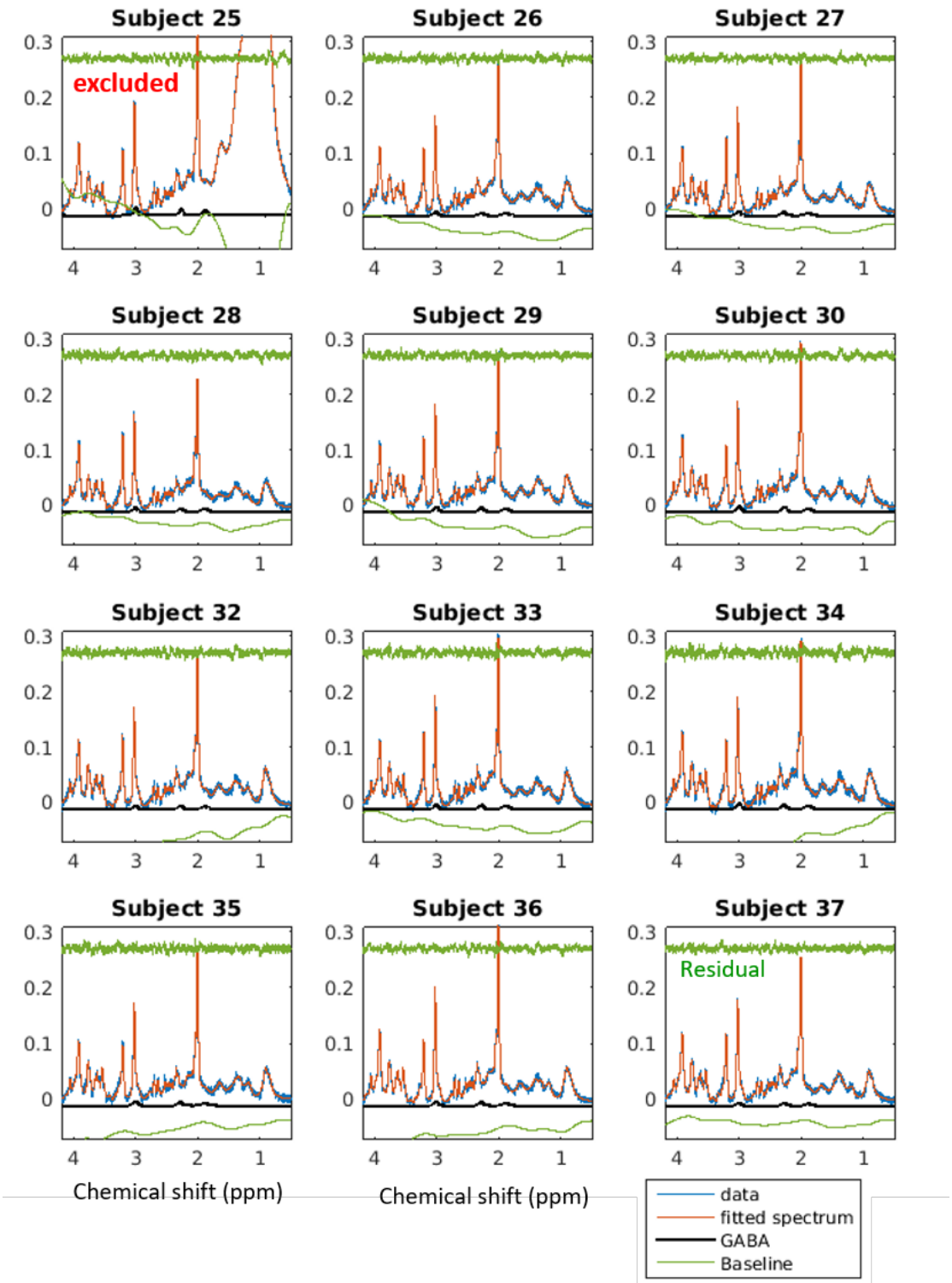



Figure D.3: First Run: STEAM data fitted by LCModel. Subject 25 was excluded because of obvious lipid contamination. Subject 31 did not take part in the MRI session.

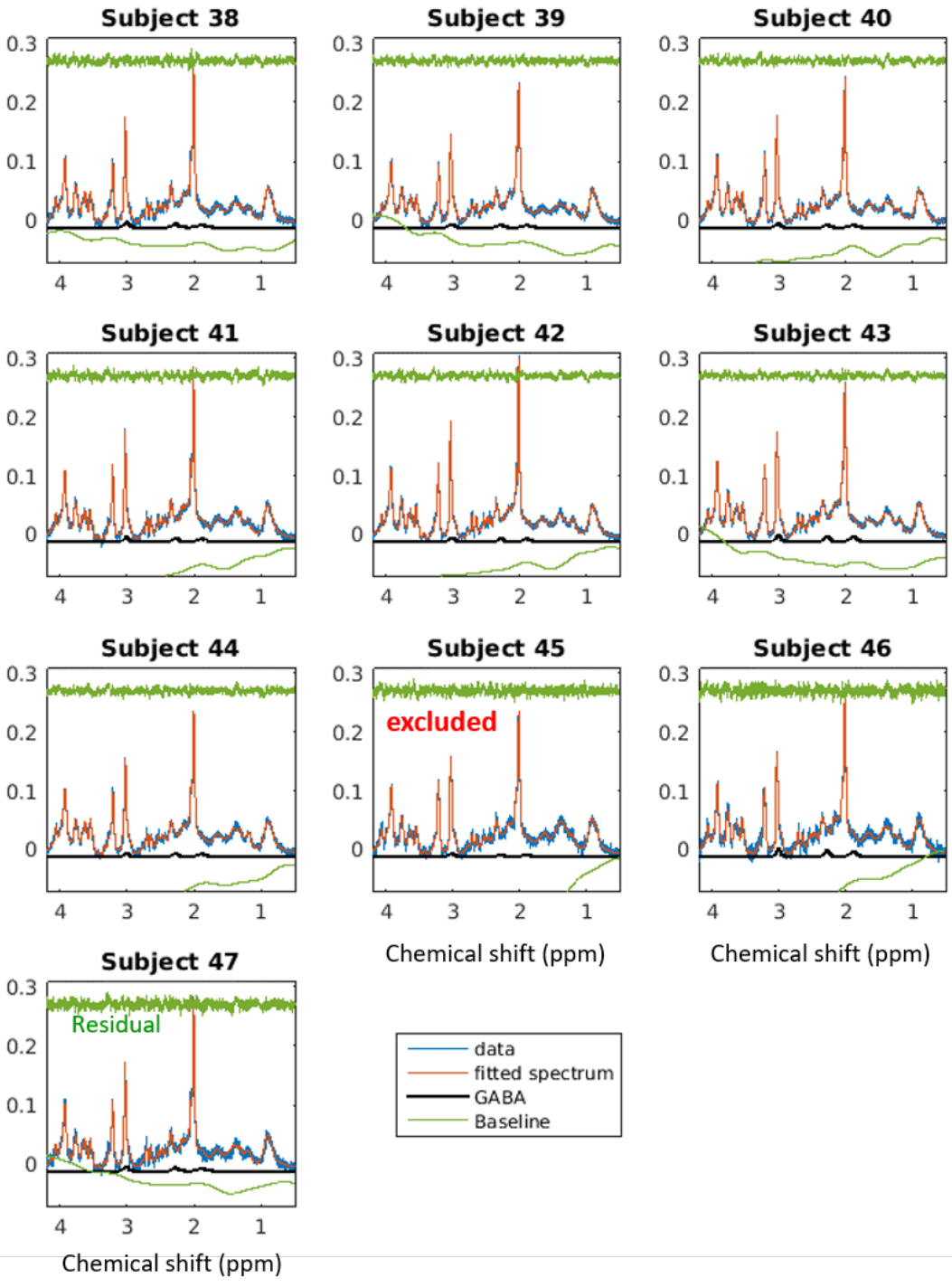



Figure D.4: First Run: STEAM data fitted by LCModel. Subject 45 was excluded because of poor water suppression and GABA Cramér-Rao lower bounds > 30%.

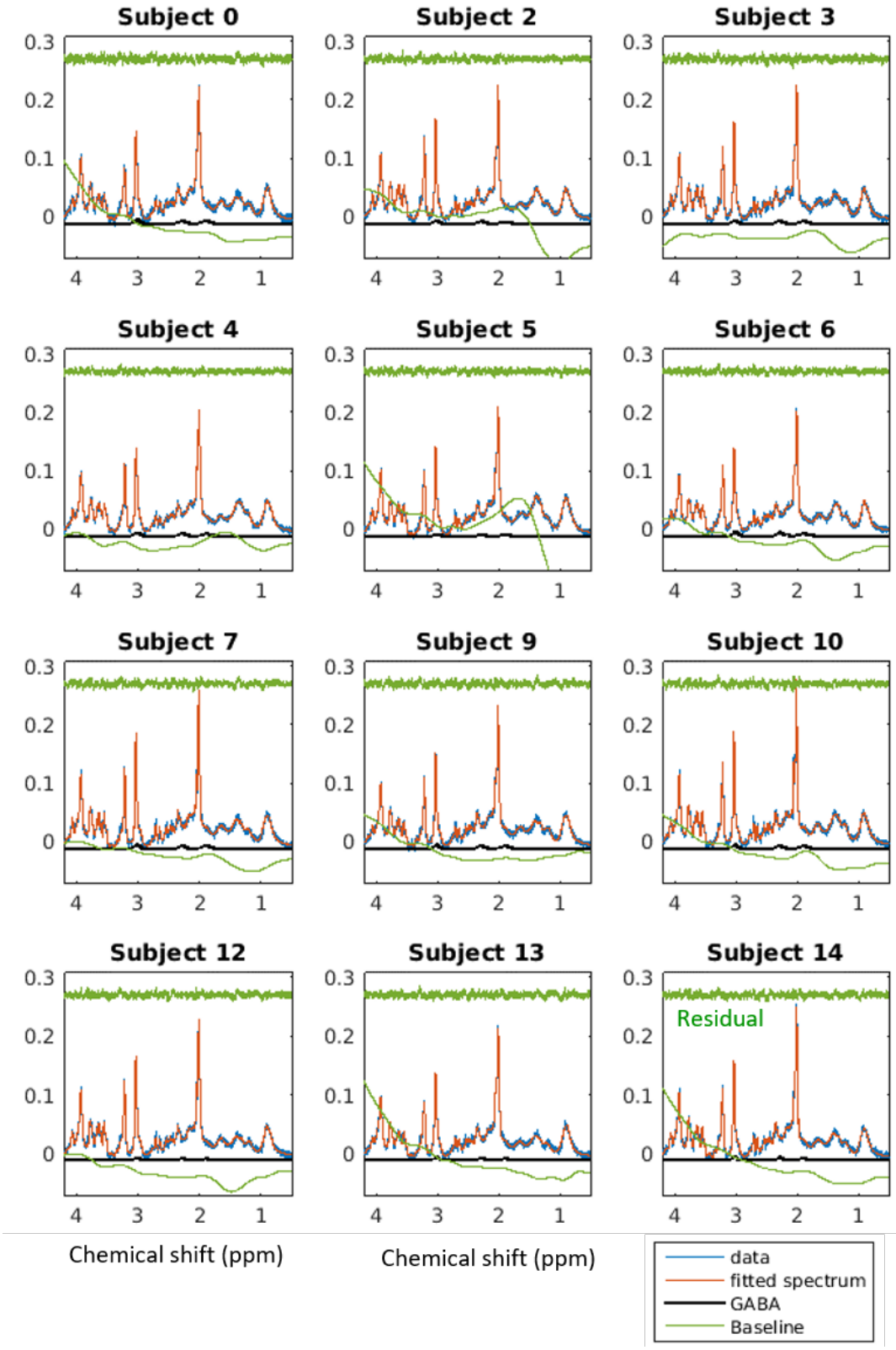



Figure D.5: Second Run: STEAM data fitted by LCModel.

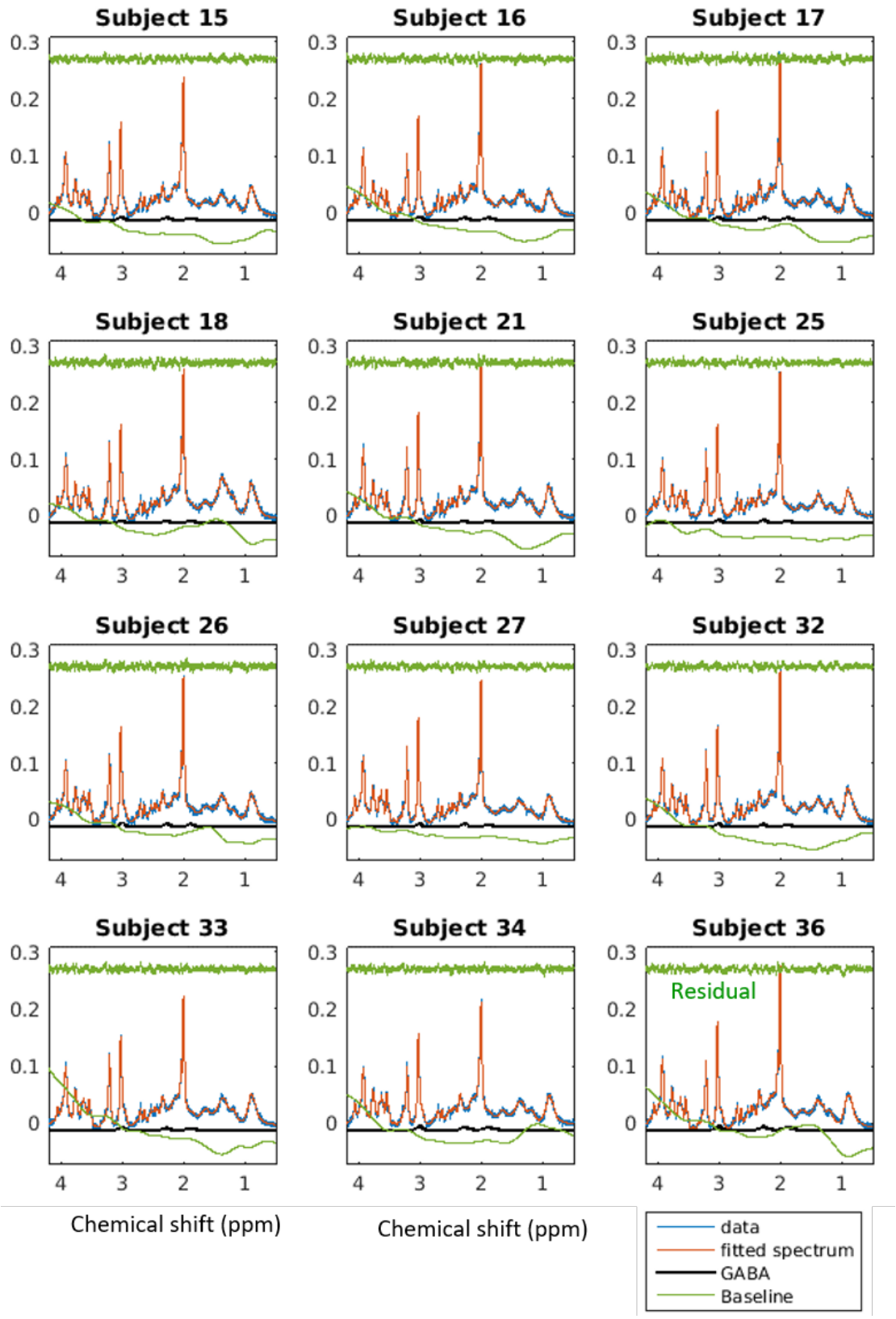



Figure D.6: Second Run: STEAM data fitted by LCModel.

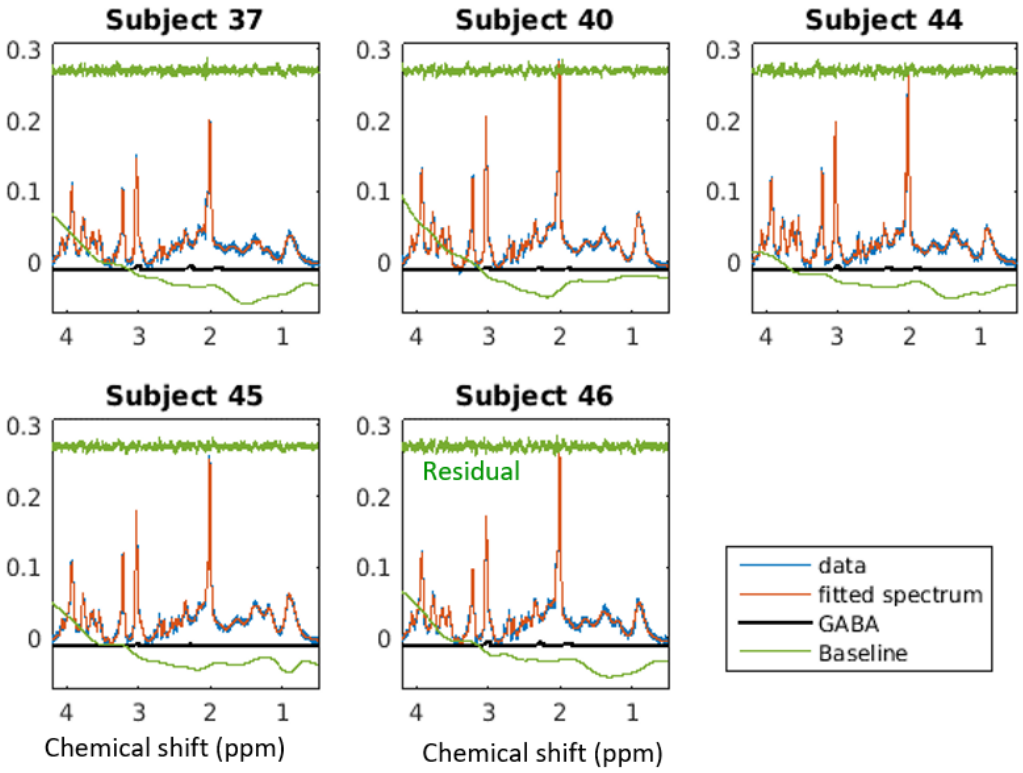



Figure D.7: Second Run: STEAM data fitted by LCModel.

# Chapter 6

# Final Remarks

Neural oscillations and functional connectivity measures in MEG data are proving to be of great importance in clinical research and the understanding of various pathologies. A number of studies have implicated beta oscillations in neurodevelopment [Gaetz et al., 2010], mental health disorders (e.g. schizophrenia [Robson et al., 2016]) and neuropathologies such as multiple sclerosis [Barratt et al., 2017], Parkinson's disease [Schnitzler and Gross, 2005] and dementia [Sami et al., 2018]. However, despite recent efforts in neural modelling [Sherman et al., 2016], the cortical origin of beta oscillations and their dependence on neurochemistry is still uncertain with current evidence pointing to a dependence of beta oscillations on the inhibitory neurotransmitter GABA observed through pharmacological manipulation [Jensen et al., 2005; Hall et al., 2011; Muthukumaraswamy et al., 2013].

In the work presented in chapter 3 I showed that resting state connectivity assessed with MEG can be a robust measure when calculated over long recordings. This robustness is key if MEG connectivity measures are to be proven valuable for clinical applications. Moreover, the reproducibility of static functional connectivity networks was found to be limited by the temporal dynamics of the networks themselves, supporting the evidence that functional networks are composed of multiple sub networks engaging and disengaging over faster timescales [Baker et al., 2014].

In chapter 4 I investigated the role of beta oscillations in the somatosensory system through a spatially-selective attention task. I was able to replicate the findings of Bauer et al. [2006] showing the beta rebound to be dependent on attention, with suppressed non-attended stimuli showing significantly stronger beta rebound compared to attended. In addition I demonstrated that the beta rebound supports a short lived ($\sim$ 500ms) increase in functional connectivity over a network involving the sensory, motor, parietal and temporal cortices. Beta power and functional connectivity in the contralateral sensory cortex were also predictive of task performance, with higher pre-stimulus beta amplitude and connectivity leading to increased detection errors. Furthermore, through MR proton spectroscopy at 7T, we show in chapter 5 that GABA concentration in the sensorimotor cortex correlates with beta power in a group of 46 subjects (greatly increasing the statistical power from the previous study by Gaetz et al. [2011] showing a similar effect). All together this evidence adds weight to the hypothesis of beta oscillations being a marker of inhibition and "top-down" control on the sensorimotor system.

## 6.1 Study limitations

The interpretation of an inhibitory role of the beta rebound in the sensorimotor system, although supported by various correlative evidence, remains speculative. Other oscillatory frequencies have not been assessed in depth, such as the gamma band, which showed a marked attentional effect in the sensory cortex, and the alpha band, which can be clearly seen in parietal and occipital cortex (Figure C.4). If the beta rebound indeed reflects "top-down" control, modulated by volitional attention, we could expect an involvement of the frontal cortex. Such an effect could be explored through metrics inferring directionality of connectivity or cross-frequency coupling, potentially between theta and gamma frequencies in the frontal cortex with the beta oscillations in the sensorimotor system.

In addition, when considering the effect of beta oscillations on behaviour, other

characteristics of neural oscillations may be worth investigating, such as latency of oscillatory responses and peak frequency. Recent work has highlighted how the beta rhythm often appears as discrete bursts of increased oscillatory amplitude rather than the sustained response seen in trial average data [Sherman et al., 2016]. The detection of beta bursts, though still in its infancy [Little et al., 2018], could add information of burst morphology and frequency of occurrence as measures of connectivity from synchronisation of bursts over separate areas of the cortex.

## 6.2 The end

The anatomical, metabolic and electrophysiological areas of neuroimaging research have often remained separate, leaving our understanding of the brain like a fragmented mosaic. In this thesis I presented a new avenue of understanding human brain function with non-invasive techniques, by integrating individual differences in electrophysiology, functional connectivity and neurochemistry. This multimodal approach offers a unique means to defragment our current disparate picture, and ultimately enable a new understanding of the human brain, in health and disease.

# References


Ahlfors, S. P., R. Ilmoniemi, and M. Hämäläinen

1992. Estimates of visually evoked cortical currents. *Electroencephalography and clinical neurophysiology*, 82(3):225–236.

Albrecht, J., M. Sidoryk-Węgrzynowicz, M. Zielińska, and M. Aschner

2010. Roles of glutamine in neurotransmission. *Neuron glia biology*, 6(4):263–276.

Allen, E. A., E. Damaraju, S. M. Plis, E. B. Erhardt, T. Eichele, and V. D. Calhoun

2014. Tracking whole-brain connectivity dynamics in the resting state. *Cerebral cortex*, 24(3):663–676.

Anderson, J. B. and R. Johnnesson

2006. *Understanding information transmission*, volume 18. John Wiley & Sons.

Andreychenko, A., V. O. Boer, C. S. Arteaga de Castro, P. R. Luijten, and D. W. Klomp

2012. Efficient spectral editing at 7 T: GABA detection with MEGA-sLASER. *Magnetic resonance in medicine*, 68(4):1018–1025.

Ashburner, J. and K. J. Friston

2005. Unified segmentation. *NeuroImage*, 26(3):839–851.

Auzias, G., O. Coulon, and A. Brovelli

2016. MarsAtlas: a cortical parcellation atlas for functional mapping. *Human brain mapping*, 37(4):1573–1592.

Azevedo, F. A. C., L. R. B. Carvalho, L. T. Grinberg, J. M. Farfel, R. E. L. Ferretti, R. E. P. Leite, W. J. Filho, R. Lent, and S. Herculano-Houzel

2009. Equal numbers of neuronal and nonneuronal cells make the human brain an isometrically scaled-up primate brain. *Journal of Comparative Neurology*, 513(5):532–541.

Baccalá, L. A. and K. Sameshima

2001. Partial directed coherence: a new concept in neural structure determination. *Biological cybernetics*, 84(6):463–474.

Baker, A. P., M. J. Brookes, I. A. Rezek, S. M. Smith, T. Behrens, P. J. P. Smith, and M. Woolrich

2014. Fast transient networks in spontaneous human brain activity. *Elife*, 3:e01867.

Bardeen, J., L. N. Cooper, and J. R. Schrieffer

1957. Microscopic theory of superconductivity. *Physical Review*, 106(1):162.

Barratt, E. L., S. T. Francis, P. G. Morris, and M. J. Brookes

2018. Mapping the topological organisation of beta oscillations in motor cortex using MEG. *NeuroImage*, 181:831–844.

Barratt, E. L., P. K. Tewarie, M. A. Clarke, E. L. Hall, P. A. Gowland, P. G. Morris, S. T. Francis, N. Evangelou, and M. J. Brookes

2017. Abnormal task driven neural oscillations in multiple sclerosis: A visuomotor MEG study. *Human brain mapping*, 38(5):2441–2453.

Bastos, A. M. and J.-M. Schoffelen

2016. A tutorial review of functional connectivity analysis methods and their interpretational pitfalls. *Frontiers in systems neuroscience*, 9:175.

Bauer, M., S. Kennett, and J. Driver

2012. Attentional selection of location and modality in vision and touch modulates low-frequency activity in associated sensory cortices. *American Journal of Physiology-Heart and Circulatory Physiology*.

Bauer, M., R. Oostenveld, M. Peeters, and P. Fries

2006. Tactile spatial attention enhances gamma-band activity in somatosensory cortex and reduces low-frequency activity in parieto-occipital areas. *Journal of Neuroscience*, 26(2):490–501.

Baule, G. M.

1963. Detection of the magnetic field of the heart. *American Heart Journal*, 66:95–96.

Belelli, D., N. L. Harrison, J. Maguire, R. L. Macdonald, M. C. Walker, and D. W. Cope

2009. Extrasynaptic $GABA_A$ receptors: form, pharmacology, and function. *Journal of Neuroscience*, 29(41):12757–12763.

Benchenane, K., A. Peyrache, M. Khamassi, P. L. Tierney, Y. Gioanni, F. P. Battaglia, and S. I. Wiener

2010. Coherent theta oscillations and reorganization of spike timing in the hippocampal-prefrontal network upon learning. *Neuron*, 66(6):921–936.

Benjamini, Y. and Y. Hochberg

1995. Controlling the false discovery rate: a practical and powerful approach to multiple testing. *Journal of the Royal statistical society: series B (Methodological)*, 57(1):289–300.

Berger, H.

1929. Über das elektrenkephalogramm des menschen. *Archiv für psychiatrie und nervenkrankheiten*, 87(1):527–570.

Betzel, R. F., M. Fukushima, Y. He, X.-N. Zuo, and O. Sporns

2016. Dynamic fluctuations coincide with periods of high and low modularity in resting-state functional brain networks. *NeuroImage*, 127:287–297.

Biswal, B., F. Zerrin Yetkin, V. M. Haughton, and J. S. Hyde

1995. Functional connectivity in the motor cortex of resting human brain using echo-planar MRI. *Magnetic resonance in medicine*, 34(4):537–541.

Bloch, F.

1946. Nuclear induction. *Physical review*, 70(7-8):460.

Borna, A., T. R. Carter, J. D. Goldberg, A. P. Colombo, Y.-Y. Jau, C. Berry, J. McKay, J. Stephen, M. Weisend, and P. D. D. Schwindt

2017. A 20-channel magnetoencephalography system based on optically pumped magnetometers. *Physics in Medicine & Biology*, 62(23):8909.

Boto, E., R. Bowtell, P. Krüger, T. M. Fromhold, P. G. Morris, S. S. Meyer, G. R. Barnes, and M. J. Brookes

2016. On the potential of a new generation of magnetometers for MEG: a beamformer simulation study. *PLoS One*, 11(8):e0157655.

Boto, E., N. Holmes, J. Leggett, G. Roberts, V. Shah, S. S. Meyer, L. D. Muñoz, K. J. Mullinger, T. M. Tierney, S. Bestmann, et al.

2018. Moving magnetoencephalography towards real-world applications with a wearable system. *Nature*, 555(7698):657.

Bottomley, P. A.

1984. Selective volume method for performing localized NMR spectroscopy. US Patent 4,480,228.

Breakspear, M., L. M. Williams, and C. J. Stam

2004. A novel method for the topographic analysis of neural activity reveals formation and dissolution of 'dynamic cell assemblies'. *Journal of computational neuroscience*, 16(1):49–68.

Brookes, M. J., J. R. Hale, J. M. Zumer, C. M. Stevenson, S. T. Francis, G. R. Barnes, J. P. Owen, P. G. Morris, and S. S. Nagarajan

2011a. Measuring functional connectivity using MEG: methodology and comparison with fcMRI. *NeuroImage*, 56(3):1082–1104.

Brookes, M. J., E. L. Hall, S. E. Robson, D. Price, L. Palaniyappan, E. B. Liddle, P. F. Liddle, S. E. Robinson, and P. G. Morris

2015. Complexity measures in magnetoencephalography: measuring "disorder" in schizophrenia. *PLoS One*, 10(4):e0120991.

Brookes, M. J., G. C. O'Neill, E. L. Hall, M. W. Woolrich, A. Baker, S. P. Corner, S. E. Robson, P. G. Morris, and G. R. Barnes

2014. Measuring temporal, spectral and spatial changes in electrophysiological brain network connectivity. *NeuroImage*, 91:282–299.

Brookes, M. J., J. Vrba, S. E. Robinson, C. M. Stevenson, A. M. Peters, G. R. Barnes, A. Hillebrand, and P. G. Morris

2008. Optimising experimental design for MEG beamformer imaging. *NeuroImage*, 39(4):1788–1802.

Brookes, M. J., M. Woolrich, H. Luckhoo, D. Price, J. R. Hale, M. C. Stephenson, G. R. Barnes, S. M. Smith, and P. G. Morris

2011b. Investigating the electrophysiological basis of resting state networks using magnetoencephalography. *Proceedings of the National Academy of Sciences*, P. 201112685.

Brookes, M. J., M. W. Woolrich, and G. R. Barnes

2012. Measuring functional connectivity in MEG: a multivariate approach insensitive to linear source leakage. *NeuroImage*, 63(2):910–920.

Brookes, M. J., J. M. Zumer, C. M. Stevenson, J. R. Hale, G. R. Barnes, J. Vrba,

and P. G. Morris

2010. Investigating spatial specificity and data averaging in MEG. *NeuroImage*, 49(1):525–538.

Buffalo, E. A., P. Fries, R. Landman, T. J. Buschman, and R. Desimone

2011. Laminar differences in gamma and alpha coherence in the ventral stream. *Proceedings of the National Academy of Sciences*, 108(27):11262–11267.

Caton, R.

1875. The electrical currents of the brain. *British Medical Journal*, 2:278.

Chang, C. and G. H. Glover

2010. Time–frequency dynamics of resting-state brain connectivity measured with fMRI. *NeuroImage*, 50(1):81–98.

Chen, C., H. P. Sigurdsson, S. E. Pépés, D. P. Auer, P. G. Morris, P. S. Morgan, P. A. Gowland, and S. R. Jackson

2017. Activation induced changes in GABA: functional MRS at 7 T with MEGA-sLASER. *NeuroImage*, 156:207–213.

Cohen, D.

1968. Magnetoencephalography: evidence of magnetic fields produced by alpha-rhythm currents. *Science*, 161(3843):784–786.

Cohen, D.

1972. Magnetoencephalography: detection of the brain's electrical activity with a superconducting magnetometer. *Science*, 175(4022):664–666.

Colclough, G. L., M. J. Brookes, S. M. Smith, and M. W. Woolrich

2015. A symmetric multivariate leakage correction for MEG connectomes. *NeuroImage*, 117:439–448.

Colclough, G. L., M. W. Woolrich, P. K. Tewarie, M. J. Brookes, A. J. Quinn,

and S. M. Smith

2016. How reliable are MEG resting-state connectivity metrics? *NeuroImage*, 138:284–293.

Coombs, J. S., D. R. Curtis, and J. C. Eccles

1957. The interpretation of spike potentials of motoneurones. *The Journal of Physiology*, 139(2):198–231.

Cousijn, H., S. Haegens, G. Wallis, J. Near, M. G. Stokes, P. J. Harrison, and A. C. Nobre

2014. Resting GABA and glutamate concentrations do not predict visual gamma frequency or amplitude. *Proceedings of the National Academy of Sciences*, 111(25):9301–9306.

Curio, G.

2000. Linking 600-hz "spikelike" eeg/meg wavelets ("ς-bursts") to cellular substrates: Concepts and caveats. *Journal of Clinical Neurophysiology*, 17(4):377–396.

Dale, A. M. and M. I. Sereno

1993. Improved localization of cortical activity by combining EEG and MEG with MRI cortical surface reconstruction: a linear approach. *Journal of cognitive neuroscience*, 5(2):162–176.

Damoiseaux, J. S., S. A. R. B. Rombouts, F. Barkhof, P. Scheltens, C. J. Stam, S. M. Smith, and C. F. Beckmann

2006. Consistent resting-state networks across healthy subjects. *Proceedings of the National Academy of Sciences*, 103(37):13848–13853.

De Pasquale, F., S. Della Penna, A. Z. Snyder, C. Lewis, D. Mantini, L. Marzetti, P. Belardinelli, L. Ciancetta, V. Pizzella, G. L. Romani, and M. Corbetta

2010. Temporal dynamics of spontaneous MEG activity in brain networks. *Proceedings of the National Academy of Sciences*, 107(13):6040–6045.

Dunkley, B. T., L. Da Costa, A. Bethune, R. Jetly, E. W. Pang, M. J. Taylor, and S. M. Doesburg

2015. Low-frequency connectivity is associated with mild traumatic brain injury. *NeuroImage: clinical*, 7:611–621.

Engel, A. K., C. Gerloff, C. C. Hilgetag, and G. Nolte

2013. Intrinsic coupling modes: multiscale interactions in ongoing brain activity. *Neuron*, 80(4):867–886.

Ferrari, M., I. Giannini, G. Sideri, and E. Zanette

1985. Continuous non invasive monitoring of human brain by near infrared spectroscopy. In *Oxygen transport to tissue VII*, Pp. 873–882. Springer.

Feynman, R. P., R. B. Leighton, and M. Sands

1965. *The Feynman lectures on physics. Vol. 3: Quantum mechanics*. Addison-Wesley Publishing Co., Inc., Reading, Mass.-London.

Finn, E. S., X. Shen, D. Scheinost, M. D. Rosenberg, J. Huang, M. M. Chun, X. Papademetris, and R. T. Constable

2015. Functional connectome fingerprinting: identifying individuals using patterns of brain connectivity. *Nature neuroscience*, 18(11):1664.

Fox, M. D., A. Z. Snyder, J. L. Vincent, M. Corbetta, D. C. Van Essen, and M. E. Raichle

2005. The human brain is intrinsically organized into dynamic, anticorrelated functional networks. *Proceedings of the National Academy of Sciences*, 102(27):9673–9678.

Fox, P. T., M. A. Mintun, M. E. Raichle, and P. Herscovitch

1984. A noninvasive approach to quantitative functional brain mapping with $H_2{}^{15}O$ and positron emission tomography. *Journal of Cerebral Blood Flow & Metabolism*, 4(3):329–333.

Frahm, J. a., H. Bruhn, M. Gyngell, K. Merboldt, W. Hänicke, and R. Sauter

1989. Localized high-resolution proton NMR spectroscopy using stimulated echoes: initial applications to human brain in vivo. *Magnetic Resonance in Medicine*, 9(1):79–93.

Fraschini, M., M. Demuru, A. Crobe, F. Marrosu, C. J. Stam, and A. Hillebrand

2016. The effect of epoch length on estimated EEG functional connectivity and brain network organisation. *Journal of neural engineering*, 13(3):036015.

Fries, P.

2005. A mechanism for cognitive dynamics: neuronal communication through neuronal coherence. *Trends in cognitive sciences*, 9(10):474–480.

Fries, P.

2015. Rhythms for cognition: communication through coherence. *Neuron*, 88(1):220–235.

Friston, K. J.

1998. The disconnection hypothesis. *Schizophrenia research*, 30(2):115–125.

Gaetz, W., J. C. Edgar, D. Wang, and T. P. Roberts

2011. Relating MEG measured motor cortical oscillations to resting $\gamma$-aminobutyric acid (GABA) concentration. *NeuroImage*, 55(2):616–621.

Gaetz, W., M. Macdonald, D. Cheyne, and O. Snead

2010. Neuromagnetic imaging of movement-related cortical oscillations in children and adults: age predicts post-movement beta rebound. *NeuroImage*, 51(2):792–807.

Geselowitz, D.

1970. On the magnetic field generated outside an inhomogeneous volume conductor by internal current sources. *IEEE Transactions on Magnetics*, 6(2):346–347.

Goldman, D. E.

1943. Potential, impedance, and rectification in membranes. *The Journal of general physiology*, 27(1):37–60.

Govindaraju, V., K. Young, and A. A. Maudsley

2000. Proton NMR chemical shifts and coupling constants for brain metabolites. *NMR in Biomedicine*, 13(3):129–153.

Granger, C. W.

1969. Investigating causal relations by econometric models and cross-spectral methods. *Econometrica: Journal of the Econometric Society*, Pp. 424–438.

Greve, D. N. and B. Fischl

2009. Accurate and robust brain image alignment using boundary-based registration. *NeuroImage*, 48(1):63–72.

Grinsted, A., J. C. Moore, and S. Jevrejeva

2004. Application of the cross wavelet transform and wavelet coherence to geophysical time series. *Nonlinear processes in geophysics*, 11(5/6):561–566.

Gross, J., S. Baillet, G. R. Barnes, R. N. Henson, A. Hillebrand, O. Jensen, K. Jerbi, V. Litvak, B. Maess, R. Oostenveld, et al.

2013. Good practice for conducting and reporting MEG research. *NeuroImage*, 65:349–363.

Guggisberg, A. G., S. M. Honma, A. M. Findlay, S. S. Dalal, H. E. Kirsch, M. S. Berger, and S. S. Nagarajan

2008. Mapping functional connectivity in patients with brain lesions. *Annals of neurology*, 63(2):193–203.

Haenschel, C., R. A. Bittner, J. Waltz, F. Haertling, M. Wibral, W. Singer, D. E. J. Linden, and E. Rodriguez

2009. Cortical oscillatory activity is critical for working memory as revealed by deficits in early-onset schizophrenia. *Journal of Neuroscience*, 29(30):9481–9489.

Hahn, E. L.

1950. Spin echoes. *Physical review*, 80(4):580.

Hall, E. L., S. E. Robson, P. G. Morris, and M. J. Brookes

2014a. The relationship between MEG and fMRI. *NeuroImage*, 102:80–91.

Hall, E. L., M. C. Stephenson, D. Price, and P. G. Morris

2014b. Methodology for improved detection of low concentration metabolites in MRS: optimised combination of signals from multi-element coil arrays. *NeuroImage*, 86:35–42.

Hall, S. D., I. M. Stanford, N. Yamawaki, C. McAllister, K. Rönnqvist, G. L. Woodhall, and P. L. Furlong

2011. The role of GABAergic modulation in motor function related neuronal network activity. *NeuroImage*, 56(3):1506–1510.

Hämäläinen, M., R. Hari, R. J. Ilmoniemi, J. Knuutila, and O. V. Lounasmaa

1993. Magnetoencephalography—theory, instrumentation, and applications to noninvasive studies of the working human brain. *Reviews of modern Physics*, 65(2):413.

Hämäläinen, M. S. and R. J. Ilmoniemi

1994. Interpreting magnetic fields of the brain: minimum norm estimates. *Medical & biological engineering & computing*, 32(1):35–42.

Hansen, P., M. Kringelbach, and R. Salmelin

2010. *MEG: an introduction to methods*. Oxford university press.

Hari, R., K. Aittoniemi, M.-L. Järvinen, T. Katila, and T. Varpula

1980. Auditory evoked transient and sustained magnetic fields of the human brain localization of neural generators. *Experimental Brain Research*, 40(2):237–240.

Hari, R., H. Hämäläinen, M. Hämäläinen, J. Kekoni, M. Sams, and J. Tiihonen

1990. Separate finger representations at the human second somatosensory cortex. *Neuroscience*, 37(1):245–249.

Harris, A. D., N. A. Puts, and R. A. Edden

2015. Tissue correction for GABA-edited MRS: Considerations of voxel composition, tissue segmentation, and tissue relaxations. *Journal of Magnetic Resonance Imaging*, 42(5):1431–1440.

Hindriks, R., M. H. Adhikari, Y. Murayama, M. Ganzetti, D. Mantini, N. K. Logothetis, and G. Deco

2016. Can sliding-window correlations reveal dynamic functional connectivity in resting-state fMRI? *NeuroImage*, 127:242–256.

Hipp, J. F., D. J. Hawellek, M. Corbetta, M. Siegel, and A. K. Engel

2012. Large-scale cortical correlation structure of spontaneous oscillatory activity. *Nature neuroscience*, 15(6):884.

Hobson, J. A. and E. F. Pace-Schott

2002. The cognitive neuroscience of sleep: neuronal systems, consciousness and learning. *Nature Reviews Neuroscience*, 3(9):679.

Holmes, N., J. Leggett, E. Boto, G. Roberts, R. M. Hill, T. M. Tierney, V. Shah, G. R. Barnes, M. J. Brookes, and R. Bowtell

2018. A bi-planar coil system for nulling background magnetic fields in scalp mounted magnetoencephalography. *NeuroImage*, 181:760–774.

Huang, M., J. C. Mosher, and R. Leahy

1999. A sensor-weighted overlapping-sphere head model and exhaustive head model comparison for MEG. *Physics in Medicine & Biology*, 44(2):423.

Huang, M.-X., R. J. Theilmann, A. Robb, A. Angeles, S. Nichols, A. Drake, J. D'Andrea, M. Levy, M. Holland, T. Song, et al.

2009. Integrated imaging approach with MEG and DTI to detect mild trau-

matic brain injury in military and civilian patients. *Journal of neurotrauma*, 26(8):1213–1226.

Hunt, B. A., P. K. Tewarie, O. E. Mougin, N. Geades, D. K. Jones, K. D. Singh, P. G. Morris, P. A. Gowland, and M. J. Brookes

2016. Relationships between cortical myeloarchitecture and electrophysiological networks. *Proceedings of the National Academy of Sciences*, 113(47):13510–13515.

Hunt, B. A. E., E. B. Liddle, L. E. Gascoyne, L. Magazzini, B. C. Routley, K. D. Singh, P. G. Morris, M. J. Brookes, and P. F. Liddle

2018. Attenuated post-movement beta rebound associated with schizotypal features in healthy people. *Schizophrenia bulletin*.

Hutchison, R. M., T. Womelsdorf, E. A. Allen, P. A. Bandettini, V. D. Calhoun, M. Corbetta, S. Della Penna, J. H. Duyn, G. H. Glover, J. Gonzalez-Castillo, et al.

2013. Dynamic functional connectivity: promise, issues, and interpretations. *NeuroImage*, 80:360–378.

Iivanainen, J., M. Stenroos, and L. Parkkonen

2016. Measuring MEG closer to the brain: Performance of on-scalp sensor arrays. *bioRxiv*.

Iivanainen, J., R. Zetter, M. Groen, K. Hakkarainen, and L. Parkkonen

2018. On-scalp MEG system utilizing an actively shielded array of optically-pumped magnetometers. *bioRxiv*, P. 471391.

Jenkinson, M., P. Bannister, M. Brady, and S. Smith

2002. Improved optimization for the robust and accurate linear registration and motion correction of brain images. *NeuroImage*, 17(2):825–841.

Jenkinson, M. and S. Smith

2001. A global optimisation method for robust affine registration of brain images. *Medical image analysis*, 5(2):143–156.

Jensen, O., P. Goel, N. Kopell, M. Pohja, R. Hari, and B. Ermentrout

2005. On the human sensorimotor-cortex beta rhythm: sources and modeling. *NeuroImage*, 26(2):347–355.

Jensen, O. and A. Mazaheri

2010. Shaping functional architecture by oscillatory alpha activity: gating by inhibition. *Frontiers in human neuroscience*, 4:186.

Johansen-Berg, H.

2010. Behavioural relevance of variation in white matter microstructure. *Current opinion in neurology*, 23(4):351–358.

Jones, S. R., C. E. Kerr, Q. Wan, D. L. Pritchett, M. Hämäläinen, and C. I. Moore

2010. Cued spatial attention drives functionally relevant modulation of the mu rhythm in primary somatosensory cortex. *Journal of Neuroscience*, 30(41):13760–13765.

Josephson, B. D.

1962. Possible new effects in superconductive tunnelling. *Physics letters*, 1(7):251–253.

Jurkiewicz, M. T., W. C. Gaetz, A. C. Bostan, and D. Cheyne

2006. Post-movement beta rebound is generated in motor cortex: evidence from neuromagnetic recordings. *NeuroImage*, 32(3):1281–1289.

Kessler, D., M. Angstadt, R. C. Welsh, and C. Sripada

2014. Modality-spanning deficits in attention-deficit/hyperactivity disorder in functional networks, gray matter, and white matter. *Journal of Neuroscience*, 34(50):16555–16566.

Klose, U.

2008. Measurement sequences for single voxel proton MR spectroscopy. *European journal of radiology*, 67(2):194–201.

Kyuhou, S. and Y. C. Okada

1993. Detection of magnetic evoked fields associated with synchronous population activities in the transverse CA1 slice of the guinea pig. *Journal of neurophysiology*, 70(6):2665–2668.

Lachaux, J.-P., E. Rodriguez, J. Martinerie, and F. J. Varela

1999. Measuring phase synchrony in brain signals. *Human brain mapping*, 8(4):194–208.

Lauterber, P. C.

1973. Image formation by induced local interactions: examples employing nuclear magnetic resonance. *Nature*, 242:190.

Lewine, J. D., J. T. Davis, E. D. Bigler, R. Thoma, D. Hill, M. Funke, J. H. Sloan, S. Hall, and W. W. Orrison

2007. Objective documentation of traumatic brain injury subsequent to mild head trauma: multimodal brain imaging with MEG, SPECT, and MRI. *The Journal of head trauma rehabilitation*, 22(3):141–155.

Lindquist, M. A., Y. Xu, M. B. Nebel, and B. S. Caffo

2014. Evaluating dynamic bivariate correlations in resting-state fMRI: a comparison study and a new approach. *NeuroImage*, 101:531–546.

Little, S., J. Bonaiuto, G. Barnes, and S. Bestmann

2018. Motor cortical beta transients delay movement initiation and track errors. *bioRxiv*, P. 384370.

Liuzzi, L., L. E. Gascoyne, P. K. Tewarie, E. L. Barratt, E. Boto, and M. J.

Brookes

2017. Optimising experimental design for MEG resting state functional connectivity measurement. *NeuroImage*, 155:565–576.

London, F.

1948. On the problem of the molecular theory of superconductivity. *Physical Review*, 74(5):562.

Löwdin, P.-O.

1950. On the non-orthogonality problem connected with the use of atomic wave functions in the theory of molecules and crystals. *The Journal of Chemical Physics*, 18(3):365–375.

Maguire, E. A., D. G. Gadian, I. S. Johnsrude, C. D. Good, J. Ashburner, R. S. Frackowiak, and C. D. Frith

2000. Navigation-related structural change in the hippocampi of taxi drivers. *Proceedings of the National Academy of Sciences*, 97(8):4398–4403.

Mansfield, P. and P. K. Grannell

1973. NMR 'diffraction' in solids? *Journal of Physics C: solid state physics*, 6(22):L422.

Mazziotta, J., A. Toga, A. Evans, P. Fox, J. Lancaster, K. Zilles, R. Woods, T. Paus, G. Simpson, B. Pike, et al.

2001. A probabilistic atlas and reference system for the human brain: International Consortium for Brain Mapping (ICBM). *Philosophical Transactions of the Royal Society of London. Series B: Biological Sciences*, 356(1412):1293–1322.

Mazziotta, J. C., A. W. Toga, A. Evans, P. Fox, J. Lancaster, et al.

1995. A probabilistic atlas of the human brain: theory and rationale for its development. *NeuroImage*, 2(2):89–101.

Meissner, W. and R. Ochsenfeld

1933. A new effect upon the occurrence of superconductivity. *Naturwissenschaften*, 21(44):787–788.

Meyer, G., T. H. Gonzalez-Hernandez, and R. Ferres-Torres

1989. The spiny stellate neurons in layer IV of the human auditory cortex. A Golgi study. *Neuroscience*, 33(3):489–498.

Meyer, S. S., J. Bonaiuto, M. Lim, H. Rossiter, S. Waters, D. Bradbury, S. Bestmann, M. Brookes, M. F. Callaghan, N. Weiskopf, et al.

2017. Flexible head-casts for high spatial precision MEG. *Journal of neuroscience methods*, 276:38–45.

Murakami, S. and Y. Okada

2006. Contributions of principal neocortical neurons to magnetoencephalography and electroencephalography signals. *The Journal of physiology*, 575(3):925–936.

Murdoch, J. and D. Lampman

1993. Beyond WET and DRY: optimized pulses for water suppression. In *Proceedings of the SMRM 12th Annual Meeting*, P. 1191.

Muthukumaraswamy, S. D., R. A. E. Edden, D. K. Jones, J. B. Swettenham, and K. D. Singh

2009. Resting GABA concentration predicts peak gamma frequency and fMRI amplitude in response to visual stimulation in humans. *Proceedings of the National Academy of Sciences*, 106(20):8356–8361.

Muthukumaraswamy, S. D., J. F. Myers, S. J. Wilson, D. J. Nutt, A. Lingford-Hughes, K. D. Singh, and K. Hamandi

2013. The effects of elevated endogenous GABA levels on movement-related network oscillations. *NeuroImage*, 66:36–41.

Niessing, J., B. Ebisch, K. E. Schmidt, M. Niessing, W. Singer, and R. A. Galuske

2005. Hemodynamic signals correlate tightly with synchronized gamma oscillations. *science*, 309(5736):948–951.

Nolte, G., O. Bai, L. Wheaton, Z. Mari, S. Vorbach, and M. Hallett

2004. Identifying true brain interaction from EEG data using the imaginary part of coherency. *Clinical neurophysiology*, 115(10):2292–2307.

Nolte, G., A. Ziehe, V. V. Nikulin, A. Schlögl, N. Krämer, T. Brismar, and K.-R. Müller

2008. Robustly estimating the flow direction of information in complex physical systems. *Physical review letters*, 100(23):234101.

Ogawa, S., T.-M. Lee, A. R. Kay, and D. W. Tank

1990. Brain magnetic resonance imaging with contrast dependent on blood oxygenation. *Proceedings of the National Academy of Sciences*, 87(24):9868–9872.

Okada, Y. C., J. Wu, and S. Kyuhou

1997. Genesis of MEG signals in a mammalian CNS structure. *Clinical Neurophysiology*, 103(4):474–485.

O'Neill, G. C., M. Bauer, M. W. Woolrich, P. G. Morris, G. R. Barnes, and M. J. Brookes

2015. Dynamic recruitment of resting state sub-networks. *NeuroImage*, 115:85–95.

O'Neill, G. C., P. Tewarie, D. Vidaurre, L. Liuzzi, M. W. Woolrich, and M. J. Brookes

2018. Dynamics of large-scale electrophysiological networks: a technical review. *NeuroImage*, 180:559–576.

O'Neill, G. C., P. K. Tewarie, G. L. Colclough, L. E. Gascoyne, B. A. Hunt, P. G.

Morris, M. W. Woolrich, and M. J. Brookes

2017. Measurement of dynamic task related functional networks using MEG. *NeuroImage*, 146:667–678.

Onnes, H. K.

1911. Further experiments with Liquid Helium G. On the electrical resistance of Pure Metals etc. VI. On the Sudden Change in the Rate at which the Resistance of Mercury Disappears. *Koninklijke Nederlandse Akademie van Weteschappen Proceedings Series B Physical Sciences*, 14:1911–1912.

Ordidge, R. J., A. Connelly, and J. A. B. Lohman

1986. Image-selected in vivo spectroscopy (ISIS). a new technique for spatially selective NMR spectroscopy. *Journal of Magnetic Resonance (1969)*, 66(2):283–294.

Palaniyappan, L. and P. F. Liddle

2012. Does the salience network play a cardinal role in psychosis? An emerging hypothesis of insular dysfunction. *Journal of Psychiatry & Neuroscience*.

Palus, M.

1997. Detecting phase synchronization in noisy systems. *Physics Letters A*, 235(4):341–351.

Pfurtscheller, G. and F. L. Da Silva

1999. Event-related EEG/MEG synchronization and desynchronization: basic principles. *Clinical neurophysiology*, 110(11):1842–1857.

Prichard, D. and J. Theiler

1994. Generating surrogate data for time series with several simultaneously measured variables. *Physical review letters*, 73(7):951.

Purcell, E. M., H. C. Torrey, and R. V. Pound

1946. Resonance absorption by nuclear magnetic moments in a solid. *Physical review*, 69(1-2):37.

Rall, W.

1959. Branching dendritic trees and motoneuron membrane resistivity. *Experimental neurology*, 1(5):491–527.

Robson, S. E., M. J. Brookes, E. L. Hall, L. Palaniyappan, J. Kumar, M. Skelton, N. G. Christodoulou, A. Qureshi, F. Jan, M. Z. Katshu, et al.

2016. Abnormal visuomotor processing in schizophrenia. *NeuroImage: Clinical*, 12:869–878.

Rooney, W. D., G. Johnson, X. Li, E. R. Cohen, S.-G. Kim, K. Ugurbil, and C. S. Springer Jr

2007. Magnetic field and tissue dependencies of human brain longitudinal $^{1}H_2O$ relaxation in vivo. *Magnetic Resonance in Medicine: An Official Journal of the International Society for Magnetic Resonance in Medicine*, 57(2):308–318.

Sami, S., N. Williams, L. E. Hughes, T. E. Cope, T. Rittman, I. T. Coyle-Gilchrist, R. N. Henson, and J. B. Rowe

2018. Neurophysiological signatures of Alzheimer's disease and frontotemporal lobar degeneration: pathology versus phenotype. *Brain*, 141(8):2500–2510.

Sarvas, J.

1987. Basic mathematical and electromagnetic concepts of the biomagnetic inverse problem. *Physics in Medicine & Biology*, 32(1):11.

Scheenen, T. W. J., D. W. J. Klomp, J. P. Wijnen, and A. Heerschap

2008. Short echo time $^{1}$H-MRSI of the human brain at 3T with minimal chemical shift displacement errors using adiabatic refocusing pulses. *Magnetic Resonance in Medicine*, 59(1):1–6.

Schmiedt, C., A. Brand, H. Hildebrandt, and C. Basar-Eroglu

2005. Event-related theta oscillations during working memory tasks in patients with schizophrenia and healthy controls. *Cognitive Brain Research*, 25(3):936–947.

Schnitzler, A. and J. Gross

2005. Normal and pathological oscillatory communication in the brain. *Nature reviews neuroscience*, 6(4):285.

Scholz, J., M. C. Klein, T. E. Behrens, and H. Johansen-Berg

2009. Training induces changes in white-matter architecture. *Nature neuroscience*, 12(11):1370.

Schreiber, T.

2000. Measuring information transfer. *Physical review letters*, 85(2):461.

Schreiber, T. and A. Schmitz

1996. Improved surrogate data for nonlinearity tests. *Physical Review Letters*, 77(4):635.

Sekihara, K. and S. S. Nagarajan

2008. *Adaptive spatial filters for electromagnetic brain imaging*. Springer Science & Business Media.

Sekihara, K., S. S. Nagarajan, D. Poeppel, and A. Marantz

2004. Asymptotic snr of scalar and vector minimum-variance beamformers for neuromagnetic source reconstruction. *IEEE transactions on biomedical engineering*, 51(10):1726–1734.

Shelly, C. D., E. A. Matrozova, and V. T. Petrashov

2016. Resolving thermoelectric "paradox" in superconductors. *Science advances*, 2(2):e1501250.

Sherman, M. A., S. Lee, R. Law, S. Haegens, C. A. Thorn, M. S. Hämäläinen, C. I. Moore, and S. R. Jones

2016. Neural mechanisms of transient neocortical beta rhythms: converging evidence from humans, computational modeling, monkeys, and mice. *Proceedings of the National Academy of Sciences*, 113(33):E4885–E4894.

Spruston, N.

2008. Pyramidal neurons: dendritic structure and synaptic integration. *Nature Reviews Neuroscience*, 9(3):206.

Stagg, C. J., V. Bachtiar, and H. Johansen-Berg

2011. What are we measuring with GABA magnetic resonance spectroscopy? *Communicative & integrative biology*, 4(5):573–575.

Stam, C. J., G. Nolte, and A. Daffertshofer

2007. Phase lag index: assessment of functional connectivity from multi channel EEG and MEG with diminished bias from common sources. *Human brain mapping*, 28(11):1178–1193.

Stam, C. J. and B. W. Van Dijk

2002. Synchronization likelihood: an unbiased measure of generalized synchronization in multivariate data sets. *Physica D: Nonlinear Phenomena*, 163(3-4):236–251.

Stenroos, M., A. Hunold, and J. Haueisen

2014. Comparison of three-shell and simplified volume conductor models in magnetoencephalography. *NeuroImage*, 94:337–348.

Stevenson, C., M. Brookes, J. D. López, L. Troebinger, J. Mattout, W. Penny, P. Morris, A. Hillebrand, R. Henson, and G. Barnes

2014. Does function fit structure? A ground truth for non-invasive neuroimaging. *NeuroImage*, 94:89–95.

Stufflebeam, S. M., H. Liu, J. Sepulcre, N. Tanaka, R. L. Buckner, and J. R. Madsen

2011. Localization of focal epileptic discharges using functional connectivity magnetic resonance imaging. *Journal of neurosurgery*, 114(6):1693–1697.

Tewarie, P., M. G. Bright, A. Hillebrand, S. E. Robson, L. E. Gascoyne, P. G.

Morris, J. Meier, P. Van Mieghem, and M. J. Brookes

2016. Predicting haemodynamic networks using electrophysiology: The role of non-linear and cross-frequency interactions. *NeuroImage*, 130:273–292.

Tewarie, P., B. A. Hunt, G. C. O'Neill, A. Byrne, K. Aquino, M. Bauer, K. J. Mullinger, S. Coombes, and M. J. Brookes

2018. Relationships between neuronal oscillatory amplitude and dynamic functional connectivity. *Cerebral Cortex*, 1:14.

Tewarie, P., L. Liuzzi, G. C. O'Neill, A. Quinn, A. Griffa, M. W. Woolrich, C. J. Stam, A. Hillebrand, and M. J. Brookes

2019. Tracking dynamic brain networks using high temporal resolution MEG measures of functional connectivity. *NeuroImage*, in review.

Thompson, R. B. and P. S. Allen

2001. Response of metabolites with coupled spins to the STEAM sequence. *Magnetic Resonance in Medicine*, 45(6):955–965.

Tikhonov, A. N.

1943. On the stability of inverse problems. In *Dokl. Akad. Nauk SSSR*, volume 39, Pp. 195–198.

Tkáč, I., Z. Starčuk, I.-Y. Choi, and R. Gruetter

1999. In vivo $^{1}$H NMR spectroscopy of rat brain at 1 ms echo time. *Magnetic Resonance in Medicine*, 41(4):649–656.

Troebinger, L., J. D. López, A. Lutti, D. Bradbury, S. Bestmann, and G. Barnes

2014. High precision anatomy for MEG. *NeuroImage*, 86:583–591.

Tzourio-Mazoyer, N., B. Landeau, D. Papathanassiou, F. Crivello, O. Etard, N. Delcroix, B. Mazoyer, and M. Joliot

2002. Automated anatomical labeling of activations in SPM using a macroscopic anatomical parcellation of the MNI MRI single-subject brain. *NeuroImage*, 15(1):273–289.

van Dellen, E., L. Douw, A. Hillebrand, I. H. Ris-Hilgersom, M. M. Schoonheim, J. C. Baayen, P. C. D. W. Hamer, D. N. Velis, M. Klein, J. J. Heimans, et al.
2012. MEG network differences between low-and high-grade glioma related to epilepsy and cognition. *PloS one*, 7(11):e50122.

Van Kerkoerle, T., M. W. Self, B. Dagnino, M.-A. Gariel-Mathis, J. Poort, C. Van Der Togt, and P. R. Roelfsema
2014. Alpha and gamma oscillations characterize feedback and feedforward processing in monkey visual cortex. *Proceedings of the National Academy of Sciences*, 111(40):14332–14341.

Van Veen, B. D., W. Van Drongelen, M. Yuchtman, and A. Suzuki
1997. Localization of brain electrical activity via linearly constrained minimum variance spatial filtering. *IEEE Transactions on biomedical engineering*, 44(9):867–880.

Vidaurre, D., A. J. Quinn, A. P. Baker, D. Dupret, A. Tejero-Cantero, and M. W. Woolrich
2016. Spectrally resolved fast transient brain states in electrophysiological data. *NeuroImage*, 126:81–95.

Vidaurre, D., S. M. Smith, and M. W. Woolrich
2017. Brain network dynamics are hierarchically organized in time. *Proceedings of the National Academy of Sciences*, 114(48):12827–12832.

Vinck, M., R. Oostenveld, M. Van Wingerden, F. Battaglia, and C. M. A. Pennartz
2011. An improved index of phase-synchronization for electrophysiological data in the presence of volume-conduction, noise and sample-size bias. *NeuroImage*, 55(4):1548–1565.

Vrba, J.
2002. Magnetoencephalography: the art of finding a needle in a haystack. *Physica C: Superconductivity*, 368(1-4):1–9.

Vrba, J. and S. E. Robinson

2001. Signal processing in magnetoencephalography. *Methods*, 25(2):249–271.

Walsh, P., N. Kane, and S. Butler

2005. The clinical role of evoked potentials. *Journal of Neurology, Neurosurgery & Psychiatry*, 76(suppl 2):ii16–ii22.

Wens, V., M. Bourguignon, S. Goldman, B. Marty, M. O. De Beeck, C. Clumeck, A. Mary, P. Peigneux, P. Van Bogaert, M. J. Brookes, et al.

2014. Inter-and intra-subject variability of neuromagnetic resting state networks. *Brain topography*, 27(5):620–634.

Wright, P. J., O. E. Mougin, J. J. Totman, A. M. Peters, M. J. Brookes, R. Coxon, P. E. Morris, M. Clemence, S. T. Francis, R. W. Bowtell, and P. A. Gowland

2008. Water proton $T_1$ measurements in brain tissue at 7, 3, and 1.5 T using IR-EPI, IR-TSE, and MPRAGE: results and optimization. *Magnetic Resonance Materials in Physics, Biology and Medicine*, 21(1-2):121.

Zimmerman, J. E., P. Thiene, and J. T. Harding

1970. Design and operation of stable rf-biased superconducting point-contact quantum devices, and a note on the properties of perfectly clean metal contacts. *Journal of Applied Physics*, 41(4):1572–1580.

Zumer, J. M., R. Scheeringa, J.-M. Schoffelen, D. G. Norris, and O. Jensen

2014. Occipital alpha activity during stimulus processing gates the information flow to object-selective cortex. *PLoS biology*, 12(10):e1001965.